Abstract

Title of Dissertation: Using *Fermi* Large Area Telescope Observations to Constrain the Emission and Field Geometries of Young Gamma-ray Pulsars and to Guide Millisecond Pulsar Searches

Megan Elizabeth DeCesar, Doctor of Philosophy, 2013

Dissertation directed by: Professor M. Coleman Miller
Department of Astronomy

This thesis has two parts, the first focusing on analysis and modeling of high-energy pulsar emission and the second on pulsar observations. In part 1, I constrain the magnetospheric emission geometry (magnetic inclination α, emission width w, maximum emission radius r, and observer colatitude ζ) by modeling $> 100\,\mathrm{MeV}$ light curves of four bright γ-ray pulsars with geometrical representations of the slot gap and outer gap emission models. I also model the $> 100\,\mathrm{MeV}$ phase resolved spectra, measuring the power law cutoff energy E_c with phase. Assuming curvature radiation reaction (CRR) is the dominant emission process, I use E_c to compute the accelerating electric field strength, $E_\parallel$.

The original contributions of this thesis to astrophysical research are the use of the force-free magnetic field solution in light curve modeling, the inclusion of an off-set polar cap in the slot gap geometry, and the calculation of $E_\parallel$ from observationally determined quantities (i.e., E_c).

The simulations reproduce observed light curve features and accurately match multi-wavelength ζ measurements, but the specific combination of best-fit emission and field geometry varies between pulsars. Perhaps pulsar magnetospheres contain some combination of slot gap and outer gap geometries, whose contributions to the

light curve depend on viewing angle. The requirement that, locally, $E_{\parallel}/B < 1$ rules out the vacuum field as a valid approximation to the true pulsar field under the CRR assumption. The $E_{\parallel}$ values imply that the youngest, most energetic pulsar has a near-force-free field, and that CRR and/or narrow acceleration gaps may not be applicable to older pulsars.

In part 2, I present discoveries of two radio millisecond pulsars (MSPs) from LAT-guided pulsar searches. I timed the first MSP, resulting in the detection of γ-ray pulsations. The second MSP is in a globular cluster. My initial timing efforts show that it is in a highly eccentric ($e \sim 0.95$) binary orbit with a massive ($> 0.7\,M_{\odot}$) companion, suggestive of past companion exchanges and an exotic nature of the current companion. Further timing will yield a measurement of the orbital precession rate and the system mass, yielding neutron star mass constraints.

Using *Fermi* Large Area Telescope Observations to Constrain the Emission and Field Geometries of Young Gamma-ray Pulsars and to Guide Millisecond Pulsar Searches

by

Megan Elizabeth DeCesar

Dissertation submitted to the Faculty of the Graduate School of the
University of Maryland at College Park in partial fulfillment
of the requirements for the degree of
Doctor of Philosophy
2013

Advisory Committee:

Professor M. Coleman Miller, chair
Dr. Alice K. Harding, co-advisor
Professor Sylvain Veilleux
Professor Suvi Gezari
Professor Kara D. Hoffman, Dean's representative

Preface

This thesis is presented in two parts. The first part contains the majority of my thesis work, which focuses on the emission geometry of young gamma-ray pulsars. I use *Fermi* Large Area Telescope (LAT) data to model the pulsars' light curves and phase-resolved spectra. The second part involves searching for and timing millisecond pulsars. This portion of my thesis was largely the result of my own initiative, especially the searches of globular clusters.

There were a number of contributors to the light curve modeling that I did for this thesis. J. Dyks and A. Harding developed the code used to simulate the light curves, C. Kalapotharakos provided the force-free magnetic field solution data, and M. C. Miller allowed me to use his Markov chain Monte Carlo (MCMC) likelihood code. I used these contributions to model the light curves. I constructed the observed LAT light curves used in this analysis, I ran the light curve simulations, and I wrote the code to calculate χ^2 between the observed and modeled light curves, which was then passed to the MCMC code. One outcome of my thesis is that this process has been automated, so that it will be straightforward to model the light curves of many more pulsars in the future. I also performed the spectral analysis of three of the pulsars considered here, automated a phase resolved spectral fitting routine, and wrote the codes and scripts to calculate the electric field under the assumptions described in the thesis. The results presented here have previously been presented (incompletely)

in the conference proceedings DeCesar et al. (2011a), DeCesar et al. (2011b), and Harding et al. (2011). Some of the results for PSR J0007+7303 were presented in Abdo et al. (2012). An upcoming paper (DeCesar et al. 2013a, in preparation) will contain all of the geometrical constraint results presented in this thesis.

I worked more independently in the second part of my thesis. My main collaborators were S. Ransom, P. Ray, and M. Roberts. For the first pulsar discovery, I searched data that was proposed for and taken by M. Roberts, J. Hessels, and M. McLaughlin. Its discovery was first published in Hessels et al. (2011) (of which I am a co-author), and the analysis presented in this thesis will be published along with similar analyses of three other millisecond pulsars in Bangale et al. (in preparation). The second pulsar was discovered through observations that I proposed with co-investigators S. Ransom and P. Ray. The discovery was presented in DeCesar et al. (2011c), and the results given in this thesis will be published in DeCesar et al. (2013b, in preparation).

This thesis is outlined as follows. In Chapter 1, I introduce the reader to rotation-powered pulsars, gamma-ray astronomy, the LAT instrument, and LAT data analysis. Chapter 2 describes interactions between photons and matter that are important in gamma-ray astronomy, and then describes the pulsar emission and magnetosphere models used to explain high-energy pulsar observations. In Chapter 3, I explain the light curve modeling procedure and give my modeling results with some interpretation. Chapter 4 begins with the phase-resolved spectral modeling of the pulsars whose light curves were modeled in Chapter 3. I then go on to present the method of calculating the magnitude of the accelerating electric field using the phase-resolved spectra—the first time this calculation has been done using real observations—and discuss the results and their implications. Chapters 5 and 6 comprise the second part of my thesis. In Chapter 5, I describe the procedures of searching for and tim-

ing radio pulsars (these methods can be applied to other wavelengths). In Chapter 6, I present my discoveries of two millisecond pulsars. I summarize and conclude my thesis in Chapter 7.

For Eliza.

Acknowledgements

I would like to begin by thanking my advisors, Cole Miller and Alice Harding, for being so helpful, knowledgeable, and supportive. I knew I wanted to work on pulsars, but it took me a while to figure out what direction I wanted to take. I really appreciate Cole's help and guidance through the difficult six months to a year during which I was transitioning to a different thesis project, and I am very grateful to Alice for taking me on as a student during that time. I thank Cole for drilling statistics into my head at every meeting, and for being so excited about astronomy that I always left his office with renewed enthusiasm for my work. I thank Alice for teaching me so much about pulsar magnetospheres and emission, for so diligently checking my work, and for being patient with me as I fumbled toward a better understanding of pulsar emission theory. Alice and Cole both helped me when I gave talks, and encouraged me to give seminars at different universities and institutions, for which I am grateful. I also want to thank them both for allowing me to branch out and work on other projects, especially on radio pulsar

searching and timing. I was very lucky to have had such flexible and understanding advisors.

Much of my thesis would not have been possible without the magnetosphere models provided by Constantinos Kalapotharakos and Ioannis Contopoulos. I'd like to especially thank Constantinos for taking the time to run the magnetosphere simulations with the specific parameters we required.

As the dissertation process would not have been completed without them, I wish to thank each of my committee members for their willingness to serve on my thesis defense committee. Sylvain Veilleux works in a very different field, and his perspective was extremely helpful in improving my analysis after our yearly committee update meetings. I very much appreciate Suvi Gezari joining my committee in the months before my defense, as well as Kara Hoffman serving as the Dean's representative. Chris Reynolds was formerly one of my committee members, but was unavailable for my defense. I'd like to thank him for his insight that helped me to improve my thesis work, for his words of advice, and for stimulating conversations about astrophysics and life as an astronomer.

The astronomy department staff, particularly MaryAnn Phillips, Eric McKenzie, Susan Lehr, and Adrienne Newman, have been essential to my success, by reminding me of graduation deadlines and handling my travel. Stuart Vogel has been an excellent department chair, and I feel lucky to have been part of the department while he was its leader. I wish to thank Derek Richardson for encouraging me to apply to UMD when we met at a AAS conference. I am grateful to the department for

giving me the opportunities to go to both the Kitt Peak and CARMA summer schools.

After my second year of graduate school, I worked on two different X-ray binary pulsar projects led by Padi Boyd and Tod Strohmayer. I am thankful to them for this exposure to a different aspect of pulsar astronomy, and for the opportunity to learn X-ray data analysis. I would like to thank my collaborators, Katja Pottschmidt, Jörn Wilms, and Slawo Suchy, as well as Craig Markwardt for help with the analysis. I am especially grateful to Padi, Katja, and Jörn: Our project on a Be/X-ray binary outburst turned into my first publication, despite my taking a several-year hiatus in response to a very discouraging referee report. These three collaborators revived the paper and helped me find the motivation to complete it. It turned into a very nice paper, and I am so grateful to them for believing in the project and in my work, as well as for the incredible amount of help they gave me in the process.

In my fourth year of graduate school, I had the good fortune to begin working with Scott Ransom, and I would like to thank him for giving me the opportunity to get involved in pulsar searches. He has been an invaluable collaborator, not to mention a very friendly and fun guy. I always wanted to find radio pulsars, and I'm so thankful to him for opening that door for me.

When I began working with Alice, I became part of the *Fermi* Large Area Telescope Collaboration. This is a huge collaboration, and I cannot begin to name, much less thank, most of its members, but I am extremely grateful to the LAT Collaboration and especially to those in leadership

roles at the NASA Goddard Space Flight Center for the chance to work with this incredible telescope. My thanks to David Thompson, Julie McEnery, Liz Hays, and Neil Gehrels for welcoming me into the LAT community at Goddard and for sincerely caring about my work and my future. Thank you to Lee Mundy and David Holdridge for running the CRESST program, through which I have been able to work at Goddard as a UMD student. I also want to thank others, both inside and outside the LAT collaboration, who encouraged me to begin working with the LAT, in particular Teddy Cheung, Andy Harris, Tyrel Johnson, and Jörn Wilms.

In joining the LAT Collaboration, I met a number of other pulsar astronomers who have been very helpful collaborators. I would especially like to acknowledge Paul Ray, Fernando Camilo, David Smith, Eric Grove, Mike Wolff, Kent Wood, Mallory Roberts, Maura McLaughlin, Matthew Kerr, Priya Bangale, and Tyrel Johnson. Paul has been on all of Scott's and my proposals to search for and time millisecond pulsars in gamma-ray-emitting globular clusters, and has provided very helpful critiques that have improved our proposals. He also took time out of his busy schedule to teach me how to time gamma-ray pulsars, and has been enthusiastic about working together on searches for pulsars at low radio frequencies. Fernando was a huge help in learning to search for and time pulsars. He taught me how to analyze polarization data, and allowed me to use his state-of-the-art computer cluster, with which I discovered both of the radio pulsars that I present in my thesis. David pushed me to be involved with the second LAT pulsar catalog, which was a very valuable experience. Eric is just the nicest guy, invited me

to all the LAT meetings at the Naval Research Lab, and treated me as a collaborator from day one. Mike and Kent welcomed me onto their X-ray proposals. Mallory was happy to have me search some of his radio observations, which resulted in my first pulsar discovery. He, Maura, Priya, and Matthew graciously invited me to contribute both radio and gamma-ray analysis to their paper on pulsars discovered in unassociated LAT sources, and Matthew was always happy to help when I had questions about the analysis. Tyrel, who is a friend and former officemate as well as a collaborator, is also always happy to help—he almost always has answers to my questions, and has helped me so much with LAT analysis over the years.

There are many people working at Goddard, mostly on the *Fermi* team, who contributed to the quality of both my work and my life at work. I'm so thankful to Jack Hewitt and Terri Brandt for teaming up with me for radio and millimeter observations of pulsar wind nebulae. Their expertise made it possible for me to branch out into this new field. I also want to thank Zaven Arzoumanian for involving me in pulsar searches at Goddard, and for many interesting conversations. I always learned something new when discussing science and software with Jamie Cohen. Tyrel Johnson, acknowledged above, and William McConville are the go-to LAT guys, and have both helped me a lot with analysis. Elizabeth Ferrara has been an incredibly helpful resource for LAT science as well as for personal advice. I had a great time baking cakes, talking about baking cakes, and sometimes also learning about gamma-ray bursts, with Sylvia Zhu, Judy Racusin, and Dave Greene—their five-year birthday cake for *Fermi* is going to be epic. My days were always brightened by

a visit from Esra Bulbul or J.C. Leyder, or a chat with Davide Donato, Rodrigo Nemmen, Sylvain Guiriec, or, longer ago, Tommy Nelson, and I'll always be amused when I remember Davide's struggle to stay awake during weekly meetings. There are so many people who I greet when we pass in the halls, some whose names I never even learned, but they all made my experience at Goddard more enjoyable and fulfilling.

Grad school wouldn't have been the same without the cast of characters that made up our late-night study sessions, which often diverged into discussions on various topics of interest. Bo, Hao, Dheeraj, Mark, Edmund, and especially my classmates Daniel, Mike, and Steve—it was a lot of fun working, talking, hanging out, and playing frisbee (and occasionally violin) with you all those years, as well as with Laura and Katherine. You were much more than classmates, and were good friends. Yana, while we didn't see much of each other, I valued the time that I did spend with you, especially when you and Alex taught me to "shift my drink" at that techno club!

Intramural soccer was a source of personal enrichment (and exercise!) during graduate school. Thank you to Matthew Knight, Hao Gong, and Alex McCormick for being such good coaches and captains over the years, and to Marc Pound for all the coaching he did from the net. I still don't know all the rules of soccer, but I had a great time on the field.

I was a member of the Repertoire orchestra my first year, and of the Equestrian Club for several years. Although the people who led those groups are no longer at UMD, I wanted to include those groups in these acknowledgements. They helped to keep me well-rounded when it would

have been so easy to allow the narrow focus of Ph.D. research to encroach on all areas of my life.

I am fortunate to have had some very good friends in graduate school. The early years were a lot of fun, thanks in large part to Ben Hall and his undying sense of adventure. I'll always remember the outings, TV nights, and parties with Lisa Wei and Rick Pernak, Vanessa Lauburg and Jamie Cohen, Jen Miller, Hannah Krug, Mike McDonald and Kelly MacIsaac, Jithin George (who knows Larry...!), Alex McCormick (who always had the most creative, as well as interactive, Halloween costume), and many more grads in the astronomy department. In more recent years, I've been lucky to make friends with the younger graduate students, and in particular want to thank Jonathan Fraine, Gabriele Betancourt-Martinez, Maxime Rizzo, and Vicki Toy for reaching out to me in my old age!

Some of these friendships were essential in later years of graduate school, when I encountered one difficult situation after another. I thank Mia Bovill for talking sense into me that night when I had myself convinced that I would never make it as an astronomer. She may not have known it, but her words helped me find the strength and motivation to finish my first pulsar search proposal and go to work with Scott Ransom, after which I was presented with many more opportunities. I am very thankful to Vanessa Lauburg, Lisa Wei, Ashley Zauderer, Sidharth Kumar, Daniel Jontof-Hutter and Laura Silverstein, Mike and Katherine Koss, Alice Olmstead, Stacy Teng, Kári Helgason, Rodrigo Herrera Camus, Violetta Impellizzeri, and Shaye Storm for being such good friends and imparting so many words of wisdom, especially during my most difficult period of graduate school. Rodrigo, you are a very dear friend, and I want to

especially thank you for all your good advice, as well as for all the ánimo.

Before going to graduate school, I was an undergraduate at Penn State University. I had originally planned to study music education, but I loved physics and math so much in my senior year of high school that I decided to also study astronomy in college. I acknowledge my excellent teachers at Oley Valley High School, Joseph Heinz and Daniel Schaeffer, for making their students think so hard. At Penn State, I worked with Robin Ciardullo, an experience that was incredibly valuable and rewarding. I am very thankful to Robin, as well as to collaborators Patrick Durrell and John Feldmeier, for the opportunity to begin research early in college. Robin was very encouraging, gave good work advice, and always told me I should continue in astronomy. The memory of his words helped me to push through periods when I lacked confidence in my abilities and in my work. I want to thank Jane Charlton and Chris Palma for introducing me to astronomy outreach and giving me the opportunity to do it often. I am thankful to Mercedes Richards for words of advice on both career and personal matters, which I continue to reflect on to this day. Finally, I wish to thank Joseph Masiero, a great friend who encouraged me to begin doing research and introduced me to Robin.

Some of the most influential people in my life exist outside the world of astronomy: my friends and my family. Gretchen Seaver and Michele Crowl are two of my best friends, and I am so grateful to them for the many discussions about school, work, and life that we've had over the years. Those discussions often sparked a renewed desire to complete my Ph.D. and use it to help others improve their own lives. I am especially indebted to Gretchen for all of the help she gave me the last few years.

Her emotional support was an important factor in my success as a Ph.D. student.

I credit my parents with unintentionally piquing my interest in astronomy at a young age. I grew up in rural Pennsylvania, where the night sky is very dark and many stars are visible. When I was about four years old, my father renovated our attic, and it became my bedroom. My windows were skylights in the roof, so I could stargaze from my bed. As I got older, I would watch the stars for hours at a time. One night I looked at the Orion Nebula through binoculars, and was amazed to see many more stars than I'd seen with my naked eye. The next day, I told my mother about the number of stars in Orion's belt, and she told me that new stars were forming there. This statement overturned my idea of the universe as a static, unchanging entity, and was the beginning of a deeper interest in astronomy.

My family has been very supportive of my decision to study astronomy. I appreciate the genuine interest they have shown in astronomy and related fields. On more than one occasion, my father has asked me to explain what I do; my mother came to one of my seminars. My brother calls to ask me physics questions, and my sister finds astronomy-related gifts to give me on holidays. Even my extended family asks about astronomy from time to time. My grandparents reminded me that astronomy can enhance anyone's life experience when they told me how much they were enjoying an astronomy lecture series they were watching on DVD. I hope that as my niece, Eliza, gets older, she will become interested in or at least appreciative of astronomy. (To give her a head start, I unofficially named the second pulsar I discovered the "Eliza pulsar"—the discovery

observation was taken the night she was born.) I am very thankful to my family, especially my parents and siblings, for their support, as well as for always being there when I've needed them. They have provided both practical and emotional support over the years, and without them I would never have been able to stay in school and work toward this degree.

Finally, I wish to acknowledge the person who has been by my side literally and figuratively, first as an incredible friend and now as a wonderful partner, over the last few years. Shaye, thank you—for practical help you gave me on talks and proposals, for helping me learn to "chillax," for introducing me to all sorts of fun things like Jónsi concerts and ice hockey, and for all the tea. Thank you for being there even at my weakest moments, and for being a consistent source of support and comfort, especially in these last few months when I was increasingly distracted by the pressures of graduating. I couldn't ask for a kinder, more supportive partner.

Contents

List of Tables

List of Figures

Chapter 1

Introduction to Gamma-ray Pulsar Astronomy

The discovery of a "bit of scruff" that turned up in graduate student Jocelyn Bell's dataset during an observing run in 1967 marked the birth of observational pulsar astronomy. What initially appeared as oscillating noise in her radio-frequency observations turned out to be, upon further inspection, a periodic signal with period $\sim 1.3\,\mathrm{s}$ (Hewish et al. 1968). More discoveries of narrowly pulsed radio signals with extremely stable periods of order 0.01–1 s followed, (e.g., Large et al. 1968), implying an astrophysical origin. It was quickly proposed that small, dense, rapidly rotating objects, supported against gravitational collapse by neutron degeneracy pressure—neutron stars—were responsible for the observed radio pulses, the periods of which corresponded to the neutron stars' rotation periods (Gold 1968). Measurements of a slight increase in pulse period with time, combined with the fact that the emission was pulsed, was consistent with emission from an inclined rotator with a strong magnetic field.

Almost 50 years later, the field of pulsar astronomy is thriving, especially since

the launch of the *Fermi* Gamma-ray Space Telescope, which is directly or indirectly responsible for the detections or discoveries of over 120 γ-ray pulsars and 50 millisecond pulsars. A recent review by Harding (2013) describes the current state of pulsar astronomy. A more in-depth discussion on γ-ray pulsars can be found in the second *Fermi* Large Area Telescope pulsar catalog (The Fermi-LAT Collaboration 2013). Two excellent references for both pulsar observation and theory are Lorimer & Kramer (2005) and Shapiro & Teukolsky (1986).

1.1 Rotation Powered Pulsars

Rotation-powered pulsars (RPPs) are rapidly rotating, highly magnetized neutron stars, with typical surface magnetic field strengths of $B_{\rm s} \sim 10^{12}\,{\rm G}$ for young RPPs. Misalignment between the magnetic and rotation axes produces a time-dependent magnetic moment, extracting rotational energy from the neutron star. Emission produced in the vicinity of the magnetic poles appears to pulsate as the radiating region sweeps past the observer's line of sight. The specific mechanism or mechanisms by which pulsars radiate are uncertain, but must involve charged particle acceleration in the extremely large electric field induced by the time-varying magnetic field. In the case of pure magnetic dipole braking, all of the rotational energy loss would be converted into magnetic dipole radiation, and the pulsar luminosity would be that of a rotating magnetic dipole. The total luminosity measured from the pulsed emission is much lower than that expected from magnetic dipole braking, suggesting that a large portion of the energy is carried away from the pulsar by a particle wind, forming the surrounding pulsar wind nebulae observed in many young systems.

Most of the $\sim$ 2000 known pulsars (Manchester et al. 2005) have been observed

to emit only at radio wavelengths (within current multi-wavelength detection limits), but emission in bands across the electromagnetic spectrum has been detected from a significant portion of the population. In particular, more than 120 RPPs have been detected at high gamma ray (γ-ray) energies (The Fermi-LAT Collaboration 2013). There are over 100 RPPs with X-ray pulsations (Harding 2013), and nearly 30 pulsars have been detected at optical, ultraviolet, or infrared wavelengths (Mignani 2012). The very young and energetic Crab pulsar, the compact remnant of SN 1054 (the supernova observed in 1054 A.D.), emits across the electromagnetic spectrum, including at TeV energies (Albert et al. 2008; VERITAS Collaboration et al. 2011). Unlike other young pulsars, the peaks in its pulse profile, or light curve, are aligned in phase at all wavelengths.

RPPs are divided into two main subclasses. Normal pulsars are younger than $\sim 100\,\mathrm{Myr}$ and have rotation periods ranging from tens of milliseconds (the Crab has spin period $\sim 0.033\,\mathrm{s}$) to a few seconds. Millisecond pulsars (MSPs) are older than 100 Myr and have spin periods $\sim$ 1–10 ms. The fastest known MSP rotates with spin frequency 716 Hz (Hessels et al. 2006). This is well below the break-up frequency. It has been suggested that the rotation speed of MSPs is limited by another physical process, likely magnetic torques, with the small but intriguing possibility of gravitational wave radiation contributing somewhat due to slight deviations from axisymmetry (Chakrabarty 2008, and references therein).

Pulsars are the stellar remnants of core-collapse supernovae with progenitor masses $> 8\,M_\odot$. Young pulsars have strong magnetic fields ($B_\mathrm{s} \sim 10^{11}$–$10^{13}\,\mathrm{G}$), high spin-down rates ($\dot{P} \sim 10^{-15}$–$10^{-12}\,\mathrm{s\,s^{-1}}$), and a large energy output from rotational losses (typical values of $\dot{E}$ are $\sim 10^{34}$–$10^{38}\,\mathrm{erg\,s^{-1}}$), much of which is released as a particle wind that cools in the surrounding interstellar medium by synchrotron radiation, observed as pulsar wind nebulae (PWNe; Gaensler & Slane 2006). Mil-

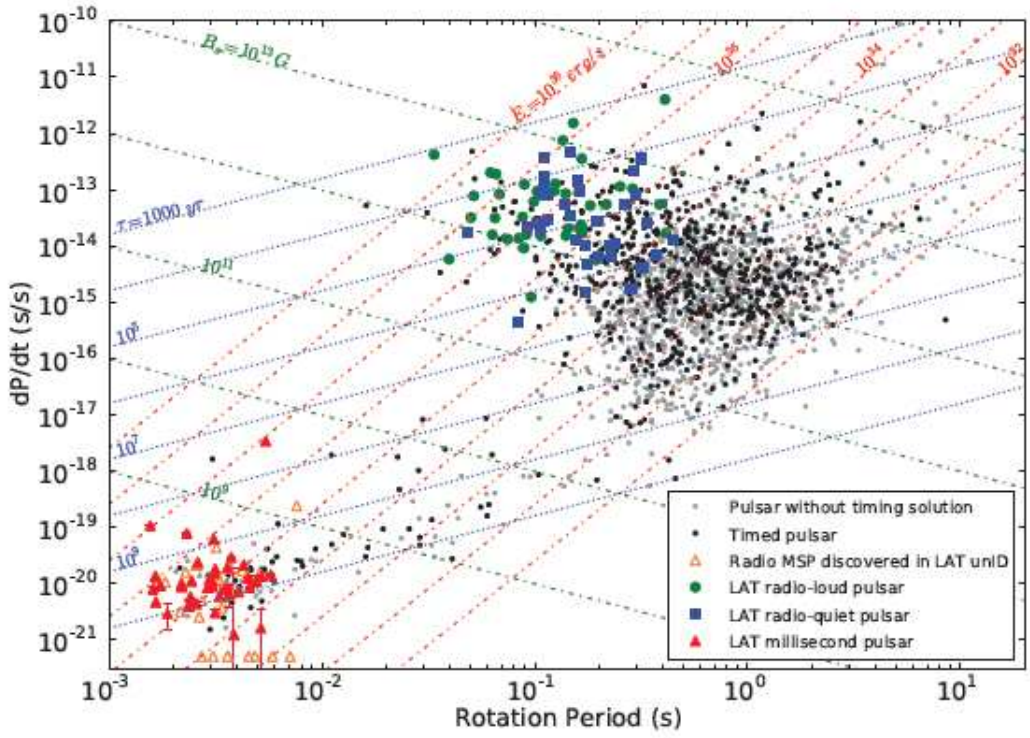

Figure 1.1: A $P - \dot{P}$ diagram for rotation-powered pulsars. The black and grey points show radio pulsars that are not also γ-ray pulsars. The green and blue points are respectively RL and RQ γ-ray pulsars, while the red and orange points are MSPs. The orange dotted lines are lines of constant $\dot{E}$, the blue lines are of the characteristic age, and the green lines show constant $B_{\rm s}$. The normal γ-ray emitting RPPs all lie at $\dot{E} \geq 5 \times 10^{33}\,{\rm erg\,s^{-1}}$, above the spindown energy of the majority of the population. The MSPs lie in a very different part of $P - \dot{P}$ space, but have $\dot{E}$ values that overlap with that of the less energetic young population. Figure reproduced from The Fermi-LAT Collaboration (2013).

lisecond pulsars instead have $B_{\rm s} \sim 10^8\,{\rm G}$, $\dot{P} \sim 10^{-20}\,{\rm s\,s^{-1}}$, and $\dot{E} \sim 10^{33}\,{\rm erg\,s^{-1}}$. They are referred to as "recycled" because they were spun up to millisecond periods by accretion from a binary companion. As will be discussed in Chapter 6, they are orders of magnitude more common by mass in globular clusters than in the field because of the increased probability of capturing a companion in the dense stellar environment (e.g., Camilo & Rasio 2005). They are very stable rotators, unlike young pulsars, which often have noisy residuals in their timing solutions. Young

pulsars also experience large glitches, events in which the period suddenly decreases and the spindown rate temporarily increases before returning to its pre-glitch value (although small glitches can occur in millisecond pulsars; Mandal et al. 2009). The $P - \dot{P}$ diagram in Figure 1.1 shows where these populations fall in terms of spin parameters, field strength, and energetics.

Rotation-powered pulsars are natural laboratories for extreme physics, particularly for the study of particle physics in strong electromagnetic fields, physics of very dense matter, and gravitational theory. Young pulsars have surface magnetic field strengths $B_{\rm s} \sim 10^{12}$–$10^{13}\,{\rm G}$, much larger than fields that can be reproduced on Earth. Thus, the study of pulsar emission allows us to probe physical processes in these strong-field regimes. Some of these processes are discussed in Chapter 2. Millisecond pulsars in particular are interesting in terms of placing limits on the maximum neutron star mass and on the neutron star equation of state, and hence on the maximum mass that can be supported against gravity. A neutron star mass of $2\,M_\odot$ rules out many non-nucleonic equations of state. Because MSPs gained some amount of mass during their accretion and spin-up phase, they are good candidates for constraining the maximum mass. Additionally, they usually are found in binary systems, a necessary condition for mass measurements (Chapters 5 and 6). Two pulsars with precisely measured masses in the range of $2\,M_\odot$ have been found (Demorest et al. 2010; Antoniadis et al. 2013). The details of neutron star structure and equations of state are reviewed in Lattimer & Prakash (2004). Finally, pulsars can be used to detect gravitational radiation. Taylor & Weisberg (1982) measured the rate of orbital period decay in the Hulse-Taylor pulsar, PSR B1913+16, and found it matched exactly with the prediction from general relativistic gravitational radiation (within error bars), thus indirectly detecting gravitational radiation. Direct detections could be made in the near future with the use of a "pulsar timing

array," in which the timing residuals of many pulsars are searched for correlations indicating the passage of a gravitational wave (Foster & Backer 1990; Hellings & Downs 1983; Lommen 2012).

1.1.1 Observational Properties of Gamma-ray Pulsars

The population of γ-ray pulsars detected by the LAT falls into three categories $\sim$equal in number: radio-loud γ-ray pulsars (RL), radio-quiet γ-ray pulsars (RQ), and γ-ray MSPs (The Fermi-LAT Collaboration 2013). Pulsars in the first group were detected by folding the LAT photon's arrival times with the pulsars' timing solutions (Section 1.3) and binning the photons in phase. The exceptions are PSR J1741−2054 (Camilo et al. 2009), PSR J1907+0602 (Abdo et al. 2010e), and PSR J2032+4127 (Camilo et al. 2009), which were discovered in blind γ-ray searches and later detected at radio wavelengths. The RQ pulsars were also discovered in such blind γ-ray searches (e.g., Abdo et al. 2009a) using the time-differencing technique of Atwood et al. (2006). The MSPs were also found by folding the LAT count arrival times with the timing solution (Abdo et al. 2009b). MSPs are usually found in binary systems, and the number of parameters to cover with a blind search of the γ-ray counts is prohibitively large. However, MSPs can be detected in pseudo-blind searches, in which the orbital parameters are known from independent multi-wavelength observations. One MSP has been blindly detected in the γ-rays in this way (Pletsch et al. 2012), and was found to be a radio emitter afterward (Ray et al. 2013).

Overall, the γ-ray light curves of these pulsars (Figure 1.2) show two narrow peaks with separation 0.1–0.5 in phase. (There are a few pulsars with single γ-ray peaks.) The γ-ray peaks of RL pulsars trail the peak in the radio profile; this phase lag between the radio and first γ-ray peak increases as the γ-ray peak separation

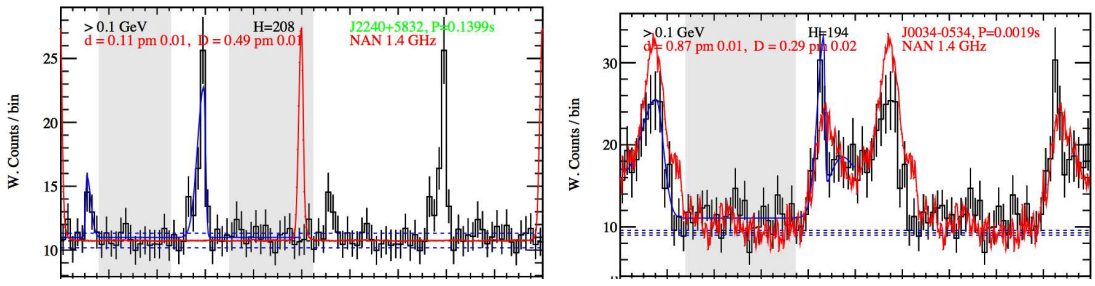

Figure 1.2: Two examples of the radio and γ-ray light curves of γ-ray pulsars. On the left is a young pulsar, PSR J2240+5832, with spin period $P \sim 0.14\,\mathrm{s}$. Its light curve displays the "classic" features of two γray peaks trailing a single radio peak. The black line shows the γ-ray profile, the red line shows the radio profile, and the blue line shows an analytical fit to the light curve (this fit is unrelated to the light curve modeling in Chapter 3). On the right is a MSP, PSR J0034−0534 ($P = 1.88\,\mathrm{ms}$). This MSP has aligned radio and γ-ray peaks, indicating co-located emission regions. The light curves were made using weighted count binning, described in Section 1.3. Figures reproduced from The Fermi-LAT Collaboration (2013).

increases (The Fermi-LAT Collaboration 2013). The very different light curve shapes from radio to γ-ray energies indicates that the emission in these bands originates from different locations in the magnetosphere. The radio emission is thought to come from low altitudes above the polar cap, while the γ-rays are produced in the outer magnetosphere. As a consequence, the γ-rays are observable from a wide range of viewing angles, while the radio is only seen if the observer's line of sight passes close to the magnetic pole. This geometrical argument explains the observations of RQ pulsars.

The above is true for most, but not all, pulsars. The Crab pulsar, along with several millisecond pulsars, displays pulsations that are aligned in phase from radio to TeV energies, suggesting co-location of the emission regions for these objects. In this case, it is likely that the radio emission is located at a higher altitude relative to the light cylinder than it is in non-aligned pulsars, and thus is caustic in origin, the same as the γ-ray peaks. Radio polarization measurements provide evidence for

a caustic origin of radio peaks: the peaks show no linearly polarized light, which is expected for photons arriving at the same time (phase) from a wide range of locations in the magnetosphere (Dyks et al. 2004; Venter et al. 2012).

The phase-averaged γ-ray pulsar spectrum is well described by a power law of spectral index $\Gamma \sim 1$–2 and an exponential cutoff above a cutoff energy $E_{\rm c} \sim 1$–$5\,{\rm GeV}$. The phase-resolved spectrum shows significant variation in the spectral parameters, and is therefore a much better probe of the magnetospheric physics than is the phase-averaged spectrum.

1.1.2 Pulsar Energetics and Magnetic Field Strength

The energy output by a pulsar due to rotational losses is

$$\dot{E} \equiv -\frac{dE_{\rm rot}}{dt} = -\frac{d}{dt}\left(\frac{I\Omega^2}{2}\right) = 4\pi^2 I \dot{P} P^{-3} \tag{1.1}$$

The true moment of inertia of a neutron star is unknown. Assuming a neutron star is a uniformly dense sphere, the moment of inertia is $I = (2/5)MR^2$. Using typical values of $R \sim 10^6\,{\rm cm}$ and $M \sim 1.4\,M_\odot$, the spin-down luminosity can be expressed as

$$\dot{E} \simeq 3.95 \times 10^{31}\,{\rm erg\,s^{-1}} \left(\frac{\dot{P}}{10^{-15}}\right)\left(\frac{P}{s}\right)^{-3} \tag{1.2}$$

If a pulsar's magnetic field is well approximated by an inclined, rotating magnetic dipole with magnetic moment $|\mathbf{m}|$, then we can equate the power emitted by the dipole,

$$\dot{E}_{\rm dipole} = \frac{2}{3c^3}|\mathbf{m}|^2\Omega^4 \sin^2\alpha, \tag{1.3}$$

with the spindown power of Equation 1.2.

$$\dot{\Omega} = -\left(\frac{2|{\rm m}|^2 \sin^2\alpha}{3Ic^3}\right)\Omega^3, \tag{1.4}$$

where α is the magnetic inclination angle.

The magnetic field strength is related to the magnetic moment as $B \approx |\mathbf{m}|/r^3$. Assuming that the spin-down process is dominated by dipole braking, and rearranging Equation 1.4, yields the surface magnetic field strength ($r = R_{\rm NS}$),

$$B_{\rm s} = \sqrt{\frac{3c^3}{8\pi^2}\frac{I}{R_{\rm NS}^6 \sin^2\alpha} P\dot{P}} \tag{1.5}$$

The surface field strength is typically evaluated assuming $\alpha = 90°$, and that I and $R_{\rm NS}$ are as given above. Under these assumptions, the field strength is

$$B_{\rm s} = 3.2 \times 10^{19}\, G\sqrt{P\dot{P}} \simeq 10^{12}\, G \left(\frac{\dot{P}}{10^{-15}}\right)^{1/2} \left(\frac{P}{s}\right)^{1/2} \tag{1.6}$$

The energetics of a pulsar can also be used to estimate its age. Equation 1.4 can be rewritten in terms of rotation frequency $\nu = 1/P$ as

$$\dot{\nu} = K\nu^n, \tag{1.7}$$

or in terms of the pulse period P as

$$\dot{P} = KP^{2-n}, \tag{1.8}$$

where K is a constant and n is the braking index; for spin-down that is purely due to magnetic dipole braking, $n = 3$. The age T of the pulsar is then

$$T = \frac{P}{(n-1)\dot{P}}\left[1 - \left(\frac{P_0}{P}\right)^{n-1}\right], \tag{1.9}$$

where P_0 is the original (birth) period of the pulsar. Assuming $P_0 \ll P$ and $n = 3$ yields the *characteristic age* of the pulsar,

$$\tau_{\rm c} \equiv \frac{P}{2\dot{P}} \simeq 15.8\,{\rm Myr}\left(\frac{P}{1\,{\rm s}}\right)\left(\frac{\dot{P}}{10^{-15}}\right)^{-1}. \tag{1.10}$$

The characteristic age assumes that the birth period of the pulsar was negligible compared to its current observed period, and can therefore be inconsistent with the true pulsar age. It is important to have independent measurements of the age, for example from the age of the supernova remnant associated with the neutron star, to determine the accuracy of the characteristic age estimate.

1.1.3 Pulsar Magnetosphere

The pulsar magnetosphere, illustrated in Figure 1.3, is described as follows. The very strong electric field induced by the rotating magnetic field of the neutron star pulls charges from the stellar surface (Chapter 2; Goldreich & Julian 1969), forming the plasma magnetosphere that corotates with the neutron star. This corotation breaks down as the corotation velocity approaches the speed of light. The *light cylinder* is defined as the cylindrical radius $R_{\rm LC}$ from the neutron star's rotation axis where the corotation velocity is c:

$$R_{\rm LC} = \frac{c}{\Omega} \approx 5 \times 10^9 \, P \text{ cm} \tag{1.11}$$

Magnetic field lines that close within the light cylinder are referred to as closed field lines. The outermost closed field line defines the boundary of the closed field line region. Beyond this boundary, the field lines remain open as they cross $R_{\rm LC}$. Charges within the closed field line region are trapped, and corotate with the star. Charges outside the closed field region flow freely outward as a pulsar wind.

The emission models considered in this thesis allow radiation to be produced very near the light cylinder. The magnetic field at the light cylinder is therefore an interesting quantity for these models. It is given by

$$B_{\rm LC} = B_{\rm s} \left(\frac{\Omega R}{c} \right)^3 \simeq 9.2 \, \text{G} \left(\frac{P}{s} \right)^{-5/2} \left(\frac{\dot{P}}{10^{-15}} \right)^{1/2} \tag{1.12}$$

The boundary between the open and closed field lines (also referred to as the last open field line), projected onto the neutron star surface, defines the rim of the magnetic polar cap. For a static dipole field in vacuum, the magnetic field lines follow the relation

$$\frac{\sin^2 \theta}{r} = \text{constant} \tag{1.13}$$

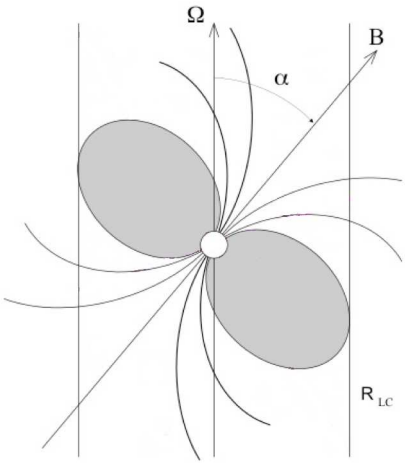

Figure 1.3: Illustration of the pulsar magnetosphere. The white circle in the center of the figure is the neutron star. Its rotation axis is labeled with Ω. Its magnetic axis is labeled with B, and is offset from the rotation axis by the magnetic inclination angle α. The light cylinder radius, the cylindrical distance from the neutron star at which the corotation velocity is the speed of light, is labeled $R_{\rm LC}$ and marked by the vertical lines. The curved lines emanating from the neutron star are the magnetic field lines. Field lines that close within the light cylinder make up the closed field line region, colored gray in this figure. The field lines that do not close within the light cylinder cross $R_{\rm LC}$ and remain open, allowing particles to flow outward into the surrounding medium. The polar cap is the boundary between the open and closed field line regions at the neutron star surface.

where θ is the angle between the magnetic axis and a point along the magnetic field line, and r is the distance to that line from the neutron star center. The polar cap radius is defined by

$$r_{\rm pc} = R_{\rm NS} \sin\theta_{\rm pc} \tag{1.14}$$

where $\theta_{\rm pc}$ is the angular radius of the polar cap. From the boundary condition $r = R_{\rm LC}$ at $\theta = 90^\circ$, the angular radius is

$$\sin\theta_{\rm pc} = \left(\frac{R_{\rm NS}}{R_{\rm LC}}\right)^{1/2} . \tag{1.15}$$

It follows that

$$r_{\rm pc} = \left(\frac{R_{\rm NS}^3}{R_{\rm LC}}\right)^{1/2} \tag{1.16}$$

These expressions can be used to approximate the true field structure. In reality, the magnetic field lines of a rotating neutron star are swept back near the light cylinder, forming a toroidal component of the field. This sweepback leads to distortions in the polar cap that are discussed further in Chapters 2 and 3.

1.1.4 Gamma Rays as Probes of Emission Physics

As noted above, the observed emission from pulsars accounts for a small fraction of the total spin-down luminosity, $\dot{E}$. The efficiency, $\eta = L/\dot{E}$ (where L is the measured luminosity of the observed electromagnetic radiation), with which the total energy loss is converted into observable radiation is $\sim 10^{-7}$–10^{-5} in the radio and optical bands. At higher energies, η increases: $\eta \sim 10^{-4}$–10^{-3} in the X-ray band, and $\sim 10^{-2}$–10^{-1} at γ-ray energies (Becker & Truemper 1997). Pure dipole radiation would imply a braking index $n = 2 - P\ddot{P}\dot{P}^{-2} = 3$, while braking indices observed thus far are < 3. The measured braking indices and efficiencies suggest that a large fraction of the rotational energy is carried away by a pulsar wind, consistent with the observations of pulsar wind nebulae surrounding many young pulsars.

Therefore, a key question in pulsar astrophysics is: What is the mechanism by which a fraction of the rotational energy, which is lost as the pulsar spins down, is converted into the electromagnetic radiation observed from these objects? Given the large electric fields that are induced by the time-varying magnetic moments of neutron stars, particle acceleration to very high energies must occur in pulsar magnetospheres, and it is the radiation from these particles that is observed. However, the details of where the particles are accelerated, and what the specific acceleration and radiation mechanisms are for a given photon energy (e.g., inverse Compton, synchrotron, or curvature radiation), are not well known. These details are potentially important for probing the physics of strong magnetic fields. Additionally, the

location and mechanism of acceleration and radiation are ingredients in pulsar population synthesis models, which calculate the total number of pulsars in the galaxy given the number that we are able to detect. At radio frequencies, where the beam is typically narrow and is thought to originate at low altitudes, there is a restricted range of observer lines of sight that will cross close enough to the magnetic pole to allow detection of a radio pulse. At γ-ray energies, where the beam is wider and generally thought to originate at higher altitudes, there is a larger range of viewing angles for which a γ-ray pulse will be seen. Differences between γ-ray emission models, described in Chapter 2, affect the observed pulse shapes (light curves) and result in different predictions from pulsar population synthesis simulations (e.g., Harding et al. 2007).

The fact that the γ-ray luminosity and hence η is so much higher than at other energies (for pulsars that display γ-ray emission) suggests that the study of this high-energy emission is more likely than other energies to provide clues to the underlying mechanism by which the rotational energy loss is converted into electromagnetic radiation. Additionally, physically motivated models of γ-ray emission exist (Chapter 2), while models of radio emission remain empirical. Thus, studying the γ-ray properties of pulsars within the context of these physically motivated models may result in a better understanding of the emission mechanism. The approach taken in this thesis is to infer the emission geometry by modeling light curves observed by the LAT with simulated light curves from geometrical representations of outer magnetosphere emission models.

1.2 Gamma-ray Astronomy with the *Fermi* Large Area Telescope

Gamma-rays are produced by non-thermal processes like those described in Chapter 2. All involve high-energy particle interactions, typically particle acceleration, inverse Compton scattering, and/or a particle traversing a magnetic field (usually a very strong one). Sources that produce γ-ray emission include active galactic nuclei (AGN), especially blazars, gamma-ray bursts (GRBs), supernova remnants (SNRs), pulsar wind nebulae (PWNe), high-mass binaries like Cyg X-3, and rotation-powered pulsars. Important sources of diffuse γ-ray emission are cosmic ray interactions with the Galactic interstellar medium and radiation fields, especially pronounced in the Galactic plane. There is also an isotropic extragalactic background from many unresolved γ-ray sources plus any diffuse component that may be present (Atwood et al. 2009). A map of the γ-ray sky above 100 MeV from three years of LAT data is shown in Figure 1.4.

The field of γ-ray astronomy began with the Explorer XI satellite in 1961, which detected fewer than 100 γ-ray photons during a four-month mission. The Vela satellites discovered GRBs two years later. Gamma-ray emission from the Crab pulsar was found in a balloon experiment in 1971 (Browning et al. 1971). It had originally been discovered in the radio shortly after the first pulsar was discovered. The SAS-2 satellite flew one year later, discovering γ-ray pulsations from the Vela pulsar, which was also known previously from the radio (Albats et al. 1974; Thompson et al. 1975). COS-B operated from 1975-1982, improving the pulsed detections of these pulsars. The field took a leap forward with the launch of the *Compton Gamma-ray Observatory*, which had onboard the Imaging Compton Telescope (0.8-30 MeV) and the Energetic Gamma Ray Experiment Telescope (EGRET; 20 MeV - 30 GeV).

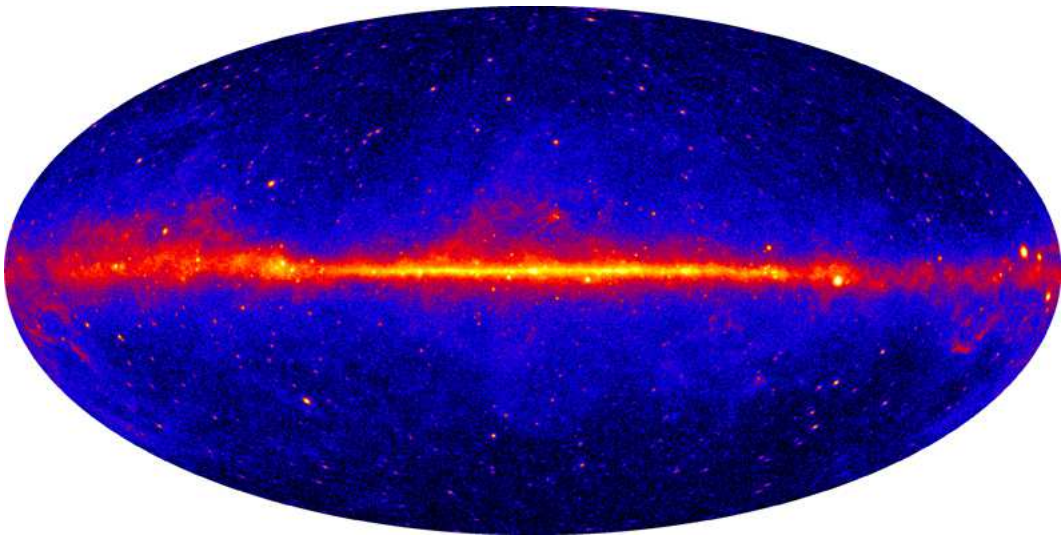

Figure 1.4: The γ-ray ($E > 100\,\mathrm{MeV}$) sky, as seen with three years of data from the *Fermi* Large Area Telescope. The bright band across the center of the figure is diffuse emission from the Galactic plane, caused by cosmic rays interacting with neutral hydrogen gas. There are ~ 1870 point sources in this map (Nolan et al. 2012), most of which are associated with blazars. Right of center, the Vela pulsar stands out prominently from the diffuse emission as the brightest point source in the LAT sky.

EGRET discovered four more high-energy γ-ray pulsars. The detected pulsars are shown in Figure 1.5.

The *Fermi Gamma-ray Space Telescope* was launched on June 11, 2008. It has two instruments onboard, the Gamma-ray Burst Monitor (GBM), which is sensitive in the energy range 150 keV–30 MeV, and the Large Area Telescope (LAT), which covers the energy range between 20 MeV and $\sim$ 300 GeV. The LAT has detected over 120 rotation-powered pulsars at the time of writing, all but six of which were new detections of γ-ray pulsations, and a third of which were new pulsar discoveries. The γ-ray analysis in this thesis is solely based on LAT observations, and will be the focus of the remainder of this work.

The *Fermi* LAT is ~ 30 times more sensitive to γ-rays than EGRET was, largely

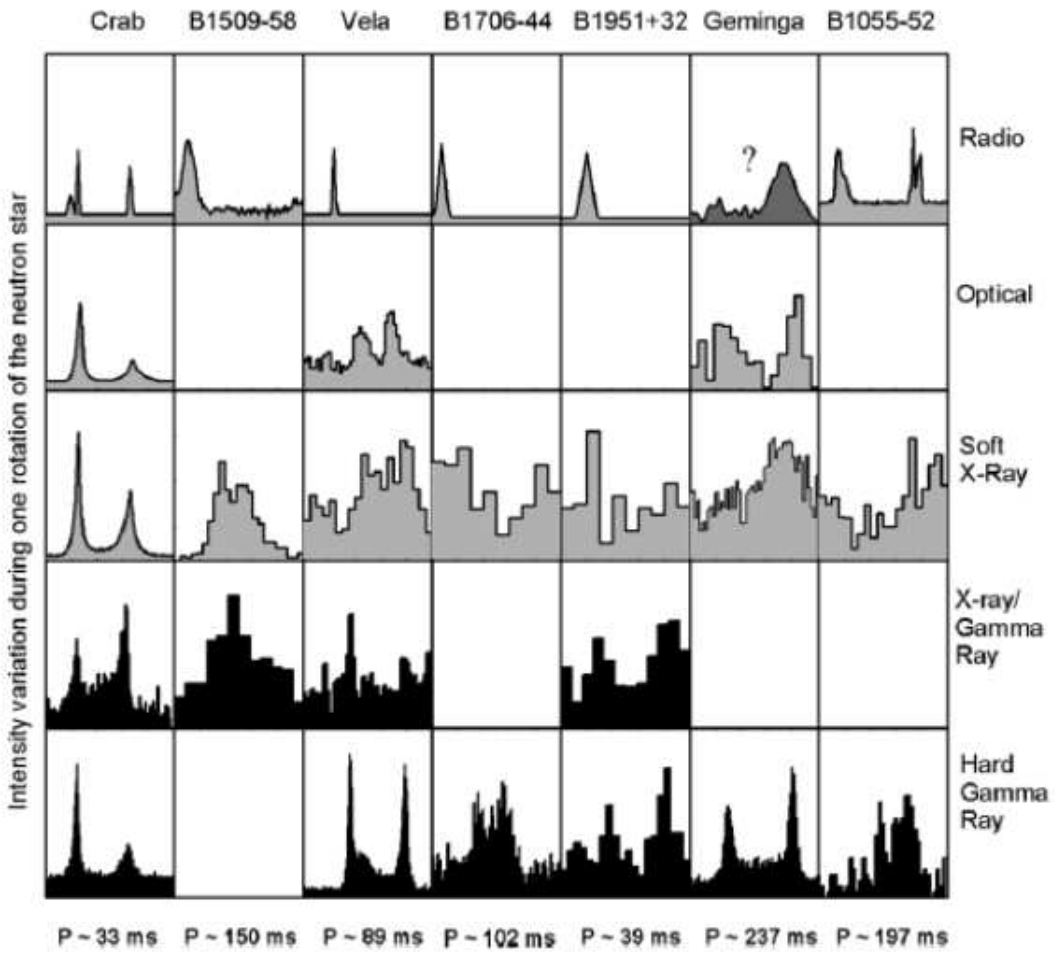

Figure 1.5: The pulse profiles of the seven pulsars observed by the Compton Gamma-ray Space Observatory. Six of these (PSR J1509−58 being the seventh) were detected at $> 20\,\mathrm{MeV}$ by EGRET. Figure reproduced from Thompson (2008).

due to a combination of increased effective area and angular resolution[1]. The spatial resolution is energy-dependent, with the 68% angular containment radius for a single photon detection improving from $\sim 3.5^\circ$ at 100 MeV to $\leq 15'$ above 10 GeV, for reasons discussed in Section 1.2.1. EGRET, in contrast, had an angular resolution of 5.8° at 100 MeV. Its peak effective area was $1500\,\mathrm{cm}^2$. In comparison, the LAT

[1]A comparison of instrument specifications between the LAT and EGRET can be found at `http://fermi.gsfc.nasa.gov/science/instruments/table1-1.html`.

effective area peaks at $9500\,\mathrm{cm}^2$ in the energy range $\sim 1 - 10\,\mathrm{GeV}$ (Atwood et al. 2009).

The LAT is by far the most sensitive γ-ray instrument ever to be flown, and it has hugely impacted every field of γ-ray astronomy. It has revolutionized the field of pulsar astronomy, both in terms of the number of pulsars it has discovered and the excellent statistics for studying individual sources.

1.2.1 Gamma-ray Detection with the *Fermi* Large Area Telescope

The LAT is a pair-conversion telescope, which means it indirectly detects γ-rays via direct detection of the positron-electron pairs that are produced in the instrument by incident high-energy photons. From these detections, the directions, energies, and arrival times of the original γ-ray photons are measured. At any given moment, the LAT is sensitive to photons arriving from within a 30° field of view, and it maps the entire sky once every two orbits (three hours).

The detector consists of a converter-tracker, within which an incoming γ-ray initiates a particle shower that is tracked by the LAT, and a calorimeter underneath the converter-tracker, which measures the γ-ray energy. The tracker is covered by an anticoincidence detector. Signals from the tracker, calorimeter, and anti-coincidence detector together are used to form online triggers, for example in the case where many γ-rays are detected from the same direction due to a γ-ray burst. A schematic of the LAT is shown in Figure 1.6.

The LAT is constructed as a 4×4 modular array, where each module consists of an 18-layer tracker (or converter-tracker) set atop an eight-layer calorimeter. The tracker layers, or "trays," consist of two single-sided silicon strip detectors (SSDs) that record the time and position of incident charged particles resulting from pair

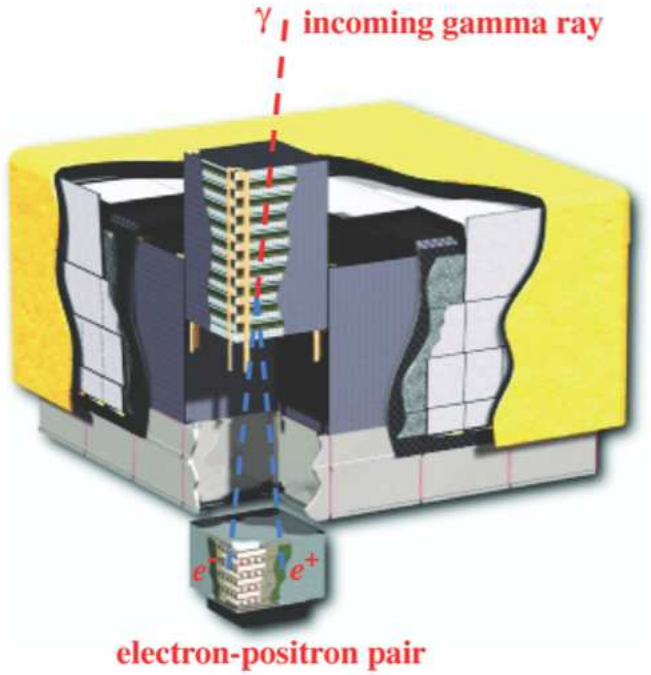

Figure 1.6: Illustration of the Large Area Telescope (LAT), one of two instruments on the *Fermi* Gamma-ray Space Telescope. The dimensions of the LAT are 1.8 m× 1.8 m × 0.72 m. The top part of the instrument is the tracker (dark gray), and the bottom is the calorimeter (light gray); the instrument is surrounding by the tiles of the anti-coincidence detector, or ACD. The diagram shows two cut-outs, the top one of the tracker and the bottom one the calorimeter. The red line shows a γ-ray traveling through the tracker and pair converting in a lower layer. The resulting electron and positron (blue lines) deposit their energy in the calorimeter. This figure was reproduced from Atwood et al. (2009).

production from incident γ-rays. Charged particles ionize the SSD and produce a current, which is read by electronics on the sides of the trays, thereby detecting the particles. The top 16 layers also contain a tungsten (W; $Z = 74$) layer that lies 2 mm above the bottom SSD in the tray; this high-Z layer promotes pair conversion, and after conversion the pairs are immediately tracked by the SSDs below. The top and bottom trays contain only one SSD, so a γ-ray incident at the top of the converter-tracker will encounter a W layer before a SSD. Neighboring trays are perpendicular to each other, allowing the (x, y) positions of the $e^{\pm}$ to be measured.

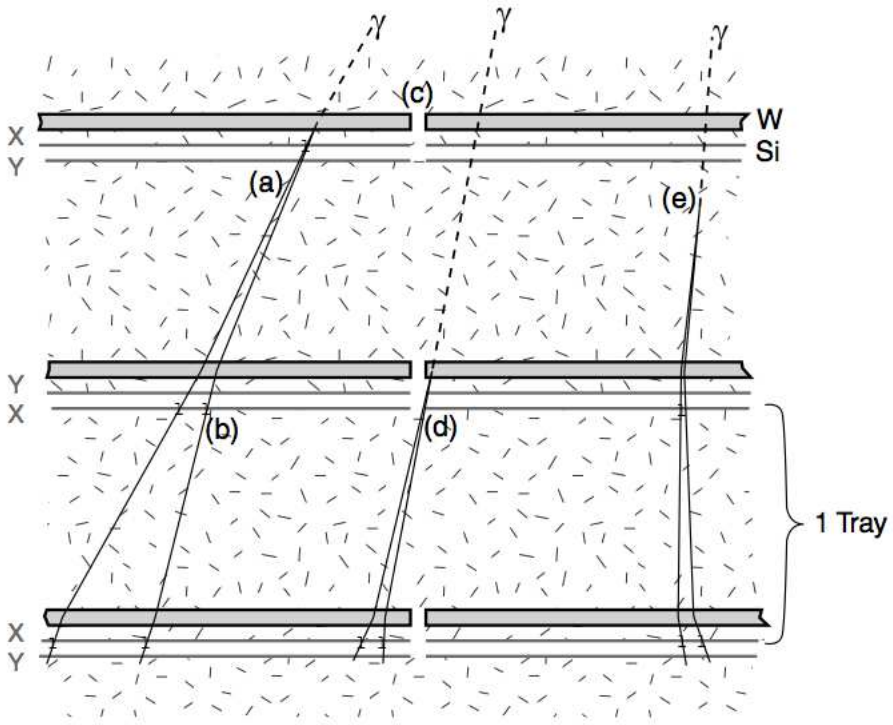

Figure 1.7: This diagram shows the arrangement of the trays in the tracker. The top layers have a tungsten (W) layer immediately followed by a silicon (Si) layer. The high Z of the W layer encourages pair conversion, so that the particle pair will be detected by the subsequent Si layers and its track can be accurately reconstructed. The letters in the diagram show the following: (a) This is the ideal conversion of a γ ray in the W layer. The pairs are immediately detected in the Si layer below, which is placed so close to the W layer to minimize multiple scatterings and constrain the particles' tracks. As a result, scattering in subsequent W layers will have little effect on the final track measurement. (b) It is possible to detect both particles separately in the Si layers, which improves the PSF and background rejection. (c) This demonstrates the way the W converter layers are set up to cover only the active part of the Si detectors, so that pair conversion in places where a close-by measurement from a Si detector is not possible is minimized. (d) This photon did not pair convert in the first W layer. As a result, the PSF can be degraded by up to a factor of 2. (e) This photon converted into a pair in material outside the W layers. Conversion in the Si or other structural layers gives the opportunity of multiple scattering, so material that is not actively used in the instrument is minimized. This figure was reproduced from Atwood et al. (2009).

The tracker (Figure 1.7) is used to reconstruct the direction of the incident γ-ray from a point source, the probability distribution of which is the point-spread function (PSF). The LAT's angular resolution is limited by multiple scatterings and bremsstrahlung. These phenomena are minimized for photons that pair convert in the first W layer and are immediately detected by the SSDs below, as there is little opportunity for scattering before that point. Multiple scattering, the effect of which is proportional to $1/E$, dominates the uncertainty in direction at lower γ-ray energies, resulting in the LAT's energy-dependent PSF that must then be taken into account in all analyses. Scattering of low-energy γ-rays increases with the effective area, while high-energy γ-rays are more rare and thus require a larger effective area to be sufficiently detected. To balance these effects, the top twelve tungsten layers are thin (0.03 radiation lengths thick) and are referred to as the "front tracker"; the bottom four, the "back tracker", are $\sim 6\times$ as thick. Note that many analyses can be done using events from both trackers, but there are cases when selecting events detected only in one tracker or the other is useful.

The calorimeter measures the energy deposited in its layers by the $e^{\pm}$ pair and images the profile of the shower produced by the particles, the latter of which aids in background rejection. Each of the 16 modules is composed of eight layers of twelve CsI(Tl) crystals, which scintillate in response to incoming particles. The crystals are long, having dimensions of $2.7\,\mathrm{cm} \times 2.0\,\mathrm{cm} \times$ 32.6cm; Carlson et al. (1996) showed that these long crystals can be used to measure photon energy and incident angle with good resolution. Additionally, calorimeters in which the showering material is also the detecting medium, as is the case for scintillating crystals, result in the best energy resolution, as low as $\sim 1\%$. The crystals lie horizontally in each layer, and neighboring layers are again rotated by 90° with respect to each other. Photodiodes at the ends of the crystals measure the scintillation light. The difference in intensity

gives a position of energy deposition in the crystal. The position measurement is more precise for higher energies (ranging from a few mm at 10 MeV to less than 1 mm above 10 GeV).

The tracker and calorimeter are used together to measure the incident γ-ray's energy and direction. The energy measurement comes primarily from the energy deposited in the calorimeter and from the shower profile. At low energies, a significant fraction of the photon energy can be deposited in the tracker as well, and must be added to the energy measured in the calorimeter. Energy deposited in the tracker is estimated from the number of silicon strips that are hit in each tracker layer. The tracker is primarily used to reconstruct the tracks of the $e^{\pm}$ pair and hence direction of the photon, but energy information from the calorimeter helps to constrain the particles' tracks.

While both the reconstructed tracks from the converter-tracker and the shower profile from the calorimeter are used to reject cosmic rays, an anti-coincidence detector (ACD; details in Moiseev et al. 2007) is used to shield the LAT from the high cosmic ray background with 0.9997 efficiency. The ACD is also designed to suppress the "backsplash effect." Secondary particles, typically 100–1000 keV photons, are created in the EM shower from the incident γ-ray and are Compton scattered to hard X-ray energies in the ACD, causing false veto signals coincident with the true γ-ray event. In order to suppress this effect, the ACD is segmented so that only the segment near the photon's entrance to the LAT contributes to backsplash (Moiseev et al. 2004). Also, veto signals are not used if the energy deposition in the calorimeter is greater than $\sim$ 10–20 GeV. The ACD is surrounded by a micrometeoroid shield to prevent penetration of the ACD and subsequent light leakage.

1.2.2 LAT Data Analysis

As mentioned above, the angular resolution (or PSF) of the LAT is energy-dependent, with the PSF decreasing with increasing energies. This introduces a major complication in the data analysis: how is one to know with any certainty that a given detected event originated from a given source, when there are several sources whose position error ellipses overlap with that of the event? Simple background subtraction, for example with an annulus around the source of interest, cannot be performed because sources are larger at low energies than at high energies. Additionally, the bright Galactic diffuse emission is clumpy enough that a background estimate obtained a few degrees away from a source will likely not represent the background at the source's position.

The solution is to perform a likelihood analysis within a region of sky surrounding the source of interest, through which each event is assigned a likelihood of being associated with one source or another. Each point source in the region of interest (ROI) is given an initial model for its position and spectrum, usually a power law. (Extended sources are given a model for their shape, for example a uniform or Gaussian disk, rather than a single position.) In this way, source positions and spectra can be obtained. The source position can be estimated to within an error circle of size ~ 0.1–0.5°, despite the PSF being $\sim 1^\circ$ at 1 GeV, depending on the number of photons and on the source spectrum (the position can be determined to higher accuracy for harder sources.) An important component in this analysis is the use of an accurate spatial and spectral model for the Galactic and extragalactic backgrounds. These models are constructed and made available by the LAT collaboration, and there is always work being done to improve the current diffuse models.

The likelihood analysis of LAT data follows that of EGRET data, which is

detailed in Mattox et al. (1996). The likelihood $\mathcal{L}$ of a LAT image, or counts map (essentially a two-dimensional array containing the number of counts detected in each pixel), given a model of the γ-ray emission that includes the sky coordinates and spectrum, is the product of the probability for each pixel in the image,

$$\mathcal{L} = \prod_{ij} p_{ij} \ . \tag{1.17}$$

Because the LAT is a photon counting instrument, Poisson statistics define the probability. In this case, p_{ij} is the Poisson probability of observing n_{ij} counts in pixel ij, given a model that predicts the number of counts to be θ_{ij}. This probability is given by

$$p_{ij} = \frac{\theta_{ij}^{n_{ij}} e^{-\theta_{ij}}}{n_{ij}!} \ . \tag{1.18}$$

It is more straightforward to calculate the logarithm of the likelihood, such that Equation 1.17 becomes

$$\ln \mathcal{L} = \sum_{ij} \ln p_{ij} \tag{1.19a}$$

$$\ln \mathcal{L} = \sum_{ij} n_{ij} \ln (\theta_{ij}) - \sum_{ij} \theta_{ij} - \sum_{ij} \ln (n_{ij}!) \ . \tag{1.19b}$$

The last term is not model dependent and therefore is not useful for parameter estimation or model comparison via the likelihood ratio test. Mathematically, the likelihood ratio test becomes a subtraction of two likelihoods in logarithm space, so the last term will cancel out. The final expression for the likelihood is then

$$\ln \mathcal{L} = \sum_{ij} n_{ij} \ln (\theta_{ij}) - \sum_{ij} \theta_{ij} \ . \tag{1.20}$$

In practice, all of the above is done using various LAT Science Tools that are distributed and updated by the collaboration. After data preparation, the likelihood analysis is performed using the `gtlike` tool, which maximizes the likelihood and computes best-fit model parameter values and uncertainties for all free parameters

in the fit. The analysis is typically done within a ROI at least $10^\circ \times 10^\circ$ in size, with a pixel scale $\sim 0.1^\circ$ per pixel. Each source within the ROI is given a spatial model (usually fixed at a known best position) and spectral model. The likelihood is calculated at the initial parameter values, and then source's parameters are fit in an iterative fashion using Newton-Raphson iteration until the likelihood is maximized.

1.3 LAT Pulsar Light Curve Construction

Young, energetic rotation-powered pulsars display γ-ray pulsations, likely due to the formation of caustics (Section 2.4) in the outer magnetosphere. Detecting these pulsations requires recording the arrival time of each photon at the detector with high accuracy. The timing accuracy of the LAT is $< 10\,\mu$s, making it an excellent instrument for the study of pulsar light curves and phase-resolved spectra.

Pulsar light curves are constructed by assigning a rotation phase to each photon and binning the photons in phase. The phase ϕ is assigned by defining a time t_0 corresponding to ϕ_0 and using the timing solution of the pulsar to calculate $\phi(t)$ of each photon after that. The timing solution consists of the spin frequency ν_0, spindown rate $\dot{\nu}_0$, and other parameters (for example, parameters describing binary motion) that together predict the time t_i of the i^{th} pulse relative to the fiducial time t_0. Then ϕ_i is calculated by

$$\phi_i = \phi_0 + \nu_0(t_i - t_0) + \frac{1}{2}\dot{\nu}_0(t_i - t_0)^2 + \ldots \tag{1.21}$$

The process of pulsar timing is discussed in Chapter 5.

As discussed above, it is not possible to know a photon's originating source with certainty. This makes it difficult to choose which photons to include in a pulsar's light curve. Ray et al. (2011a) used the "cookie cutter" method, in which all photons within a certain radius from the pulsar position and within a certain energy range

are included in the light curve. The radius and energy range are determined by maximizing the signal-to-noise of the light curve.

In this thesis, the light curves were constructed using an energy-dependent inclusion radius optimized for bright pulsars (e.g., Abdo et al. 2010b),

$$\theta < \max[1.6 - 3\log_{10}(E_{\rm GeV}), 1.3], \tag{1.22}$$

where $E_{\rm GeV}$ is the photon energy measured in GeV. All counts falling within an angular distance θ from the given pulsar were binned in pulse phase to make the light curves.

Another method developed by Kerr (2011) is to first model the spectrum of the pulsar and then determine, for each photon, the probability that it originated from the pulsar of interest. The light curves are then constructed by weighting each photon in the region with its probability (photons that are far from the pulsar will have essentially zero probability, and will not contribute to the light curve). This method was used to construct light curves for the second LAT pulsar catalog (The Fermi-LAT Collaboration 2013).

Chapter 2

High-Energy Pulsar Emission

2.1 High-Energy Particle and Photon Interactions

2.1.1 Particle Acceleration

Charged particles are accelerated in the presence of an electric field **E**. Across a potential drop Φ, a particle of charge q will gain energy $\epsilon = q\Phi$, and as it accelerates it will emit electromagnetic (EM) radiation. In the non-relativistic regime, in which the magnitude of the particle's velocity $v \ll c$, the power emitted by the particle is given by the Larmor formula,

$$P = \frac{2}{3}\frac{q^2 a^2}{c^3} \tag{2.1}$$

where a is the magnitude of the particle's acceleration.

Particles must be accelerated to extremely high (GeV–TeV) energies in order to emit high-energy γ-ray photons like those detected by the *Fermi* LAT, which is most sensitive to photons in the energy range $0.02\,\mathrm{MeV} < \epsilon < 300\,\mathrm{GeV}$. At these particle energies, $\beta \equiv v/c \gg 1$, and the particle's Lorentz factor

$$\gamma \equiv \frac{1}{\sqrt{1-\beta^2}} \gg 1 \tag{2.2}$$

The relativistic Larmor formula, or Liénard formula, must be used to calculate the power emitted by such highly accelerated particles:

$$\begin{aligned} P &= \frac{2}{3}\frac{q^2}{c^3}\mathbf{a}' \cdot \mathbf{a}' = \frac{2}{3}\frac{q^2}{c^3}({a'_\parallel}^2 + {a'_\perp}^2) \\ &= \frac{2}{3}\frac{q^2}{c^3}\gamma^4(a_\perp^2 + \gamma^2 a_\parallel^2) \end{aligned} \tag{2.3}$$

The primed frame is the particle's instantaneous rest frame, which is related to the inertial frame by a Lorentz transformation, such that

$$a'_\parallel = \gamma^3 a_\parallel, \quad a'_\perp = \gamma^2 a_\perp \tag{2.4}$$

Pulsar magnetospheres contain enormous potential drops, with $\Phi \sim 10^{13}\,\mathrm{V}$ induced by the rapidly rotating magnetic field with surface strength $B \sim 10^{12}\,\mathrm{G}$. The induced electric field $\mathbf{E}$ has a component $E_\parallel$ that is parallel to the magnetic field (Deutsch 1955) along which particles are accelerated to GeV energies. Particle acceleration, and subsequent EM radiation, in pulsar magnetospheres is a natural explanation for the γ-ray emission observed from these objects. Additionally, it provides a means of converting the rotational energy lost by the pulsar, which is essentially a rotating magnet, into observed radiation.

2.1.2 Synchrotron Emission

Synchrotron radiation is a special case of curvature radiation, discussed in the following section, in which a relativistic particle's acceleration is perpendicular to the magnetic field. Neglecting radiation losses, the particle's equations of motion are

$$\frac{d}{dt}(\gamma m \mathbf{v}) = \frac{q}{c}\mathbf{v} \times \mathbf{B}, \tag{2.5a}$$

$$[1ex]\frac{d}{dt}(\gamma m c^2) = q\mathbf{v} \cdot \mathbf{E} = 0. \tag{2.5b}$$

where m is the particle mass. In this case, γ and $|\mathbf{v}|$ are constant, and

$$m\gamma\frac{d\mathbf{v}}{dt} = \frac{q}{c}\mathbf{v} \times \mathbf{B} \tag{2.6}$$

The velocity components parallel and perpendicular to the magnetic field evolve according to

$$\frac{d}{dt}\mathbf{v}_{\parallel} = 0 \tag{2.7a}$$

$$\frac{d}{dt}\mathbf{v}_{\perp} = \frac{q}{\gamma mc}\mathbf{v}_{\perp} \times \mathbf{B} \tag{2.7b}$$

The particle therefore travels at a constant velocity parallel to the magnetic field and with acceleration perpendicular to the field, resulting in a helical motion of the particle through the field. The frequency of gyration (rotation around a field line) is

$$\omega_s = \frac{qB}{\gamma mc} = \frac{qBc}{\epsilon} \tag{2.8}$$

and the gyroradius (radius of curvature) is

$$\rho = \frac{v}{\omega_s} = \frac{\epsilon}{qB} \text{ for } v \approx c \tag{2.9}$$

Because the particle is accelerated, it radiates and deviates from the assumption of zero radiation losses used above. Substituting the magnitude of the acceleration $a_{\perp} = \omega_c v_{\perp}$ into the Liénard formula (Equation 2.3) yields the total power emitted by synchrotron emission from a population of particles with an isotropic velocity distribution:

$$P = \frac{2q^2}{3c^3}\gamma^4 \frac{q^2B^2}{\gamma^2 m^2 c^2} v_{\perp}^2 \tag{2.10a}$$

$$= \frac{2}{3} r_0^2 c \beta_{\perp}^2 \gamma^2 B^2 \tag{2.10b}$$

where $r_0 = e^2/(mc^2)$ is the classical radius of a charged particle ($r_0 \approx 2.8 \times 10^{-13}\,\mathrm{cm}$ for an electron and $1.5 \times 10^{-16}\,\mathrm{cm}$ for a proton) and $e = 1.602 \times 10^{-16}\,\mathrm{C}$ is the fundamental unit of charge. On timescales shorter than the energy loss timescale, Equations 2.5–2.7 are adequate, and the particle's motion will follow the helical motion described. As it radiates, it will deviate from this simple case.

The relativistic motion of the particle causes its radiation to be beamed into a cone of half-angle $\theta = 1/\gamma$. An important outcome of the beaming of synchrotron radiation is that, because the particle is accelerated in a circular pattern in a direction perpendicular to its velocity, the radiation that reaches the observer is pulsed within a time interval a factor of γ^3 smaller than the gyration period and has a broad spectrum (Rybicki & Lightman 1979). The total synchrotron power radiated per unit angular frequency by a single particle is

$$P(\omega) = \frac{\sqrt{3}}{2\pi}\frac{q^3 B}{mc^2}\sin(\chi) F\left(\frac{\omega}{\omega_c}\right), \tag{2.11}$$

where the critical frequency $\omega_c \equiv (2/3)\gamma^3 \omega_s \sin(\chi)$, $\chi = \tan^{-1}(\beta_\perp/\beta_\parallel)$ is the pitch angle between the electron's velocity and $\mathbf{B}$, and

$$F(x) = x\int_x^\infty K_{5/3}(\xi)d\xi \tag{2.12}$$

$K_{5/3}$ is the modified Bessel function of second order with $n = 5/3$. For $\omega \ll \omega_c$, $F \propto \omega^{1/3}$, while for $\omega \gg \omega_c$, $F \propto \omega^{1/2}\exp(-\omega/\omega_c)$.

For $\gamma \gg 1$ (commonplace in pulsar magnetospheres), the pitch angle χ and the parallel velocity $\beta_\parallel$ are constant, and χ is equivalent to the (also constant) half-angle of emission $1/\gamma$. In this limit, Equation 2.11 can be rewritten in terms of γ (e.g., Yadigaroglu 1997):

$$P(\omega) = \frac{\sqrt{3}}{2\pi}q^2\left(\frac{\gamma}{\rho}\right)F\left(\frac{\omega}{\omega_c}\right) \tag{2.13a}$$

$$\omega_c = \frac{3c\gamma^3}{2\rho} \tag{2.13b}$$

$$\rho = \frac{E}{qB_\perp} = \frac{\gamma mc^2}{qB_\perp} \tag{2.13c}$$

The spectrum of a population of particles with some distribution of γ factors can then be found by integrating Equation 2.11 or 2.13a over the γ distribution. Astrophysical sources are often found to have a power law distribution of energies, such

that the number of particles with a given γ is

$$N(\gamma)d\gamma \propto \gamma^{-p}d\gamma \tag{2.14}$$

where p is the power law index. Integrating the synchrotron spectrum yields another power law spectrum, $P(\omega) \propto \omega^{-s}$, with spectral index s related to the particles' power law index p by

$$s = \frac{p-1}{2} \ . \tag{2.15}$$

Free electron energy levels are quantized in the presence of a magnetic field. For $B \ll \gamma(\gamma-1)B_{\rm c}$, where $B_{\rm c} = m_e^2/(c^3 e\hbar) = 4.414 \times 10^{13}\,{\rm G}$, these quantum effects can be ignored as in the discussion above. However, in pulsar magnetospheres, the field strength can be comparable to or greater than $B_{\rm c}$. The classical treatment of synchrotron radiation breaks down for field strengths $B > \gamma(\gamma-1)B_{\rm c}$ because the critical radiation frequency exceeds the electron kinetic energy, violating energy conservation (e.g., Brainerd & Lamb 1987). To not violate energy conservation, electrons lose all of their energy in single emission events as the peak of the photon energy spectrum approaches the electron kinetic energy, resulting in a sharp cutoff at this energy (e.g., Harding & Preece 1987). For magnetic fields approaching $B_{\rm c}$, quantum synchrotron formulae (Sokolov et al. 1968; Harding & Preece 1987; Harding & Lai 2006) must instead be used.

2.1.3 Curvature Radiation

Synchrotron radiation is a form of curvature radiation (CR) in which the particle's momentum has a significant component perpendicular to the magnetic field. In the case where $\mathbf{v}_\perp = 0$, a particle travels along a field line with pitch angle $\chi = 0$. To maintain such motion, the particle must be continuously accelerated along the field line by an electric field, $E_\parallel$. In the case of synchrotron radiation, the radius of

curvature ρ was the gyroradius of the particle's circular motion around the magnetic field line. For curvature radiation, $\rho = \rho_c$ is instead the instantaneous radius of curvature of the field line. The power emitted by a particle via CR is

$$P = \frac{2}{3}\frac{q^2 c}{\rho_c^2}\beta^4\gamma^4 \tag{2.16}$$

which is again beamed forward in a cone of half-angle $1/\gamma$.

Similarly to the synchrotron spectrum, the energy spectrum of CR has a critical energy

$$\epsilon_{\rm CR} = \frac{h\omega_{\rm CR}}{2\pi} = \frac{3}{2}\frac{c\hbar}{\rho_c}\gamma^3 \ . \tag{2.17}$$

where $h = 6.626 \times 10^{-27}\,{\rm erg\,s^{-1}}$ is Planck's constant and $\hbar = h/(2\pi)$. This critical energy is often instead expressed as

$$\epsilon_{\rm CR} = \frac{3}{2}\frac{\lambda\!\!\!^{-}_c}{\rho_c}\gamma^3 mc^2 \tag{2.18}$$

where h from the previous equation has been replaced by $\lambda_c mc$, $\lambda\!\!\!^{-}_c = \lambda_c/(2\pi)$, and $\lambda_c \equiv h/mc = 0.02426\,{\rm \AA}$ is the Compton wavelength.

The spectrum is essentially the same as Equation 2.11. The power emitted at photon energy ϵ from a single charge accelerated along a field line with instantaneous radius of curvature ρ_c is essentially Equation 2.11. Expressing the power as a function of energy, and using $\omega = c\beta/\rho_c$ (Jackson 1975), the single-particle spectrum is:

$$P_{\rm CR}(\epsilon) = -\sqrt{3}\frac{q^2}{\hbar c}\frac{\gamma c}{2\pi\rho_c}\,F\left(\frac{\epsilon}{\epsilon_{\rm CR}}\right) \tag{2.19}$$

Again, for $\epsilon \ll \epsilon_c$, $F \propto \epsilon^{1/3}$, and for $\epsilon \gg \epsilon_c$, $F \propto \epsilon^{1/2}\exp\left(-\epsilon/\epsilon_c\right)$.

High-energy pulsar emission is thought to be from curvature radiation of electrons that are accelerating in the pulsar magnetosphere in the radiation reaction (RR) regime. In the radiation reaction limit, the energy a particle loses by radiation is equivalent to that gained by acceleration, so the particle has a steady-state

γ. The energy balance is (e.g., Yadigaroglu 1997)

$$\frac{d}{dt}(\gamma mc^2) = -P_{\rm CR} + qE_{\parallel}c \tag{2.20}$$

where the second term represents the acceleration of the particle by the electric field parallel to the magnetic field line. In steady state, $d\gamma/dt = 0$. For $\beta \approx 1$,

$$\gamma_{\rm RR} = \left(\frac{3}{2}\frac{E_{\parallel}}{q}\rho_{\rm c}^2\right)^{1/4} \tag{2.21}$$

In a pulsar magnetosphere, where the surface magnetic field strength $B \sim 10^{12}\,{\rm G}$, the electric potential $\Phi \sim 10^{13}\,{\rm V}$ results in $E_{\parallel} \sim 10^4\,{\rm V\,cm^{-1}}$. In such a strong field, particles are accelerated to a steady-state $\gamma \sim 3 \times 10^7$ (e.g. Yadigaroglu 1997) on a timescale $\sim 10^{-4}\,{\rm s}$. The cutoff energy of CR in the radiation reaction regime is

$$\epsilon_{\rm CR,RR} = \frac{3}{2}\frac{\lambda\!\!\!^{-}_c}{\rho_{\rm c}}\gamma_{\rm RR}^3 mc^2 \sim 5\,{\rm GeV} \tag{2.22}$$

This cutoff energy is consistent with that measured in pulsars' γ-ray spectra, suggesting that radiation from particles accelerated in pulsar magnetospheres is dominated by CR in the RR limit.

It is useful to note here that these extremely high Lorentz factors result in the cone of radiation from the particle having a half-angle $\theta = 1/\gamma \sim 0$, i.e. the radiation is emitted almost tangent to the field line. This approximation is used in Chapter 3, in which pulsar emission is simulated for photons emitted tangent to $\mathbf{B}$.

2.1.4 Inverse Compton Scattering

Compton scattering refers to the general process by which radiation is scattered off of free electrons. A photon that undergoes Compton scattering changes its direction of propagation by an angle θ relative to its original direction, and undergoes a change in its energy ϵ. The post-scatter photon energy ϵ_1 is related to the initial photon

energy ϵ by (Rybicki & Lightman 1979)

$$\epsilon_1 = \frac{\epsilon}{1 + \frac{\epsilon}{mc^2}(1 - \cos\theta)} \tag{2.23}$$

The difference in wavelengths

$$\lambda_1 - \lambda = \lambda_{\rm c}(1 - \cos\theta), \tag{2.24}$$

where the Compton wavelength $\lambda_{\rm c} \equiv h/mc = 0.02426\,\text{Å}$ for electrons. For long wavelengths $\lambda \gg \lambda_{\rm c}$ (low photon energies, $h\nu \ll mc^2$), scattering is nearly elastic, so $\epsilon_1 \sim \epsilon$. Thus, at low photon energies, Compton scattering is approximated by classical Thomson scattering, for which the scattering cross section is

$$\sigma_T = \frac{8\pi}{3} r_0^2 = 6.65 \times 10^{-25}\,\text{cm}^2 \tag{2.25}$$

where $r_0 = e^2/(mc^2) \approx 2.8 \times 10^{-13}\,\text{cm}$ is the classical electron radius. At higher photon energies, quantum effects become important, resulting in the differential cross section for unpolarized radiation given by the Klein-Nishina formula (Heitler 1954),

$$\frac{d\sigma}{d\Omega} = \frac{r_0^2}{2}\frac{\epsilon_1^2}{\epsilon^2}\left(\frac{\epsilon}{\epsilon_1} + \frac{\epsilon_1}{\epsilon} - \sin^2\theta\right) \tag{2.26}$$

As ϵ increases, the scattering cross section decreases from its classical size. The total Klein-Nishina cross section is

$$\sigma = \frac{3}{4}\sigma_{\rm T}\left[\frac{1+x}{x^3}\left(\frac{2x(1+x)}{1+2x} - \ln(1+2x)\right) + \frac{1}{2x}\ln(1+2x) - \frac{1+3x}{(1+2x)^2}\right] \tag{2.27}$$

where $x \equiv h\nu/mc^2$. For $x \ll 1$, $\sigma \sim \sigma_{\rm T}$, while for extremely high energies,

$$\sigma_{\rm K} = \frac{3}{8}\sigma_{\rm T} x^{-1}\left(\ln 2x + \frac{1}{2}\right), x \gg 1\ . \tag{2.28}$$

In high energy astrophysics, often the kinetic energy of the electron is comparable to or greater than the photon energy, in which case net energy can be transferred

from the electron to the photon. This process is inverse Compton scattering. In the electron's (primed) frame, the initial energy of the photon is

$$\epsilon' = \epsilon\gamma(1 - \beta\cos\theta) \tag{2.29}$$

where ϵ and β are the photon energy and electron velocity in the lab frame. The post-scatter energy of the photon, in the lab frame, is

$$\epsilon_1 = \epsilon_1'\gamma(1 + \beta\cos\theta') \tag{2.30}$$

The result is that, for highly relativistic electrons, the final photon energy is $\epsilon_1 \sim \gamma^2\epsilon$.

The total power from inverse Compton scattering of an isotropic radiation field incident on an isotropic electron distribution is

$$P = \frac{4}{3}\sigma_T c\gamma^2\beta^2 U_{\rm rad} \tag{2.31}$$

where $U_{\rm rad}$ is the energy density of the radiation field, and it is assumed that each photon is scattered once by each electron. The energy spectrum of inverse Compton radiation is again a power law with spectral index $s = (p-1)/2$, assuming an electron population with γ distributed as a power law with index p.

The above equations all assume photon energies $\leq 100\,\mathrm{keV}$, for which the treatment is classical and the Thomson cross section is valid. At higher photon energies like those probed by the *Fermi* LAT, it is necessary to include quantum effects through use of the Klein-Nishina cross section, which is smaller than σ_T.

The next three sections focus on high-energy processes in very strong magnetic fields, and closely follow Sections 5.4 and 5.6 of Harding & Lai (2006).

2.1.5 Single Photon Pair Production

Single photon pair production is the process by which an individual photon produces an electron-positron pair. In a field-free space, this process cannot occur because energy and momentum cannot both be conserved. However, in the presence of a strong magnetic field with a nonzero transverse component to the photon direction, the field absorbs the extra momentum, and single photon pair production can occur. As will be seen in the following sections, single photon pair production is an important process in pulsar magnetospheres. In this and the next two sections, it is assumed that $c = \hbar = 1$ and that all energies are in units of mc^2.

In strong magnetic fields, the quantization of energy states becomes important for free particles, and as a result, a photon can only produce an electron and positron in these discrete states (Landau states). The energy and momentum conservation equations are

$$E_n + E_{n'} = \epsilon \tag{2.32}$$

$$p + q = \epsilon \cos\theta \tag{2.33}$$

where ϵ is the photon energy and θ is its angle to $\mathbf{B}$; p is the electron momentum parallel to the photon's direction of propagation and q is the parallel momentum of the positron; and $E_n = (1+p^2+2nB/B_c)^{1/2}$ and $E_{n'} = (1+q^2+2n'B/B_c)^{1/2}$ are the electron and positron energies. To produce a pair with parallel momentum in the ground state ($n = n' = 0$), the photon must have energy at or above the threshold energy,

$$\epsilon_0 = 2/\sin\theta \tag{2.34}$$

Single photon pair production is an important process for $B \geq 0.1B_c$. Additionally, for high photon energies and low magnetic fields, single photon pair production

becomes important when $\epsilon B \sin\theta/(2B_c) \geq 0.1$, and the probability of one-photon pair production increases exponentially with increasing ϵ and transverse B.

The above assumes that the particles' momenta are parallel to the photon's motion, i.e. $\mathbf{E} = 0$. In the presence of a perpendicular electric field, these equations are modified slightly (see Harding & Lai 2006).

The inverse process of single photon pair production is single photon pair annihilation, in which an electron-positron pair annihilates to form a single photon. This process is also allowed only in very strong magnetic fields ($B \geq 0.1B_c$). The rate of one-photon pair annihilation increases exponentially with increasing B, and surpasses two-photon pair annihilation at $B \sim 10^{13}\,\mathrm{G}$ (Wunner 1979; Daugherty & Bussard 1980).

2.1.6 Two-Photon Pair Production

Pair creation by two photons conserves both energy and momentum and therefore can occur in the absence of a magnetic field, for sufficiently high photon energies. For this process to occur, the product of the photon energies must exceed $\approx (m_e c^2)^2$ in the center of momentum (c.o.m.) frame, where $m_e = 511\,\mathrm{keV}$ is the electron rest mass. The exact expression defining the c.o.m. energy ϵ_{CM} is $\epsilon_1\epsilon_2 \geq 2\epsilon_{\mathrm{CM}}^2/(1-\cos\theta)$, where all energies are in units of $m_{\mathrm{e}}c^2$. For two-photon pair production to occur, the threshold condition $\epsilon_{\mathrm{CM}} > 1$ must be met.

In a strong magnetic field, the energy and parallel momentum must be conserved:

$$\epsilon_1 + \epsilon_2 = E_n + E_{n'} \tag{2.35}$$

$$\epsilon_1 \cos\theta_1 + \epsilon_2 \cos\theta_2 = p + q \tag{2.36}$$

where θ_1 and θ_2 are the angles of the photons' propagation relative to $\mathbf{B}$. The

requirement for production of a ground state pair is (Daugherty & Bussard 1980)

$$(\epsilon_1 \sin\theta_1 + \epsilon_2 \sin\theta_2)^2 + 2\epsilon_1\epsilon_2[1 - \cos(\theta_1 - \theta_2)] \geq 4. \tag{2.37}$$

The first term comes from the fact that only parallel momentum, and not perpendicular momentum, must be conserved. This means that photons propagating parallel to each other can pair produce, in contrast to a field-free space.

As for single photon pair production, the inverse of two-photon pair production is the annihilation of a pair into two photons. This process is sharply cut off above $B \sim 0.2B_c$. Additionally, as B increases, an asymmetry in the energies of the produced photons grows so that the process begins to resemble single photon pair annihilation (Wunner 1979; Daugherty & Bussard 1980).

2.1.7 Photon Splitting

Photon splitting is a process by which one photon propagating through a strong magnetic field divides into two or more photons. Although it conserves energy and momentum in the absence of a field, photon splitting only occurs due to quantum electrodynamical (QED) effects that are beyond the scope of this discussion. In a weakly dispersive medium, three photon polarization modes are permitted by QED: $\perp \rightarrow \parallel\parallel$, $\parallel \rightarrow \perp\parallel$, and $\perp \rightarrow \perp\perp$. The attenuation coefficient for each of these polarization modes goes as

$$R_{\rm sp} \propto \alpha_{\rm fs}^3 \epsilon^5 \left(\frac{B}{B_c}\right)^6 \sin^6\theta \tag{2.38}$$

where $\alpha_{\rm fs} \approx 1/137$ is the fine structure constant, ϵ is the incident photon energy, and θ is the angle of propagation relative to the field (Adler 1971; Baring 1991). Photon splitting can occur at any photon energy, unlike pair production, which has an energy threshold. At field strengths $B \gg B_c$, $(B/B_c)^6 \rightarrow 1$ and the rate becomes essentially independent of B (Harding & Lai 2006).

The fine structure constant is included in Equation 2.38 in order to point out the dependence of the photon splitting rate on $\alpha_{\rm fs}$. The rate is $\propto \alpha_{\rm fs}^3$, making photon splitting a third-order process. Single photon pair production is instead a first-order process; therefore, above the pair production energy threshold, in general the rate of photon splitting is a factor of $\alpha_{\rm fs}^2 \sim 0.5 \times 10^{-4}$ smaller than that of single photon pair production. However, because $R_{\rm sp}$ is so sensitive to B, in very strong magnetic fields photons may split before reaching the pair production threshold (Baring 1991; Harding et al. 1997). This is an important effect for particle acceleration and radiation in the low-altitude, polar cap region of pulsar magnetospheres. Attenuation via photon splitting becomes a dominant mechanism for $B \geq B_c$ (Baring & Harding 1998).

2.2 Pulsar Emission Models

According to Faraday's law, a rotating magnetic field will induce an electric field,

$$\boldsymbol{\nabla} \times \mathbf{E} + \frac{\partial \mathbf{B}}{\partial t} = 0. \tag{2.39}$$

For a star, rotating in a vacuum, whose magnetic field axis is inclined to the rotation axis, the induced $\mathbf{E}$ has parallel and perpendicular components, $E_\parallel$ and $E_\perp$, to the magnetic field. This result was shown by Deutsch (1955), who derived analytic expressions for the electromagnetic field of a non-axisymmetric dipole field of a finite-radius star rotating in a vacuum. Given this result, Goldreich & Julian (1969) showed that for a fast-spinning pulsar with a typical surface field strength $B_{\rm s} \sim 10^{12}$ G, the induced electric potential parallel to $\mathbf{B}$ exceeds the gravitational potential and the work function of the surface material by many orders of magnitude. Particles are pulled from the neutron star surface and accelerated along magnetic field lines by the parallel component of the electric field, $E_\parallel = \mathbf{E} \cdot \mathbf{B}/B$. Thus, a neutron star

cannot exist in a vacuum. If this process continues until the magnetosphere becomes filled with charge, then $E_\parallel = 0$. The Lorentz force vanishes, and it follows that

$$\mathbf{E} + \boldsymbol{\beta} \times \mathbf{B} = 0, \tag{2.40}$$

where

$$\boldsymbol{\beta} = \frac{\mathbf{v}}{c} = \frac{\boldsymbol{\Omega} \times \mathbf{r}}{c} \tag{2.41}$$

is the normalized velocity of a point in the magnetosphere as it corotates with the neutron star. Equation 2.40 is the condition defining the ideal force-free magnetosphere (Goldreich & Julian 1969). The accelerating field vanishes at the critical charge density (Goldreich & Julian 1969)

$$\rho_{\rm GJ} = \frac{\nabla \cdot E}{4\pi} \approx -\frac{\boldsymbol{\Omega} \cdot \mathbf{B}}{2\pi c}, \tag{2.42}$$

commonly known as the Goldreich-Julian charge density.

In the Goldreich & Julian (1969) model, charge separation occurs due to the outflow of negative charges in regions where $\Omega \cdot B > 0$ and the outflow of positive charges elsewhere. The magnetosphere is split into four quadrants populated with particles of the same charge, which alternates between quadrants. The regions are separated by null charge surfaces (NCS) of $\boldsymbol{\Omega} \cdot \mathbf{B} = 0$.

The force-free magnetosphere is fully conductive, and $E_\parallel = 0$; as a result, no charge acceleration or radiation occurs in a force-free magnetosphere. However, radiation is of course observed from pulsars, suggesting that regions of non-zero $E_\parallel$ must exist and remain stable over long timescales. Several qualitatively different emission models predicting the locations of these regions have been proposed, three of which (Figure 2.1) will be discussed here. In the polar cap model, acceleration takes place near the surface, over the polar cap. The outer gap model instead invokes a narrow vacuum gap lying along the boundary between the open and closed field

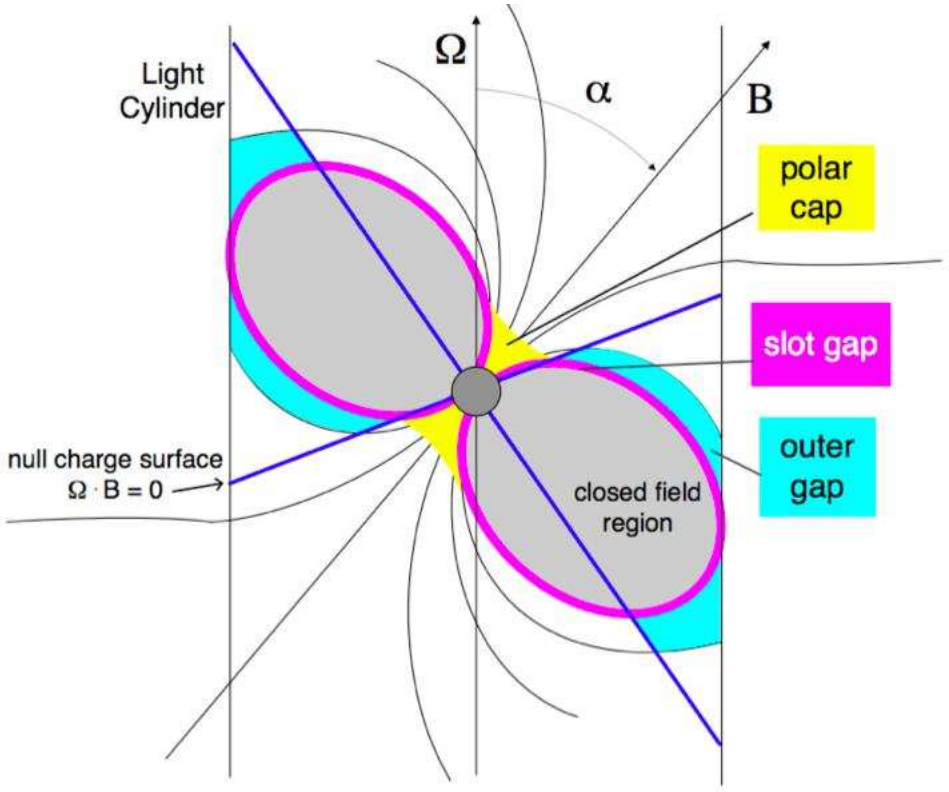

Figure 2.1: Illustration of the geometries of three emission models, two of which are considered in Chapter 3. The polar cap (yellow) is a low-altitude model in which particles are accelerated near the surface. The particles emit γ-rays, which pair produce in the strong magnetic field; those particles then accelerate and radiate, leading to further pair production. A pair production front is formed above the polar cap, screening the electric field and preventing acceleration and subsequent radiation at higher altitudes. Thus far, the LAT has only detected emission from the outer magnetosphere, and the polar cap was therefore not considered in this work. The slot gap (magenta) is an extension of the polar cap. Emission occurs within the slot gap from altitudes near the neutron star surface out to near, or perhaps even beyond, the light cylinder. The outer gap (cyan) model has a different physical motivation, depending on a vacuum that forms between the null charge surface, the boundary across which the net charge changes sign (see Section 2.2.3), and the light cylinder, rather than on pair cascades and electric field screening as in the polar cap and slot gap models. Figure provided by A. K. Harding.

lines (the "last open field lines") at very high emission altitudes, near the light cylinder. The slot gap model extends the polar cap accelerator to high altitudes, so that acceleration and radiation occur in a narrow gap lying along the the last open field lines. An emission model not discussed here that has gained traction in recent years is that of the "separatrix layer," or "annular gap" (Bai & Spitkovsky 2010a; Du et al. 2010).

2.2.1 Polar Cap Accelerator

In polar cap emission models, charges are accelerated near the pulsar surface, above the polar cap. Sturrock (1971) first proposed acceleration above the polar cap as a means for producing γ-ray pulsar emission. He noted that little or no current density should exist along the magnetic axis, and that at the outer edge of the polar cap, where the open and closed field zones meet, there would be a high charge and current density. Thus, $E_\parallel \neq 0$ above the polar cap, and $E_\parallel \to 0$ along the last open field line boundary. Although Goldreich & Julian (1969) found that the electric field induced by the changing magnetic moment of a rotating neutron star would be sufficiently large to pull charges from the surface and populate the magnetosphere, the lattice structure of the neutron star surface (due to the strong surface magnetic field) leads to the requirement that the surface temperature exceed the thermionic temperature in order for particles to escape into the magnetosphere (Usov & Melrose 1995). Thus, two main types of polar cap accelerators have been proposed: vacuum gaps, in which the surface charge density $\rho = 0$ and $E_\parallel \neq 0$(Ruderman & Sutherland 1975), and space-charge limited flow (SCLF) gaps (Arons & Scharlemann 1979; Harding & Muslimov 1998), within which $\rho = \rho_{\rm GJ}$ at the surface. In the SCLF accelerator, the surface $E_\parallel = 0$. The true charge density decreases with radius as $\rho \propto r^{-3}$, faster than $\rho_{\rm GJ}$, resulting in an electric field that grows with altitude according to

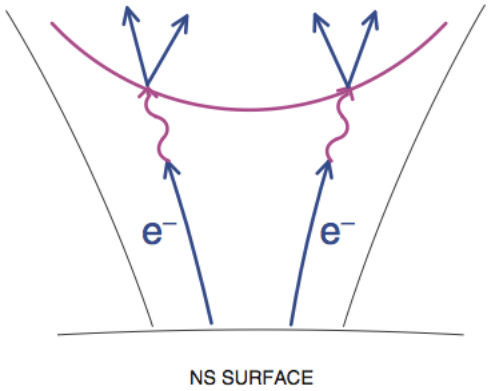

Figure 2.2: A schematic showing the polar cap emission region, from Harding (2009). In this figure, space-charged limited flow (SCLF) is illustrated: particles, in this case electrons, are pulled from the neutron star surface by the very strong $E_\parallel$ (the electric field component parallel to the magnetic field lines). This builds up a charge density ρ until $\rho = \rho_{\rm GJ}$ and $E_\parallel = 0$ at the surface. Above the surface, $\rho < \rho_{\rm GJ}$, and $E_\parallel$ increases, accelerating the electrons along the magnetic field lines. The electrons radiate γ rays, which propagate a short distance before pair producing in the strong magnetic field. A pair cascade results as particles produced in pairs also accelerate and radiate γ rays, which subsequently produce new pairs. The pink curve marks the pair formation front (PFF), where the particles that were formed in the cascades act to screen $E_\parallel$ at higher altitudes. This prevents acceleration and radiation above the PFF, allowing emission to occur only near the neutron star surface.

$\boldsymbol{\nabla} \cdot E_\parallel = (\rho - \rho_{\rm GJ})/\epsilon_0$. Measurements of neutron star surface temperatures find $T \sim 10^6\,{\rm K}$ (e.g., Pavlov et al. 2009), above the thermionic temperature for both electrons and ions for surface magnetic fields $B_{\rm s} \leq 10^{13}\,{\rm G}$, suggesting SCLF is valid at the polar caps of most pulsars.

The SCLF accelerator is populated with charges from the surface. For $\Omega \cdot B > 0$, electrons accelerate upward, while positrons accelerate downward (and vice versa for $\Omega \cdot B < 0$). The upward-accelerating charges reach high enough Lorentz factors to radiate γ-rays, which are beamed with a very small opening angle $\theta = 1/\gamma$. In very strong magnetic fields, γ-rays can pair produce if they cross the magnetic

field lines. Because the photons are emitted essentially parallel to the field, they must propagate a certain distance until the magnetic field line curvature becomes significant, at which point the photons pair produce. The resulting particles are then accelerated and radiate γ-rays, which also produce pairs. The net effect is a cascade of pair production above the acceleration region, forming a pair formation front (PFF) above which $E_{\parallel}$ is screened (Arons & Scharlemann 1979; Harding & Muslimov 1998). For $\mathbf{\Omega} \cdot \mathbf{B} > 0$, electrons that reach the PFF continue outward into the pulsar wind, while positrons formed near the PFF accelerate toward the pulsar surface, heating the polar cap.

The pair cascades can result from pair production by photons that have gained enough energy through inverse Compton scattering in the magnetosphere (IC; Sturner et al. 1995), or by curvature radiation (CR; Daugherty & Harding 1982) photons emitted by charged particles. The latter require much larger Lorentz factors in order to pair produce, because for a given γ the peak CR energy, $\epsilon = 3\lambda_{\rm c}\gamma^3/(2\rho_{\rm c})$ is much lower than that of the IC peak energy (Harding & Muslimov 1998). Only in the magnetospheres of very young and energetic pulsars can CR-emitting charges achieve high enough energies to radiate photons that will pair produce in the field (Harding & Muslimov 2001). The polar cap, heated by returning particles (Harding & Muslimov 2001, 2002), radiates thermal X-ray emission at $kT \sim 0.2 - 0.3\,\mathrm{keV}$ and has been observed for a number of pulsars (e.g., Pavlov et al. 2009).

There is a chance that photons emitted in the polar cap region, where the magnetic field is strongest, will undergo photon splitting before reaching the pair creation threshold. The attenuation of γ-rays by photon splitting results in a reprocessed phase-averaged γ-ray pulsar spectrum that has a sharper cutoff than the purely exponential cutoff expected from CR (Harding et al. 1997). Phase averaged pulsar spectra from the *Fermi* LAT instead show a sub-exponentially cutoff power law.

This does not necessarily rule out γ-ray emission from the polar cap, but implies that if polar cap emission is present, it is not dominant at LAT energies. The emission seen by the LAT must come from the outer magnetosphere so as to not be attenuated. For this reason, we do not include the polar cap model in our light curve fits of Chapter 3.

2.2.2 Slot Gap Accelerator

The slot gap model extends the low-altitude polar cap acceleration region to higher altitudes in a narrow gap that follows the last open field lines to radii near the light cylinder. The original model (Arons & Scharlemann 1979) did not include general relativistic effects, and was able to produce radiation only along certain preferred field lines for relatively high inclination angles. This model was revised by Muslimov & Harding (2003) to include relativistic frame dragging (Muslimov & Tsygan 1992a) and to correctly treat the boundary conditions of the gap ($E_{\parallel} = 0$ along both edges). The slot gap emission region was extended to near the light cylinder by Muslimov & Harding (2004). Preferred field lines were found to be no longer required for high-energy radiation to be produced in the slot gap.

The physical motivation for a slot gap rather than only a polar cap acceleration region is that, because $E_{\parallel} = 0$ at the polar cap boundary, there must be a tapering of $E_{\parallel}$ near the polar cap rim rather than a sudden drop to zero (Arons & Scharlemann 1979). As a result of the decreasing $E_{\parallel}$ toward the polar cap rim, charges that are accelerated near the edge of the polar cap must travel to higher altitudes in order to achieve Lorentz factors sufficient for the emission of γ-ray photons. The PFF produced by pair production cascades is thus extended to much higher altitudes, and γ-rays are emitted across a broad range of emission radii.

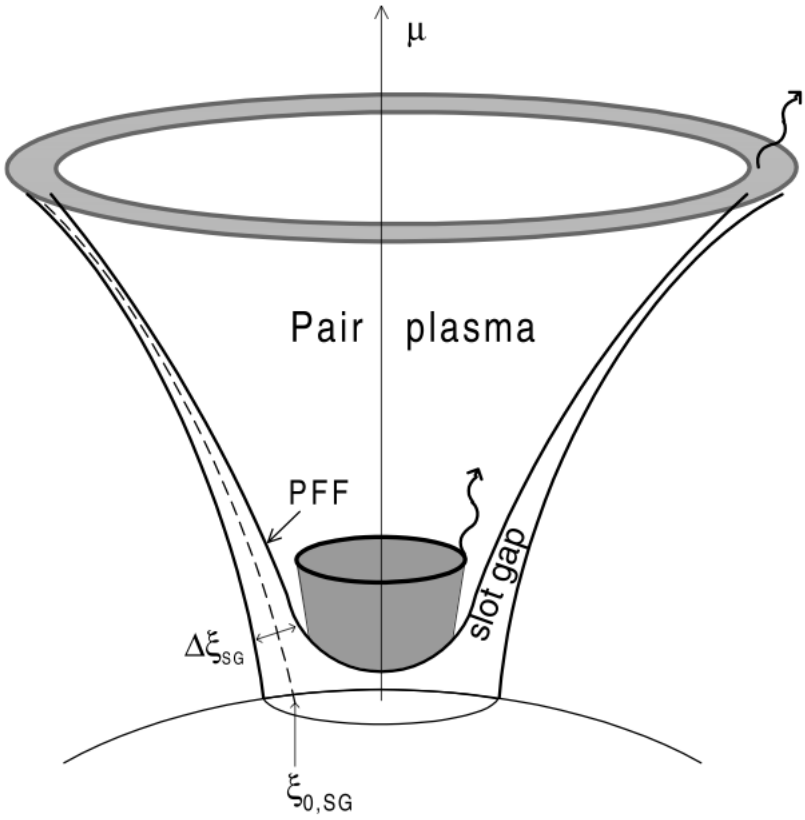

Figure 2.3: A schematic showing the slot gap emission region, from Muslimov & Harding (2003). The outer-most boundary is the boundary between the open and closed field line regions, defining the polar cap on the neutron star surface. The vertical arrow labeled μ is the magnetic moment. The pair formation front, labeled PFF, is formed from pair production of γ-rays in the strong magnetic field. The PFF occurs at low altitudes across most of the polar cap, but extends to higher altitudes near the polar cap rim, forming the region of nonzero $E_{\parallel}$ which is the slot gap. The central magnetic field line is labeled $\xi_{0,\mathrm{SG}}$, and the width of the gap is $\Delta\xi_{\mathrm{SG}}$ (Muslimov & Harding 2003). The gray cylinder at low altitudes shows emission from polar cap pair cascades, while the gray ring at higher altitudes shows a cone of emission from the slot gap.

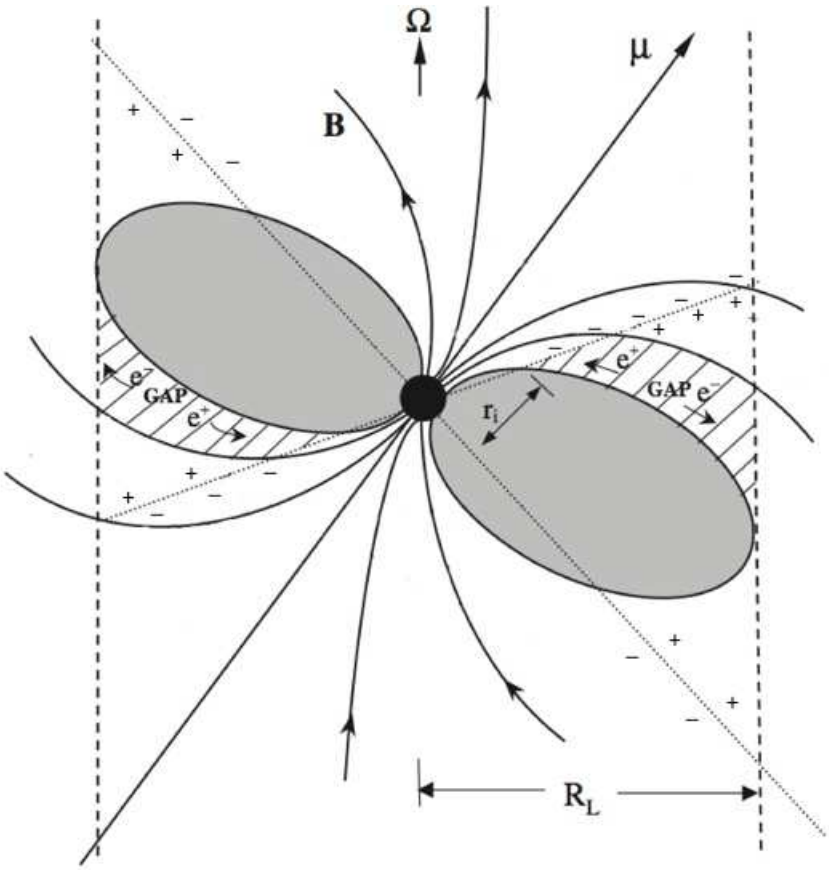

Figure 2.4: A schematic of the pulsar magnetosphere, with null charge surfaces (NCSs, dotted lines) and outer gaps (shaded regions). Charge separation occurs along the NCS (Goldreich & Julian 1969). Oppositely charged particles on opposite sides of the NCS are attracted, while particles of the same charge are repelled, opening a vacuum region called an outer gap. The outer gap extends from radius r_i, the intersection between the NCS and the last closed field line, out to the light cylinder ($R_{\rm L}$ in this figure). This figure was modified from the original Figure 18.2 of Cheng (2009).

2.2.3 Outer Gap Accelerator

The outer gap model (Cheng et al. 1986a,b; Romani 1996) is fundamentally different from the previous models, as it does not rely on particle acceleration near the stellar surface. In this model, particles are accelerated in a narrow region that begins near the intersection of the null charge surface (NCS), defined by $\mathbf{\Omega} \cdot \mathbf{B} = 0$) and the open field line region. The NCS forms a boundary between regions of oppositely

charged particles in the magnetosphere. Figure 2.4 illustrates the four neighboring regions of opposite charge that are separated by NCSs, shown as dotted lines, and the resulting outer gaps (shaded regions). The gap forms as follows: Part of the open field zone lies below the NCS and above the closed field line region. In the region on the right-most side of the figure, for example, $\mathbf{\Omega} \cdot \mathbf{B} < 1$ and the charges contained in the region are positive (positrons). The positrons are drawn to the electrons in the neighboring region. Any electrons in the region will be repelled and flow away from the NCS. This causes a vacuum to form between the NCS and the closed field line region. This vacuum region is the outer gap; it extends from the intersection of the NCS and the last closed field line out to the light cylinder.

Particles that cross into the outer gap are accelerated to high energies and radiate through curvature radiation. The radiated γ-rays produce pairs that radiate synchrotron and inverse Compton-scattered photons (Cheng et al. 1986b). Alternatively, the pairs produce γ-rays through inverse Compton scattering of thermal photons from the surface. The pair production front that forms limits the width of the gap.

2.3 The Pulsar Magnetosphere

The true pulsar magnetosphere has a field structure that is intermediate between the two extremes of the vacuum and force-free fields. In the absence of a self-consistent solution describing the physical $\mathbf{E}$ and $\mathbf{B}$ in a pulsar magnetosphere, the vacuum and force-free field solutions are used as approximations.

2.3.1 Vacuum Approximation

Before the force-free solution was found, the vacuum field was used as an approximation to the field of a charge-filled magnetosphere. The static vacuum dipole is the same as the non-rotating dipole field, and is rigidly attached to the rotating pulsar:

$$\mathbf{B} = \frac{1}{r^3}[3(\boldsymbol{\mu} \cdot \mathbf{r})\mathbf{r} - \boldsymbol{\mu}] \tag{2.43}$$

where $\boldsymbol{\mu}$ is the dipole moment and $\mathbf{r}$ is a radial unit vector. For pulsar rotation about the z axis, $\boldsymbol{\mu}$ evolves as

$$\boldsymbol{\mu}(t) = \mu(\sin\alpha\cos\Omega t\hat{x} + \sin\alpha\sin\Omega t\hat{y} + \cos\alpha\hat{z}) \tag{2.44}$$

where Ω is the angular rotation velocity and α is the magnetic inclination (the angel between the magnetic and rotation axes). This solution is not valid as $r \to R_{\rm LC}$, because in order to corotate with the pulsar, the rotation velocity must exceed the speed of light outside $R_{\rm LC}$. Thus, the magnetic field lines must be swept back at large radii, introducing a toroidal component to the field.

The full solution of the dipole rotating in a vacuum is that of the retarded dipole,

$$\mathbf{B} = -\left[\frac{\boldsymbol{\mu}(t)}{r^3} + \frac{\dot{\boldsymbol{\mu}}(t))}{cr^2} + \frac{\ddot{\boldsymbol{\mu}}(t)}{c^2 r}\right] + \mathbf{rr}\cdot\left[3\frac{\boldsymbol{\mu}(t)}{r^3} + 3\frac{\dot{\boldsymbol{\mu}}(t)}{cr^2} + \frac{\ddot{\boldsymbol{\mu}}(t)}{c^2 r}\right] \tag{2.45}$$

At low altitudes, the retarded field is approximately that of the static dipole.

The finite size of the star slightly alters the magnetic field structure. The vacuum retarded dipole field of a star with finite radius R and misaligned rotation and magnetic axes was solved analytically by Deutsch (1955). The Deutsch solution for $\mathbf{B}$ is generally used as an approximation to the pulsar magnetic field in light curve simulations, including those of Chapter 3.

The polar cap rim is defined as the location of the boundary between the open and closed field lines at the stellar surface. Because of rotational sweepback, the

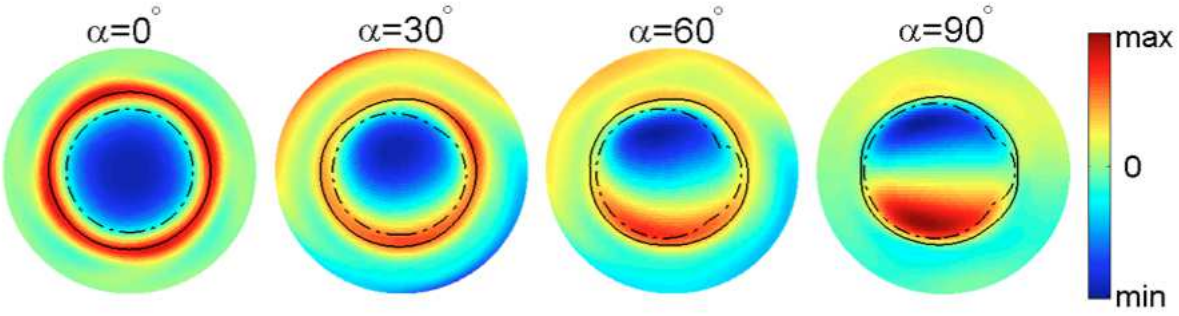

Figure 2.5: The polar cap is distorted due to magnetic sweepback of the field lines near the light cylinder. The distortion is more apparent in the vacuum field, the polar caps of which are plotted with dot-dashed lines. At large inclination angles, the notch and other critical point become more pronounced. The polar cap of the force-free field is shown with the solid line. The color shows the current to flux ratio on the pulsar surface, which is not discussed here. This figure was reproduced from Bai & Spitkovsky (2010a).

polar cap is distorted. Specifically, the polar cap shape is that of two different curves that meet at critical points on the star surface: the field lines emerging from each curve form a different spiral pattern tangent to the light cylinder (Yadigaroglu 1997; Dyks et al. 2004). The critical points were resolved by Dyks et al. (2004), and one was shown to be a discontinuous "notch" that is likely smoothed out in the physical magnetosphere (Figure 1 of Dyks et al. 2004). The polar cap shapes for different magnetic inclinations are shown in Figure 2.5 (Bai & Spitkovsky 2010a).

2.3.2 Ideal Force-free Field Solution

Goldreich & Julian (1969) postulated that the electric field induced by a rapidly rotating, highly magnetized neutron star will pull charges from the surface of a neutron star, populating the magnetosphere to a maximum charge density. They introduced a series of force-free equations to describe the pulsar magnetosphere. In

particular, the ideal force-free solution requires

$$\mathbf{E} + (\boldsymbol{\beta} \times \mathbf{B}) = 0, \tag{2.46}$$

$$\rho\mathbf{E} + \frac{\mathbf{j} \times \mathbf{B}}{c} = 0 \tag{2.47}$$

where the second equation is referred to as the "force-free condition", and satisfies $\mathbf{E} \cdot \mathbf{B} = 0$ everywhere; $\boldsymbol{\beta} \equiv (\boldsymbol{\Omega} \times \mathbf{B})/c$. In the force-free field, the critical charge density is (Gruzinov 2006; Bai & Spitkovsky 2010a)

$$\rho = \frac{\boldsymbol{\nabla} \cdot \mathbf{E}}{4\pi} = -\frac{\boldsymbol{\Omega} \cdot \mathbf{B}}{2\pi c} + \frac{\boldsymbol{\beta} \cdot (\boldsymbol{\nabla} \times \mathbf{B})}{4\pi} \tag{2.48}$$

which equals the value of the Goldreich-Julian charge (Goldreich & Julian 1969) under the assumption of charge separation (Bai & Spitkovsky 2010a).

In seeking a solution to the force-free field, Scharlemann & Wagoner (1973) and Michel (1973) derived the *pulsar equation*, which specifies the poloidal magnetic flux of an axisymmetric rotator and thus the structure of the (time-independent) axisymmetric magnetosphere:

$$(1 - x^2)\left(\frac{\partial^2\Psi}{\partial x^2} - \frac{1}{x}\frac{\partial\Psi}{\partial x} + \frac{\partial^2\Psi}{\partial z^2}\right) - 2x\frac{\partial\Psi}{\partial x} = -R_{\rm LC}^2 A\frac{\partial A}{\partial\Psi} \tag{2.49}$$

where $x \equiv R/R_{\rm LC}$ and $z \equiv Z/R_{\rm LC}$ in a cylindrical coordinate system (R, ϕ, z); Ψ is the magnetic flux; and $A(\Psi)$ is a function describing the current distribution in the magnetosphere. Note that the vacuum field is a special case of the pulsar equation, in which $A(\Psi) = 0$. A self-consistent solution to this equation remained elusive for many years due to an apparent discontinuity in the magnetic field across the light cylinder (Michel 1982). The time-independent solution of the ideal force-free field was finally found by Contopoulos et al. (1999), and was reproduced and revised by a number of authors (Goodwin et al. 2004; Gruzinov 2005; Contopoulos 2005; Timokhin 2006).

Time-dependent force-free field solutions were explored by, e.g., Komissarov (2006) and McKinney (2006). Spitkovsky (2006) was the first to find a solution to the three-dimensional, time-dependent force-free equations. He treated force-free electrodynamics (FFE) as the low-inertia limit of magnetohydrodynamics, as in (Komissarov 2002). In this limit, Equation 2.47 is satisfied. For a perfectly conducting plasma satisfying the force-free condition, Maxwell's equations are (e.g., Blandford 2002):

$$\frac{1}{c}\frac{\partial \mathbf{E}}{\partial t} = \boldsymbol{\nabla} \times \mathbf{B} - \frac{4\pi}{c}\mathbf{j}, \quad \frac{1}{c}\frac{\partial \mathbf{B}}{\partial t} = -\boldsymbol{\nabla} \times \mathbf{E}, \tag{2.50a}$$

$$\mathbf{j} = \frac{c}{4\pi}\boldsymbol{\nabla} \cdot \mathbf{E}\frac{\mathbf{E} \times \mathbf{B}}{B^2} + \frac{c}{4\pi}\frac{(\mathbf{B} \cdot \boldsymbol{\nabla} \times \mathbf{B} - \mathbf{E} \cdot \boldsymbol{\nabla} \times \mathbf{E})\mathbf{B}}{B^2}. \tag{2.50b}$$

Spitkovsky (2006) solved these equations using a finite-difference time domain method (FDTD; Yee 1966), but did not run the simulations long enough to reach a steady-state solution. Kalapotharakos & Contopoulos (2009) implemented the same FDTD method, with the additional use of the Perfectly Matched Layer technique (Berenger 1994, 1996). Their simulations were able to run for a longer time and converge to a steady state; their results agreed qualitatively with those of Spitkovsky (2006).

Some notable features of the force-free solution are that an aligned rotator with a force-free magnetosphere has a non-zero Poynting flux due to the current, unlike the aligned rotator in the vacuum field; the poloidal field lines in the open field line zone are straightened by current loading; the force-free toroidal fields are more tightly wound than in the vacuum field; and $|B|$ falls off more slowly with radius in the force-free field than for the vacuum dipole.

2.3.3 Realistic Pulsar Magnetospheres

Recently, finite-conductivity fields were introduced as self-consistent solutions to the pulsar equation by Kalapotharakos et al. (2012b) and soon after by Li et al. (2012). These resistive solutions lift the requirement that $\mathbf{E} \cdot \mathbf{B} = 0$ everywhere. One prescription for the current density is

$$\mathbf{j} = c\rho \frac{\mathbf{E} \times \mathbf{B}}{B^2} + \sigma \mathbf{E}_{\parallel} \tag{2.51}$$

(Case B of Kalapotharakos et al. 2012b), introducing a finite conductivity σ and nonzero $E_{\parallel}$ to Equation 2.47. Kalapotharakos et al. (2012b) find that the resistive solution naturally introduces a non-zero $E_{||}$.

2.4 High-Energy Pulsar Light Curves from Outer Magnetosphere Models

In the next chapter, I present model light curves that were simulated from geometrical representations of the slot gap and outer gap models, using both the vacuum (Deutsch 1955) and force-free (Kalapotharakos & Contopoulos 2009) prescriptions for the magnetic field. The light curves are formed from emission occurring over a wide range of altitudes. Morini (1983) showed that the combined relativistic effects of light travel time and aberration of the direction of photon propagation result in photons, with different phases in the corotating frame, spreading out in phase on the leading side of the polar cap and bunching in phase on the trailing side, in the observer frame. (The "leading side" refers to the side of the polar cap where the direction of the magnetic field lines is the same as the direction of rotation, while the "trailing side" has field lines pointed in the opposite direction to the rotation. In the open volume coordinates introduced in Chapter 3, these respectively correspond to

azimuthal angle $\phi = 90°$ and $270°$ around the polar cap rim.) Aberration and light travel time each alter the photons' phases by $-r_{\rm em}/R_{\rm LC}$, where $r_{\rm em}$ is the radius from the neutron star center at which a photon is emitted; together, they change the photons' phases by $-2r_{\rm em}/R_{\rm LC}$. These combined changes in phase cancel the changes in phase resulting from emission along the curved dipole field on the trailing edge of the polar cap. The outcome of this is the formation of light curves with caustic peaks, in which the photons from the trailing edge are observed to arrive at the same rotational phase.

Modeling the light curves from different emission models, assuming geometry is the most important effect for the light curve shapes, allows constraints to be placed on the emission geometry, in particular the magnetic inclination angle and observer viewing angle. This method has been used by a number of authors (Dyks & Rudak 2003; Dyks et al. 2004; Watters et al. 2009; Venter et al. 2009; Romani & Watters 2010; Johnson 2012) for both young/normal and millisecond pulsars. Incorporating radiation physics into the simulations allows modeling of the energy-dependent light curves and spectra (Harding et al. 2008).

The emission models described above have the following limitations. The polar cap model requires the observer to have a small viewing angle β relative to the magnetic axis in order for high-energy pulses to be observed. This implies that almost all γ-ray pulsars would also be radio pulsars, which is not the case. The outer gap model has no low-altitude emission, which results in the need for high inclination angles in order to observe emission from outer gaps over all observer angles ζ. The outer gap does produce lower off-peak emission than the slot gap as a result of the absence of low-altitude emission. However, it tends to be unable to reproduce wings seen at the edges of light curve peaks. The slot gap over-predicts the level of off-peak emission because it has emission at low altitudes in addition

to the high altitudes. It produces emission over the full (α, ζ) space, so there is no inherently preferred magnetic inclination or viewing angle.

Chapter 3

Modeling the Light Curves of *Fermi* LAT Pulsars

The high-energy pulsar emission models discussed in Chapter 2 produce a variety of light curve shapes. A way of testing which emission model is correct is to compare pulsar light curves predicted by the models to those that have been observed by the *Fermi* LAT. A physical emission model that correctly characterizes the generation and propagation of γ-rays in the pulsar magnetosphere should reproduce the high-energy light curves and spectra (phase averaged and resolved) observed from γ-ray pulsars. Such a model would include the physics of pulsar magnetospheres, for example magnetospheric currents, particle acceleration, and radiation. These processes are not well understood. An alternative approach to studying pulsar emission is to assume that the geometry of the emission region in the pulsar magnetosphere and its orientation relative to the observer's line of sight is largely responsible for the major features in the energy-integrated HE light curves. This is the approach taken by, e.g., Venter et al. (2012) and Romani & Watters (2010) and Johnson (2012) in order to constrain pulsar emission geometries, and is the approach taken here.

Geometrical modeling simplifies the problem and allows one to study the size and location of the emission region. Knowledge of the emission geometry can later be used to guide physical models of pulsar emission.

In this chapter, I describe modeling the light curves of four bright γ-ray pulsars, Vela, Geminga, Crab, and PSR J0007+7303, the pulsar in the CTA 1 supernova remnant. These light curves were modeled using geometrical representations of the slot gap and outer gap emission models; for the slot gap, both azimuthally symmetric and asymmetric geometries (offset dipole; Harding & Muslimov 2011a,b) were used. The geometries of both the vacuum and force-free magnetic fields were used as well. As will be described in the results sections, there are multi-wavelength constraints on the viewing geometry of the Vela and Crab pulsars, as well as other, looser constraints on other emission geometry parameters for the other pulsars. In modeling the light curves, no prior knowledge of the emission or viewing geometry is included. Instead, the best-fit geometrical parameters are found from the γ-ray light curve fits, and are then compared with the multi-wavelength constraints. In this way, an independent estimate of the emission geometry is found, and it is then possible to determine how well or how poorly light curve modeling reproduces the results found from other methods. Additionally, some groups (e.g., Venter et al. 2012) model both the radio and γ-ray light curves. To do this, an empirical model of the radio emission is used. In this work, only the γ-ray light curves are modeled. The γ-ray emission geometries are motivated by physical models, and may be biased toward unphysical geometries through the use of empirical radio emission models. Modeling only the γ-ray emission may lead to more accurate determinations of the emission geometry, which may pave the way for improved, possibly physical, models of the radio emission.

The light curve modeling results of PSR J0007+7303, using only the vacuum

field and the outer gap and symmetrical slot gap geometries, were published in Abdo et al. (2012). The new results for PSR J0007+7303, as well as the modeling results for the other three pulsars, will be presented in DeCesar et al. (2013a, in preparation).

3.1 Light Curve Modeling Procedure

To model LAT pulsar light curves, I simulated high-energy light curves from geometrical representations of the outer gap and slot gap emission models using a code developed by J. Dyks and A. Harding. These simulations were performed within two magnetic field geometries: the vacuum retarded dipole field, the analytic solution of which is given by Deutsch (1955), and the force-free field, for which a solution was found by several authors (Spitkovsky 2006; Kalapotharakos & Contopoulos 2009). We incorporated the force-free solution of Kalapotharakos & Contopoulos (2009) into the simulations. The model light curves were fit to light curves of γ-ray pulsars observed by the *Fermi* LAT using a Markov Chain Monte Carlo maximum likelihood fitting routine.

Light curves generated in the force-free field have not been fit to observed light curves prior to this work. Thus, we obtain the first geometrical parameters for pulsars with force-free magnetospheres, the configuration of which is believed to be more physical than the vacuum dipole approximation (Goldreich & Julian 1969). We also fit light curves from the slot gap with offset dipole for the first time. Additionally, our light curve modeling differs from efforts like those of Romani & Watters (2010) in that we have more free geometrical parameters, particularly the gap width and the maximum emission radius. Recent work by, e.g., Johnson (2012) allows similar freedom in the parameters; they also employ a MCMC to explore the parameter

space.

The details of our modeling are described in the following sections.

3.1.1 Light Curve Construction

I constructed the light curves of the Vela, Geminga, and Crab pulsars using 30 months of LAT data, taken between 2008 August 4 and 2011 February 12 (MJD 54682.6–55064, or MET 239557417–319161600), which had been processed with the `Pass7_V6` instrument response functions (IRFs). Only "source" class events within $< 100^\circ$ from the LAT zenith were used in the dataset; this zenith cut was used to avoid contamination of the dataset by photons from the Earth limb. The events were filtered using `gtmktime` to determine good time intervals; the filter used was that recommended by the *Fermi* Science Support Center [1] (FSSC), `DATA_QUAL==1 && LAT_CONFIG==1 && ABS(ROCK_ANGLE)<52`. The Tempo2 *fermi* plug-in was used to assign a pulse phase to each event in the dataset of each pulsar, based on the pulsar's timing solution. The timing solutions were derived using only LAT counts, as described in Ray et al. (2011b), and were valid for the full length of our observations.

The energy-dependent Region of Interest (ROI) for bright pulsars, adapted by, e.g., Abdo et al. (2010b), was used to determine which γ-ray events would be contained in the light curves. This ROI is given by

$$\theta < \max[1.6 - 3\log_{10}(E_{\rm GeV}), 1.3] \ . \tag{3.1}$$

All counts falling within an angular distance θ from the given pulsar were binned in pulse phase to make the light curves.

The Vela pulsar light curve was made using fixed count binning as in Abdo et al. (2010b), in which phase bin edges are defined such that each phase bin contains the

[1] `http://fermi.gsfc.nasa.gov/ssc/`

same number of γ-ray counts. For Vela, each bin contains ~ 3000 counts. The bins are narrowest in the peaks, allowing very fine features of the light curve to be seen. The phase resolved spectrum of Vela (Chapter 4) has the same fixed-count bins as the light curve used in the modeling in this chapter. Fixed-count light curves of Geminga and Crab were also made in order to model their phase resolved spectra. However, these light curves had many fewer bins than Vela, so light curves with fixed-width bins were used for the light curve modeling. Geminga's light curve was binned in order to match the phase bins of the simulated light curves, which have 180 bins of width 0.005556, and the Crab's light curve has 90 bins such that the simulated light curves are easily re-binned to match the data.

For PSR J0007+7303, I used the light curve from Abdo et al. (2012). This light curve was made from 2 years of data (2008 August 4 to 2010 August 4) that had been processed with the `Pass6_V11` IRFs. The same zenith and good time interval cuts as described above were made to this dataset. All γ-ray events within 1.6° of the pulsar's timing position were used to make the light curve; this angular radius was chosen because it maximized the signal-to-noise of the pulse. The light curve was binned into 32 fixed-width phase bins.

The background level for each pulsar light curve was found using `gtsrcprob`, which calculates the probability that a given event originated from the pulsar of interest. The probability is based on the radial distance from the event to the source position and on the source's phase averaged spectrum (Section 4.1). This value is important for light curve modeling, as it defines the number of counts that are not due to pulsed magnetospheric emission, and must be subtracted from the light curve prior to fitting. Table 3.1 lists the background count level and other relevant information about the pulsar light curves.

Table 3.1. Light Curve Characteristics

Pulsar	$N_{\rm bins}$	Background Level
Vela	156	88430.8[a]
Crab	90	656.9
Geminga	180	182.1
PSR J0007+7303	32	195.0

Note. — The number of bins and the background count level, determined using `gtsrcprob`, for each pulsar light curve. [a]The total counts and background level of Vela are not really in units of γ-ray counts, but rather in units of counts per bin width. The Vela light curve has fixed-count bins of ~ 3000 counts per bin, so the phase bins are defined in this way and therefore have different widths. To build the light curve, the counts must be divided by the width of the bin.

3.1.2 Light Curve Simulations

We simulated the high-energy light curves with geometrical representations of the slot gap and outer gap emission zones within the vacuum retarded dipole and ideal force-free field geometries, described above. The simulations were performed for a neutron star with radius $R = 10^6\,\mathrm{cm}$ and spin period 0.1 s, using the *toypol* code developed by Dyks & Rudak (2003) and Dyks et al. (2004) and modified by A. Harding to allow for magnetic field configurations other than the vacuum retarded dipole. The spin period does not have a significant effect on the phase plots, so a single set of simulations can be used for comparisons with any young/normal pulsar (millisecond spin periods do significantly change the emission pattern, so these simulations cannot be used for light curve modeling of millisecond pulsars). The code is described below, but more details can be found in Dyks et al. (2004).

The simulations begin with a Runge-Kutta integration along the magnetic field lines to determine the boundary between open and closed field lines, i.e., field lines that respectively close outside or inside the light cylinder radius, $R_{\rm LC}$. (This boundary is also referred to as the last open field line. In reality, field lines that do not close within the light cylinder may remain open and extend outward to connect with the pulsar wind.) The rim of the polar cap (PC), which separates the open and closed zones, is found in this way. One or more rings of open field lines, which are anchored to the surface of the star along and/or interior to the PC rim, are defined as the field lines along which the emission will be calculated.

The polar cap rim and the "footpoints" (Dyks et al. 2004) of the field lines are defined in open volume coordinates. This coordinate system is defined in terms of the PC rim rather than the magnetic pole, as the symmetry of the magnetic field around the dipole axis breaks down with the introduction of rotation. Such coordinate systems were introduced by Yadigaroglu (1997) and Cheng et al. (2000), but these still contained reference to the magnetic pole. Dyks et al. (2004) redefined the open volume coordinate system with the coordinates ($r_{\rm ovc}$, $l_{\rm ovc}$), which are used to identify points on the stellar surface independently of the magnetic pole's location. The first coordinate $r_{\rm ovc} = 1 \pm d_{\rm ovc}$, where $d_{\rm ovc}$ is the minimum distance from a given point on the stellar surface to the PC rim, normalized by the standard PC radius $r_{\rm PC} = (\Omega R_{\rm NS}^3/c)^{1/2}$. The second coordinate $l_{\rm ovc}$ of a point at $r_{\rm ovc}$ is the length of the arc "measured along the deformed ring of fixed $r_{\rm ovc}$ at which the point lies" (Dyks et al. 2004) in the direction of increasing azimuth angle ϕ_m, where $l_{\rm ovc} = 0$ at $\phi_m = 0$. The "deformed ring" refers to the shape of the polar cap, which is circular for an aligned rotator but is distorted and shifted with respect to the magnetic pole for non-zero magnetic inclination angles α (Section 2.3; Yadigaroglu 1997; Dyks et al. 2004).

The photon emission from electrons traveling along each field line is calculated in the corotating frame (CF) and then transformed to the inertial observer's frame (IOF). The field lines are divided into small segments, and their positions correspond to the positions of emission, $\mathbf{r}'_{\rm em}$. The direction of the emission, $\hat{\boldsymbol{\eta}}'_{\rm em}$ is assumed to be the same direction as the electron's velocity, and is therefore defined as tangent to the magnetic field line in the CF. The emissivity is assumed to be uniform along the magnetic field lines, which is reasonable given that the electron energy will be $\sim$ constant over a wide range of emission altitudes in the regime of curvature radiation reaction. To obtain uniform emissivity, the intensity of emission from a given segment is defined as the length of that segment. The emission is calculated from field line segments out to a user-defined maximum radius r, measured in units of $R_{\rm LC}$, beyond which the emissivity is zero. The emission calculation is also restricted in the direction perpendicular to the rotation axis within a cylinder of radius $r_{\rm cyl}$ from the neutron star center, such that the emissivity drops to zero for $r > r_{\rm cyl}$.

To assign an observed rotation phase to the photons, the emission direction must be transformed from the CF to the IOF, and the photon travel time from different positions in the magnetosphere must be taken into account. In the IOF, the position of an emission point is $\mathbf{r}_{\rm em}$ and the photon direction is $\hat{\boldsymbol{\eta}}$. The observed photon phase is

$$\phi = -\phi_{\rm em} + \phi_{\rm d} \tag{3.2}$$

where $\phi_{\rm em}$ is the phase of $\hat{\eta}$ and $\phi_{\rm d}$ is the delay in rotational phase due to light travel time,

$$\phi_{\rm d} = -\mathbf{r}_{\rm em} \cdot \hat{\boldsymbol{\eta}} / R_{\rm LC} \ . \tag{3.3}$$

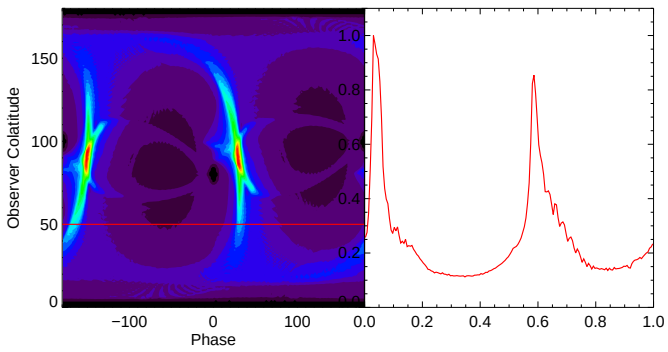

Figure 3.1: *Left:* An example of an emission pattern from a pulsar with $\alpha = 80°$. *Right:* A cut across the emission pattern at observer angle $\zeta = 50°$ yields a double-peaked light curve.

The IOF and CF are related by a coordinate transformation in rotation,

$$\begin{aligned} x' &= x\cos\Omega t + y\sin\Omega t, \\ y' &= -x\sin\Omega t + y\cos\Omega t, \\ z' &= z, \\ t' &= t\ . \end{aligned}$$

To account for special relativistic aberration of the direction of photon propagation, a Lorentz transform is used to find $\hat{\eta}$ in the IOF,

$$\hat{\boldsymbol{\eta}} = \frac{\hat{\boldsymbol{\eta}}' + [\gamma + (\gamma - 1)(\boldsymbol{\beta}\cdot\hat{\boldsymbol{\eta}}')/\boldsymbol{\beta}^2]\boldsymbol{\beta}}{\gamma(1 + \boldsymbol{\beta}\cdot\hat{\boldsymbol{\eta}}')} \tag{3.4}$$

where $\boldsymbol{\beta} = \mathbf{v}/c$ is the local corotation velocity and $\gamma = (1-\beta^2)^{-1/2}$.

Once the photons have been assigned a phase, they are accumulated in bins of phase ϕ and observer viewing angle (colatitude) $\zeta = (\boldsymbol{\eta}_{\rm em})_z$. The resulting two-dimensional emission intensity pattern $I(\phi, \zeta)$ is shown in Figure 3.1. Cutting across a single line of sight ζ results in a light curve.

3.1.3 Emission Geometries

We use geometrical representations of the outer gap (OG; Romani 1996) and slot gap (SG; Muslimov & Harding 2003, 2004) models in our light curve simulations. Two versions of the slot gap are used—the standard slot gap with azimuthal symmetry in emissivity around the polar cap rim (sSG), and a slot gap with an offset dipole that has azimuthally asymmetric emissivity (aSG; Harding & Muslimov 2011a,b). Both the OG and SG models were motivated by the need for regions of charge depletion in an otherwise charge-filled magnetosphere so that particle acceleration can take place. These models are described in Chapter 2.

For the outer gap model, the emission occurs along the inner edge of the vacuum gap. In this work, this emission is treated as lying along a single field line in the simulations. The slot gap geometry used here is the same as the two-pole caustic (TPC) model (Dyks & Rudak 2003), which is a geometrical rendition of the slot gap model, and was used by Dyks et al. (2004) to reproduce the γ-ray light curve of Vela. Dyks et al. (2004) allowed emission out to a cylindrical radius $r_{\rm cyl} = 0.95\,R_{\rm LC}$. More recently, Romani & Watters (2010) fit 1-year LAT light curves of some of the brighter pulsars from the first *Fermi* pulsar catalog (The Fermi-LAT Collaboration 2013) with the TPC model, but they used $r_{\rm cyl} = 0.75\,R_{\rm LC}$ and were not able to obtain a good fit to the light curve. In our simulations, we return to $r_{\rm cyl} = 0.95\,R_{\rm LC}$, and we refer to the model as the slot gap rather than the TPC to avoid confusion.

The differences between the OG and SG geometries in our simulations are (1) the SG extends from the neutron star surface, while the OG begins at the null charge surface, defined by $\Omega \cdot B = 0$ for the vacuum field and $\nabla \cdot E = 0$ for the force-free field (see Chapter 2); (2) there is emission throughout the gap in the SG, while emission from the OG is restricted to a single field line on the inner edge of

the gap (the field line closest to the magnetic pole that is still contained within the gap width); and (3) the emission extends closer to the light cylinder in the OG than in the SG.

The azimuthally asymmetric slot gap geometry represents the slot gap with an offset polar cap from Harding & Muslimov (2011b) (their Case "B"). Physically, the polar cap is shifted or offset in the trailing direction (opposite the direction of rotation) due to the sweepback of the magnetic field lines near the light cylinder. This property of the polar cap was noted by Dyks & Harding (2004), and its effect on $E_{||}$ was explored by Harding & Muslimov (2011a,b). They found that particles can reach higher Lorentz factors from a larger $E_{||}$ on the trailing side of the polar cap, which affects the light curves by enhancing the peaks and reducing the off-peak emission (Harding et al. 2011). Note that because the dipole offset is a surface and low-altitude phenomenon, the azimuthal asymmetry is considered only in the slot gap geometry and not in the outer gap.

In the limit of curvature radiation reaction (CRR), the emissivity $\mathcal{E} \propto E_{||}$. The emissivity varies with the azimuthal magnetic field coordinate ϕ as

$$\mathcal{E} \propto \frac{\theta_0^{2a}}{(1+a)^2} \tag{3.5}$$

where $a = \epsilon \sin\phi$ and $0 \leq \epsilon < 1$ is the offset parameter (Harding & Muslimov 2011a). The amount $\Delta r_{\rm PC}$ by which the polar cap is shifted/offset is not a free parameter in the light curve fits, but rather is determined numerically by the light curve simulation code, and increases with increasing magnetic inclination angle α. Its value is given by

$$\Delta r_{\rm PC} \simeq R_{\rm NS}\theta_0(1-\theta_0^{\epsilon}) \tag{3.6}$$

(Harding & Muslimov 2011a). Here $\theta_0 = (\Omega R_{\rm NS}/c)^{1/2}$ is the half-angle of the static polar cap, Ω is the rotation rate, and $R_{\rm NS}$ the neutron star radius. As described

in Section 3.1.2, the first step in the light curve simulation is to trace the magnetic field lines to the surface to find the polar cap rim, which is naturally distorted due to the sweepback of the field lines at higher altitudes; $r_{\rm PC}$ is determined by this calculation of the polar cap rim. The offset parameter is then given by

$$\epsilon = -\log\left(R_\phi / R_{\rm PC}\right) / \log\theta_0 \tag{3.7}$$

where R_ϕ is the radius of the polar cap at azimuthal angle ϕ. The maximum offset occurs at $\phi = 270°$, corresponding to the trailing edge of the polar cap where the caustic peaks are formed; $r_{\rm PC}$ and ϵ are therefore evaluated at $\phi = 270°$.

3.1.4 Magnetic Field Geometries

In this work, we model the LAT light curves with the geometrical emission regions discussed in Section 3.1.3 and with two magnetic field geometries, those of the vacuum retarded dipole (VRD, Deutsch 1955) and of the ideal force-free (FF) field solution from Kalapotharakos & Contopoulos (2009). The core differences between the VRD and FF solutions that affect the simulations' output are that the magnetic field strength along a field line is larger for a given radius in the FF field than in the VRD; the FF field lines are straighter in the poloidal frame due to current loading, causing the larger magnetic field strength as well as larger radii of curvature of the magnetic field lines; and the FF field has more tightly wound toroidal field lines, leading to a larger polar cap offset and therefore γ-ray peaks arriving later in phase. The true configuration of the pulsar magnetic field must lie somewhere between the VRD and ideal FF solutions. In using the VRD and ideal FF solutions in our simulations, we are treating them as the two extremes of pulsar magnetic field structures, and we are testing whether one field leads to better predictions of the observed light curves than the other. For the vacuum field, we employ the Lorentz

transformation of the field from the inertial observer to the corotating frame pointed out by Bai & Spitkovsky (2010b). The FF field was incorporated into the *toypol* code by reading numerical tables of the B and E field components and performing 3D interpolation to obtain the field vector at a given point. The numerical tables were generated by C. Kalapotharakos, using the method of Kalapotharakos & Contopoulos (2009). Below an altitude of $0.2\,R_{\rm LC}$, the field was defined to be a vacuum retarded dipole, which was then smoothly connected to the FF solution between altitudes 0.2–$0.4\,R_{\rm LC}$. We note that our modeling done with the force-free solution is distinct from the modeling presented in Romani & Watters (2010), in which a "pseudo-force-free" solution was used.

3.1.5 Geometrical Parameters and Simulated Light Curves

The light curve simulation code takes as input the magnetic inclination angle α, the maximum allowed emission altitude r, the maximum cylindrical radius $r_{\rm cyl}$, and the width of the emitting gap w. These geometrical parameters are illustrated in Figure 3.2. The radii are in units of $R_{\rm LC}$. The width corresponds to the distance, in units of the open volume coordinate $r_{\rm ovc}$, between the polar cap rim and the innermost ring of emitting magnetic field lines $r_{\rm in}$, thus $w = 1 - r_{\rm in}$. For the slot gap geometry, all of the field lines within the gap emit photons, while in the outer gap geometry the gap is a vacuum and only the innermost field line produces emission. The implementation of these emission model geometries and of the vacuum and force-free magnetic fields are described in the following sections.

The light curves were simulated for magnetic inclinations $0^\circ \leq \alpha \leq 90^\circ$ with resolution 1° in the vacuum field and 5° in the force-free field; in the latter case, the minimum α is 5°. The FF simulations, for which the magnetic field data points were provided by C. Kalapotharakos, have lower resolution in α because the numerical

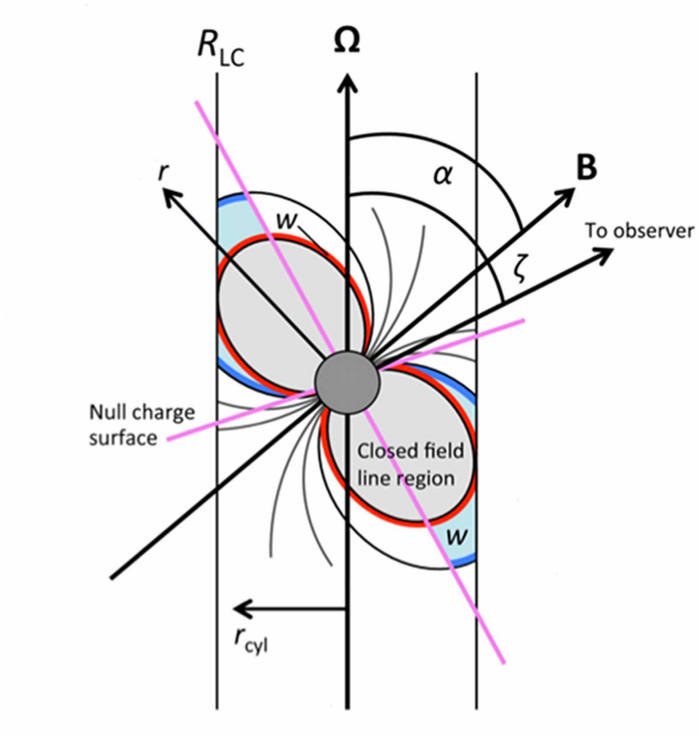

Figure 3.2: A schematic showing the geometrical emission regions and parameters used for the light curve simulations. The red region along the boundary between the open and closed field lines represents the slot gap emission zone, while the blue regions show the outer gap. The slot gap width, shown by w at the top left of the figure, extends from the polar cap rim to an open field line specified in a given simulation; emission occurs throughout the slot gap width. In the outer gap case, w is the width of the blue regions, extending from the polar cap rim to a given open field line. The dark blue region shows the location of the outer gap emission region, which in our simulations has zero width, meaning the emission occurs along a single field line at the outer edge of the gap. The light blue region is the remainder of the gap, which is a vacuum. For both emission geometries, the width was held constant with emission radius. Four parameters were varied in the simulations: the magnetic inclination angle α, the observing viewing angle (or pulsar colatitude) ζ, the width of the acceleration gap w, and the maximum height to which emission is followed by the simulation, r. The fifth fitting parameter, not shown here, is the amount by which the simulated light curve is shifted in order to best match the observed light curve, as described in Section 3.1. The additional parameter shown here is the cylindrical radius $r_{\rm cyl}$, which was fixed at $0.95\,R_{\rm LC}$ for the slot gap geometry and as close to $1\,R_{\rm LC}$ as was possible for the outer gap (see the text in Section 3.1.2 for details).

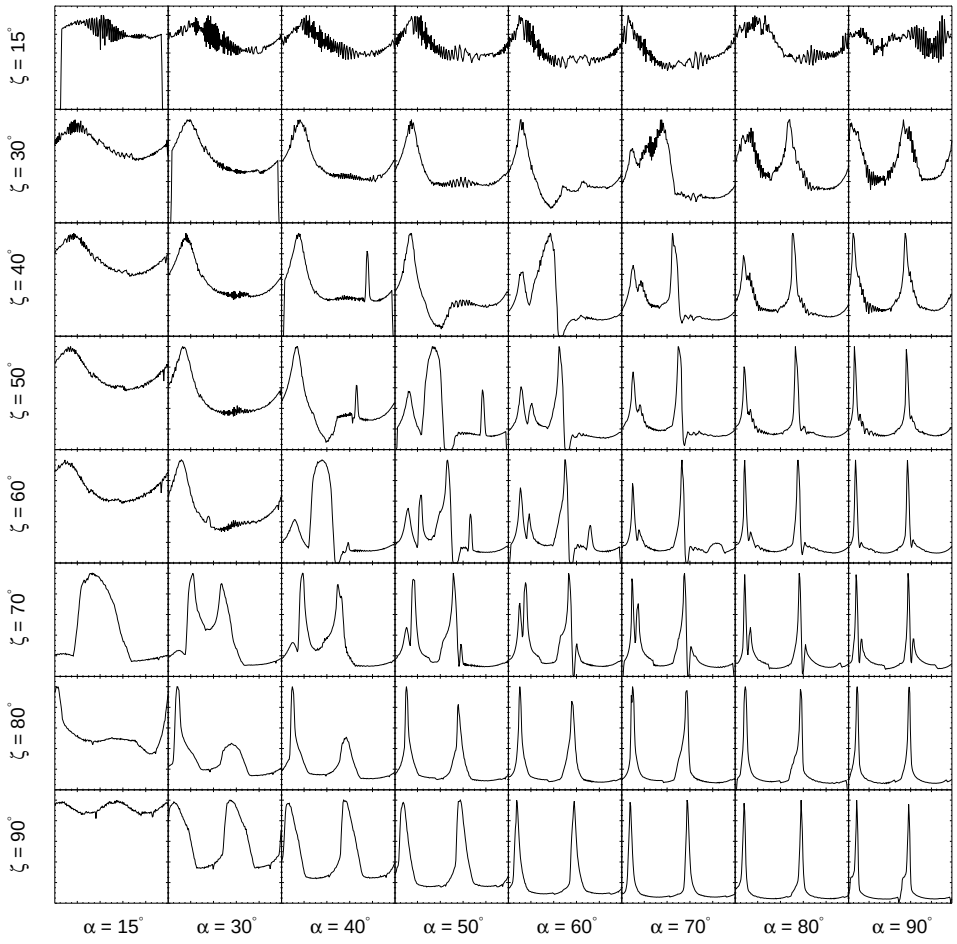

Figure 3.3: A light curve atlas demonstrating the many shapes of light curves over the α-ζ space. These light curves were simulated using $w = 0.05$ and $r = 1.0\,R_{\rm LC}$.

magnetic field simulations from which we obtained the **B** were very computationally intensive. The range of α was chosen because the emission patterns of simulations with α and $180 - \alpha$ are identical, save for a 180° phase shift.

The model gap widths were $w = [0, 0.01, 0.02, \ldots, 0.09, 0.1, 0.12, 0.14, \ldots, 0.3]$, corresponding to $r_{\rm in} = [1, 0.99, 0.98, \ldots, 0.91, 0.9, 0.88, 0.86, \ldots, 0.7]$. For the OG model, the maximum emission radius $r = [0.9, 1.0, \ldots, 2.0]\,R_{\rm LC}$, while for the SG models $r = [0.7, 0.8, \ldots, 2.0]\,R_{\rm LC}$ in order to probe the effects of low- vs. high-

altitude emission. The value of $r_{\rm cyl}$ is fixed at $0.95\,R_{\rm LC}$ for the slot gap geometry, and ranges from 0.97–$1.0\,R_{\rm LC}$ for the outer gap. This range in values is due to intricacies of the code: at large values of r, the cylindrical radius must be decreased in order to find the polar cap rim.

The intensity pattern $I(\phi, \zeta)$ is output every 2° in phase for $-180^\circ \leq \phi \leq 180^\circ$ (simply due to a convention in the code) and with 1° resolution in observer colatitude for $0.5^\circ \leq \zeta \leq 179.5^\circ$. The light curves have a similar symmetry in ζ as the emission pattern has in α—they are identical except for a 180° phase shift between light curves of ζ and $180^\circ - \zeta$. For this reason, we only considered the range of observer colatitudes $0^\circ \leq \zeta \leq 90^\circ$.

The simulations were run over a grid of (α, ζ, w, r) with the above parameter ranges. Varying the model parameters yields a suite of light curve shapes, some of which are shown in Figure 3.3.

3.1.6 Estimation of Geometrical Model Parameters

The best fit geometrical model parameters were determined using a Markov chain Monte Carlo (MCMC) maximum likelihood algorithm. The MCMC code was written by M. C. Miller, and the algorithm follows that of Verde et al. (2003). The MCMC draws parameter values from the posterior probability distribution, $\mathcal{P}(\mathbf{M}|D)$, of a set of model parameters $\mathbf{M}$ given the data D. The posterior distribution, from Bayes' theorem, is

$$\mathcal{P}(\mathbf{M}|D) = \frac{\mathcal{P}(D|\mathbf{M})\mathcal{P}(\mathbf{M})}{\int \mathcal{P}(D|\mathbf{M})\mathcal{P}(\mathbf{M}) d\mathbf{M}} \tag{3.8}$$

where $\mathcal{P}(D|\mathbf{M})$ is the likelihood of D given $\mathbf{M}$ and $\mathcal{P}(\mathbf{M})$ is the prior probability density (i.e., information about the model parameters that is known prior to the calculation of the posterior distribution). Applied to light curve modeling, D represents the LAT light curve and $\mathbf{M}$ is the set of parameters (α, ζ, w, r) of the simulated

light curves. No prior knowledge of $\mathbf{M}$ is applied to the likelihood calculation, so $\mathcal{P}(\mathbf{M})$ is constant and its integral is 1[2].

The MCMC begins at a randomly selected point in parameter space $\mathbf{M}_1$ and calculates the likelihood $\mathcal{L}_1$ there. A new point $\mathbf{M}_2$ is chosen from a proposed distribution $\mathcal{P}_p(\mathbf{M}_2|\mathbf{M}_1)$ based on the current parameters, as described in Lo et al. (2013). The proposed value for each new parameter is drawn from a normal distribution $N(\mathbf{M}_1 - \mathbf{M}_2, \boldsymbol{\sigma})$, for which the standard deviations $\boldsymbol{\sigma}$ of the parameters are defined by the user. If $\mathcal{L}_2/\mathcal{L}_1 \geq 1$, then the parameters $\mathbf{M}_2$ are stored; the stored parameters make up a "chain." If $\mathcal{L}_2/\mathcal{L}_1 < 1$, then a random number x is drawn from a uniform distribution between 0 and 1. If $x < \mathcal{L}_2/\mathcal{L}_1$, then $\mathbf{M}_2$ are saved in the chain. If $x \geq \mathcal{L}_2/\mathcal{L}_1$, then $\mathbf{M}_2$ are not saved, and a step from $\mathbf{M}_1$ is again taken to a new set of parameters. It is unlikely that the MCMC will randomly choose a first $\mathbf{M}$ near the global maximum in $\mathcal{L}$. The first half of each chain is therefore deemed the "burn-in" phase, and only parameters in the second half of the chain are used in the final analysis.

The LAT light curves have high counts in each bin, allowing the use of Gaussian rather than Poisson statistics in the likelihood calculation. For the Gaussian probability distribution, the likelihood is

$$\mathcal{L} \equiv \mathcal{P}(D|\mathbf{M}) = \prod_i \frac{1}{\sqrt{2\pi}\sigma_i} e^{-[d_i - m_i(\mathbf{M})]^2/2\sigma_i^2} \tag{3.9}$$

where d_i is the number of counts in the i^{th} phase bin of the LAT light curve, $m_i(\mathbf{M})$ is the number of counts in the same bin of the model light curve simulated from the parameters $\mathbf{M}$, and $\sigma_i = \sqrt{d_i}$ is the error on d_i. For the Gaussian probability

[2]There are independent, multi-wavelength constraints on some parameters which could be used as priors. We chose to instead perform a blind search of the parameter space so as to not bias our results, and ultimately to test the validity of the models.

distribution, Wilks' Theorem (Wilks 1938) states that

$$\Delta \ln \mathcal{L} = -\frac{\Delta\chi^2}{2}. \tag{3.10}$$

Because the acceptance of a set of parameters into a chain depends on the likelihood ratio and hence on the difference in $\ln \mathcal{L}$, Equation 3.10 allows us to treat $\mathcal{L}$ as if it were equivalent to $-\chi^2/2$ (see Appendix C for details).

The parameter space is large, and the light curve simulations take between a few seconds and $\sim$5 minutes each, depending on the gap width. To minimize computation time, we first performed all the simulations, using the grid of parameters described above, and then applied the MCMC routine. The MCMC chooses a position in parameter space from a continuous distribution of parameters, so the chosen parameters $\mathbf{M}$ were mapped to the closest parameter values $\mathbf{M}_{\rm g}$ in the (α, ζ, w, r) grid. The simulated light curve corresponding to $\mathbf{M}_{\rm g}$ was then compared with the observed light curve as follows: The background count level of the observed light curve was subtracted from the counts in each phase bin so that only the pulsed emission would be compared with the model light curve. The model light curve was then normalized so that the total number of simulated "counts" (in quotation marks because the intensity is dimensionless) was equal to the total number of pulsed counts in the LAT light curve. If necessary, the simulated light curve was rebinned to match the binning of the LAT light curve, which has N bins in rotation phase $0 \leq \phi \leq 1$. The phase ϕ_B of the magnetic pole in the simulation corresponds to $\phi = 0$; $\phi = 1$ corresponds to 360°, or one full rotation. The simulated light curve was shifted by one phase bin N times, and the new phase of the magnetic pole was recorded for each phase shift. The χ^2 between the simulated and observed light curves was calculated for each phase shift (effectively, for each ϕ_B). This introduced a fifth parameter, ϕ_B, in the likelihood space. The minimum χ^2 found via the light curve shifting was used to compute $\mathcal{L}$, which was fed back to the MCMC code. If

the conditions for recording the parameters in a chain were met, then the ϕ_B at which χ^2 was minimized was recorded along with the four geometrical parameters.

The MCMC chains tended to converge quickly toward a local maximum in the 5-dimensional parameter space. Because the parameter space is not smooth, there are many local maxima; additionally, because the pulsars considered here are very bright, it is difficult to move away from a given local maximum enough to satisfy the chain acceptance criteria of a new set of parameters. By the same token, if a point in parameter space lies near the global maximum, then the global maximum will be found quickly. The problem of convergence to a (non-global) local maximum can be mitigated by dramatically increasing the allowed step size from the current location in parameter space; however, smaller steps are useful for sampling the space near a local maximum and building confidence intervals. Our compromise was to run many MCMC chains. This ensured that the full parameter space was adequately sampled, such that the global maximum should be contained in multiple chains, while also allowing adequate exploration of the regions surrounding local maxima. We confirmed that the space had been adequately sampled by recording all the parameter values "tried" by the MCMC, including those that were not saved in chains, and plotting the values that were tried. In all cases, the MCMC sampled the full range of parameter values, meaning that it would have found all local maxima. Additionally, we confirmed that multiple chains converged to the same global maximum $\mathcal{L}$.

To find the absolute global maximum and to create confidence contours, we identified local maxima in the parameter space whose likelihoods fell within 3σ of the global maximum likelihood. We performed scans over the complete parameter set within the regions surrounding these local maxima, calculating $\mathcal{L}$ at each point. More details about the creation of confidence intervals, specific to the pulsars modeled here, are described in the results section below.

3.1.7 Quality of Light Curve Fits

Light curve modeling of bright pulsars yields qualitatively good fits between simulated and observed light curves, but usually not good statistical fits. Because there are so many counts and the features in the light curves are so well defined, models with few parameters usually cannot match detailed light curve features. (For faint pulsars, because the statistical errors in each phase bin are much larger, it is possible to achieve reduced χ^2 values of ~ 1.) Models with a larger number of parameters may be able to reproduce more details of the light curves, with the trade-off of reduced fit significance. Another effect for bright pulsars is that there is only a small region in the phase space of the geometrical parameters where the fit is acceptable, because a small deviation from the best fit values will lead to a much larger χ^2.

Despite its large value for bright pulsars, χ^2 minimization (likelihood maximization) is used to constrain the best-fit geometrical parameters of the model light curves. Because it is difficult to quantify the absolute goodness of fit, it is useful to also consider what qualitative features of the light curve are important. First and foremost, a qualitatively well-fitting model light curve should have peaks at the same phases as the observed light curve. It is also desirable to have peaks that have similar heights and generally the same shape as the observed light curve. For example, the peaks are typically wider at the base than at the highest point, and often have wings connecting the peak emission with the emission on either side of the peak. A second feature is the level of the off-peak and bridge (between peaks) emission. As will be seen below, the outer gap and slot gap models give very different results for the emission outside the peaks—light curves simulated in the outer gap geometry typically have little or no off-peak emission, while the slot gap geometry tends to over-predict the off-peak emission level. Additionally, the azimuthally

asymmetric slot gap geometry yields a lower level of off-peak emission. The emission at phases outside the peaks can therefore be used to qualitatively discriminate between emission geometries.

The geometrical parameters of the model light curve with the lowest χ^2 can be compared with the same parameters obtained from observations at other wavelengths. A number of pulsars have independent measurements of α, ζ, and/or $\beta = |\alpha - \zeta|$ from multi-wavelength observations. Constraints on the emission geometry can be determined using, for example, X-ray torii in pulsar wind nebulae, or by performing a Rotating Vector Model (RVM; Radhakrishnan & Cooke 1969a) fit to the phase-varying position angles of polarized radio pulse profiles. Additionally, loose constraints can be placed on the expected value of β by considering whether or not the pulsar is radio-loud. Radio-loudness and -quietness are usually attributed to viewing geometry, particularly to β, which is the angle between the observer's line of sight and the magnetic pole. If the observer's line of sight crosses near the magnetic pole (small β), then the radio emission will be observed and the pulsar will be radio-loud. The larger β is, the less likely it is that the observer will view radio emission from the magnetic pole. Therefore, a qualitative comparison between the modeled and observed light curve is the value of β, which should be large ($\sim 20^\circ$ or more) for radio-quiet pulsars and small for radio-loud pulsars. Note that this geometrical explanation breaks down for pulsars that are inherently faint radio emitters at radio frequencies above $\sim$ few hundred MHz, at which radio pulsars are often observed. Pulsars that have extremely steep spectra may be radio-quiet to within detection limits at these radio frequencies.

Finally, for radio-loud pulsars, the phase of the main radio peak (often defined to be $\phi = 0$) should occur near the phase of the magnetic pole, ϕ_B, in the model light curve. (The model light curves are shifted in order to best fit the observed

light curves, so ϕ_B is not necessarily zero.) To be more exact, the phase of the radio peak should coincide with ϕ_B or else precede it by $\sim 2r/R_{\rm LC}$ in phase (Dyks & Harding 2004), where r is the emission height and $R_{\rm LC}$ is the light cylinder radius. The radio peak phase must be considered because the radio pulse profiles are not fit jointly with the γ-ray profiles in this work. While it is common to fit the radio cone as well as the γ-ray light curves (e.g., Venter et al. 2012), we chose to only fit the HE light curves and consider multiwavelength constraints afterward. This is because the radio emission location is uncertain, so we do not want to bias our HE models with a radio model.

3.2 Results: Four Bright Gamma-ray Pulsars

The best fit light curves and their confidence intervals are shown in Figures 3.5–3.11 and given in Table 3.2. The flux correction factor f_Ω is also given for each fit, for ease of comparison with other work. This factor accounts for the fact that the measured γ-ray flux $F_{\rm obs}$ is not necessarily the true flux averaged over the sky (Harding et al. 2007; Watters et al. 2009). Using each best fit geometry, we calculate the factor as

$$f_\Omega(\alpha, \zeta_\oplus) = \frac{\int\int F_\gamma(\alpha, \zeta, \phi) \sin\zeta d\zeta d\phi}{2\int F_\gamma(\alpha, \zeta_\oplus, \phi) d\phi} \tag{3.11}$$

where α and $\zeta_\oplus$, the observer's viewing angle, are found from light curve modeling. The true γ-ray luminosity is then

$$L_\gamma = 4\pi f_\Omega F_{\rm obs} D^2 \tag{3.12}$$

where D is the distance to the pulsar. For high-altitude, high-energy pulsar beaming models, $f_\Omega \sim 1$ for many observer viewing angles (Watters et al. 2009).

Asymmetric confidence intervals were determined by exploring the parameters in the vicinity of a local maximum in the likelihood $\mathcal{L}$. We first identify regions of

maximum $\mathcal{L}$ in our MCMC results—the MCMC routine finds local maxima, but by design it does not calculate $\mathcal{L}$ for every combination of parameters. We "zoom into" these regions and calculate χ^2 for every contained set of $(\alpha, \zeta, w, r, \Delta\phi)$. Within these completely explored regions, we use $\Delta\chi^2$ to find the 68%, 90%, 95%, and 99.7% confidence intervals ($\Delta\chi^2 = 5.86, 9.24, 11.07$, and 17.96, respectively). This approach assumes Gaussian errors, and can result in patchy confidence intervals because the parameter space near a local maximum in $\mathcal{L}$ is not necessarily smooth (for example, a shift of 1° in α or ζ can change whether or not a peak is observed).

Statistically good fits cannot be obtained for the light curves of these bright pulsars using simplified, purely geometrical models, as will be discussed further in the sections below. The reduced χ^2_ν values for the fits are therefore very large. As a result, the $\Delta\chi^2$ test yields very small confidence regions, falsely suggesting that the fits are excellent. We therefore normalize the χ^2 values with the best fit χ^2 to estimate the confidence intervals for the fit parameters. Then the new statistic $\xi^2 = \chi^2/\chi^2_{\rm best}$, such that the best fit geometry yields $\xi^2_\nu = 1$, and replace $\Delta\chi^2$ with $\Delta\xi^2$ to calculate the confidence intervals.

For most of the models, there are multiple regions in parameter space with light curve fits falling within 99.7% (3σ) of the best ξ^2. In the confidence interval plots (Figures 3.4, 3.6, 3.8, and 3.10), we show all regions in the parameter space that contain best fit light curves whose ξ^2 values are within 3σ of the absolute best fit. From these regions, we choose the best fit light curve (shown for each pulsar and emission/field geometry in Figures 3.5, 3.7, 3.9, and 3.11) to be that which yields the lowest ξ^2, except for cases where the best statistical fit is missing one of the peaks. In those cases, we do not include the absolute statistical best fit in Table 3.2 or the light curve figures, and instead choose another light curve with a higher ξ^2 that does reproduce the peaks at the correct phases of the LAT light curve.

Table 3.2. Best Fit Geometrical Parameters

	Vacuum Retarded Dipole			Ideal Force-Free		
Parameter	Outer Gap	Slot Gap	Asymmetric Slot Gap	Outer Gap	Slot Gap	Asymmetric Slot Gap
Vela						
$\alpha(^\circ)$	88^{+2}_{-3}	44^{+4}_{-1}	65^{+1}_{-2}	80^{+0}_{-0}	15^{+0}_{-0}	55^{+10}_{-20}
$\zeta(^\circ)$	$66.5^{+0.0}_{-0.0}$	$54.5^{+1.0}_{-5.0}$	$65.5^{+2.0}_{-1.0}$	$52.5^{+0.0}_{-0.0}$	$68.5^{+0.0}_{-0.0}$	$54.5^{+4.0}_{-14.0}$
$w(r_{\rm ovc})$	$0.00^{+0.00}_{-0.00}$	$0.14^{+0.06}_{-0.02}$	$0.09^{+0.03}_{-0.03}$	$0.04^{+0.00}_{-0.00}$	$0.00^{+0.00}_{-0.00}$	$0.04^{+0.02}_{-0.03}$
$r(R_{\rm LC})$	$0.9^{+0.0}_{-0.0}$	$0.7^{+0.0}_{-0.0}$	$1.2^{+0.2}_{-0.0}$	$1.6^{+0.1}_{-0.1}$	$0.9^{+0.0}_{-0.0}$	$0.9^{+1.1}_{-0.0}$
ϕ_B	$-0.028^{+0.000}_{-0.006}$	$0.450^{+0.011}_{-0.006}$	$0.044^{+0.011}_{-0.006}$	$-0.039^{+0.000}_{-0.000}$	$-0.089^{+0.000}_{-0.000}$	$0.028^{+0.117}_{-0.017}$
$\chi^2/151$	372.1	977.3	1046.7	309.5	1080.4	1180.8
f_Ω	1.0	1.4	1.0	1.1	0.6	0.8
Crab						
$\alpha(^\circ)$	10^{+9}_{-6}	58^{+12}_{-23}	67^{+7}_{-13}	90^{+0}_{-35}	70^{+5}_{-25}	65^{+5}_{-15}
$\zeta(^\circ)$	$84.5^{+1.0}_{-4.0}$	$72.5^{+4.0}_{-5.0}$	$57.5^{+12.0}_{-11.0}$	$64.5^{+25.0}_{-6.0}$	$64.5^{+12.0}_{-14.0}$	$60.5^{+11.0}_{-11.0}$
$w(r_{\rm ovc})$	$0.14^{+0.02}_{-0.05}$	$0.04^{+0.04}_{-0.04}$	$0.16^{+0.04}_{-0.09}$	$0.00^{+0.14}_{-0.00}$	$0.08^{+0.06}_{-0.06}$	$0.30^{+0.00}_{-0.08}$
$r(R_{\rm LC})$	$1.1^{+0.8}_{-0.1}$	$1.1^{+0.2}_{-0.1}$	$1.0^{+0.2}_{-0.2}$	$1.6^{+0.4}_{-0.6}$	$1.3^{+0.7}_{-0.4}$	$0.7^{+0.1}_{-0.0}$
ϕ_B	$-0.078^{+0.006}_{-0.011}$	$-0.072^{+0.006}_{-0.017}$	$-0.039^{+0.006}_{-0.017}$	$-0.372^{+0.283}_{-0.000}$	$-0.100^{+0.006}_{-0.006}$	$-0.050^{+0.006}_{-0.006}$
$\chi^2/85$	243.7	197.0	146.9	199.5	224.8	168.4
f_Ω	0.1	0.9	1.0	0.7	1.1	0.9
Geminga						
$\alpha(^\circ)$	10^{+0}_{-2}	82^{+3}_{-12}	83^{+2}_{-12}	85^{+0}_{-0}	15^{+5}_{-5}	55^{+10}_{-5}
$\zeta(^\circ)$	$83.5^{+0.0}_{-0.0}$	$80.5^{+4.0}_{-2.0}$	$80.5^{+4.0}_{-2.0}$	$24.5^{+2.0}_{-0.0}$	$72.5^{+0.0}_{-2.0}$	$85.5^{+3.0}_{-5.0}$
$w(r_{\rm ovc})$	$0.12^{+0.00}_{-0.00}$	$0.10^{+0.02}_{-0.02}$	$0.10^{+0.02}_{-0.02}$	$0.04^{+0.00}_{-0.00}$	$0.03^{+0.01}_{-0.03}$	$0.30^{+0.00}_{-0.10}$
$r(R_{\rm LC})$	$1.4^{+0.6}_{-0.3}$	$1.2^{+0.1}_{-0.2}$	$1.1^{+0.2}_{-0.0}$	$1.6^{+0.4}_{-0.0}$	$1.0^{+1.0}_{-0.1}$	$0.7^{+0.1}_{-0.0}$
ϕ_B	$0.022^{+0.000}_{-0.000}$	$0.067^{+0.006}_{-0.006}$	$0.067^{+0.006}_{-0.006}$	$-0.039^{+0.000}_{-0.000}$	$-0.050^{+0.006}_{-0.006}$	$0.078^{+0.006}_{-0.017}$
$\chi^2/175$	119.9	105.6	106.8	115.2	103.1	117.8
f_Ω	0.2	1.0	1.0	0.5	0.5	0.9
PSR J0007+7303						
$\alpha(^\circ)$	6^{+5}_{-5}	8^{+4}_{-0}	8^{+4}_{-0}	85^{+5}_{-15}	20^{+35}_{-15}	10^{+15}_{-5}
$\zeta(^\circ)$	$74.5^{+15.0}_{-4.0}$	$69.5^{+0.0}_{-0.0}$	$69.5^{+0.0}_{-0.0}$	$8.5^{+19.0}_{-1.0}$	$65.5^{+3.0}_{-13.0}$	$68.5^{+1.0}_{-4.0}$
$w(r_{\rm ovc})$	$0.04^{+0.18}_{-0.04}$	$0.00^{+0.01}_{-0.00}$	$0.00^{+0.01}_{-0.00}$	$0.02^{+0.03}_{-0.02}$	$0.03^{+0.07}_{-0.03}$	$0.03^{+0.02}_{-0.03}$
$r(R_{\rm LC})$	$1.0^{+1.0}_{-0.1}$	$1.0^{+1.0}_{-0.0}$	$1.0^{+0.7}_{-0.0}$	$1.1^{+0.9}_{-0.2}$	$1.0^{+1.0}_{-0.1}$	$0.9^{+1.1}_{-0.0}$
ϕ_B	$0.006^{+0.083}_{-0.028}$	$-0.011^{+0.011}_{-0.000}$	$-0.011^{+0.011}_{-0.000}$	$0.328^{+0.000}_{-0.322}$	$-0.028^{+0.033}_{-0.017}$	$-0.056^{+0.028}_{-0.000}$
$\chi^2/27$	22.5	11.3	11.0	26.6	16.2	19.5
f_Ω	0.2	0.4	0.4	0.6	0.6	0.4

Note. — The light curve fit parameters, with confidence intervals denoted as error bars, within each geometry. For all, α and ζ are measured in degrees, w in open volume coordinates (Section 3.1.2), and r in $R_{\rm LC}$. We include the best reduced χ^2 ($\chi^2/N_{\rm dof}$) for each model. Some parameters have error bars of value zero, which is due to the error being smaller than the resolution in that parameter.

We note it may be surprising that the best fit found by the MCMC routine can in some cases miss one of the peaks, but this can be explained by the fact that the bridge and off-peak emission in these light curves also contribute significantly to the likelihood. Poorly modeled off-peak emission can therefore direct the fits away from strongly peaked model light curves. This can be a problem for these geometrical models, as it is typical that the slot gap model will over-predict the off-peak emission, while the outer gap often produces no off-peak emission. This issue was addressed by Romani & Watters (2010) with their use of the new χ_3 statistic, which was designed to give more weight to the light curve peaks. Another method that may be considered is to only fit the peak and bridge emission for pulsars that have no off-peak emission. We chose to continue fitting the full phase light curves because the off-peak emission is also an important diagnostic of the emission models—it may be a geometrical effect that some pulsars, like Geminga, have detectable magnetospheric off-peak emission, while others do not. The use of fixed count, as opposed to fixed width, binning of the light curve leads to more bins in the peaks than in the bridge and off-peak regions. This results in the peaks contributing more to the likelihood than the rest of the light curve, and is used for Vela (see Section 3.2.1). Finally, for the slot gap model, applying the asymmetry in $\mathcal{E}$ from the offset dipole decreases the off-peak emission. In general, we find that this improves the prediction of the off-peak emission, giving more emphasis to the peaks in the slot gap light curves.

We chose to use fixed count binning for Vela's light curve, and used the same bins as for the phase resolved spectral fitting. For the other three pulsars, we used fixed width bins. In principle, fixed count bins could be used for Geminga and Crab as well, but it was deemed necessary for Vela because it is so much brighter than the others. The fixed count bins lead to sharper features in the light curve. There

are more bins in the peaks, which in principle naturally gives more weight to the peaks than the off-peak emission when fitting. It does happen that some of the LAT light curve phase bins are smaller than those in the light curves output from the simulations. When rebinning the simulated light curves, if the new bin is smaller than the old bin, it keeps the (dimensionless) intensity value of the original bin.

The Crab and Vela pulsars have multiwavelength constraints, in particular fits to the X-ray torii in their nebulae which provide the viewing angle to the rotation axis ζ. Vela also has polarimetric radio observations giving a constraint on $\beta = |\alpha - \zeta|$, the angle between the observer line of sight and the rotation axis. For these radio-loud pulsars, we plot the best fit light curve in Figures 3.5 and 3.7; in the contour plots, we mark its geometrical parameters with a star, and we mark the multiwavelength constraints as well.

3.2.1 Vela

Vela is a radio-loud pulsar that lies within the pulsar wind nebula Vela X. The orientation of the X-ray torus, observed by Chandra in the inner part of the nebula, implies an observing angle of $63.6^{+0.07}_{-0.05} \pm 0.6$ degrees (Ng & Romani 2008). The torus is assumed to be perpendicular to the pulsar's rotation axis, so this provides a strong constraint on the value of ζ. From radio polarimetry, for which the Rotating Vector Model (RVM) for surface or low-altitude emission is used to fit the polarization angle swing, $\beta = |\alpha - \zeta|$ is constrained to 6.5° by Johnston et al. (2005). They deem the PA swing of Vela's polarized profile to be compatible with the RVM, in which case the geometry obtained from this model can be considered reliable.

We find that the outer gap emission geometry, within the force-free field geometry, produces the best statistical fit. Examining the light curves by eye, we identify the asymmetric slot gap emission geometry, within the vacuum field geometry, as

the model that best reproduces the qualitative features of the Vela LAT light curve as well as several quantitative multi-wavelength constraints such as the values of ζ and ϕ_B. We discuss these findings below. Additionally, an important result is that, regardless of the geometrical model, the best-fit values of ζ are within $\sim 10^\circ$ of that found by Ng & Romani (2008).

The results of the light curve fits are shown in Figures 3.4 and 3.5. In Figure 3.4, contours for intervals of $\Delta\xi^2 = 5$ are shown in color, while the 68.3, 95, and 99.7% contours are given by the dashed lines. The location of the best statistical fit is shown with a star. The confidence contours give some indication of the patchiness of the likelihood surface. In some cases, there are multiple regions with comparably good statistical fits; some regions are fairly smooth, while others are misshapen. The best fit values of w and r vary from one point in (α, ζ) space to another, and marginalizing over (holding constant) single fixed values of w and r can lead to even patchier confidence intervals. For this reason, we "marginalize" over ranges of w and r that correspond to the 99.7% confidence intervals for each parameter. More specifically: at each (α, ζ), we find the best-fit (w, r) lying within the 99.7% confidence intervals listed in Table 3.2. To plot confidence contours, a grid of χ^2 at each (α, ζ) is needed. We assign the χ^2 of the best fit for (α, ζ, w, r) to the two-dimensional array of χ^2 values in (α, ζ) space. These ranges are determined after a scan over all possible values of (α, ζ, w, r) is done in the regions in parameter space identified by the MCMC to contain local maxima.

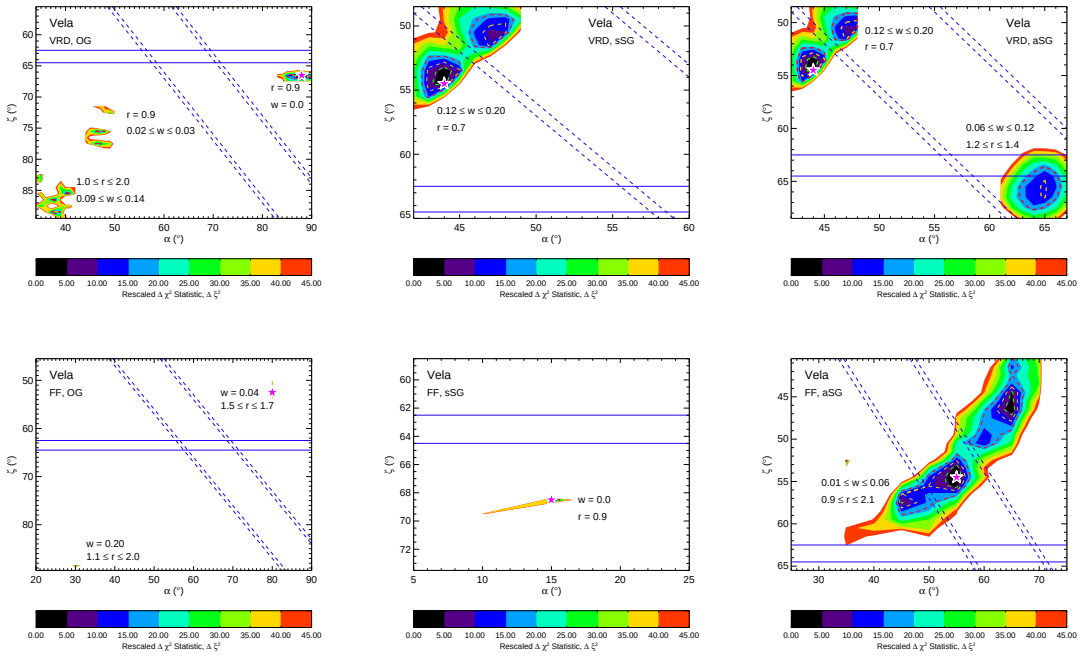

Figure 3.4: Confidence intervals for Vela. The pink star shows the location of the absolute best fit for each model. The constraint on ζ is $\zeta = 63.5 \pm 1.0$. Johnston et al. (2005) finds $\beta = 6.5°$, meaning $\alpha = 70.5$ or 57.5.

3.2.1.1 Outer Gap Light Curves in the VRD and FF Fields

In both the vacuum and force-free field geometries, the outer gap geometry results in the best statistical fits, with the FF field giving the best fit overall. The VRD OG misses most of the first peak, as was also found by Romani & Watters (2010), while the FF OG reproduces both peaks relatively well. The OG in both fields has no off-peak emission at this geometry (this is common for most OG geometries), matching the observed light curve well in this regard.

For the VRD OG, the best fit is found at (88, 66.5, 0, 0.9). The light curve is shifted to earlier phase such that the magnetic pole falls at $\phi_B = -0.0278$ (or, one cycle later, 0.9722). For low-altitude emission (below $\sim 2r/R_{\rm LC}$), it is physically realistic for $\phi_{\rm B} > \phi_{\rm radio}$ (Dyks et al. 2004), where $\phi_{\rm radio} = 0$ as defined by the timing

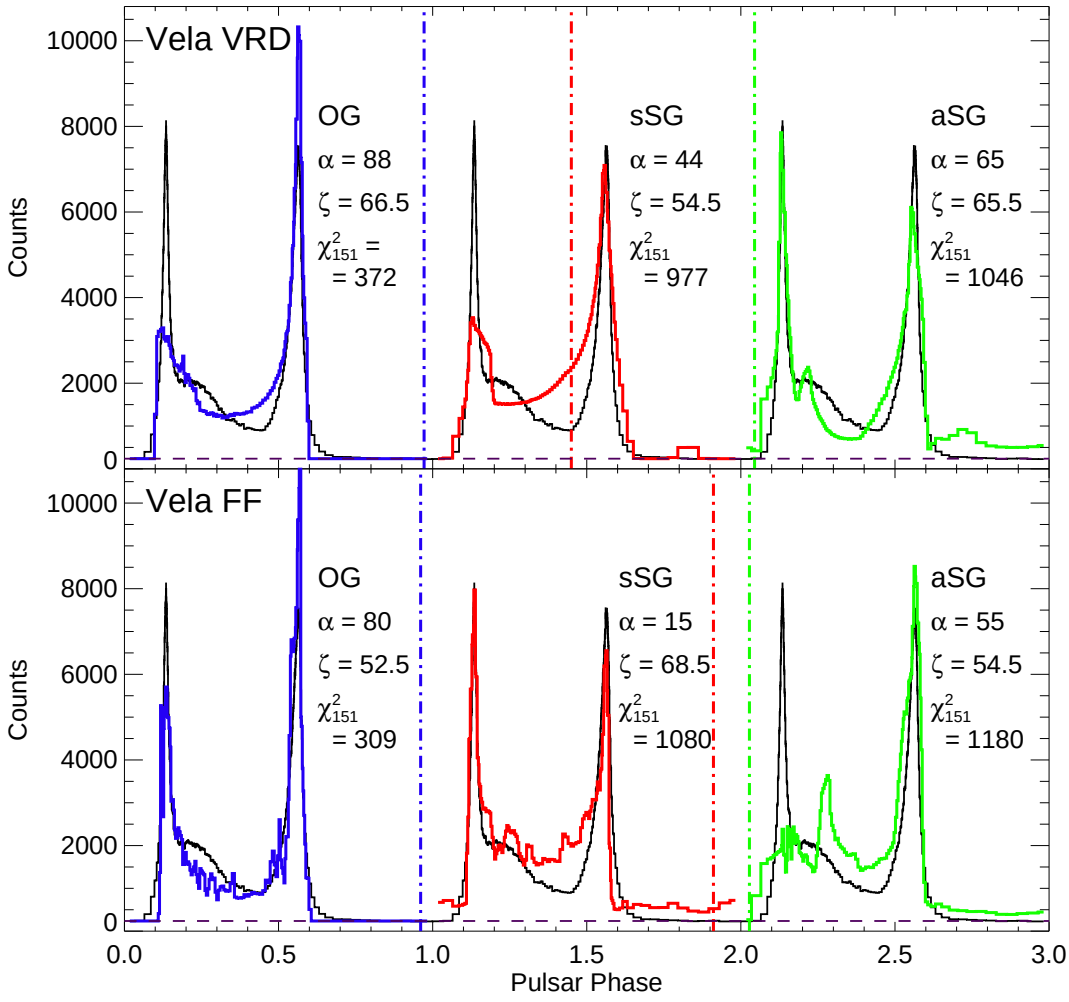

Figure 3.5: Best fit Vela light curves made using the Pass 7 phase bin definitions (same bins as in the phase resolved spectra of Figure 4.2). The top panel shows light curves simulated in the vacuum field, and the bottom panel shows those from the force-free field. The black line is the Crab's light curve as observed by the LAT, and is repeated three times to show all the fitted light curves. From left to right are the best fits for the OG (blue), sSG (red), and aSG (green) models. These fits were found after multiplying the likelihoods obtained from the MCMC fitting routine by the prior on ζ. They correspond to the confidence intervals containing the best fit light curves (68%, purple confidence intervals) in Figure 3.4. The light curve for the VRD aSG is the exception: the lower-confidence region from Figure 3.4 was chosen because ϕ_B has a sensible value there (near the radio peak), and the first peak is more prominent than in the highest-confidence region. This reasoning was not used for the VRD sSG because there was no other region with a high enough likelihood to show up as a confidence interval.

model used to produce these light curves. For caustic HE emission, the first peak will occur at a larger phase than $\phi_{\rm B}$. The VRD OG therefore finds a best fit geometry in which the phase of the magnetic pole is not physically realistic.

In the FF case, the best fit is found at $(\alpha, \zeta) = (80,\ 52.5)$. There is a second region that barely reaches a significance of 3σ, at $(\alpha, \zeta) = (30,\ 89.5)$. This fit lies farther from the expected ζ, and under current understanding, $\beta = |\alpha - \zeta|$ yields a radio-quiet or -faint pulsar, so we do not include this second region of high likelihood here. As in the vacuum case, the value of ϕ_B is again too low to be physically realistic for this model.

3.2.1.2 Slot Gap Light Curves in the VRD Field

For the symmetric SG geometry, the confidence contours show two connected regions containing model light curves that match the LAT light curves to within 3σ. The best fit light curve in Figure 3.5 (b) has too low a first peak, and does not reproduce the bridge emission between the peaks. It has very low off-peak emission, as in the OG case. The phase of the magnetic pole is $\phi_B = 0.45$. This is not physically realistic, as we know the phase of the radio peak to be $\phi_{\rm radio} = 0$; therefore, for radio emission below an altitude of $-2r/R_{\rm LC}$, ϕ_B should occur after $\phi_{\rm radio}$, but precede the phase of the first HE peak (Dyks et al. 2004), as discussed for the OG cases.

The same region in phase space containing the best fit geometry for the sSG model is statistically preferred in the aSG model. However, the same issues with the lack of a strong first peak and a physically unrealistic ϕ_B remain. A second region, at $(\alpha,\ \zeta) = (65,\ 65.5)$ is also significant in the aSG. While this region does not give as good a statistical fit as does the region near $(\alpha,\ \zeta) = (44, 54.5)$, the peaks, inner peak, and bridge emission are qualitatively reproduced much better than for the best statistical fit. Unlike ϕ_B associated with the statistical best fit, the value of

ϕ_B in this second region is physically realistic, falling between the phases of the radio peak and the first γ-ray peak. Additionally, the value of $\zeta = 65.5°$ that we obtain with this geometry is very close to the independent measurement of $\zeta \sim 63.6°$. For these reasons, we chose this model light curve as the best aSG fit, and show it in Figure 3.5(c) rather than the light curve resulting from the same statistically best fit geometry as found in the sSG case.

The light curve with the same parameters in the sSG geometry has higher off-peak emission relative to the peak emission. The fact that the aSG lowers the off-peak emission and enhances the peak emission results in this new best fit in the aSG geometry. It is also the only model that produces an emission shoulder reminiscent of that seen in the LAT light curve of Vela.

3.2.1.3 Slot Gap Light Curves in the FF Field

The sSG and aSG geometries in the force-free field give comparable, but slightly worse, statistical fits than in the vacuum field. The FF sSG gives a qualitatively good fit in the peaks, but does not match the bridge emission leading up to the second peak. It also again over-predicts the off-peak emission. The value of $\phi_{\rm B}$ is much too large to be physical (Dyks et al. 2004), as discussed above for other models. Most condemning to this geometry is that it produces a radio-quiet pulsar (large β), which is of course in conflict with observations. The FF aSG model misses the first peak almost completely; we find a diminished first peak to be a common feature of the slot gap geometry in the force-free field. The second peak matches the LAT light curve quite well, and the off-peak emission following the second peak is nearly consistent with what is observed. This again points to the off-peak emission being suppressed in the aSG geometry. The value of $\phi_{\rm B}$ is consistent with the radio constraints.

In former fits (DeCesar et al. 2011b) with different bin definitions, background estimation, and the Pass6_V8 rather than Pass7_V6 instrument response function, it was found that the VRD tended to have more physically acceptable values of ϕ_B than the FF field. The more recent fits presented in this paper do not find this result because we find slightly different emission geometries than we had previously. This is likely due to the subtle differences in the analysis listed above. In particular, a change in background level can lead to different results (Abdo et al. 2012), so it is possible that the more recent background estimate with the Pass7_V6 IRF is the cause of this discrepancy.

In general, the FF field does tend to shift the first peak to later phases than does the VRD, such that the phase of the magnetic pole in the model may not be consistent with the phase of the radio peak (Harding et al. 2011). However, the shift can vary depending on the specific geometry. For our best fits, we find that the magnetic pole occurs at too late a phase in the VRD OG, FF OG, and FF sSG. In the VRD sSG, it occurs at an unrealistic phase of 0.45. In the VRD and FF aSG, it occurs at a physically realistic phase; between the two, the light curve matches the VRD aSG best.

We note that the fact that the value of ϕ_B has changed in some cases demonstrates how sensitive the fits are to differences in binning, background estimation, instrument response function, and other choices made within the analysis.

3.2.2 Crab

Like Vela, the Crab pulsar is radio-loud and lies within an X-ray nebula. From a fit to the X-ray torus of the Crab Nebula, our viewing angle to the rotation axis of the Crab pulsar is $\zeta = 61.3^\circ \pm 0.1 \pm 1.1$ (Ng & Romani 2008). The pulsar peaks are aligned from radio to γ-ray energies, and the radio peaks are thought to result

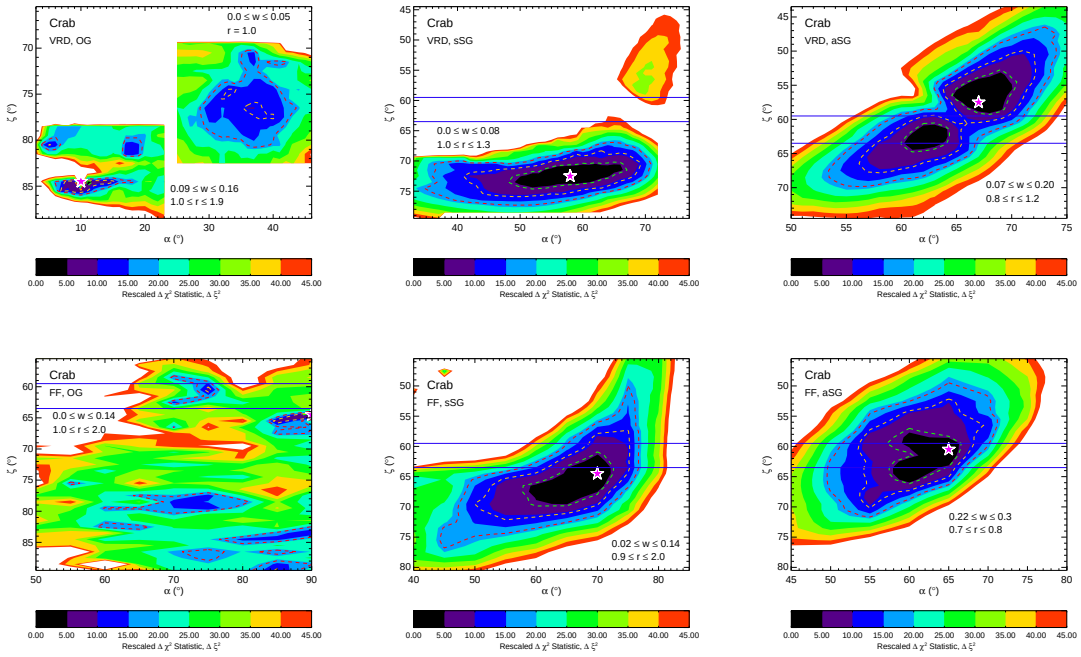

Figure 3.6: Confidence intervals for Crab. The pink star shows the location of the absolute best fit for each model. The vertical lines show the constraint $\zeta = 61.5° \pm 2.0°$ from the X-ray torus fit (Ng & Romani 2008), with the error convolved to the resolution in ζ of our simulations.

from high-altitude, caustic emission like that which forms the γ-ray peaks (Harding et al. 2008). This means the constraint on $\phi_{\rm B}$ discussed for Vela does not apply to the Crab pulsar's main peaks, nor does the RVM apply to their PA sweeps, and the value of β has no bearing on the pulsar's observed radio-loudness. However, the radio profile of the Crab shows a precursor located ~ 0.1 in phase before the first main peak. This precursor may be low-altitude emission from near the magnetic pole, in which case we expect $0.9 \leq \phi_{\rm B} \leq 1.0$. Whether or not the precursor marks a phase near that of the magnetic pole, we do expect that the magnetic pole would come at an earlier phase than the first γ-ray peak (or a later phase than the second γ-ray peak).

The confidence contours and light curve fits are shown in Figures 3.6 and 3.7.

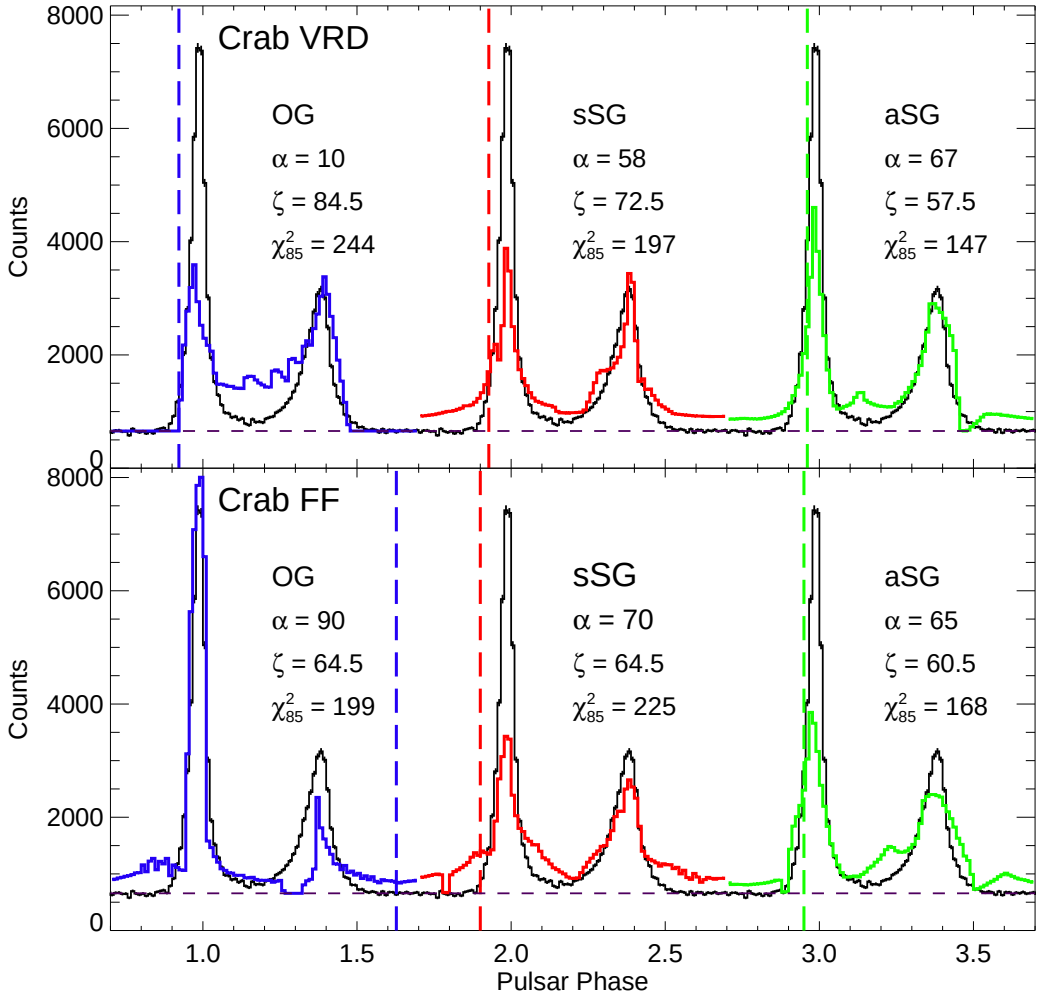

Figure 3.7: Absolute best fit light curves for the Crab pulsar; also see Table 3.2. The lines and colors are the same as in Figure 3.5. For the FF aSG light curve, we obtain the same best fit for the torus constraint as for the absolute fit. The horizontal dashed line shows the background level estimated with `gtsrcprob`. The vertical lines show the location of the magnetic pole, or phase zero, for the model light curves, so that one can see how much the model light curves were shifted in the fits. For radio-loud pulsars like the Crab and Vela, the first radio peak falls at phase 0.

The best statistical fit is given by the aSG model in the VRD field. The aSG in both the VRD and FF fields give best fits that are already close to or consistent with the torus constraint, and in both field geometries the aSG model light curves give the best overall fits.

The sSG light curves are similar to their asymmetric counterparts, giving slightly higher χ^2 values due to the effect of enhanced peaks and reduced off-peak emission in the aSG geometry. The best ζ in the FF sSG geometry is close to the torus constraint, with the VRD sSG having ζ within $\sim 10^\circ$ of the expected value.

The OG in the VRD field finds a best fit light curve more reminiscent of Geminga than the Crab, and too high a ζ value. However, the FF OG model light curve fits the LAT light curve very well qualitatively, reproducing the location and relative heights of the peaks, but introducing excessive off-peak emission. Its confidence contours are very patchy, with only very small regions that produce fits within 3σ of the best fit.

For all but the VRD OG geometries, $\zeta \sim 61^\circ$ falls within the 99.7% confidence intervals. The uncertainty range on ζ from Ng & Romani (2008), accounting for (convolved to) our resolution in ζ of 1°, is $61.5^\circ \pm 2.0^\circ$, and is plotted where applicable in the contour plots (Figure 3.6). All the best fit geometries have $\phi_{\rm B}$ slightly before the first γ-ray peak, or after the second peak in the case of the FF OG. All but the FF OG are consistent with the constraint on $\phi_{\rm B}$ imposed by a low-altitude precursor. In the FF OG case, $\phi_{\rm B}$ precedes the radio precursor. We note that for all but the VRD OG parameters, β is small enough that we might expect to see such low-altitude radio emission from the Crab.

3.2.3 Geminga

Geminga is considered a radio-quiet pulsar, as it has not been definitively detected by a radio telescope. However, there have been claims of radio detections from this pulsar at 102.5 MHz (e.g., Malofeev & Malov 1997; Vats et al. 1999). If these detections are real, then Geminga must have a very soft radio spectral index, with a lower limit of 2.7 (McLaughlin et al. 1999). It is therefore unclear whether Geminga has little or no radio emission due to geometry, such that the observer's line of sight is far from the magnetic pole and radio emission site (implying a large value of $\beta = |\alpha - \zeta|$), or to inherent radio faintness at typical observing frequencies above $\sim$ few hundred MHz. In the latter case, if our line of sight were to cross the radio emission zone, radio observations could still yield non-detections. Thus, we cannot rule out geometries with similar α and ζ (small β).

A loose constraint can be placed on ζ by considering the geometry of the pulsar bow shock. Caraveo et al. (2003) find that the inclination of the bow shock, and therefore its direction of travel, to the plane of the sky is $i < 30°$. If the rotation axis and velocity vectors are aligned, as has been suggested (Johnston et al. 2005; Rankin 2007), then $\zeta > 60°$ (Pierbattista et al. in preparation).

The location of the magnetic pole is less important here because there is no firm detection of radio emission to use as a constraint. We still expect the pole to fall shortly before the first peak, judging from the location of the radio peak in radio-loud pulsars.

The confidence intervals for the Geminga light curve fits are shown in Figure 3.8, and the light curves in Figure 3.9. We find that all geometries give similarly good fits, with the reduced χ^2 ranging between 103–120, despite the geometrical parameters being quite different from one model to the next. The OG model in the VRD field

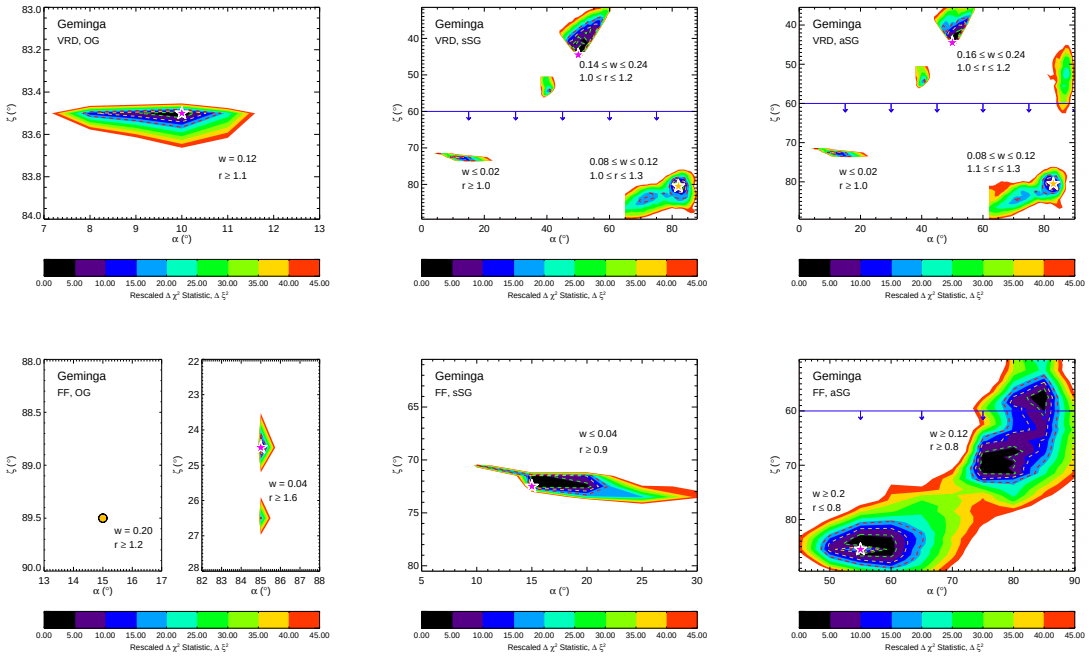

Figure 3.8: Confidence intervals for Geminga. The pink star shows the location of the absolute best fit for each model, while a yellow star shows a secondary geometry that has been chosen for other reasons as the best fit. *(Top)* the VRD OG model finds a geometrically radio-quiet pulsar. In the VRD sSG and aSG models, we choose a formal best fit geometry (yellow star) other than the statistical best fit (pink star). This choice was made because the statistical best fit light curve lacks the first peak and has an unreasonable $\phi_B \sim 0.5$. Additionally, the statistical best fit lies at a lower ζ than is predicted by Caraveo et al. (2003). As noted in the text (Section 3.2.3), either of the two regions at high ζ with 3σ confidence contours may be the true best fit, as it is unknown whether or not Geminga is radio-loud. *(Bottom)* For the FF OG case, the best statistical fit is shown by the pink star. A second-best fit is shown with the black-outlined yellow circle. This secondary geometry lies within the range of ζ assumed given the work by Caraveo et al. (2003); since that ζ constraint depends on assumptions about the system, we do not formally choose it as the best fit, hence being marked with a circle rather than a star. The range on α and ζ lie within their respective simulation resolutions, hence the lack of contours. The FF sSG geometry finds a geometrically radio-quiet pulsar, while the geometries in the FF aSG may imply intrinsically faint radio emission.

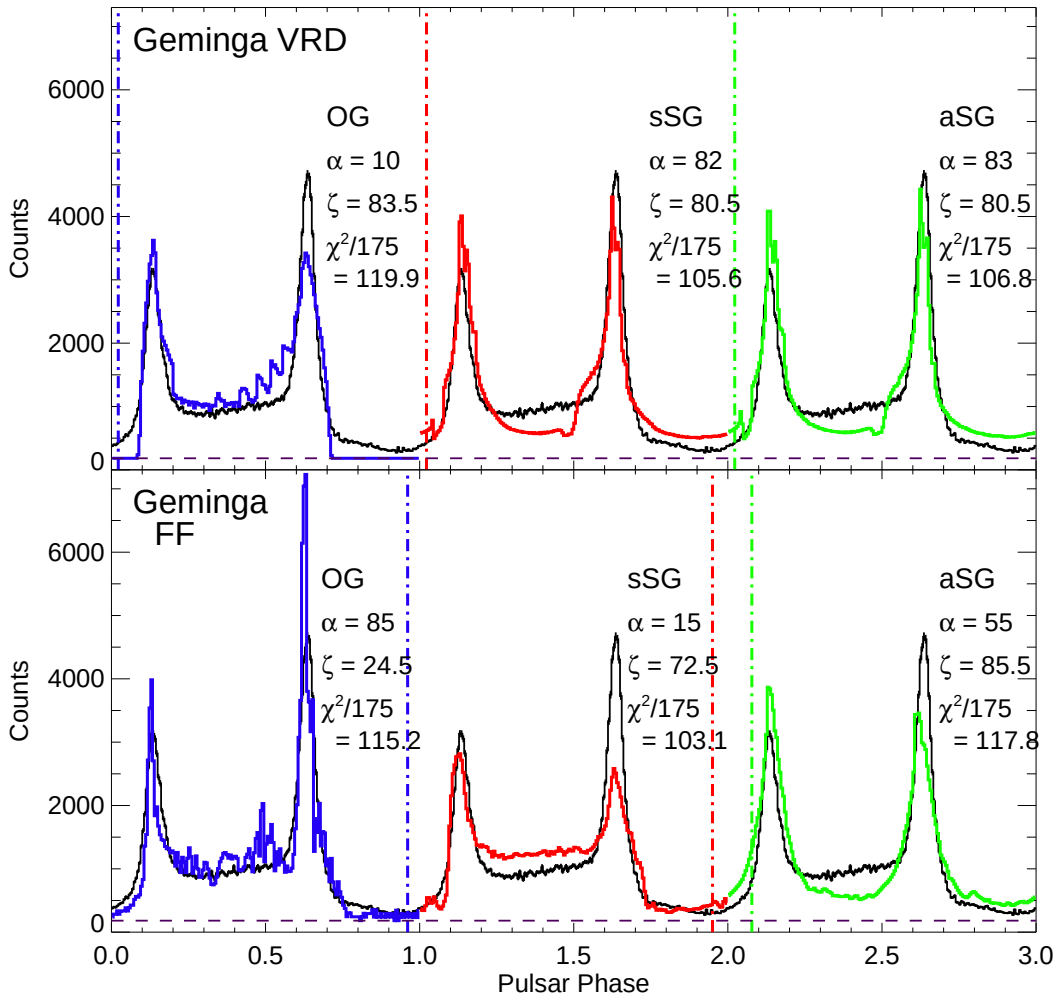

Figure 3.9: The best fit light curves for Geminga. The lines and colors are the same as in the previous figures.

finds a geometrically radio-quiet pulsar, with a large β, and $\zeta > 60°$. The best fit in the FF OG geometry is found at high α and low ζ, again giving a radio-quiet pulsar from geometry. However, while we take these parameters to give the best fit, if the constraint of $\zeta > 60°$ is correct, then these parameters are ruled out. In that case, the secondary fit found at $(15°, 89.5°)$ would become the best fit. This fit is shown with a circle rather than confidence contours because, even after rescaling the χ^2 values, this point in (α, ζ) space was the only one lying above 3σ. The circle

is colored the same as other secondary fits that have been chosen as best fits (e.g., the aSG geometry in the VRD field for Vela); it is a circle rather than a star because the constraint on ζ was not determined as directly as in Vela and the Crab, and therefore we have not chosen it as the best fit geometry.

The VRD sSG finds a statistically best fit at $(\alpha, \zeta, w, r) = (50°, 44.5°, 0.18\, r_{\rm ovc}, 1.1\, R_{\rm LC})$ with $\chi^2/175 = 104.1$, shown by the star in the confidence contour plots (Figure 3.8). However, the light curve for these parameters completely misses the first γ-ray peak, and additionally, the value of $\phi_{\rm B} = 0.5333$ for this geometry is not sensible. We therefore choose the best fit to lie in the second-best region ($\chi^2/175 = 105.6$), at $(82°, 80.5°, 0.1\, r_{\rm ovc}, 1.2\, R_{\rm LC})$. This light curve has two peaks and a reasonable value of $\phi_{\rm B} = 0.0667$, and ζ is consistent with the constraint from Caraveo et al. (2003). This geometry would lead to radio loudness, which cannot be ruled out due to the possible radio detections discussed above. However, if Geminga is radio-quiet, then the geometry may instead lie near $(11°, 72.5°, 0.01\, r_{\rm ovc}, 1.0\, R_{\rm LC})$, for which the model light curve gives a qualitatively different but statistically similar fit ($\chi^2/175 = 108.5$). The large β ensures a radio-quiet pulsar, and $\phi_B = -0.0222$ is a reasonable phase for the magnetic pole.

The results are nearly identical between the sSG and aSG geometries in the VRD field. For the same reasons as above, for the aSG we choose the region in parameter space giving the second best statistical fit, $(83°, 80.5°, 0.1\, r_{\rm ovc}, 1.1\, R_{\rm LC})$, as the location of the best fit. The third significant region again appears in the aSG, at $(11°, 72.5°, 0.01\, r_{\rm ovc}, 1.1\, R_{\rm LC})$, with the same ϕ_B and χ^2.

The sSG model in the FF field finds a similar best fit geometry, $(\alpha, \zeta, w, r) = (15°, 72.5°, 0.03\, r_{\rm ovc}, 1.0\, R_{\rm LC})$, as the third significant region in the VRD aSG. In the FF aSG geometry, there are two statistically similar regions in Figure 3.8, with the best fit lying at $(\alpha, \zeta) = (55°, 85.5°)$. The second region has best-fit parameters

$(85°, 57.5°, 0.22\,r_{\rm ovc}, 0.8\,R_{\rm LC})$, with $\phi_B = 0.0722$ and $\chi^2/175 = 117.8$. The lower β in the aSG model may allow viewing of part of the radio emission zone, depending on its size, hence this geometry is more consistent with intrinsic radio faintness (but may still allow for radio quietness due to geometry).

3.2.4 PSR J0007+7303

The "CTA 1 pulsar," PSR J0007+7303 in the CTA 1 supernova remnant, is also radio-quiet to within current detection limits. All the fits give large β values, consistent with expectations for a pulsar that is radio-quiet because of geometry, as was found in vacuum OG and sSG fits by Abdo et al. (2012). The best fit is found in the vacuum sSG and aSG geometries; because of the very low α, the symmetric and asymmetric SG light curves are very similar, and the best geometrical parameters are identical. The aSG model does find the second region of high likelihood seen in Figure 3.10 (b) and (c), near $(\alpha, \zeta) = (12,\ 69.5)$, to be more significant than this same region for the sSG model, meaning that the increase in asymmetry with α leads to improved fits in that part of phase space.

Moving to the slot gap geometries in the FF field, we find larger values of α for both the sSG and aSG geometries than in the vacuum field; this may be due in part to the lower resolution in α of the FF simulations. The vacuum field light curves give much better fits than those of the FF field, but this may again be an effect of missing the best FF fit because of the lower α resolution relative to that in the VRD.

For the CTA 1 pulsar, the OG model results in the statistically worst light curve fits. For the VRD OG, the likelihood surface is very patchy, but there are two main regions at opposite corners in phase space that result in similar statistical fits. The best fit light curve has a shape similar to that of the LAT light curve, but with

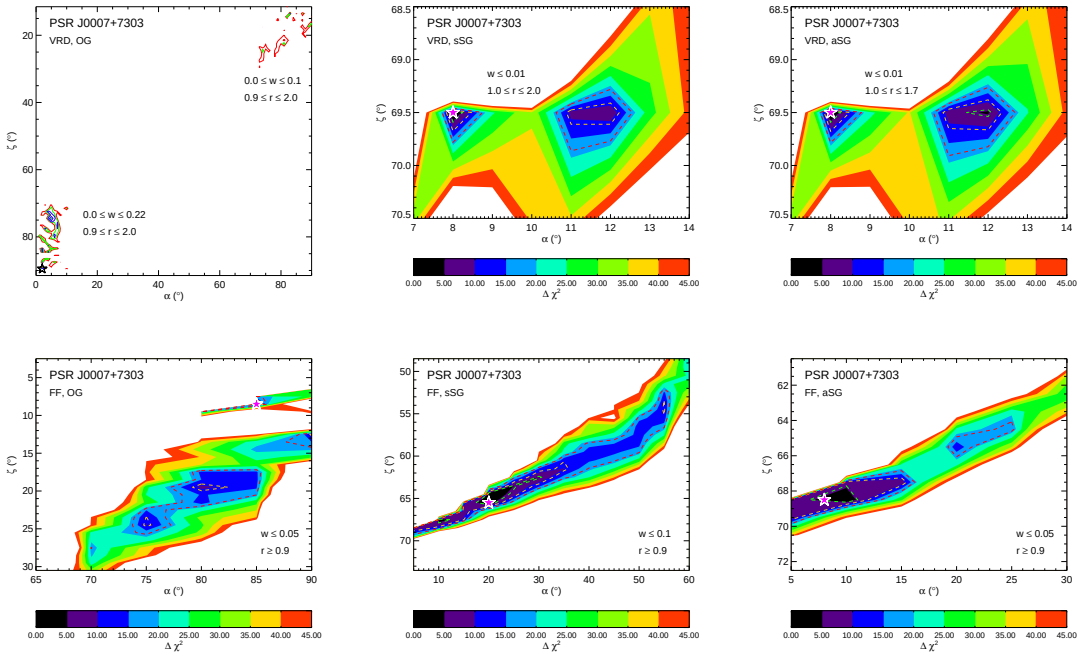

Figure 3.10: Confidence intervals for PSR J0007+7303. The pink star shows the location of the absolute best fit for each model. For the VRD OG, there was one slightly better fit at (2°, 89.5°), but it was an outlier compared to all points around it, had only a slightly lower χ^2 than the best fit chosen (21.8 vs. 22.4), and had only one peak as opposed to two closely separated peaks. For these reasons, the fit at $(\alpha, \zeta) = (2°, 89.5°)$ was not considered as a best fit. Also for the VRD OG, the χ^2 contours are very messy, hence plotting the 1, 2, and 3σ contours without the underlaid χ^2 contours. The open contours in the FF sSG and aSG result from the fact that the lowest α considered was 5°.

too shallow a dip between peaks and too low off-peak emission. The FF OG has a somewhat smoother phase space, with a few regions lying within 99.7% confidence of the best fit. The light curve is essentially a single, rounded peak rather than two closely spaced peaks. While ϕ_B was not a consideration in the other geometries, for this geometry it falls within the first peak of the LAT light curve, which is likely not physical; we expect that the magnetic pole will precede the first peak.

In Abdo et al. (2012), it was noted that the best fit geometrical model changes depending on whether the detected off-peak emission is considered to be magne-

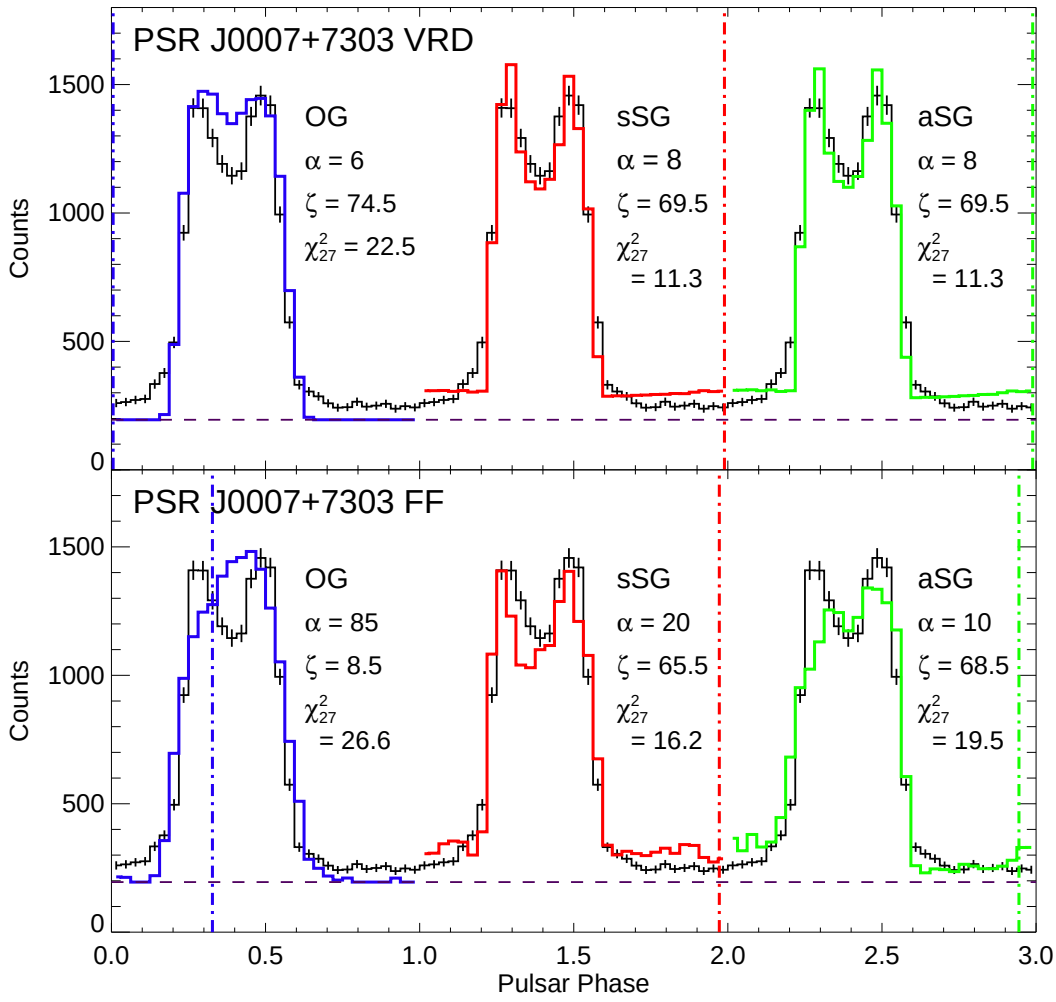

Figure 3.11: The best fit light curves for the CTA 1 pulsar, PSR J0007+7303. The lines and colors are the same as in the previous figures.

tospheric or PWN emission. In the second LAT pulsar catalog (The Fermi-LAT Collaboration 2013), this off-peak emission is classified with a "U" for its "Unidentified" origin. If from a PWN, then it would be considered part of the background, and the pulsed emission would go to zero in the off-peak. If it is magnetospheric, then the background level lies below the observed off-peak level. We have therefore interpreted the off-peak emission in this pulsar to be magnetospheric in origin. If we were to assume the emission is from a PWN, the OG would have lower χ^2 values and

may fit the light curves better than the SG models as it did in Abdo et al. (2012), simply because it matches low-level or nonexistent off-peak emission better than the SG. The authors also related the best-fit values of $\phi_{\rm B}$ to X-ray observations by Caraveo et al. (2010): the X-ray peak falls $\sim 90^\circ - 110^\circ$ before the first γ-ray peak, while $\phi_{\rm B}$ fell $36^\circ - 94^\circ$ before the first peak. In the best fit light curves presented in this paper, $\phi_{\rm B}$ lies within a similar range ($\sim 90^\circ$) of the first peak, except in the FF OG geometry.

3.3 Discussion

We modeled the observed LAT light curves of the four pulsars with geometrical representations of the outer gap, slot gap, and offset dipole slot gap emission models, and the vacuum retarded dipole (Deutsch 1955) and ideal force-free magnetosphere (Contopoulos & Kalapotharakos 2010) magnetic field models (Section 2.3). Using a Markov chain Monte Carlo maximum likelihood fitting routine (Verde et al. 2003) as in Section 3.1, we found the best fit values of the parameters $(\alpha, \zeta, r_{\rm max}, w, \Delta\phi)$ for each combination of emission and field geometries, listed in Table 3.2. When comparing models, there is not a particular emission or field geometry that stands out as clearly the best. The light curve modeling finds best fits for different combinations of emission and field geometries for each pulsar.

It is interesting and somewhat unexpected to find that the vacuum retarded dipole field leads to better fits than the FF in some cases. As discussed in Section 4.4.2, the FF field leads to more physical values of $E_{||}$, the accelerating electric field. Those pulsars for which the VRD best predicts the light curves may have magnetic field that are closer to the VRD than FF field, and the small amount of current that is present straightens the field lines enough to get large radii of curvature to

lower $E_{||}/B$.

There are a few overall conclusions we can draw from the light curve modeling. The first is that for geometrical representations of the slot gap to successfully reproduce LAT light curves, emission must be allowed at higher altitudes than has been typical for the geometrical analog of the slot gap, the two-pole caustic (TPC). Watters et al. (2009) and Romani & Watters (2010) use a cylindrical radius $r_{\rm cyl} = 0.75\,R_{\rm LC}$, and in many cases do not reproduce one or both of the peaks in the pulsar light curves they model. In this work, we extended this radius to $r_{\rm cyl} = 0.95\,R_{\rm LC}$, and in general we recover the peaks.

Secondly, introducing azimuthal asymmetry along the polar cap rim in the SG geometry as in Harding & Muslimov (2011a,b) leads to lower off-peak emission and enhanced peak emission, consistent with their findings. This result implies that a more realistic emission zone structure, with some azimuthal asymmetry, will better match the observed light curves.

Finally, in most cases, some emission below the null charge surface is needed to replicate the low-level off-peak emission, for example in the phases between the peaks (or, in the case of Geminga, the persistent magnetospheric emission). This emission is over-predicted by the slot gap models, even with some azimuthal asymmetry, and under-predicted by the outer gap, as has been known from prior modeling attempts. A more physical representation of the slot gap, a slot gap with weaker low altitude emission, or an extended outer gap as has been proposed by Takata et al. (2007), may better produce this common light curve feature. Another scenario that one might imagine is that a pulsar magnetosphere can have both a slot gap and an outer gap, so that the emission we observe comes from a blend of these two regions.

Chapter 4

Phase Resolved Spectroscopy of LAT Pulsars and Implications for the Strength of the Accelerating Electric Field

It has been found that the spectral parameters, in particular the power law spectral index and cutoff energy, vary significantly with pulse phase. In this chapter, I model the phase-resolved spectra of the same pulsars whose light curves I modeled in the previous chapter. I use the phase-resolved cutoff energy values to estimate the magnitude of the accelerating electric field, $E_{\|}$, which leads to constraints on the magnetic field geometry.

4.1 Phase Averaged Spectroscopy

We modeled the phase-averaged 0.1–300 GeV spectrum of each pulsar with a sub-exponentially cut-off power law. The differential photon flux is given by

$$\frac{dN}{dE} = N_0 \left(\frac{E}{E_0}\right)^{-\Gamma} \exp\left[-\left(\frac{E}{E_c}\right)^{b}\right] \text{ph cm}^{-2}\,\text{s}^{-1}\,\text{MeV}^{-1}, \tag{4.1}$$

where the flux prefactor N_0 is the differential flux (photons $\text{cm}^{-2}\,\text{s}^{-1}\,\text{MeV}^{-1}$) at energy E_0, E_0 is the pivot energy provided by the second (2FGL) *Fermi* source catalog (Nolan et al. 2012), Γ is the photon index, E_c is the cutoff energy, and b is the exponent determining the exponential ($b = 1$), super-exponential ($b > 1$) or sub-exponential ($b < 1$) shape of the cutoff. As stated above, for the phase-averaged spectral fits, we used $b < 1$, corresponding to a sub-exponential cutoff. A $20^\circ \times 20^\circ$ region of sky centered on the pulsar of interest was modeled using the `P7SOURCE_V6` instrument response function (IRF). Included in the spectral and spatial model were all 2FGL sources in a 20° radius from the central pulsar. The spectral parameters of all sources within a 10° radius of the pulsar were left free, while those of sources outside 10° and within 20° were fixed. After an initial phase-averaged fit to an absolute tolerance of 0.01, all sources with $TS \leq 0$ were removed from the model. The spectral fit was repeated, to an absolute tolerance of 0.001, until the values converged. We used the phase-averaged fit to estimate the background count level, given in Table 4.2, using the *Fermi* tool `gtsrcprob`[1].

The purpose of the phase-averaged spectral fits was to establish a good background model for the phase resolved fits. Examination of the residual σ maps allows us to determine whether or not the phase averaged fit provides a sufficient descrip-

[1]Usage notes for `gtsrcprob` can be found at `http://fermi.gsfc.nasa.gov/ssc/data/analysis/scitools/help/gtsrcprob.txt`

Table 4.1. Phase Averaged Spectral Parameters

Pulsar	N_0	Γ	E_c	b	F_{100}	G_{100}	TS
Vela	18.85 ± 0.06	1.16 ± 0.01	0.52 ± 0.01	0.54 ± 0.01	11.0 ± 0.03	58.0 ± 0.14	1268669
Crab	1.56 ± 0.57	1.69 ± 0.13	1.51 ± 1.34	0.58 ± 0.15	2.0 ± 0.02	8.2 ± 0.08	85056
Geminga	5.0 ± 0.29	0.96 ± 0.03	0.84 ± 0.09	0.69 ± 0.02	4.1 ± 0.01	26.4 ± 0.09	771308

Note. — The phase averaged spectral parameters of the three pulsars for which we performed spectral fits. N_0 is in units of 10^{-9} photons cm^{-2} s^{-1} MeV; E_c is in GeV; F_{100} is the photon flux in units of 10^{-6} photons cm^{-2} s^{-1}; and G_{100} is the energy flux, in units of 10^{-10} erg cm^{-2} s^{-1}. The parameters for Vela X and the Crab Nebula are given in the text in Sections 4.2.1.1 and 4.2.1.2. The parameters for PSR J0007+7303 are found in Abdo et al. (2012).

tion of the background. The map is calculated as

$$\sigma_{i,j} = \left(\frac{C_{i,j} - M_{i,j}}{M_{i,j}} \right)^{1/2} \tag{4.2}$$

where $\sigma_{i,j}$ is the residual value of the pixel at image coordinate (i, j), $C_{i,j}$ is the number of observed γ-ray counts in that pixel, and $M_{i,j}$ is the number of counts expected in the pixel, given the spectral and spatial model of the region. The residual map of the Crab is shown in Figure 4.1 as an example of the desired background residuals.

Any details on the phase averaged or off-peak fits relevant to individual pulsars follow in Sections 4.2.1.1–4.2.1.3, in which we describe our phase resolved spectral fits. The best fit parameters for the phase averaged spectra are provided in Table 4.1.

4.2 Phase Resolved Spectroscopy

4.2.1 Data Analysis

For the phase-resolved spectral analysis, a similar approach was taken. Either the phase-averaged or off-peak spectral fit was used as the initial model of the background sources. All parameters of sources farther than 5° from the pulsar were

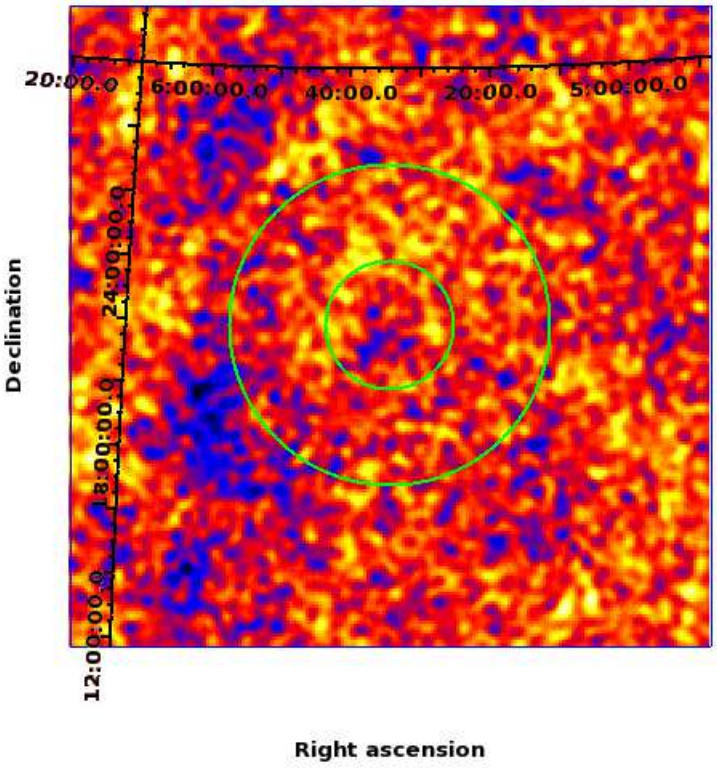

Figure 4.1: The residual σ map from the phase averaged spectral fit of the Crab pulsar and nebula. The color scale ranges from $\sigma = -0.9$ (dark blue) to $\sigma = 0.6$ (yellow), where $\sigma^2 = (\text{counts} - \text{model})/\text{counts}$. The residuals are fairly flat, with variations due to fluctuations in the diffuse background relative to the background model. The green circles are of radius 2° and 5°, and are centered on the Crab pulsar's location. Especially within these circles, the residuals are flat and sufficient for phase resolved spectral modeling.

fixed, while the normalizations of sources within a 5° radius were left free (all other parameters of these sources were fixed). The LAT events were grouped into bins defined as having $\sim$ 3000 pulsed events per bin, where a pulsed event was defined as an event falling within the energy-dependent angular radius given above. The source prefactors (N_0) were renormalized according to the width of each phase bin. An exponentially cutoff power law, with $b = 1$, was fit in each bin using the *Fermi* LAT tool `gtlike`[2].

[2] `http://fermi.gsfc.nasa.gov/ssc/data/analysis/scitools/help/gtlike.txt`

Above, I discussed the need for $b < 1$ in the phase-averaged spectral fits. In the case of poor statistics, it is not possible to constrain b, so it must be fixed in order to obtain meaningful constraints on the other parameters. Additionally, the phase-averaged value of $b < 1$ is believed to result from the blending of different values of the spectral parameters as they vary with phase, and hence does not represent the true physical spectrum at any particular phase. For curvature radiation, which is expected to dominate the radiation spectrum at energies $>$ few MeV, $b = 1$; in small phase bins where blending of spectral parameters is diminished, the curvature radiation spectrum should be recovered. For these reasons, we fixed $b = 1$ in the phase resolved spectral fits.

Following are details of the phase resolved spectral fits for each pulsar.

4.2.1.1 Vela

The Vela pulsar lies on top of faint γ-ray emission from the Vela X pulsar wind nebula. Because the nebula and pulsar contributions may be degenerate in the spectral model, we first modeled the nebula only, using data from the off-peak phases of the pulsar light curve. We modeled the spatial extent of the nebula as a uniform disk, using the extended template of Vela X from Abdo et al. (2010b). The spectrum was fit with a power law, fixing the spectral parameters of the nebula to $N_0 = 4.73 \times 10^{-7}\,\mathrm{cm^{-2}\,s^{-1}\,MeV^{-1}}$ and $\Gamma = 2.41$ as in Abdo et al. (2010b), and followed the procedure described above to obtain a phase-averaged fit. The phase-averaged background spectrum was used as the starting point for the phase-resolved spectral fits.

4.2.1.2 Crab

The Crab pulsar sits within the Crab nebula, a point source in the LAT. In order to accurately describe the nebula's spectrum we first fit the unpulsed emission in the phase window $0.535 \leq \phi \leq 0.885$, as defined by Abdo et al. (2010c). We modeled the nebula as in Buehler et al. (2012): the synchrotron component is modeled as a power law (`Powerlaw2` in the LAT tools), while the inverse Compton component is modeled with a smoothed broken power law. The spectrum of the nebula is therefore modeled as

$$\begin{aligned} \frac{dN}{dE} &= N_{\rm s}\left(\frac{E}{E_0}\right)^{-\Gamma_{\rm s}} \\ &+ N_{\rm I}\left(\frac{E}{E_0}\right)^{-\Gamma_{\rm I1}}\left(1+\left(\frac{E}{E_{\rm b}}\right)^{\frac{\Gamma_{\rm I1}-\Gamma_{\rm I2}}{\beta}}\right)^{-\beta} \mathrm{cm}^{-2}\,\mathrm{s}^{-1}\,\mathrm{MeV}^{-1}\ . \end{aligned} \tag{4.3}$$

For the synchrotron component, $N_{\rm S}$ is the 0.1–300 GeV integral flux and $\Gamma_{\rm S}$ the power law index. We found best fit values for these parameters of $N_{\rm S} = 2.36 \pm 0.08 \times 10^{-7}\,\mathrm{cm}^{-2}\,\mathrm{s}^{-1}$ and $\Gamma_{\rm S} = 3.8 \pm 0.1$ in the off-peak phase window ($\Delta\phi = 0.35$); normalizing the integral flux to all phases ($\Delta\phi = 1$), $N_{\rm S} = 6.76 \pm 0.23\,\mathrm{cm}^{-2}\,\mathrm{s}^{-1}$. For the inverse Compton component, $N_{\rm I}$ is the flux prefactor, $\Gamma_{\rm I1}$ and $\Gamma_{\rm I2}$ are the pre- and post-break power law indices, $E_{\rm b}$ is the break energy, and $\beta = 0.2$ (fixed) is the smoothing factor. Our best-fit values for these parameters were $N_{\rm I} = 2.2 \pm 0.5 \times 10^{-10}\,\mathrm{cm}^{-2}\,\mathrm{s}^{-1}\,\mathrm{MeV}^{-1}$ for the off-peak phase window ($6.2 \pm 1.4 \times 10^{-10}\,\mathrm{cm}^{-2}\,\mathrm{s}^{-1}\,\mathrm{MeV}^{-1}$ for the full phase window); $\Gamma_{\rm I1} = 1.52 \pm 0.06$; $\Gamma_{\rm I2} = 2.18 \pm 0.16$; and $E_{\rm b} = 15.3 \pm 5.7\,\mathrm{GeV}$. For both components, the scale factor E_0 was fixed at 100 MeV. While there may be some concern about the degeneracy of the two spectral components, it has been shown in previous work (Abdo et al. 2010c) that the synchrotron and IC components clearly contribute separately to the nebula emission, and the specific model parameters used were taken from the spectrum published by

Buehler et al. (2012). Also included in the fit was the nearby supernova remnant IC 443, for which we used a Gaussian disk extended source template as in Abdo et al. (2010c); only the normalization of this extended source was left free. We fit the Crab nebula spectrum with and without contribution from the pulsar and found that the addition of a source with a cutoff power law spectrum at the pulsar position did not significantly improve the fit, confirming the nondetection of magnetospheric emission in this phase range.

After fitting the off-peak spectrum, we renormalized all the source flux prefactors N_0 to the full phase and fit the pulsar phase-averaged spectrum. The spectral parameters of the two nebula emission components were fixed at the values obtained in the off-peak fit, with their normalizations corrected to the full phase interval. The flux prefactors and power law indices of all other sources within 5° of the pulsar were left free. The Crab pulsar spectral and spatial model was added to the model, at the same position as the nebula, with its spectral parameters free, and its spectrum was fit using `gtlike`. We chose to use the off-peak fit as the starting point for our phase-resolved analysis.

4.2.1.3 Geminga

Geminga has magnetospheric emission at all phases (Abdo et al. 2010d), so no off-peak phase range exists for this pulsar. We modeled the phase averaged spectrum, using the same extended source template for IC 443 as in the Crab fit, and used the resulting model (with renormalized source fluxes) in the phase resolved spectral fits.

4.2.1.4 PSR J0007+7303

The phase resolved parameters for PSR J0007+7303 were taken directly from Abdo et al. (2012).

4.2.2 Results: Phase Resolved Spectroscopy

Here we describe the results of the phase resolved spectroscopy of each pulsar, and compare their features in Section 4.2.3. The phase resolved Γ and E_c are shown in Figures 4.2–4.5 and listed in Appendix D. We note that the data points used to make Figure 4.5 were taken directly from Table 2 of Abdo et al. (2012) in which the phase resolved parameters of PSR J0007+7303 are listed, hence we do not replicate the table in this thesis.

4.2.2.1 Vela

There is a clear rise in the photon index before the first peak, also observed in the γ-ray (this work) and X-ray (Weisskopf et al. 2011) phase-resolved index of the Crab. There was some evidence for this spectral softening in Abdo et al. (2010b), which we are now able to confirm with our longer dataset. The index reaches a maximum of $\Gamma \sim 1.8$ and then decreases (hardens) through the first peak. The minimum occurs at the phase of the inner peak, P3; the index then rises slowly through the bridge toward the second peak, stays $\sim$constant at $\Gamma \sim 1.5$ through the peak, and rises to a second maximum of $\Gamma \sim 1.86$ at $\phi \sim 0.62$. It falls immediately afterward. The errors on the remaining points are too large to determine whether or not this downward trend continues.

The cutoff energy results match overall with those in Abdo et al. (2010b). The largest values of E_c have decreased slightly, but are consistent within the errors. We

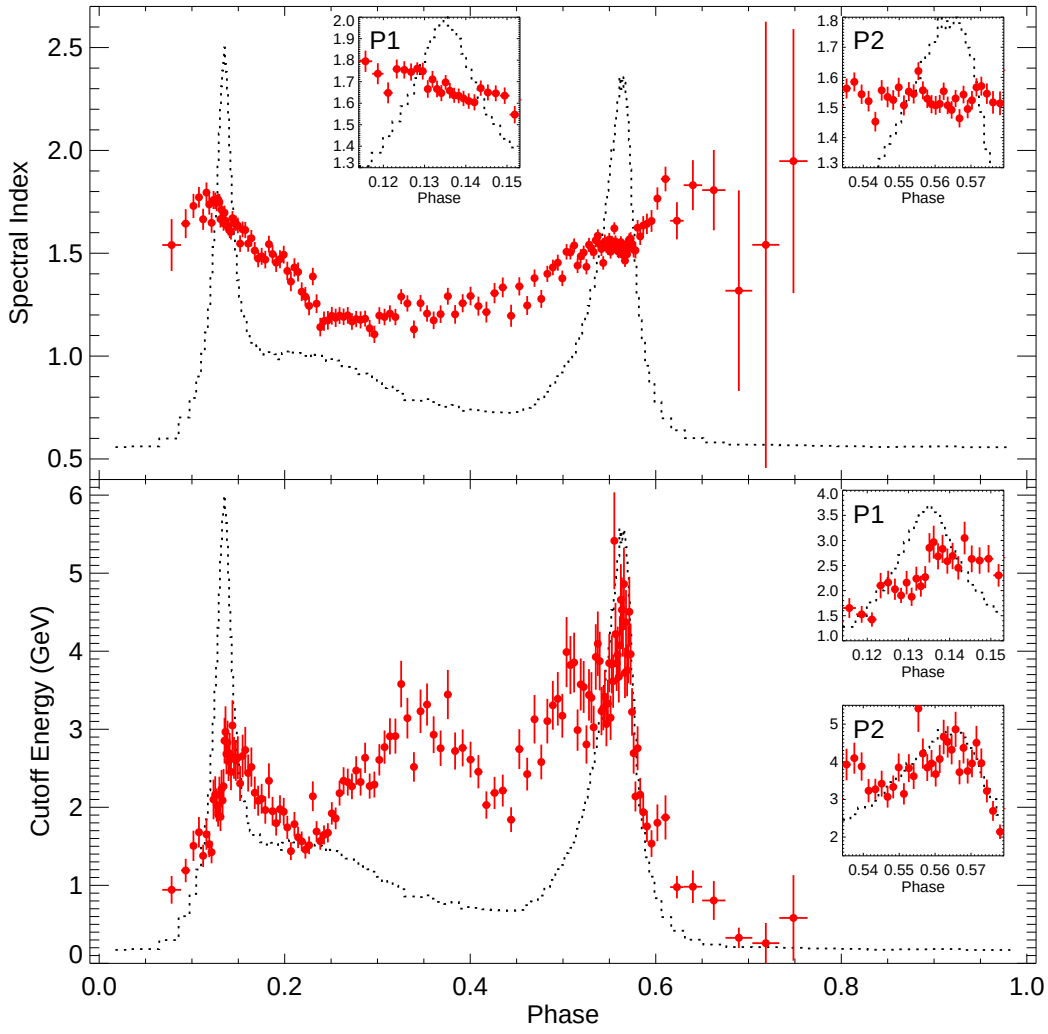

Figure 4.2: The phase resolved spectral index (top) and cutoff energy (bottom) of the Vela pulsar, determined over the energy range of $0.1\,\mathrm{MeV} \leq E \leq 300\,\mathrm{GeV}$. The black dotted lines show the Vela light curve, while the red points show the spectral parameters. Displaying the light curve and spectral parameters together is done to guide the eye, so that one can see what features of the phase-resolved spectra correspond to features in the light curve. The insets show zooms of the peaks for clarity. The spectral parameters, especially the cutoff energy, vary dramatically with pulse phase, with the cutoff energy being highest at the phases of the light curve peaks, especially P2. The phase of the middle peak in E_c is consistent with that of the inner peak in the $> 8.0\,\mathrm{GeV}$ light curve at high energies (Abdo et al. 2010b). A more detailed discussion of the spectral features is given in the text of Section 4.2.1.1.

no longer see a dramatic rise and fall at $\phi \sim 0.1$. E_c rises through P1, declines at $\phi \sim 0.15$, and reaches a minimum at $\phi \sim 0.23$, in the middle of P3. There seems to be some structure in the phase-resolved parameters between $0.25 \leq \phi \leq 0.3$, where the variation in both E_c and Γ appears to be slightly concave down. The phase range of this structure corresponds to the location of P3 in the $> 8\dot{\mathrm{G}}$eV light curves in Figure 2 of Abdo et al. (2010b) (in these light curves, P3 clearly moves to later phase with increasing energy).

E_c varies between 2.5 and 3.6 GeV in the phase range 0.3–0.45, as seen in Abdo et al. (2010b). As noted in that paper, the location of the peak in E_c corresponds to the location of P3 in the 3–20 GeV light curves (again shown in Figure 2 of Abdo et al. 2010b). There is more variation through this structure than was seen previously; for example, the dramatic fall and subsequent rise in E_c between $0.325 < \phi < 0.35$ can also be seen in the photon index. We note that the Crab pulsar may also have a peak in E_c in its bridge emission, though it is not as significant as what is observed for Vela.

From $\phi \sim 0.45$ through P2, E_c increases to a maximum of ~ 5.5 GeV. There are at least three rapid rise-and-fall components in E_c in this phase range. After P2, the cutoff energy decreases to its pre-P1 value, save for another small rise and fall at $\phi \sim 0.6$. Coming out of P2, the photon index increases slightly as E_c is falling, and rises more dramatically along with E_c at $\phi \sim 0.6$. Beyond this phase, both Γ and E_c return to values consistent with those measured before P1. There is definitely interplay between Γ and E_c, and the fact that in most cases they have the same, rather than opposite, behavior suggests that their simultaneous variation is real as opposed to originating from covariance in the two spectral parameters.

4.2.2.2 Crab

As stated in Section 4.2.2.1, the power law index increases prior to P1 in the Crab, matching the behavior seen by Weisskopf et al. (2011) in the X-ray phase resolved spectra. In the peaks of the Crab's light curve, the spectrum gets harder as the cutoff energy increases. This trend may continue in the bridge emission, but the errors are larger there, so it is difficult to make a concrete statement about this. There is a dip-like feature in both index and cutoff in the first peak at the phase of the maximum photon counts; in $E_{\rm c}$, this may be analogous to the rise and fall of $E_{\rm c}$ in Vela's phase resolved spectrum.

In P2, the index reaches its hardest value as the cutoff energy increases to a maximum. At the center of P2, $E_{\rm c} > 10\,{\rm GeV}$, but the error on the measurement is large as well. This large uncertainty on $E_{\rm c}$ may be due to the cutoff energy varying very quickly across the phase bin containing the peak flux, so that if the phase bins were sufficiently small, we would measure a single $E_{\rm c}$ in each bin with high enough counts. In practice, the spectra may be better fit with a sub-exponential cutoff ($b < 1$). A slightly different case is one in which the peak emission is caustic in nature (as predicted by the models we examine in this paper), such that the emission is composed of photons emitted from a large range of radii and therefore samples a blend of cutoff energies at every phase, also resulting in $b < 1$. As an attempt to test the origin of the large error in the measurement, we split the peak phase bin in half and fit the spectra in these bins. We found that the cutoff increases even more in these smaller bins, but the errors increase as well due to the decrease in counts. With current statistics, it is not possible to determine whether or not the cutoff energy is "well-behaved" in much smaller phase bins.

We note that the very high value of $E_{\rm c}$ in P2 may be related to the VHE pulsations discovered by MAGIC (at $E > 60\,{\rm GeV}$) (Albert et al. 2008) and VERITAS

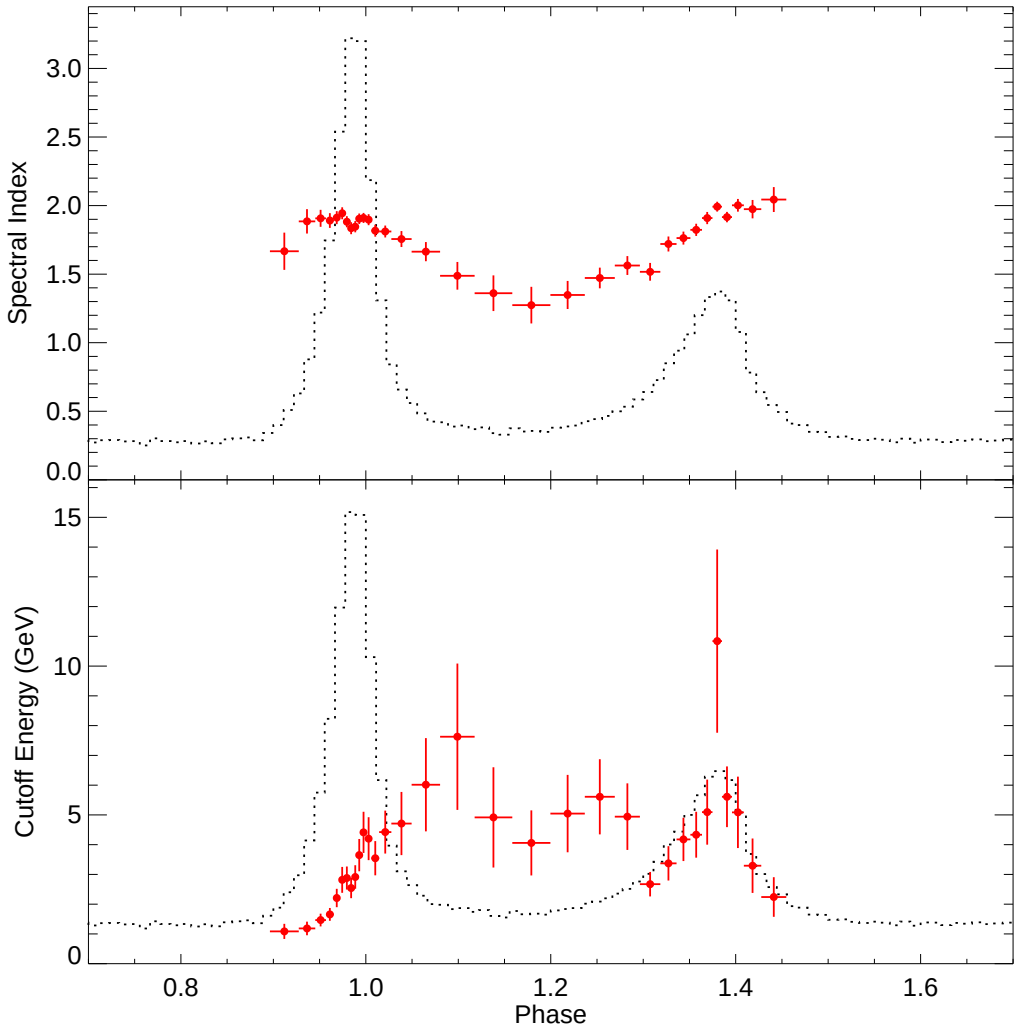

Figure 4.3: The phase resolved spectra parameters, as in Figure 4.2, for the Crab pulsar, discussed in Section 4.2.1.2.

($E > 400\,\mathrm{GeV}$) (VERITAS Collaboration et al. 2011). The VHE peaks are very narrow and are coincident in phase with the highest points in the LAT peaks, and therefore coincident, in P2, with the phase of the largest value of E_c. However, if this high value of E_c is related to the VHE mission, then it is curious that we only see this sudden increase in E_c in P2 and not in P1.

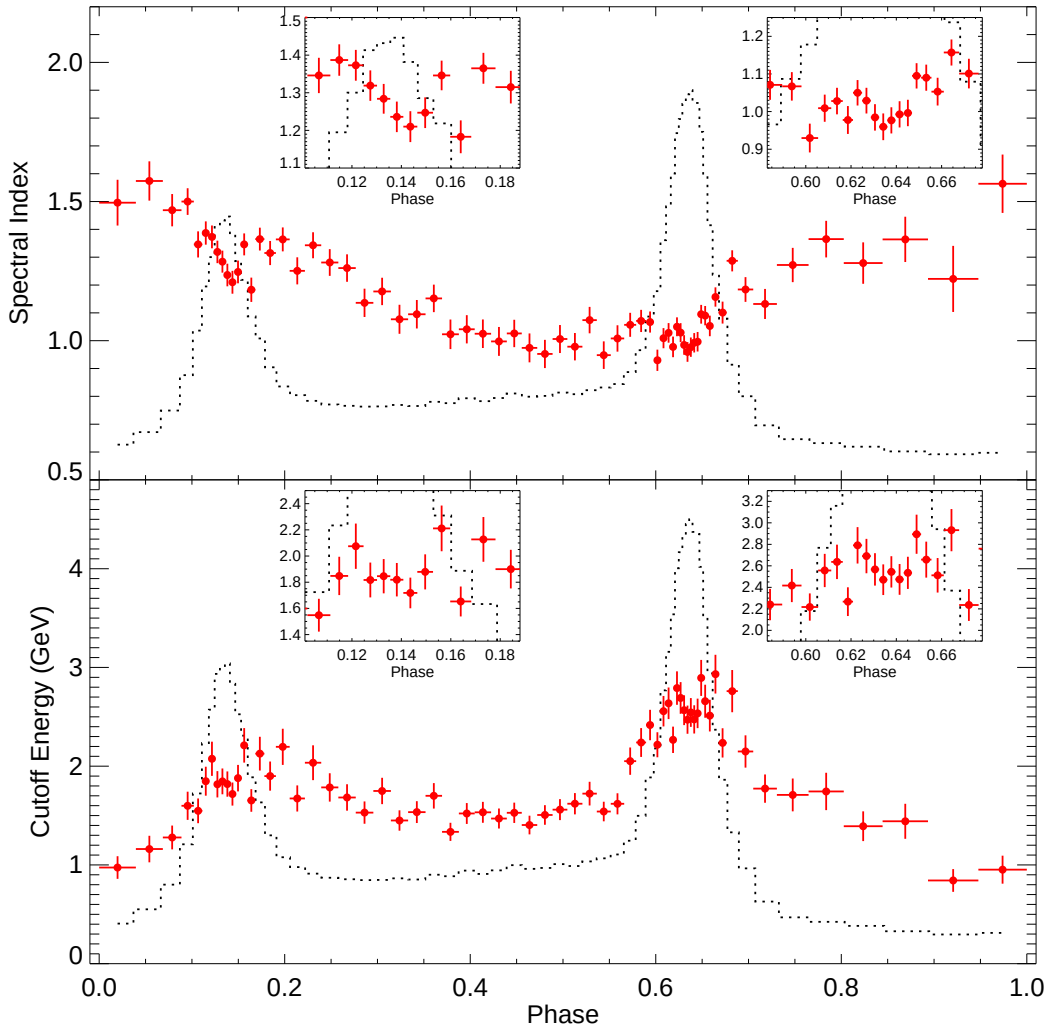

Figure 4.4: The phase resolved spectral parameters of the Geminga pulsar (Section 4.2.1.3), with zooms of the peaks inset in the plot.

4.2.2.3 Geminga

Geminga is the only pulsar of the four considered here for which a cutoff energy can be measured at all rotation phases, meaning that we are observing magnetospheric emission throughout the pulsar's rotation. The values of both Γ and E_c measured before P1 match those after P2, serving as a consistency check considering the arbitrary nature of the phase definition (if the phases were shifted and the spectra

measured in differently defined bins, the results would be consistent with those measured here).

The first peak is softer and has a lower cutoff than the second peak, consistent with the phase resolved spectral results and energy-dependent light curves of Abdo et al. (2010d). The dipping behavior of Γ and E_c seen in the first peak of the Crab is seen even more strongly in Geminga's peaks. The index and cutoff move together, again suggesting the variation is real. The bridge emission hardens from P1 to P2, while the cutoff remains nearly constant (with some variation, mostly within the errors).

4.2.2.4 PSR J0007+7303

This pulsar has significant off-peak emission (Abdo et al. 2012), but the statistics are too poor to determine whether the emission is of magnetospheric or nebular origin. If magnetospheric, the spectrum would be better fit with an exponentially cutoff power law (Equation 4.1) than a power law. Like Geminga, it is radio-quiet to within detection limits (Halpern et al. 2004), but judging from the dissimilar light curve and phase-resolved spectra, the emission and viewing geometries are likely quite different.

The phase-variant spectral parameters shown in Figure 4.5 are taken directly from Abdo et al. (2012); we replot them here for completeness and ease of comparison between figures.

The photon index hardens through the first peak and softens through the second, returning to near the same value after P2 as before P1. Although the peaks are much closer together, the cutoff is still higher in the second peak. This suggests that we are dealing with the same general emission region and mechanism as for the other pulsars, but with a different particular geometry (viewing and/or inclination

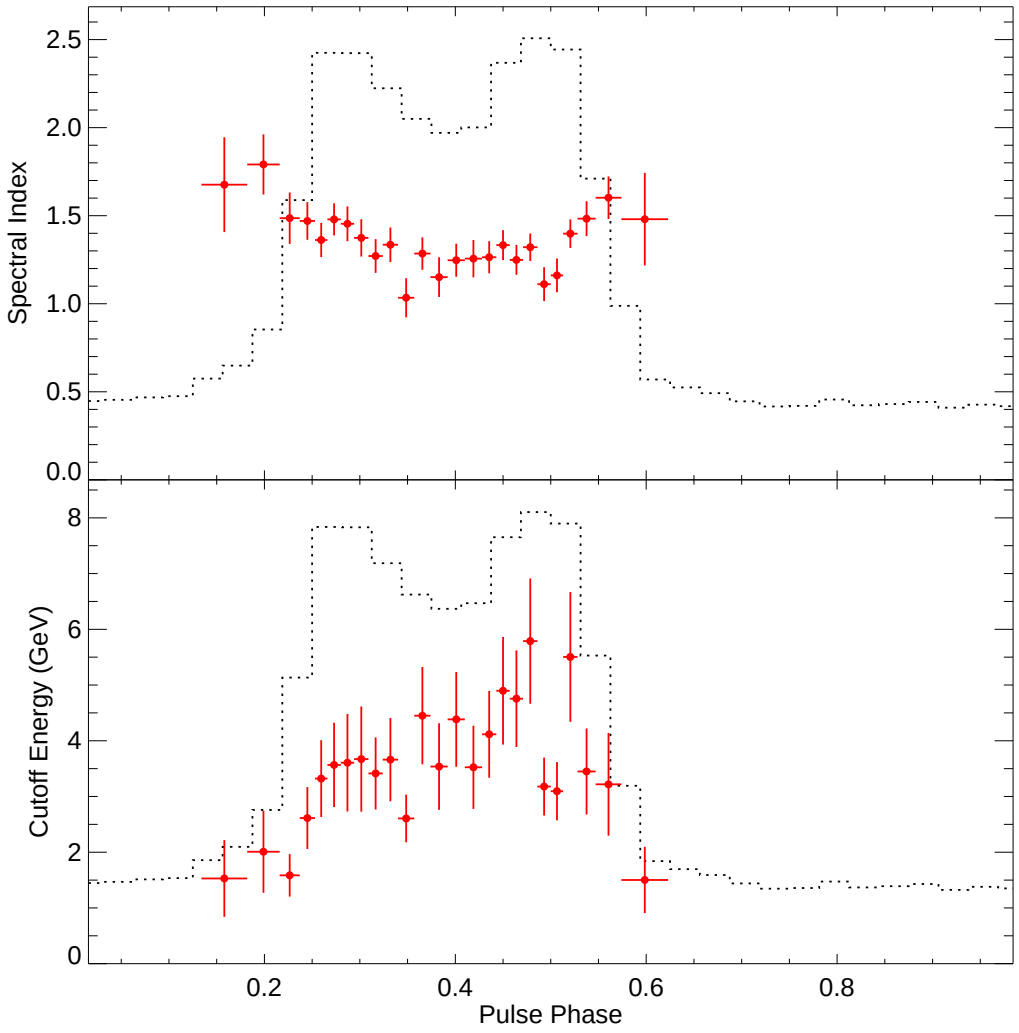

Figure 4.5: The phase resolved spectral parameters of PSR J0007+7303 (Section 4.2.2.4), replotted from Table 2 and Figure 4 of Abdo et al. (2012).

angle). In P2, there is a sudden dip and rise in E_c similar to that seen in the Crab and Geminga pulsars, matched by a smaller but similar variation in Γ, at $0.475 < \phi < 0.525$.

4.2.3 Comparison and Interpretation of Spectral Results

For Vela and Crab, the peaks are softer than the bridge, with a range of $\Gamma = 1.5-1.8$ in Vela's peaks and $\Gamma = 1.6-2.1$ in the Crab's. For Geminga, the peaks are harder or as hard as the bridge; P1 has $1.2 \leq \Gamma \leq 1.4$, and P1 has $0.9 \leq \Gamma \leq 1.2$. It is difficult to say for sure what is peak vs. bridge emission (if there is any) for PSR J0007+7303, but the photon index varies between $1 \leq \Gamma \leq 1.6$ within the phases containing the peak emission, more similar to Geminga than to the two radio-loud pulsars. In all cases, P2 has a higher cutoff energy than P1.

In general, for short-timescale features like dips in the peaks, the index and cutoff move together. There is not a clear trend like this for longer-timescale features, partly because the only pulsar with significant emission outside the peaks and bridge is Geminga. In its case, the index rises as the cutoff falls outside the peaks—there are many fewer high-energy photons outside the peak and main bridge regions. In the bridge, E_c stays nearly constant or falls slightly as Γ falls (hardens). So in the case of Geminga, outside the peaks the emission softens and the cutoff decreases, while within and between the peaks, the emission hardens, the cutoff stays relatively constant, and the parameters move together in short intervals, for example within the dips in the peaks.

As noted in Abdo et al. (2010b), the bridge emission of Vela has a very obvious peak in E_c at $\phi \sim 0.34$, matching the rightmost location of P3 in the energy-dependent light curves of this pulsar (Abdo et al. 2010b). There may be one or two small bumps similar to this in the bridge emission of the Crab (at $\phi \sim 0.24$ and 0.6), though the errors are just large enough for E_c to be consistent with a constant value. There are no structures like this seen in the bridge emission of Geminga or PSR J0007+7303; though for the latter, the statistics are too poor to see small

features in the spectral parameters, and additionally it is difficult to discern the peak from the bridge emission well enough to determine whether such features are present.

There were hints of dipping behavior in Geminga's peaks in Abdo et al. (2010d), but the behavior is quite obvious with our longer dataset. The same behavior is seen in P1 of the Crab, and possibly in P2 of PSR J0007+7303. It is not possible to say whether or not there is a dip in the first peak of PSR J0007+7303 at this time. There may be dipping in Vela's peaks as well; there is definite variation, but it seems more complex than one or two clear dips through each peak, so it may or may not be the same phenomenon seen in the other cases. It is interesting that in the Crab, the first peak has a clear dip at the same phase in index and cutoff energy, but the second peak is completely different—instead of a dip, both parameters increase, especially with the drastic increase in cutoff energy. This leads to the question of whether or not there could be some fundamental difference between the γ-ray production in the two peaks. Both peaks are seen in VHE data, yet the LAT cutoff energy is very high only in P2, suggesting that the cutoff energy measured by the LAT is not necessarily connected to the VHE emission. Alternatively, a power law or a sub-exponential cutoff may give a better fit to the P2 spectrum.

4.3 Geometrical Constraints from Phase Resolved Spectroscopy

Knowledge of the accelerating electric field, $E_{||}$, is needed in order to model the acceleration of charges in pulsar magnetospheres and to calculate the resulting γ-ray luminosities. It is calculated by solving Poisson's equation within the acceleration gap (Muslimov & Tsygan 1992b), which is bounded by surfaces of $E_{||} = 0$ along

the closed field line region and along the inner edge of the gap of width w. Some information on the value of $E_{||}$ can be deduced by comparing observed pulsar luminosities with those predicted from model-dependent $E_{||}$ calculations (Harding et al. 2002), for example those of Harding & Muslimov (2001, 2002).

Because of the excellent sensitivity of the LAT, phase resolved spectroscopy is possible at energies $> 100\,\mathrm{MeV}$, as shown in the previous sections. My collaborators and I suggest that the phase resolved cutoff energies can be used to estimate $E_{||}$ from observational measurements for the first time. In the remainder of this chapter, I describe our method and show how tighter constraints on the emission and field geometries can be obtained by using E_{c} to calculate $E_{||}$.

4.3.1 Calculation of Accelerating Electric Field

In many HE pulsar emission models, the GeV emission is dominated by curvature radiation. The accelerated particles are found to be at the curvature radiation reaction (CRR) limit in both the outer gap (Romani 1996) and slot gap (Muslimov & Harding 2004) models. In this limit, the particles reach a steady-state Lorentz factor (Daugherty & Harding 1982)

$$\gamma_{\mathrm{CR}} = \left(\frac{3}{2}\frac{E_{||}\rho_{\mathrm{c}}^2}{e}\right)^{1/4} \tag{4.4}$$

that is estimated to be $\gamma_{\mathrm{CR}} \sim (2-3)\times 10^7$ for outer magnetosphere models. The cutoff energy of the particles' emission is

$$E_{\mathrm{CR}} = \frac{3}{2}\frac{\lambda}{\rho_{\mathrm{c}}}\gamma_{\mathrm{CR}}^3 = 0.32\lambda_{\mathrm{c}}\left(\frac{E_{||}}{e}\right)^{3/4}\rho_{\mathrm{c}}^{1/2} \sim 1-5\,\mathrm{GeV} \tag{4.5}$$

Thus, $E_{||}$ at a given point along a field line can be estimated with knowledge of the field line radius of curvature ρ_{c} and the cutoff energy of the curvature radiation E_{CR} emitted from that point.

We make two assumptions about the high-energy emission in order to estimate $E_{||}$ within the context of our models: 1) The high-energy emission is dominated by curvature radiation in the radiation-reaction limit. Therefore, $E_{\rm CR} = E_{\rm c}$ from Section 4.2. 2) The optimal set of parameters for each combination of emission (OG, SG, or aSG) and field (VRD or FF) geometries obtained through light curve fitting describes the true geometry of the pulsar's emission region and magnetic field. As described in Section 3.1, the simulations from which we obtained the model light curves also calculate the minimum and maximum emission radii ($r_{\rm min}$ and $r_{\rm max}$) and radii of curvature ($\rho_{\rm min}$ and $\rho_{\rm max}$) sampled by the field lines in each rotation phase bin ϕ.

Rearranging equation 4.5, equating $E_{\rm CR}$ with the measured cutoff energies $E_{\rm c}$ of the pulsars considered in this paper, and equating $\rho_{\rm c}$ with the radii of curvature $\rho_{\rm min,max}$ from the best fit light curve modeling geometries, gives us an equation for $E_{||}$:

$$E_{||} = e \left(\frac{E_{\rm c}}{0.32 \lambda_{\rm C}} \right)^{4/3} \rho^{-2/3} \tag{4.6}$$

The minimum $E_{||}$ sampled in a given phase bin is obtained using the maximum $\rho_{\rm max}$ output by the *toypol* code in that bin, and the maximum $E_{||}$ from the minimum $\rho_{\rm min}$. To obtain the extrema of the magnetic field strength, $B_{\rm min}$ and $B_{\rm max}$, at each ϕ, we re-ran the simulations for the best-fit geometries, and input the measured surface field strengths, spin periods, and period derivatives, listed in Table 4.2. We next discuss our estimates of $E_{||}$ for each pulsar.

Table 4.2. Physical Characteristics of Modeled Pulsars

Pulsar	P (ms)	$\dot{P}$ ($10^{-15}\,\mathrm{s\,s^{-1}}$)	$\dot{E}$ ($10^{35}\,\mathrm{erg\,s^{-1}}$)	B_{S} ($10^{12}\,\mathrm{G}$)	B_{LC} ($10^{4}\,\mathrm{G}$)
Vela	89.4	125.0	69.0	3.322	4.381
Crab	33.6	420.0	4360.6	3.742	95.9
Geminga	237.1	11.0	0.33	1.6	0.113
PSR J0007+7303	315.9	357.0	4.48	10.7	0.313

Note. — P and $\dot{P}$ are the spin period and period derivative of each pulsar, and $\dot{E}$ is the total rotation energy output. These values were taken from the ATNF pulsar catalog (Manchester et al. 2005) and the second *Fermi* LAT pulsar catalog (The Fermi-LAT Collaboration 2013). B_{S} and B_{LC} are the surface and light cylinder magnetic field strengths, and were calculated using Equations 1.5 and 1.12.

4.3.2 Results: $E_{||}$ Estimates

4.3.2.1 Vela

Figure 4.6 shows the results for Vela. Panel (a) provides the observed light curve and cutoff energies to help guide the eye in the plots below. Panels (b) and (c) correspond to the vacuum retarded dipole, and (d) and (e) to the force-free magnetosphere. Results for the outer gap, slot gap, and asymmetric slot gap are shown from left to right.

In panel (b), the minimum and maximum emission radii are plotted respectively as blue and purple dashed lines, while the minimum and maximum radii of curvature are the green and red solid lines. Because the outer gap light curve has zero emission in the first and last two bins with a cutoff energy measurement, the emission and curvature radii in those bins are not plotted here.

The maximum strength of the local magnetic field, B_{max}, is plotted with the blue

line in panel (c), along with the minimum and maximum $|E_{||}|$ ($|E_{||,\min}|$ and $|E_{||,\max}|$, in units of the light cylinder field strength $B_{\rm LC}$ from Table 4.2) in the red and green points, respectively. $|E_{||}|$ was calculated with equation 4.6; the minimum values correspond to the maximum ρ, and maximum to the minimum ρ, from panel (b). $B_{\max}$ was calculated numerically in the light curve simulation code, for which the parameters were the same as the best fit geometrical parameters given in Table 3.2.

In panel (d), the emission radii and radii of curvature are plotted as in panel (b), here for the force-free field geometry. Panel (e) shows $B_{\max}$, $|E_{||,\min}|$, and $|E_{||,\max}|$ for the force-free field. From this point on, $E_{||} = |E_{||}|$ unless otherwise noted.

For an electric field induced by the motion of a magnetic field, the magnetic field strength must exceed that of the electric field. To test our model fits, we compared the $E_{||,\min}$ with the local $B_{\max}$, the latter of which must physically be larger than the induced local parallel electric field. This comparison accounts for the fact that the maximum $E_{||}$ possible in a given phase bin (or at a given radius) may be larger than the local $|B|$, but the true $E_{||}$ may be smaller (as small as $E_{||,\min}$). Comparing the extreme values therefore gives the most room for a given geometrical model to produce physically acceptable values of $E_{||}$.

We find that, for Vela, the necessary condition $E_{||,\min} < B_{\max}$ is just barely satisfied in the OG and aSG geometries of the VRD field (panel c). More realistic would be the scenario where $E_{||,\min}$ lies well below $B_{\max}$. The sSG geometry satisfies this more stringent condition, but as discussed in Section 3.2.1, the parameters of the best sSG fit are thought to be unrealistic. The FF field significantly lowers $E_{||,\min}/B_{\max}$ for the slot gap geometries (panel e). The OG still just meets $E_{||,\min}/B_{\max} < 1$ in the FF case.

These results can also be seen in Figure 4.7, which shows the minimum values of $E_{||}$ (again in units of $B_{\rm LC}$) and the ratio $E_{||,\min}/B_{\max}$ plotted against the minimum

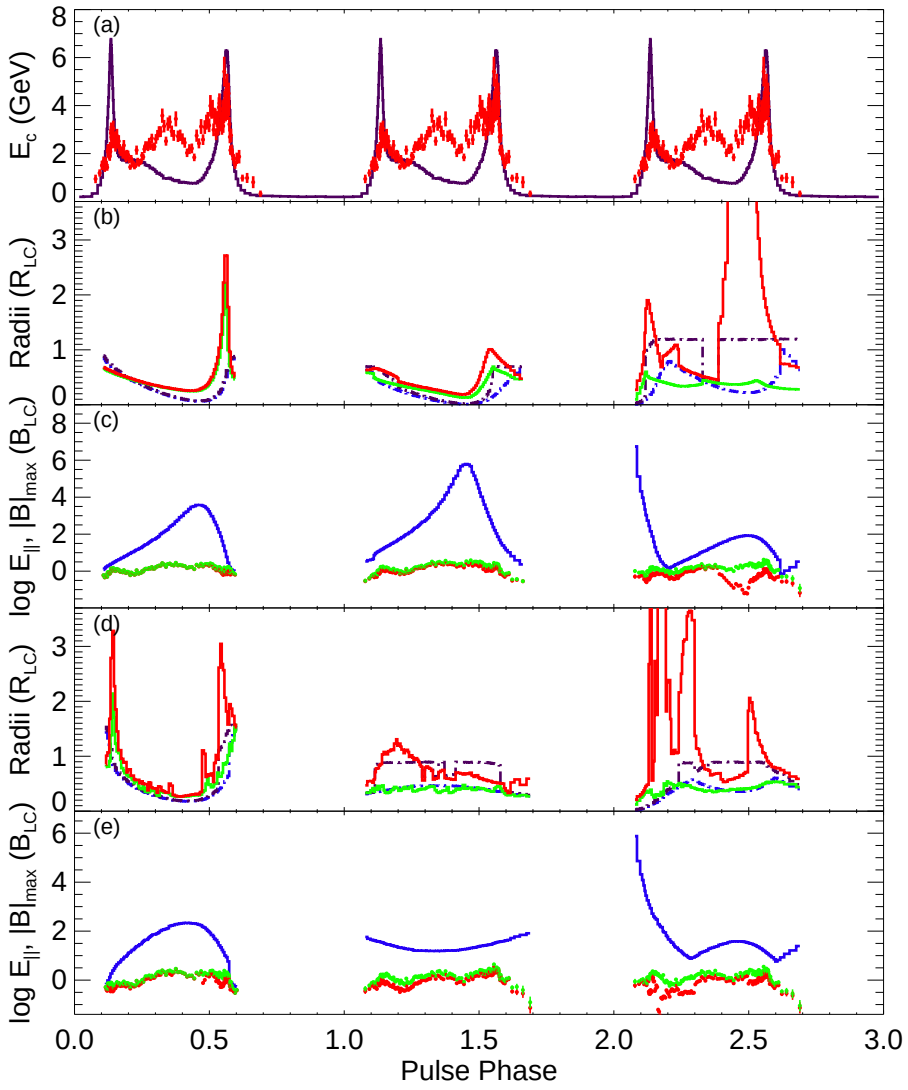

Figure 4.6: Vela: The calculation of $E_{||}$. From left to right, the results in panels (b)-(e) correspond to the OG, SG, and aSG geometries. (a) The phase-varying cutoff energy is plotted in red, with the shape of the LAT profile underlaid in purple to guide the eye. (b) This panel shows the radii output by the toypol code for the VRD field geometry. The minimum and maximum emission radii in each phase bin are plotted respectively in blue and purple dot-dashed lines. The minimum and maximum field line radii of curvature are shown with the green and red solid lines. (c) The maximum $|B|$ in each bin, where the vacuum retarded dipole B field was input to the simulations, is plotted in blue. The maximum and minimum values of $|E_{||}|$, calculated from the cutoff energies in (a) and the minimum and maximum ρ in (b), are plotted in green and red, respectively. (d) Same as (b), for the force-free geometry. (e) Same as (c), for the force-free geometry.

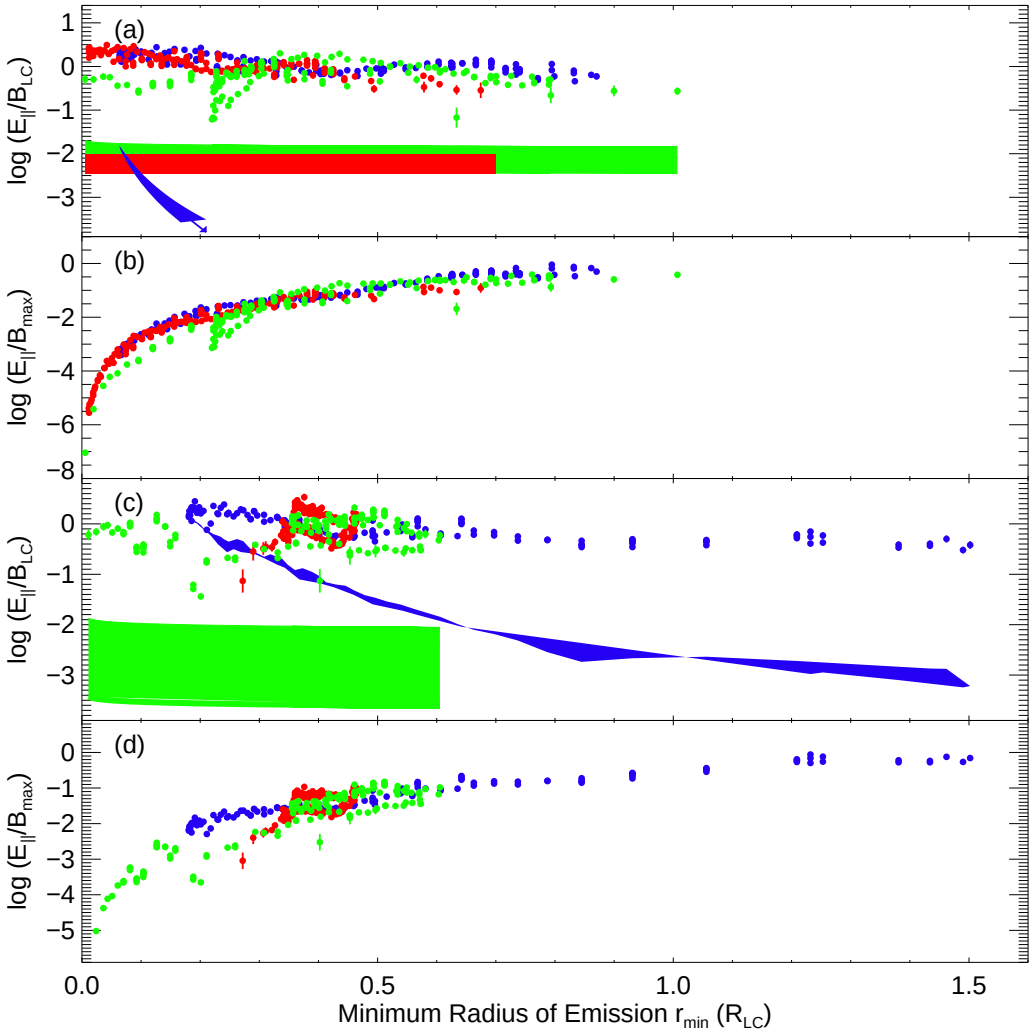

Figure 4.7: The points show the values of $E_{||,\mathrm{min}}/B_{\mathrm{LC}}$ and $E_{||,\mathrm{min}}/B_{\mathrm{max}}$, where B_{max} is the maximum strength of the local magnetic field, for Vela: (a) $\log\left(E_{||,\mathrm{min}}/B_{\mathrm{LC}}\right)$ for the three models in the VRD field; (b) $\log\left(E_{||,\mathrm{min}}/B_{\mathrm{max}}\right)$ for the three models in the VRD field; (c) same as (a), for the FF field; (d) same as (b), for the FF field. In panels (a) and (c), the predicted values of $E_{||,\mathrm{min}}/B_{\mathrm{LC}}$ (see Section 4.3.3) are plotted as colored bands. In each panel, the values corresponding to the OG, sSG, and aSG emission geometries are shown in blue, red, and green, respectively. The blue points with black outlines in panel (a) have been outlined only in order to be visible within the blue band of predicted values. In the y-axis labels, "$E_{||,\mathrm{min}}$" has been shortened to "$E_{||}$" for aesthetic purposes.

emission radius calculated in each light curve phase bin. The $E_{||}$ we obtain is slowly varying with emission radius. The FF field lowers $E_{||,\rm min}/B_{\rm max}$ significantly for the slot gap geometries. The OG in the FF field still has $E_{||,\rm min}$ that is marginally high at radii beyond the light cylinder. It is difficult to compare one geometry to the next, as the parameters are different in each case, hence it is not immediately obvious why the FF field consistently lowers this ratio. Generally speaking, the decrease in $E_{||,\rm min}/B_{\rm max}$ for the sSG and aSG geometries can be explained in part by the fact that the lowest values of $B_{\rm max}$ are larger in the FF field than in the VRD, because B falls off more slowly than $1/r^3$. Also, $\rho_{\rm max}$ tends to have larger values in the FF case because the field lines are straighter than those of the VRD due to current loading, therefore decreasing $E_{||,\rm min}$. Finally, for the particular geometrical parameters considered here, the emission from the FF geometry originates at lower altitudes in the sSG and aSG compared to the emission altitudes in the VRD field, as can be seen in Figure 4.7. This means that the B sampled by the emission regions is stronger in the FF than VRD field.

4.3.2.2 Crab

In Figures 4.8 and 4.9, we clearly see that $E_{||,\rm min} >> B_{\rm max}$ at most rotation phases for all three emission models in the VRD field geometry. $E_{||,\rm min}/B_{\rm max}$ drops dramatically in the FF field. The general explanation is the same as above. The maximum $\rho_{\rm c}$ is larger in the FF case, which lowers $E_{||,\rm min}$; and $|B|$ is larger at a given radius in the FF field than in the VRD. For the particular geometrical parameters considered here, it appears that the former effect of increasing $\rho_{\rm c}$ in the FF field is the main driver in decreasing $E_{||,\rm min}/B_{\rm max}$ from the VRD to FF in the sSG and aSG geometries, as $B_{\rm max}$ does not increase significantly in the FF field in this case.

$E_{||,\rm min}/B_{\rm max}$ is again large but acceptable for the OG model in the FF field.

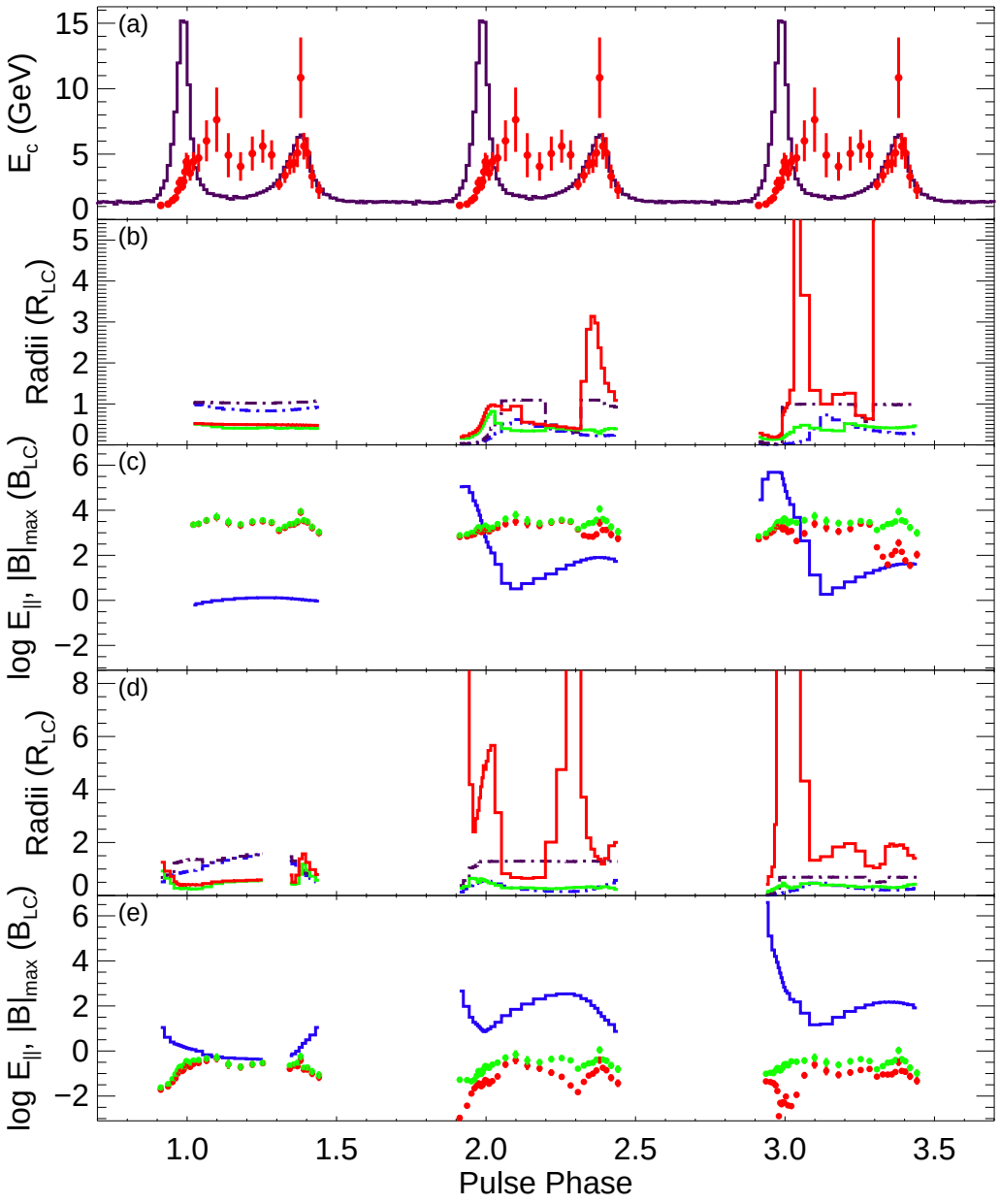

Figure 4.8: Crab: Same as figure 4.6 for the Crab pulsar.

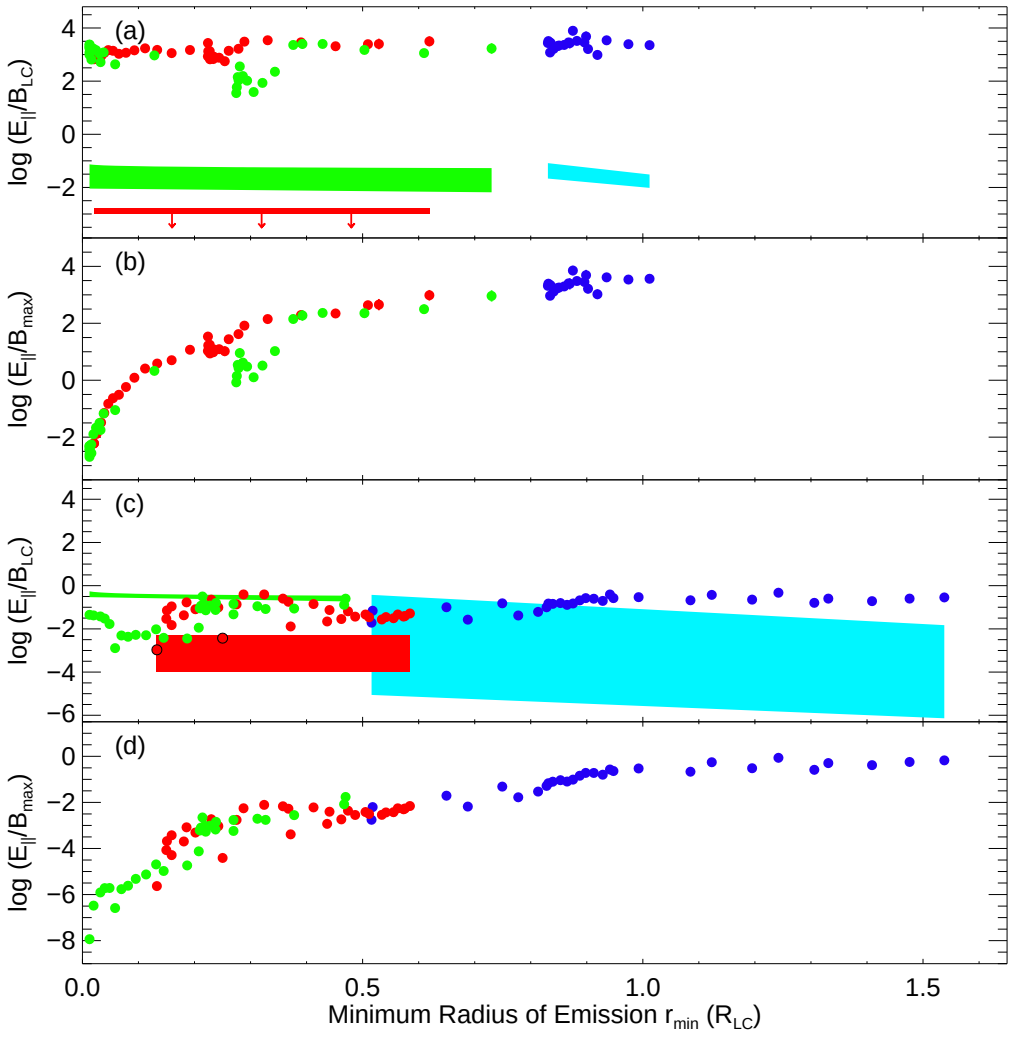

Figure 4.9: Same as Figure 4.7 for the Crab pulsar. The predicted $E_{||}$ are shown in cyan so that the blue OG points in the FF field are still visible.

Because the OG only allows emission at higher altitudes (as opposed to the SG, which allows emission down to the neutron star surface), the magnetic field strength is lower in the OG emission region. This leads to $E_{||,\mathrm{min}}/B_{\mathrm{max}}$ being larger for the OG than the SG. Neither ρ_{max} nor B_{max} changed substantially from the VRD to the FF field in the OG geometry, for the best fit parameters of the Crab; the small increase in ρ_{max} in the FF field did decrease $E_{||,\mathrm{min}}$ just enough to be physically possible.

For the SG geometries in both fields, the maximum ρ_c seems to peak near the light curve and E_c peaks. This is slightly suggestive of a more direct relationship between ρ_c and E_c. A similar relationship is seen for the Vela SG models.

In Figure 4.9, $E_{||}$ is fairly constant with r_{min} for the VRD case (panels a and b), but increases slightly with r_{min} in the FF field (c and d). The dramatic drop in $E_{||,min}/B_{max}$ can again be seen between the VRD and FF fields.

4.3.2.3 Geminga

The reduction of $E_{||,min}/B_{max}$ by the FF field is less dramatic, though still present, for Geminga. In Figure 4.10(c), $B_{max} < E_{||,min}$ in the VRD/OG geometry, and B_{max} dips below the minimum and maximum values of $E_{||}$ in the VRD/SG geometries. The models have very different best fit parameters in the FF case, which makes it difficult to compare with the VRD geometries. In the FF field, $E_{||,min} < B_{max}$ at all ϕ for the SG models, but $E_{||,min} > B_{max}$ at most phases for the OG model (Figure 4.10(e)).

In the SG models of both the VRD and FF fields, we see some correlation between the locations of the peaks in the γ-ray light curve, E_c, and ρ_{max}, as was also noted in the Crab results in the previous section. In the VRD case, the peaks also show up in ρ_{min}, though they are lower. In the FF aSG case, the dips in the centers of the ρ_{max} peaks may be connected with the dips in the peaks of E_c.

We again find $E_{||,min}$ varying slowly with emission radius in Figure 4.11. The two sets of slot gap model parameters in the VRD field are nearly identical because the best fit α and ζ values are almost the same, so the values of $E_{||,min}$ for the sSG and aSG (red and green) also have almost identical values in panel (a). Panels (b) and (d) show $E_{||,min}/B_{max}$ reaching much higher values in the OG model than in the SG models. $E_{||}$ has similar values in the VRD and FF geometries, as one can see

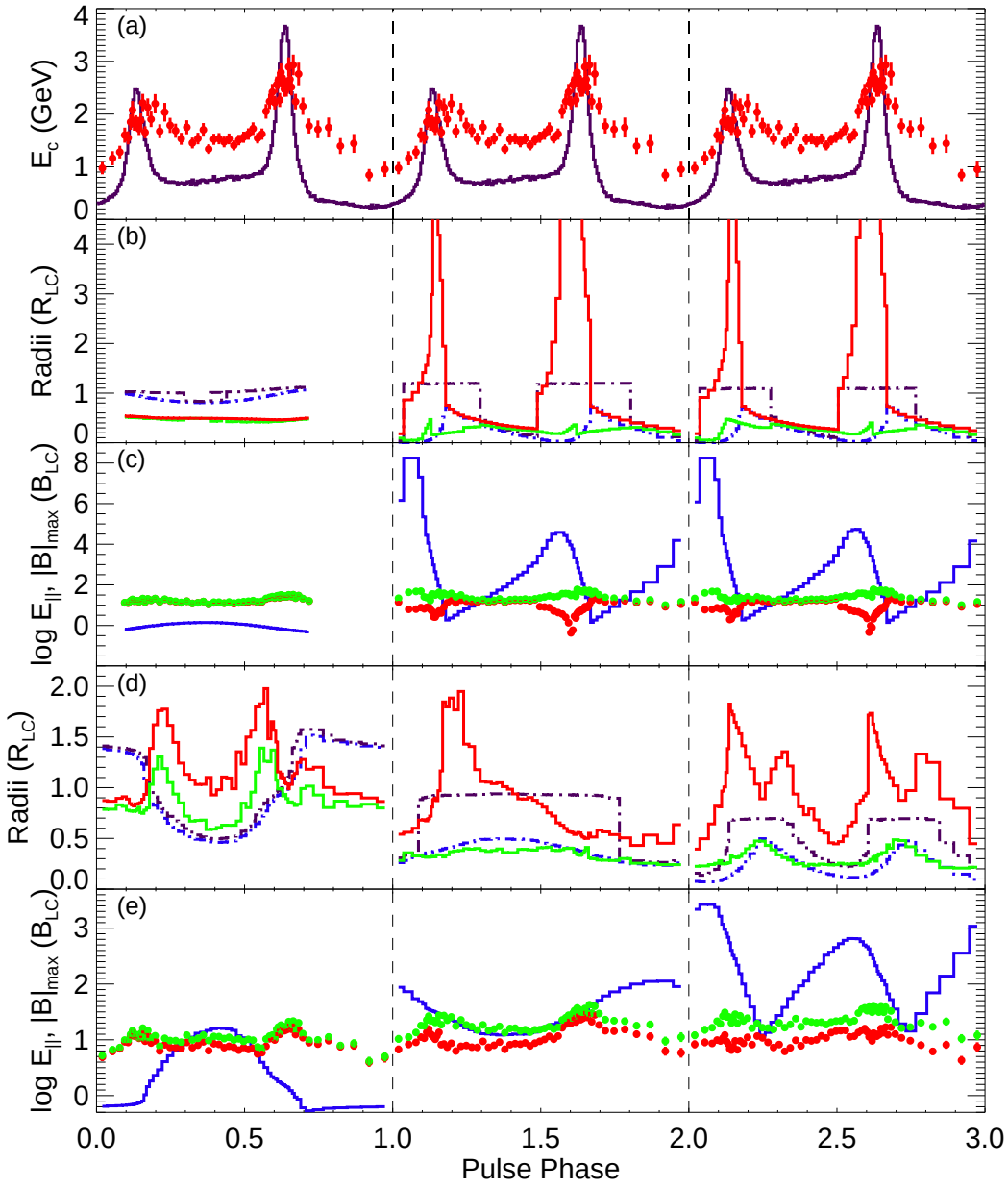

Figure 4.10: Same as figure 4.6 for the Geminga pulsar.

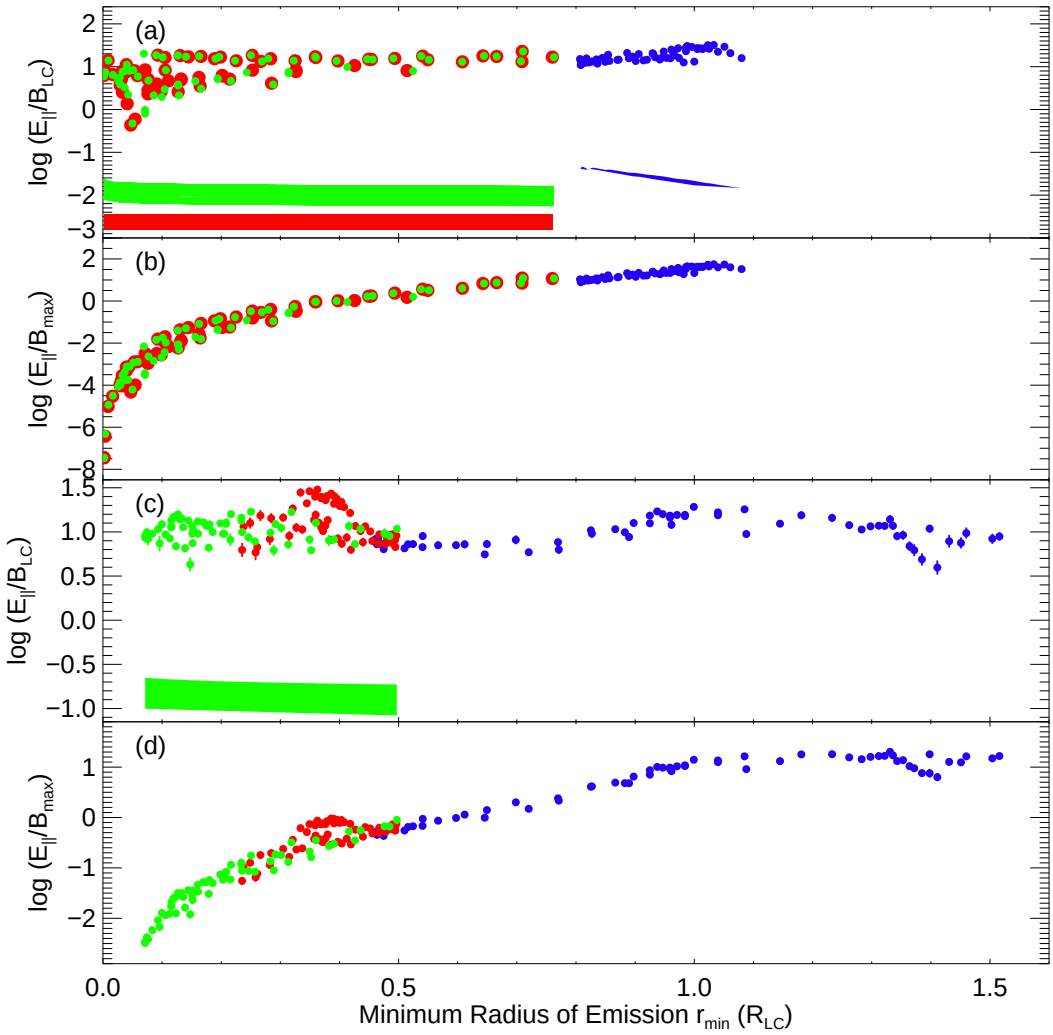

Figure 4.11: Same as Figure 4.7 for the Geminga pulsar. The range of $E_{||}$ is not shown for the FF sSG model in panel (c) because it lies too far below the other points on the plot: $-6.6 \leq \log\left(E_{||,\mathrm{min}}/B_{\mathrm{LC}}\right) \leq -3.4$ for the FF sSG model.

from panels (a) and (c). The drop in $E_{||,\mathrm{min}}/B_{\mathrm{max}}$ seen in the SG geometries of the FF field is caused by a decrease in both B_{max} and $E_{||,\mathrm{min}}$, along with an increase in the minimum values of B_{max}, seen in panels (c) and (e) of Figure 4.10.

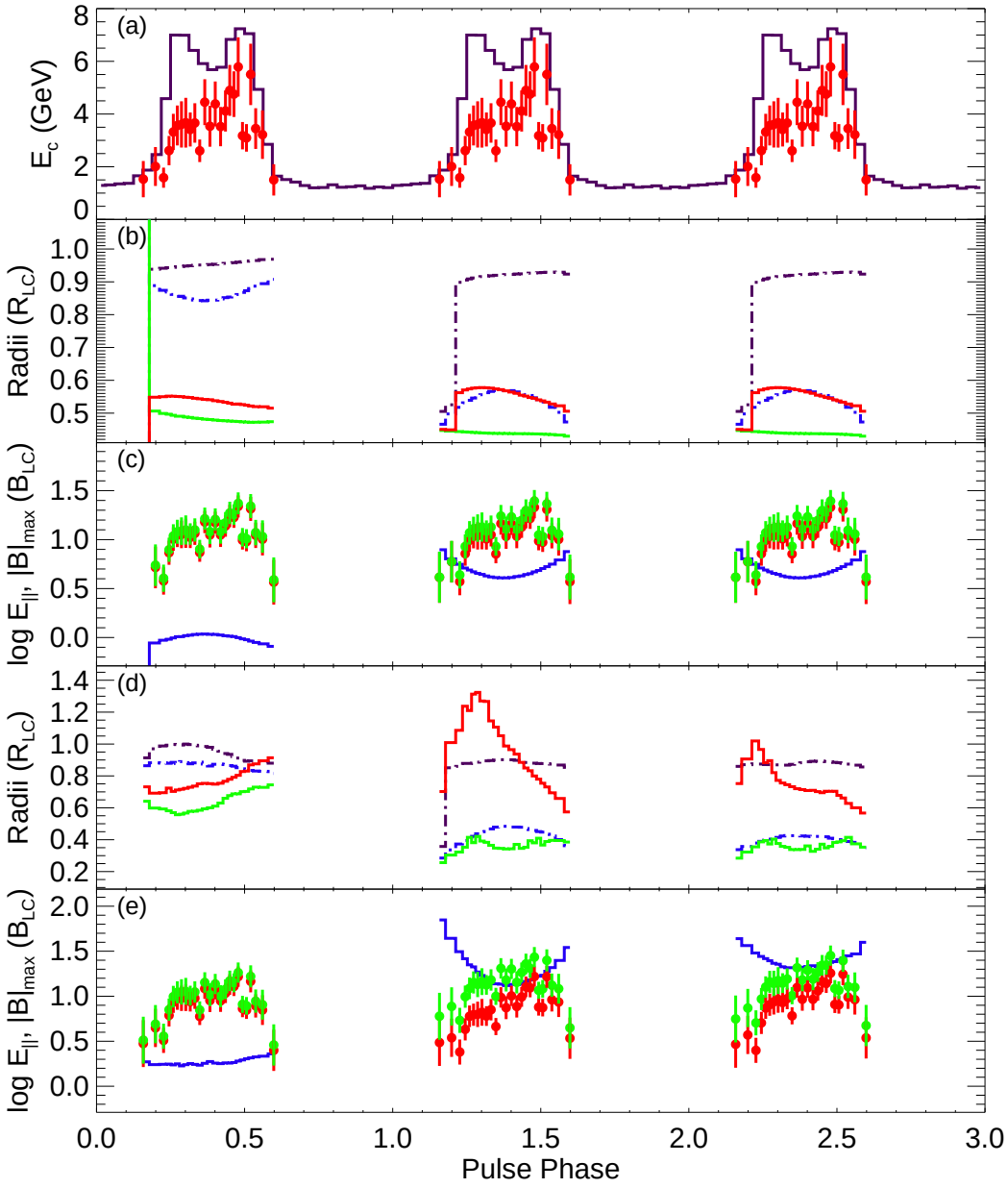

Figure 4.12: Same as figure 4.6 for PSR J0007+7303.

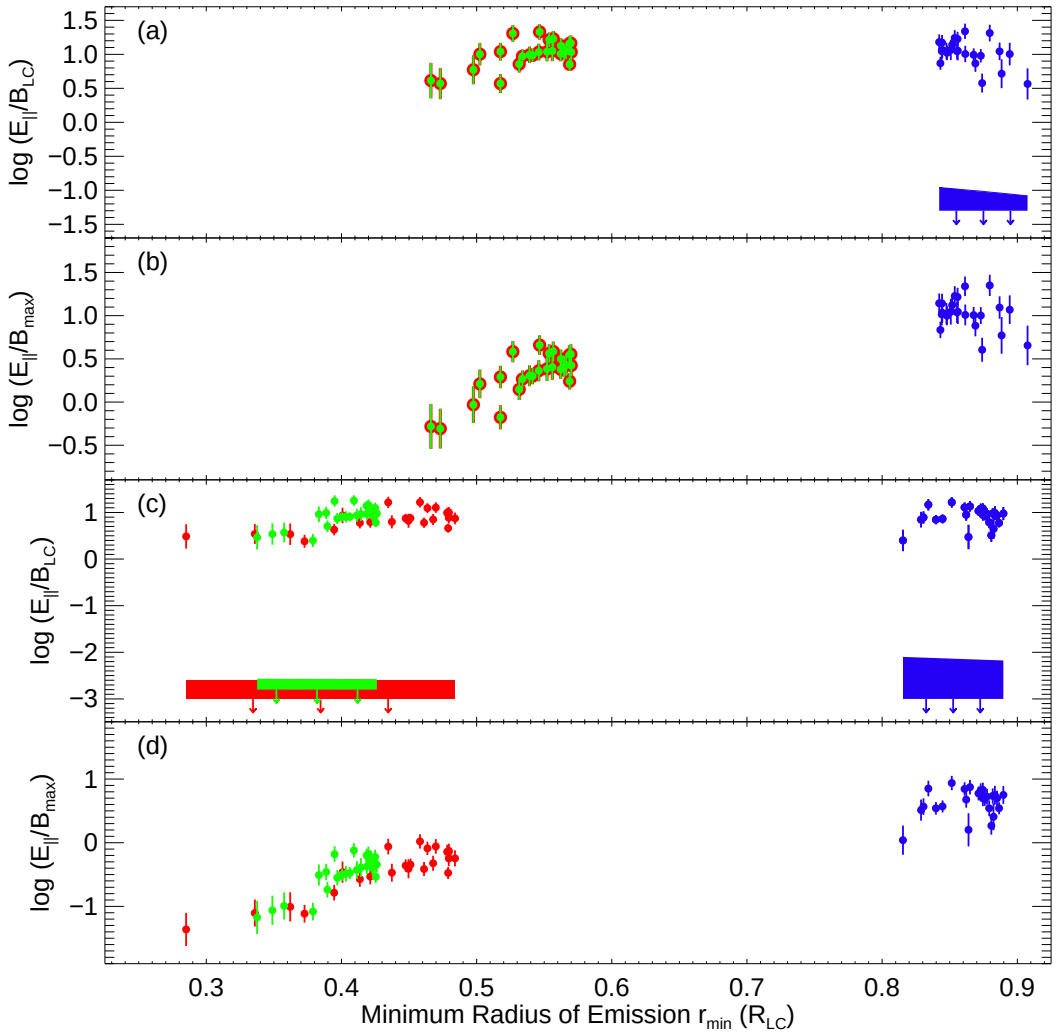

Figure 4.13: Same as Figure 4.7 for the CTA 1 pulsar.

4.3.2.4 PSR J0007+7303

In the case of the pulsar in the CTA 1 supernova remnant, the values of $E_{||}$ change little from the VRD to FF field in panels (c) and (e) of Figure 4.12, but $B_{\rm max}$ increases in the FF field. This increase in $B_{\rm max}$ results from emission being produced at lower radii in the FF field (Figure 4.12, panels (b) and (d), and Figure 4.13). The maximum $\rho_{\rm c}$ also increases from the VRD to FF fields in the SG geometries, lowering the minimum of $E_{||}$ with which we compare $B_{\rm max}$ in Figure 4.13. The emission radii

are lowered in the FF field, causing the increase in $B_{\rm max}$. Only the aSG geometry in the FF field meets the requirement that $E_{||,\rm min}/B_{\rm max} < 1$.

4.3.3 Comparison of $E_{||}$ Estimates with Theoretical Values

Previous calculations of $E_{||}$ in the vacuum field geometry include those of the outer gap (Cheng et al. 1986a; Hirotani 2008), of the azimuthally symmetric slot gap (Muslimov & Harding 2004), and of the azimuthally asymmetric (offset dipole) slot gap (A. Harding, private communication; Harding & Muslimov 2011b). Except for the comparison of my OG results with Hirotani (2008), I used analytic expressions for all of the calculations of predicted $E_{||}$.

For the OG model, Cheng et al. (1986a) derive the parallel electric field to be

$$E_{||,\,\rm OG} \approx \frac{\Omega B}{c\rho_{\rm c}}\, a^2, \tag{4.7}$$

where $\Omega = 2\pi/P$ is the angular spin frequency, P is the pulsar spin period, $B = B(r)$ is the local magnetic field strength at radial distance r, $\rho_{\rm c}$ is the radius of curvature of the magnetic field line along which $E_{||}$ is evaluated, $a = wR_{\rm LC}$ is a physical gap thickness, and w is the dimensionless width of the gap, measured as a fraction of the polar cap radius, for which I use the best-fit OG gap widths from Table 3.2. Using $R_{\rm LC} = c/\Omega$, this expression reduces to

$$E_{||,\,\rm OG} \approx \frac{Bw^2}{\rho_{\rm c}/R_{\rm LC}}\ . \tag{4.8}$$

Note that $E_{||}$ is dependent on r in this expression, as both B and $\rho_{\rm c}$ vary with radius from the neutron star.

For the sSG model, Muslimov & Harding (2004) calculate the value of $E_{||,\rm high}$ at large radii and connect it to the value at smaller radii, $E_{||,\rm low}$ (Muslimov & Harding 2003). They find that for $\alpha = 45°$, the altitude where $E_{||,\rm high}$ and $E_{||,\rm low}$ are smoothly

connected is $\sim 1.4R$, very close to the star's surface and below the emission radii of our simulations in most cases. We therefore compare our calculated $E_{||,\rm min}$ only with $E_{||,\rm high}$ from Equation 54 of Muslimov & Harding (2004),

$$E_{||,\,\rm sSG} \approx \frac{1}{4}\left(\frac{R}{R_{\rm LC}}\right)^3 B_{\rm S}\, w^2, \tag{4.9}$$

where $B_{\rm S}$ is the surface magnetic field strength, given in Table 4.2, R is the neutron star radius, $R_{\rm LC}$ is the light cylinder radius, and w is the best-fit sSG gap width from Table 3.2.

The predicted value of $E_{||}$ varies with azimuth angle ϕ around the polar cap in the aSG model. The light curve peaks are produced from emission on the trailing side, where the angular distance from the dipolar magnetic pole is largest and $E_{||}$ reaches its maximum value; in the coordinate system of Harding & Muslimov (2011a,b) and this work, $E_{||}$ is maximum at the polar cap angle $\phi = 270°$. The value of $E_{||}$ can be approximated by

$$E_{||,\,\rm aSG} \approx \mathcal{E} E_{||,\,\rm sSG}, \tag{4.10}$$

$$\mathcal{E} = \frac{x^a}{(1+a)^2}, \tag{4.11}$$

where $\mathcal{E}$ is the ϕ-dependent emissivity of the gap, $x = r/R_{\rm LC}$, $a = \epsilon \sin\phi$, and ϵ is the offset parameter of Harding & Muslimov (2011a,b). Note that for $r = R_{\rm NS}$, Equation 4.11 reduces to Equation 3.5, since $\theta_{\rm PC} \approx (R_{\rm NS}/R_{\rm LC})^{1/2}$.

The offset parameter ϵ is determined from the amount $\Delta r_{\rm PC}$ by which the polar cap is offset from the center of the star (Equation 3.6); $\Delta r_{\rm PC}$ is found from the numerical calculation of the polar cap rim in the light curve simulations. At $\phi = 270°$, $\Delta r_{\rm PC}$ and ϵ are at their maximum values, and $a = -\epsilon$. The value of ϵ, and hence a, was calculated from $\Delta r_{\rm PC}(\phi = 270°)$ in the light curve simulations using Equation 3.6; its absolute value increases with increasing magnetic inclination α,

and is larger in the FF field than the VRD field for the same α. To plot bands of $E_{||,\rm min}$ for the aSG model as in Figure 4.7, I used $r = r_{\rm min}$ from the models. The value of $\mathcal{E}$ used to plot the predicted $E_{||,\rm min}/B_{\rm LC}$ in these figures, for the aSG geometry, was therefore calculated as

$$\mathcal{E} = \left(\frac{r_{\rm min}}{R_{\rm LC}}\right)^{-\epsilon} \frac{1}{(1-\epsilon)^2} \ . \tag{4.12}$$

I calculated $E_{||}$ predicted by the above analytic expressions for each of the four pulsars, in each emission and field geometry. In Figures 4.7, 4.9, 4.11, and 4.13, I have plotted the ranges of the predicted $E_{||,\rm min}/B_{\rm LC}$ for each model. Where applicable, $E_{||}$ was calculated using $\rho_{\rm max}$, $B_{\rm max}$, w, and/or ϵ corresponding to the best-fit model light curve. The ranges of $E_{||}$ values result from the fact that there is a range of gap widths w for which I calculated $E_{||}$. I have, in effect, ignored the confidence intervals of the other three parameters, as I am only considering how $E_{||}$ may change with gap width under the assumption that the other best-fit geometrical parameters are correct; note that the range of $E_{||}$ presented here is narrower than it would be if all parameters were varies. In models with $w = 0$, I used $w = 0.001$ to calculate $E_{||}$. For all of the models, a larger w will result in a higher $E_{||}$. For the same w, the aSG model will yield a higher $E_{||}$ compared to that of the sSG model.

One consideration specific to the OG model is that the predicted $E_{||}$ depends on $\rho_{\rm c}$ and $B_{\rm local}$, and its values may change depending on whether the minima or maxima of these parameters are used. I first calculated $E_{||}(\rho_{\rm c} = \rho_{\rm max}, B = B_{\rm max})$ for the OG model, where $\rho_{\rm max}$ and $B_{\rm max}$ were numerically calculated in the light curve simulations. The $E_{||}$ evaluated at these values of ρ and B corresponds to $E_{||,\rm min}$. I also calculated $E_{||}(\rho_{\rm c} = \rho_{\rm max}, B = B_{\rm min})$, and found there was very little difference between these and the former values of $E_{||}$. Because I have plotted $E_{||,\rm min}$ against $r_{\rm min}$ in the aforementioned figures, I chose to use $E_{||}(\rho_{\rm max}, B_{\rm max})$ for this comparison. I note that I could also have calculated $E_{||}(\rho_{\rm min}, B_{\rm max})$ and $E_{||}(\rho_{\rm min}, B_{\rm min})$; these

would be more appropriately compared with $E_{||,\max}$, which is not plotted.

I find that for all of the pulsars, except the Crab in the FF field, the predicted values of $E_{||}$ are orders of magnitude lower than the measured values. ("Measured" values of $E_{||}$ refer to those calculated using E_c from the phase resolved spectroscopy and $\rho_{\max}$ from the best-fit geometrical light curve parameters, while "predicted" values refer to $E_{||}$ as calculated from Equations 4.8, 4.9, and 4.11.) This finding is consistent with the under-prediction of γ-ray luminosities, calculated from e^-e^+ pair multiplicities in acceleration gaps, compared to those measured by the *Fermi* LAT (e.g., Harding & Muslimov 2011a).

The predicted and measured $E_{||}$ values are consistent for the Crab pulsar for all emission geometries in the FF field. The Crab is the youngest of the four pulsars considered here, and it differs from the others in several ways. It is 100 times more energetic than Vela, with $\dot{E} \sim 4.4 \times 10^{38}\,\mathrm{erg\,s^{-1}}$ compared to Vela's $\dot{E} \sim 6.9 \times 10^{36}\,\mathrm{erg\,s^{-1}}$; PSR J0007+7303 and Geminga have still lower $\dot{E}$ values (Table 4.2). Its pulses are aligned across the electromagnetic spectrum, implying co-location of the emission regions at all wavelengths. It is also the only pulsar currently known to display pulsations at $> 100\,\mathrm{GeV}$ (Albert et al. 2008; VERITAS Collaboration et al. 2011). It is interesting to find agreement in $E_{||}$ only for the case of this already unique pulsar.

In addition to the agreement in $E_{||}$, the model light curves in the FF geometry reproduce most of the qualitative features of the Crab light curve, the geometrical parameters are similar for the three emission geometries in the FF field, and the best-fit ζ agrees with the independent measurement from Ng & Romani (2008). Together with the $E_{||}$ results, these findings suggest that the Crab pulsar has a near-force-free magnetosphere in which narrow acceleration gaps form. It may be that models invoking narrow acceleration gaps are more applicable to the Crab than to the other

older pulsars considered here. The consistency between the predicted and measured $E_{||}$ also lends support to the assumption that the Crab's γ-ray emission in the LAT energy range is dominated by curvature radiation in the CRR limit, such that it is valid to estimate $E_{||}$ from Equation 4.6. The origin of the higher-energy emission at $E > 100\,\mathrm{MeV}$ is not clear, but may be another mechanism, perhaps synchrotron self-Compton. The lack of consistency in $E_{||}$ for the other pulsars suggests that for those objects, the assumption of CRR is not valid, and/or that narrow gap models do not work as well for older pulsars, perhaps because their fields are farther from force-free. Recently, Breed et al. (2013, in preparation) have found that CRR is not reached in the magnetosphere of Vela due to a low $E_{\|}$, supporting our findings that only pulsars as energetic as the Crab may accelerate particles to the curvature radiation reaction limit.

4.4 Discussion

4.4.1 Phase Resolved Spectra

We modeled the phase-resolved spectra of each pulsar in fixed count bins with ~ 3000 counts per bin. The phase-varying Γ and E_{c} are shown in Figures 4.2–4.5.

We find, consistent with previous results, that the cutoff energy is highest in the light curve peaks. Vela, and the Crab to a lesser extent, has a peak in the cutoff energy within the bridge emission that corresponds to the location of P3, the third light curve peak, above 3 GeV. The second Crab peak has a very high cutoff energy with a large error bar. When we split this phase bin in two and fit the spectra of each bin individually, the cutoff energy and error both increased. This is suggestive of a large variation in E_{c}, and a very high maximum value, within the second peak, perhaps connected to the $> 400\,\mathrm{GeV}$ emission observed by VERITAS.

A feature which has come out of modeling these pulsars with improved statistics is the dipping behavior observed in the first peak of the Crab, both peaks of Geminga, and at least the second peak of PSR J0007+7303. In these peaks, both the index and the cutoff energy rapidly decrease in value and then return to their pre-dip value. This behavior was not observed previously, simply due to the lower number of counts available in earlier analyses. It is not clear if the dips are physical or artifacts of inadequate spectral fitting. It will be necessary to model the phase-resolved spectra of more pulsars with high counts to see if this dipping behavior is a physical feature of pulsar emission, and if it is common in other pulsars.

Finally, we have modeled the phase-resolved spectra with the assumption that within a small enough phase bin, $b = 1$. This is satisfactory for the current spectra, given the number of counts available. However, if E_c is changing very rapidly, or if within a single bin the true spectrum is a blend of many different spectral shapes, with improved statistics we may find that even in small phase bins, $b < 1$; we discuss this further in Section 4.4.2. We note that the choice of b may contribute to the dipping behavior discussed above if the dips are related to caustic emission, which naturally requires $b < 1$ due to a wide range of E_c. Fitting the phase resolved spectra with $b \neq 1$ is another test that must be done on these bright pulsars as the *Fermi* mission continues to collect data in the coming years.

4.4.2 $E_{||}$ Estimation

In radiation models of pulsar emission, the strength of the accelerating electric field $E_{||}$ must be calculated from Poisson's equation with assumed boundary conditions in order to obtain light curves and spectra. In this paper, we have instead used purely geometrical models combined with LAT observations to obtain estimates of $E_{||}$. Using the measured spectral cutoff energies plotted in Figures 4.2–4.5 and the

simulated emission and curvature radii from the best fit parameters of each model geometry, and assuming curvature radiation reaction, we calculated the (phase- and emission radius-varying) magnitude of $E_{||}$ (Equation 4.6) for each of the four pulsars considered in this paper.

We find that $E_{||,\rm min}/B_{\rm max} > 1$ for all emission model geometries in the VRD field, and also for the OG emission geometry in both VRD and FF field structure, except for the Vela pulsar (for which $E_{||,\rm min}/B_{\rm max} \simeq 1$ in the VRD geometry). The OG emission takes place at higher altitudes than in the SG geometries; the magnetic field strength is lower at these large emission radii, allowing $E_{||,\rm min} > B_{\rm max}$.

There are two effects that cause $E_{||,\rm min}/B_{\rm max}$ to decrease from the VRD to FF field. First, $B_{\rm max}$ in FF magnetospheres falls off more slowly with radius than the dipolar $1/r^3$ (Spitkovsky 2006, Figure 1c). $B_{\rm max}$ is therefore larger at a given emission radius in the FF case than it would be in the VRD. Secondly, the poloidal field lines in the FF field are straighter than in the VRD field (e.g., Figure 1a in Spitkovsky 2006), resulting in a larger radius of curvature $\rho_{\rm c}$ of the field lines. Assuming the γ-ray-emitting particles satisfy curvature radiation reaction, a larger $\rho_{\rm c}$ will lower $E_{||}$ (equation 4.6). This indicates that physically, the field lines of pulsar magnetospheres cannot be as curved as in the VRD field. An interesting potential outcome of this is that, for a given $E_{||}$, as particles are accelerated in the FF field, they lose less energy to radiation. They may therefore be accelerated to larger energies, and to larger Lorentz factors—the γ for curvature radiation reaction may be larger in the FF field than in the VRD, producing higher $E_{\rm c}$.

As discussed above, the light curve fits do not favor a particular combination of emission and field geometry. Especially interesting is that in some cases, the best fit light curve is simulated from the VRD field, both in terms of the pulse profile shape and the phase lag δ. The pulsar magnetosphere certainly does not satisfy

the conditions of the ideal force-free magnetosphere, and it may be that in at least some cases, the field is actually closer to a vacuum retarded dipole than to the force-free field. With a small amount of current, the field lines become considerably straighter than in the VRD (Spitkovsky 2006). Additionally, Harding et al. (2011) find that the phase lag $\delta_{\rm pole}$ between the model magnetic pole and the first γ-ray peak increases as the field structure is shifted from VRD to FF. This would explain how the light curves could appear closer to what is expected from the VRD field, and δ could be consistent with observations, while $\rho_{\rm c}$ could still reach large enough values to satisfy $|E_{||}| < |B|$ locally.

The radius of curvature tends to reach its largest values at the phases of the light curve peaks, and also has the largest range of values at these phases. In particular, we find that the geometrical model parameters that best reproduce the observed light curves also result in $\rho_{\rm max}$ and $E_{||}$ peaking where the light curve peaks as well. This can be understood by the caustic nature of the emission in the peaks—these photons are emitted over a large range of emission heights, and the particles from which they were emitted therefore sampled a large range of $\rho_{\rm c}$. The observed spectral cutoff energies therefore result from a blend of curvature radii. Such an effect is observed in phase-averaged spectra: The measured $E_{\rm c}$ is really a blend of many different cutoff energies (e.g., Abdo et al. 2010b), resulting in a sub-exponential ($b < 1$) cutoff power law as the best fit spectral model. For caustic emission, even the narrowest of phase bins contains photons from many different locations in the magnetosphere, and therefore samples many different $\rho_{\rm c}$ and $E_{\rm c}$ (where we assume here that $E_{\rm c} = E_{\rm CR}$). We would therefore expect that even for small phase bins, phase resolved spectra should reveal $b < 1$ for emission in the peaks. With better statistics, we can begin to test this hypothesis.

4.4.3 $E_{||}$ in the Context of Theoretical Predictions

In each of the gap models considered here, $E_{||} \propto Bw^2$, where B may be the surface field or a radius-dependent field, depending on the model. The proportionality constant changes depending on what model is used to calculate $E_{||}$. Calculations of the acceleration of charges, and subsequent radiation and pair production, in pulsar magnetospheres yield expressions for the luminosity of primary particles and hence the luminosities expected from pulsars (Muslimov & Harding 2003, 2004). In narrow acceleration gaps, the maximum attainable value of $E_{||}$ is limited by the requirement that $E_{||} = 0$ at the gap boundaries. The smaller the gap width, the smaller $E_{||}$. Very narrow gap widths therefore lead to under-predictions of pulsar γ-ray luminosities when compared with observations. A larger gap width leads to larger pair multiplicities, and hence larger luminosities; however, a small gap width is needed in order to reproduce the narrow light curve peaks.

In general, the predicted values of $E_{||}$ calculated here are orders of magnitude lower than the $E_{||}$ calculated from the measured spectral cutoff energies and modeled field line radii of curvature. This is consistent with the expectation that the predicted luminosity will be lower than that observed. The calculations of predicted $E_{||}$ in Section 4.3.3 show that the offset dipole increases $E_{||}$ on the trailing side of the polar cap where caustics form. This was first shown by Harding & Muslimov (2011a), who also found that pair multiplicities increase with increasing dipole offset and may be able to reconcile theoretical luminosity predictions with observations. $E_{||}$ of the slot gap with an offset dipole is further increased in the FF field, for which the offset is inherently larger. These improvements do not change $E_{||}$ enough to be consistent with the measured values, in all cases except that of the Crab in the FF field.

For the Crab, the geometrical parameters found from light curve modeling are similar for all three models in the FF field, and the predicted and measured $E_{||}$ are consistent. This lends additional support to the constraints on the emission geometry found from light curve modeling, and suggests that the field structure is close to that of the FF field. It may be that the assumptions of curvature radiation reaction and/or of acceleration occurring in narrow gaps are valid for the Crab, but not for older pulsars (a hypothesis that is supported by the recent work of Breed et al. 2013, in preparation). This is an interesting prospect that requires much further examination. Additionally, because all the emission geometries in the FF field have similar parameters (including a value of ζ that matches X-ray measurements), and because all have consistent measured and predicted $E_{||}$ values, it is again not possible to determine whether only an outer gap or slot gap is present in the Crab pulsar. These results do not necessarily further support the prospect of both types of gaps existing simultaneously, but they do allow for that possibility.

Finally, one caveat to note is that in the geometrical models, the gap widths were held constant. More complex emission regions with variable gap widths may produce different values of $E_{||}(r)$.

Chapter 5

Pulsar Searching and Timing

Pulsar studies are inherently dependent on the ability to accurately determine their spin frequency and spin-down rate, as well as on the ability to increase the sample of known pulsars with new pulsar discoveries. In this chapter, I describe how pulsar searching and timing is done. The chapter is focused on the methods that are applied to radio pulsars, but the concepts, as well as many of the practical aspects, are similar or identical at other wavelengths. The procedures described here will be referred to in Chapter 6, in which I describe my own work on pulsar searching and timing.

Much of this chapter is based on information found in the Pulsar Handbook Lorimer & Kramer (2005), which is generally regarded as the definitive text on pulsar observing. I will limit the discussion to the aspects of pulsar observing that are relevant to this thesis.

5.1 Effects of the Interstellar Medium on Radio Pulses

Radio waves in the wavelength range typically used to study pulsars ($\sim 100\,\mathrm{MHz}$–$5\,\mathrm{GHz}$) experience several different effects of propagating through the cold, ionized interstellar medium (ISM). I describe three of these effects, pulse dispersion, scattering, and scintillation, in this section. It should be noted that dispersion can be corrected, while scattering and scintillation cannot. Additionally, these effects, while complicating pulsar studies, can be quite useful for studying the ISM as well as for obtaining additional information about the pulsar in question (for example, distance estimates and velocity measurements).

5.1.1 Dispersion

The presence of free electrons in the ISM results in a frequency-dependent index of refraction,

$$\mu = \sqrt{1 - \left(\frac{f_\mathrm{p}}{f}\right)^2} \tag{5.1}$$

where f is the frequency of a radio wave and f_p is the plasma frequency $f_\mathrm{p} = \sqrt{e^2 n_\mathrm{e}/(\pi m_\mathrm{e})}$, where e is the fundamental electrical charge, m_e is the electron mass, and n_e is the free electron density along the line of sight. For typical values of $n_\mathrm{e} \sim 0.03\,\mathrm{cm}^{-3}$, measured from pulse dispersion in the Galactic plane Gomez-Gonzalez & Guelin (1974); Ables & Manchester (1976), $f_\mathrm{p} \sim 1.5\,\mathrm{kHz}$. A broadband pulse propagating through the ISM will therefore be refracted such that lower-frequency waves within the pulse will be delayed relative to higher frequencies, thus smearing the pulse in time. The time by which a wave of frequency f is delayed, compared

to an infinite-frequency wave (whose propagation time is just d/c), is

$$t(f) \equiv \mathcal{D}\frac{\mathrm{DM}}{f^2} \tag{5.2}$$

where $\mathcal{D}$ is the dispersion constant and DM is the dispersion measure, given respectively by

$$\mathcal{D} = \frac{e^2}{2\pi m_\mathrm{e} c} = 4.148808 \pm 0.00003 \times 10^3 \mathrm{MHz}^{-2}\,\mathrm{pc}\,\mathrm{cm}^{-3}\,\mathrm{s}, \tag{5.3}$$

$$\mathrm{DM} = \int_0^d n_\mathrm{e}\,\mathrm{d}l \tag{5.4}$$

where d is the pulsar distance. The difference in propagation times of two waves with frequencies f_1 and f_2 is then

$$\Delta t(f_1, f_2) = \mathcal{D} \times DM \times (f_1^{-2} - f_2^{-2}) \tag{5.5}$$

By applying Equation 5.5 to the measured frequencies and arrival times of a pulse, the frequency-dependent delay is removed, and the pulse is "de-dispersed."

Pulsars are quite useful in ISM studies because their pulsed emission allows dispersion to be measured. The S/N of a pulse is maximized when the pulse is de-dispersed at the proper DM value (Section 5.2.2). If the distance to a pulsar is known, for example from a measurement of its timing parallax (Section 5.3.1.6), then the average value of n_e along the line of sight can be calculated using Equation 5.4. Models of the free electron density in the ISM have been constructed in this way; the model most commonly used in the pulsar community is the NE2001 model Cordes & Lazio (2002).

Likewise, a pulsar's distance can be estimated through measurement of its DM and an estimate of n_e along the line of sight to the pulsar. Such distance estimates can have quite large errors, in some cases $\sim 100\%$, due to variations in n_e that are not captured in electron density models. For example, in regions of ongoing

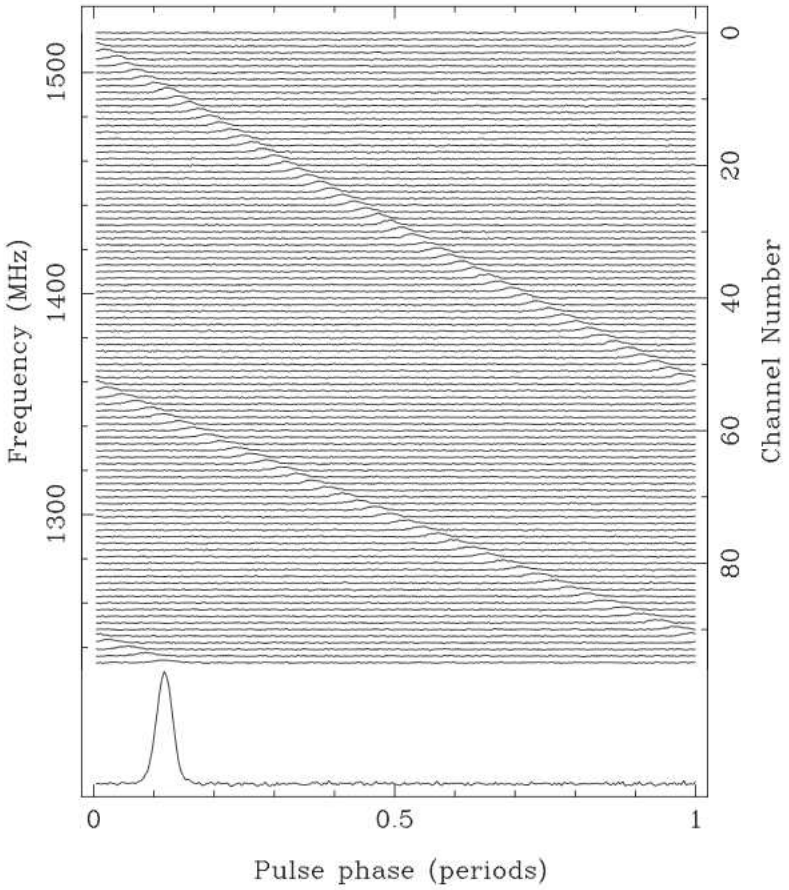

Figure 5.1: Frequency-dependent dispersion of radio pulses from PSR B1356−60, taken from Lorimer & Kramer (2005) and originally provided by Andrew Lyne. The time series has been folded on the pulsar period of 128 ms Manchester et al. (1978, 2005). This pulsar has a large DM of $295\,\mathrm{cm}^{-3}\,\mathrm{pc}$, resulting in dramatic pulse dispersion. The top panel shows the phase of the pulse arrival time as a function of spectral frequency—prior to correcting for dispersion, the pulse is smeared over the timescale of 2 full rotation periods. The bottom panel shows the pulse profile that results from incoherently de-dispersing the time series and summing the signal in each time sample over the spectral window.

star formation, the density of the ISM is much higher than the average value. A pulsar lying within or behind the star formation region will have a much larger DM than an unobstructed pulsar lying at the same distance, and the NE2001 model will therefore overestimate the distance to the former pulsar.

5.1.2 Scattering

From Equation 5.1, one can see that changes in $f_{\rm p}$ will result in changes in the refractive index μ. Because $f_{\rm p}$ depends on $n_{\rm e}$, density variations $\Delta n_{\rm e}$ present in the turbulent ISM cause changes in direction, perturbing or scattering the phases of radio waves as they propagate.

To first order, the total effect of scattering on a radio pulse can be considered to occur within a thin screen placed mid-way between the pulsar and Earth; this is the thin screen model of Scheuer (1968), illustrated in Figure 5.2. The screen has a thickness a that corresponds to the typical sizes of density inhomogeneities in the ISM. The root mean square phase variation $\Delta\Phi$ can be represented as a bending of the wavefront by an angle $\theta_0 = \Delta\Phi/(ka)$, where $k = (2\pi/c)\mu f$ is the wavenumber and, from Lorimer & Kramer (2005),

$$\Delta\Phi \simeq \frac{2e^2}{m_{\rm e}c}\frac{\sqrt{ad}\Delta n_{\rm e}}{f}. \tag{5.6}$$

An image of the pulsar through the screen would show the pulsar surrounded by a diffuse disk of radius $\theta_{\rm d} = \theta_0/2$, due to scatter broadening, with an intensity profile $I(\theta) \propto \exp\left(-\theta^2/\theta_{\rm d}^2\right)$.

Radio waves that were deflected by an angle $\theta \leq \theta_{\rm d}$ are delayed by $\Delta t(\theta) = \theta^2 d/c$ relative to those that were not deflected. The intensity profile in θ can therefore be used to derive the intensity of radio waves in the pulse as a function of time,

$$I(t) \propto \exp\left(\frac{-c\Delta t}{\theta_{\rm d}^2 d}\right) \equiv e^{-\Delta t/\tau_{\rm s}} \tag{5.7}$$

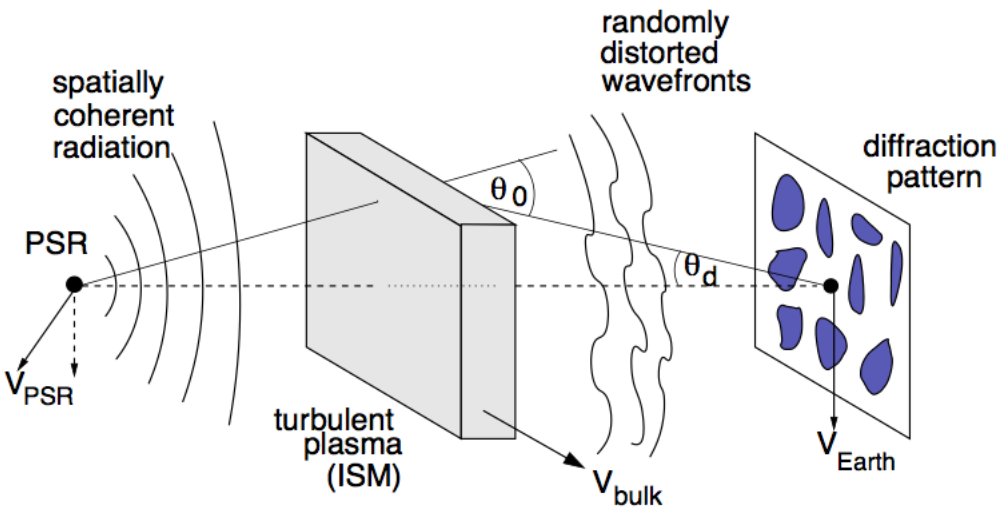

Figure 5.2: Illustration of the thin screen model for pulse scattering by the ISM. The figure is taken from Lorimer & Kramer (2005) and Cordes (2002).

The scattering timescale, $\tau_{\rm s}$, over which the pulse is broadened, is given by

$$\tau_{\rm s} = \frac{\theta_{\rm d}^2 d}{c} = \frac{e^4}{4\pi^2 m_{\rm e}^2} \frac{\Delta n_{\rm e}^2}{a} d^2 f^{-4} \tag{5.8}$$

The thin screen model is an approximation to the true physical situation—in reality, turbulent zones have different sizes and densities, and scattering occurs over the full path length rather than only at the midpoint between the pulsar and observatory. An example of a more realistic model of turbulence is one in which energy cascades from larger to smaller scales, resulting in a Kolmogorov power law spectrum Kolmogorov (1941, 1991) with spectral index 11/3. For this model, the scattering timescale is instead $\tau_{\rm s} \propto f^{-4.4}$.

Radio pulses that have been highly scattered show a signature exponential scattering tail over a timescale of $\tau_{\rm s}$. The timescale is strongly dependent on frequency and distance; for this reason, it can be helpful to use higher frequencies for pulsar timing, for which sharper pulses provide more accurate arrival time measurements.

However, pulsars are much weaker at higher radio frequencies because of their steep spectral index, so there is a trade-off between decreasing scattering and maintaining sensitivity. This trade-off is a limiting factor in searches for distant pulsars, for which scattering is larger but the flux is lower due to distance, and for pulsars near the Galactic Center, where $n_{\rm e}$ is large and pulses may be completely scattered by the ISM.

5.1.3 Scintillation

The scattering tail seen in some pulsar profiles is composed of signals that have been delayed in phase relative to the phase of the pulse peak by $\delta\Phi \sim 2\pi f \tau_{\rm s}$. These signals interfere, producing an interference pattern along the observer plane. If the pulsar, ISM density fluctuations, and the Earth were all at rest relative to each other, this interference pattern would be constant in time. However, because the relative velocities between each component are non-zero, the interference pattern changes with time, resulting in the intensity variations, or scintillation, observed on short timescales and over short frequency bandwidths in many pulsar profiles.

Signals separated by more than 1 radian do not interfere, resulting in the scintillation bandwidth

$$\Delta f = \frac{1\,\text{radian}}{2\pi\tau_{\rm s}} \propto f^4 \tag{5.9}$$

Both the scattering timescale and the scintillation bandwidth are calculated using the NE2001 model, in addition to pulsar DM or distance. To minimize the effects of scintillation, the observing bandwidth should be larger than Δf. Scintillation also decreases with decreasing f, but scattering increases.

Scintillation can be used to study the ISM and pulsar motion. Pulsar intensity varies in both time and frequency due to scintillation; a dynamic spectrum can be used to measure the size of an individual scintle, or region of enhanced flux density,

in time and frequency space. This measurement can be used to calculate the pulsar velocity transverse to the line of sight.

5.2 Pulsar Searching

A single dish radio observation with the primary purpose of finding a new pulsar, confirming a pulsar detection, or beginning to determine the timing (spin and orbital, if relevant) parameters of a newly discovered pulsar will be taken in *search mode*. The voltage of the telescope receiver is recorded with very high time resolution, typically tens of microseconds, so that the sampling time is much shorter than the millisecond to second periodicities for which the data will be searched. The signal is recorded with a spectrometer, so that each time sample contains a spectrum over the instrument bandwidth. To give an example of typical spectral bandwidth and resolution, the pulsar spectrometer currently in use at the Green Bank Telescope has a bandwidth of 800 MHz at central radio frequency 2 GHz; that bandwidth is split into 2048 frequency channels, each with a channel bandwidth of 0.39 MHz.

The raw data are therefore a series of high time resolution spectra. Aside from exceptionally bright pulsars, any pulsar emission present in the data will not be obvious by eye. Rather, the data appear as noise, within which various periodicities are hidden, and the time series must be transformed to the Fourier domain in order to search for periodic behavior.

There are several methods of searching for pulsars, but the most common procedure is as follows. One begins by excising as much Earth-based radio frequency interference (RFI) from the dataset as is possible. The data are then barycentered and corrected for frequency-dependent pulse dispersion caused by propagation through the interstellar medium; after the data have been de-dispersed, the signal within in-

dividual time samples are summed over frequency, creating a one-dimensional *time series*. This de-dispersion step must be done at many different values of dispersion measure (DM; Sections 5.1.1 and 5.2.2.1), thus many different time series are made. A fast Fourier transform is performed on each time series and is searched for pulsar-like periodic signals lying above a user-defined threshold, recording the frequency ν, frequency derivative $\dot{\nu}$, and DM of all candidate pulsar signals (Sections 5.2.3 and 5.2.4). The time series are folded on each set of these parameters, the result of which are pulse profiles of each candidate. Promising candidates are then used to fold the raw data, during which a fine search is done over a small range of ν, $\dot{\nu}$, and DM in order to obtain more precise parameter values (Section 5.2.5). The profiles of the raw folds allow further scrutiny to determine whether or not a candidate may be a pulsar; in particular, the signal from a real pulsar will peak in brightness over a very narrow range of DM values.

The entire search process can be done using the PulsaR Exploration and Search TOolkit (PRESTO[1]), a C and Python package developed by Scott Ransom Ransom (2001), who has also written a tutorial[2] on pulsar searching with PRESTO. Here I will summarize the main aspects of the search procedure, with reference to PRESTO routines.

5.2.1 Removing RFI Prior to Searching

It is important to remove as much radio frequency interference as is possible, without significantly reducing the size of the dataset, in order to be more sensitive to weaker signals in the data. Strong narrow-band RFI and broadband, short-duration RFI is masked using the PRESTO routine `rfifind`. This routine replaces bursts of RFI

[1] `http://www.cv.nrao.edu/~sransom/presto/`

[2] `http://www.cv.nrao.edu/\%7Esransom/PRESTO_search_tutorial.pdf`

in the frequency and time domains with median values drawn from data on either side of the RFI burst.

There are also forms of RFI that are longer lasting, and usually periodic. A good example of this is the radio emission from electrical lines at 60 Hz in the United States (and 50 Hz in the rest of the world). Because RFI is Earth-based, it occurs at DM = 0; the same incoherent de-dispersion method used in a pulsar search (Section 5.2.2.1) can be used to identify and remove periodic RFI. The data are de-dispersed at DM=0 and summed over frequency to create a time series (Equation 5.10). The time series is not transformed to the Solar System barycenter frame, as RFI occurs in the same reference frame as the observatory (the topocentric frame). The time series is transformed to the Fourier domain (Equation 5.16) and searched for strong frequencies. These frequencies, and their harmonics, are then masked so that they will not be chosen as pulsar candidates later in the analysis.

At this stage, the barycentric frequencies of any known pulsars are also masked (and labeled in the mask as barycentric rather than topocentric). This is usually an issue only when searching for MSPs in a globular cluster in which other pulsars have already been found.

5.2.2 De-dispersion of Time Series

Interstellar dispersion causes low-frequency radio waves from a single pulse to arrive later than high-frequency waves from that same pulse. In order to detect periodic pulsations, it is necessary to correct the data for dispersion so that the pulses arrive in the same time sample across the spectral window of the observation. This is done by incoherent de-dispersion, in which the data are de-dispersed across the full bandwidth at many different DM values after the observation is complete. When the pulsar DM is known or can be estimated with reasonable accuracy, coherent

de-dispersion can be used during the observation to perform real-time de-dispersion within individual spectral channels.

5.2.2.1 Incoherent De-dispersion

Because we do not know a priori the pulsar dispersion measure, we must search for frequencies in the data at many different DMs. The first step is to incoherently de-disperse the data; the process is "incoherent" because it is done after the observation is complete, when no information about the signal phase is available. The effect of de-dispersing at the pulsar's true DM is that the frequency-dependent delay of the pulse will be removed, such that the pulse will occur in the same set of time bins at every frequency; compressing the data in frequency (adding the channels within each time interval) will then result in detection of the pulse. If the DM used for de-dispersion is not the correct pulsar DM, then the delay will not be removed properly and the pulse will still occur in a different time bin in each frequency channel. It will be smeared out and undetectable when the frequency channels in each time interval are summed. Near the correct DM, the pulse will appear weakly. The pulse is therefore detected at several DMs, but is strongest at a particular DM.

Incoherent de-dispersion of a raw dataset is done by summing the signal in time and frequency bins that are related by the frequency-dependent DM delay from Equation 5.5. The raw data consist of a 2-dimensional array, with time samples along the x-axis and $n_{\rm chan}$ observing frequency channels with non-zero bandwidth $\Delta f_{\rm chan}$ along the y-axis. $R_{j,l}$ is the signal in the $j^{\rm th}$ time sample and $l^{\rm th}$ frequency channel, where $l = 1$ corresponds to the highest frequency. To obtain a time series at DM=0 (no de-dispersion), the signals in each frequency channel of a given time sample are summed:

$$\mathcal{T}_j(\mathrm{DM} = 0) = \sum_{l=1}^{n_{\rm chan}} R_{j,l} \tag{5.10}$$

Zero-DM time series are often used to identify and remove Earth-based radio frequency interference (RFI), while a pulsar will have a nonzero DM. To de-disperse at DM > 0, Equation 5.10 becomes

$$\mathcal{T}_j(\mathrm{DM}) = \sum_{l=1}^{n_{\mathrm{chan}}} R_{j+k(l),l} \tag{5.11}$$

where $k(l)$ is an integer corresponding to the number of time bins by which a signal has been delayed due to dispersion, given by

$$k(l) = \left(\frac{t_{\mathrm{samp}}}{4.15 \times 10^6\,\mathrm{ms}}^{-1}\right)\left(\frac{\mathrm{DM}}{\mathrm{cm}^{-3}\mathrm{pc}}\right)\left[\left(\frac{f_l}{\mathrm{MHz}}\right)^{-2} - \left(\frac{f_1}{\mathrm{MHz}}\right)^{-2}\right] \tag{5.12}$$

To search for a new pulsar, time series are made at many different DM values and searched for periodicities. The resolution in DM, ΔDM, must be chosen so that a pulse with true dispersion $\mathrm{DM}' = \mathrm{DM} + \Delta\mathrm{DM}$ will not be so dispersed at dispersion measure DM that it is undetectable by the search. (There is software available to optimize ΔDM.) Additionally, the dataset must be de-dispersed over the full range of possible DM values for a given pointing direction, so that very nearby or very distant pulsars are not missed. In a typical search, one will create time series from $\mathrm{DM} = 0 - 1000\,\mathrm{cm}^{-3}\,\mathrm{pc}$ with step size $\Delta\mathrm{DM} \sim 0.1 - 0.5\,\mathrm{cm}^{-3}\,\mathrm{pc}$.

De-dispersion is computationally expensive, and is typically done in parallel. Each node produces N de-dispersed time series, where N is specified by the user and must be divisible by the number of processors on the node. The time series are usually barycentered as well, such that the sample times are corrected to the Solar System barycenter by removing time delays due to the Earth's motion and other effects of light propagation through the Solar System (see Section 5.3.1.4 for more details). The barycenter is the best suited reference frame in which to search for a pulsar of unknown velocity relative to the Earth.

In PRESTO, the `prepdata` and `prepsubband` commands are used to de-disperse the raw data into time series (the former is used to de-disperse at a single DM, and

the latter at many DM values). Prior to running `prepsubband`, the de-dispersion plan should be optimized using `DDplan.py`.

5.2.2.2 Coherent De-dispersion

Incoherent de-dispersion removes pulse smearing over the full observing bandwidth, but the pulse is still smeared within individual frequency channels. The faster the pulsar's rotation and the narrower the pulse, the more significant smearing within channels becomes. This effect can be removed using coherent de-dispersion Hankins & Rickett (1975), in which the individual channels are de-dispersed in real time at a single DM through manipulation of the phase of the incoming voltage. Coherent de-dispersion results in sharper profiles, often revealing fine structures that would not otherwise be resolved (Figure 5.3).

Changes to a signal propagating through the ISM can be described with a transfer function, H, which acts as a filter only on the phase of the signal. The complex voltage $v(t)$ induced in the telescope feed by incoming radiation can be thought of as the intrinsic complex voltage, $v_{\rm int}(t)$, of the pulsar convolved with the transfer function. The original pulsar signal can therefore be recovered. For a single spectroscopic frequency channel with center frequency f_0 and bandwidth Δf, the Fourier transforms $V(f)$ and $V_{\rm int}(f)$ of the raw voltages $v(t)$ and $v_{\rm int}(t)$ can be written as

$$V(f_0 + f) = V_{\rm int}(f_0 + f)H(f_0 + f) \ . \tag{5.13}$$

The transfer function H used to de-disperse the signal in real time is

$$H(f_0 + f) = \exp\left[i\,\frac{2\pi\mathcal{D}}{(f + f_0)f_0^2}\,{\rm DM}\,f^2\right], \tag{5.14}$$

where $\mathcal{D}$ is the dispersion constant from Equation 5.3. This function was derived by Hankins & Rickett (1975) and is reproduced in Lorimer & Kramer (2005). The end result is that the intrinsic voltage is converted to a real signal, which is recorded

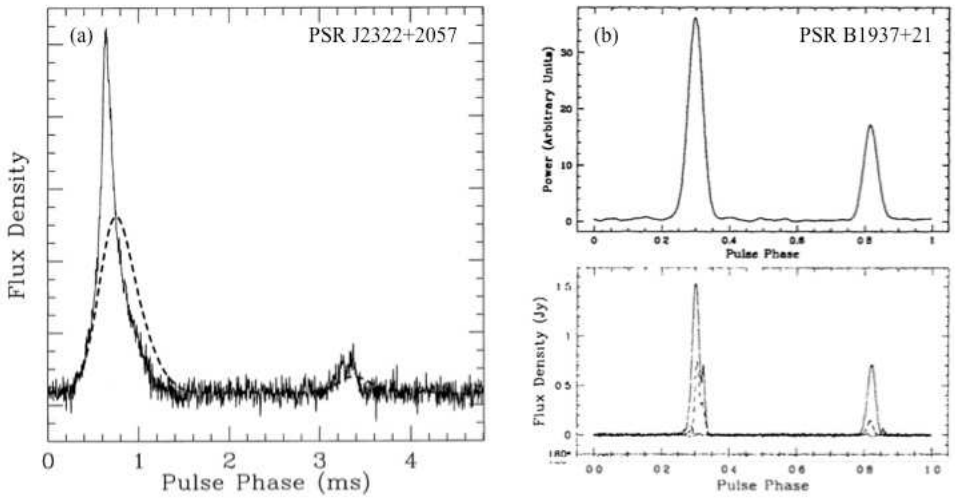

Figure 5.3: (a) The pulse profile of PSR J2322+2057. The dashed line shows the profile recovered using only incoherent de-dispersion, while the solid line is the profile resulting from coherently de-dispersing the signal during the observation. The plot is taken from Stairs et al. (2000). (b) The pulse profile of PSR B1937+21, the second fastest millisecond pulsar known ($P = 1.56$ ms Backer et al. (1982); Manchester et al. (2005)) and the first millisecond pulsar discovered (Backer et al. 1982). The top profile shows the total intensity I, and has been incoherently de-dispersed only. The bottom profile was coherently de-dispersed, and reveals finer structure than is seen in the top profile. The total intensity is plotted with the solid line, and the linear polarization with the dotted line. Without the use of coherent de-dispersion, these features are smeared out by dispersion within the individual spectral channels. The plot is taken from Stairs (2002).

as raw data and searched with the standard procedure using PRESTO or another pulsar searching package. Note that incoherent de-dispersion must still be performed over the full bandwidth, as coherent de-dispersion only corrects for dispersion within individual channels.

To observe using coherent de-dispersion, a DM must be specified prior to beginning the observation. This means that in most cases, standard (incoherent) de-dispersion is used to first detect a pulsar and measure its DM. Then coherent de-dispersion can be used in follow-up search mode observations, which are needed

to confirm the detection and obtain an initial timing solution (Section 5.3.1.5). In some targeted searches, the DM of the (thus-far undetected) pulsar for which the search is targeted may already be known or can be estimated. This is true, for example, for globular cluster pulsar searches. If some pulsars are already known to exist in the cluster, then the DM is already known, and searches employing coherent de-dispersion at that DM may result in additional pulsar discoveries. Alternatively, in the absence of previously detected pulsars, the DM of a cluster can be estimated from the NE2001 model given a distance measurement. (Globular cluster distances can be determined from the turnoff in the main sequence of its stellar population, RR Lyrae stars, astrometry, and other distance indicators, reviewed in Chaboyer (1999).) In Chapter 6, I describe the search for and discovery of a new MSP in the globular cluster NGC 6652, in which coherent de-dispersion at an estimated DM was used.

5.2.3 Searching for Periodicity in the De-dispersed Time Series

Periodic signals in the time domain can be reconstructed with Fourier series, in which sine and cosine wave functions of different frequencies and amplitudes are summed until the periodic signal is adequately described. The Fourier transform of a periodic signal contains the frequencies and amplitudes (or power) of those wave functions. For example, sinusoidal signal in the time domain will appear as a delta function at a specific frequency in the Fourier domain. Allowing the period to approach infinity results in the continuous Fourier Transform (FT),

$$\mathcal{F}(f) = \int_{-\infty}^{\infty} f(t) e^{-2\pi i t f}\, dt \tag{5.15}$$

where $i = \sqrt{-1}$.

In real data, periodicities are finite and the time intervals are discrete. The Discrete Fourier Transform (DFT) is used to find periodicities in a discretely sampled data set like $\mathcal{T}_j$. The k^{th} frequency-domain Fourier component of the DFT is

$$\mathcal{F}_k = \sum_{j=0}^{N-1} \mathcal{T}_j e^{2\pi i j k/N} \tag{5.16}$$

where N is the number of time samples considered in the DFT. For a dataset of total length T in time and with equally spaced time samples of length t_{samp}, the width of each frequency bin in the Fourier domain is $\Delta\nu_{\text{samp}} = 1/T$, and the frequency of the k^{th} frequency bin is $\nu_k = k/T$. The highest frequency sampled is the Nyquist frequency, $\nu_{\text{Nyquist}} = 1/(2t_{\text{samp}})$.

The computation time to calculate the DFT is of order N^2. The Fast Fourier Transform (FFT) refers to a family of algorithms that reduces this computational time to order $N \log_2 N$. The FFT is calculated most quickly when the factors of N are small integers (e.g., 2, 3, 5, or 7), so time series are often either lengthened with zero-padding or shortened to a more convenient length. Lengthening short time series with zero padding has the additional effect of increasing the frequency resolution and the maximum (Nyquist) frequency in the Fourier domain.

Only purely sinusoidal signals appear as delta functions at a single frequency in Fourier space. Pulsars typically have narrower pulses, and therefore have many harmonics in the frequency domain (about P/W harmonics, where P is the pulsar period and W is the pulse width in time). Summing the power distributed over these harmonic frequencies results in better sensitivity to the narrow pulsed signals. For $W/P = 0.05$, the number of harmonics is $\sim P/W = 20$; in a typical search, up to 16 harmonics are summed in order to increase the pulse S/N. Fourier transforms of de-dispersed time series are performed in PRESTO using the command `realfft`.

5.2.4 Acceleration Searches for Binary Pulsars

The measured pulse frequency ν from pulsars in binary systems appears to vary with time as the pulsar's line-of-sight velocity $v_{\rm los}$ changes through its orbit, according to the Doppler equation,

$$\nu(t) = \nu_0(1 - v_{\rm los}(t)/c), \tag{5.17}$$

where ν_0 is the true pulsar spin frequency in its rest frame. This results in the time interval between pulses changing as the pulsar moves through its orbit. For orbital periods that are considerably longer than the observation's integration time, the changes in pulse frequency can be described by a non-intrinsic, Doppler-induced frequency derivative $|\dot{\nu}_{\rm D}| = a_{\rm los}\nu_0/c$, where $a_{\rm los}$ is the line-of-sight acceleration. A substantial $\dot{\nu}_{\rm D}$ can cause the signal frequency to change by one or more frequency bins in the Fourier domain over the course of the observation, spreading the signal over several neighboring frequency bins and decreasing its S/N in a single bin, as illustrated in Figure 5.4. The number of bins over which the signal drifts can be quantified as

$$N_{\rm drift} = \dot{\nu}_{\rm D}T/\Delta\nu = a_{\rm los}\nu_0T^2/c, \tag{5.18}$$

where T is the integration time, $\Delta\nu = 1/T$ is the width of a single Fourier bin. Acceleration searches are used to correct for a constant frequency derivative and thus recover the total power in the frequency-drifting signal.

When searching for a pulsar in a known binary orbit, for which the orbital parameters and $v_{\rm los}$ are already known, then the orbital motion can be removed by Doppler-correcting the time samples to the pulsar's rest frame prior to performing an FFT of the time series. If the pulsar exists, its spin frequency will show up in the Fourier domain. In a blind binary pulsar search, however, any accelerations the pulsar may experience are not known a priori, and one must search over a grid of

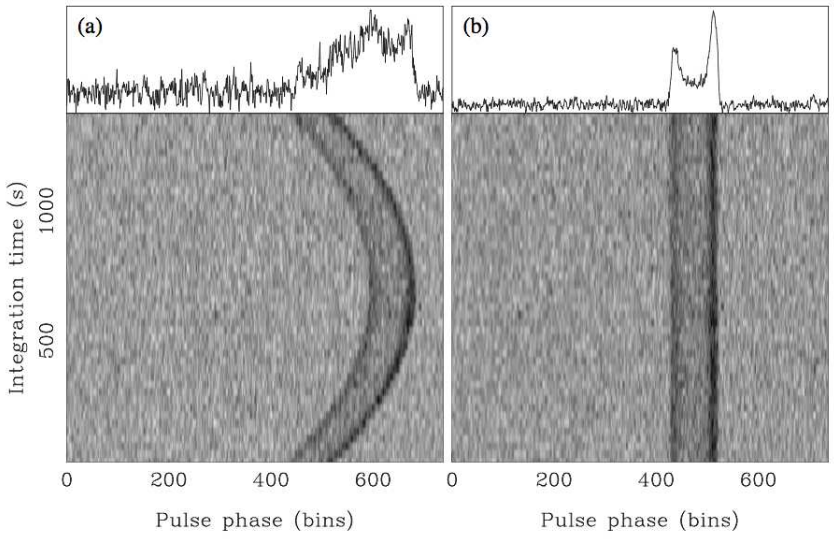

Figure 5.4: The folded pulse profiles of PSR B1913+16, the first binary pulsar discovered Hulse & Taylor (1975), as a function of time. The observation was taken with the Arecibo telescope. The integration time was 22 min, much shorter than the orbital period of 7.75 h Hulse & Taylor (1975). In panel (a), no acceleration search was done, so the pulse profile is Doppler shifted as the pulsar moves through its orbit, and the summed profile is Doppler broadened. In (b), the time series fold accounts for an acceleration $a_{\rm los} = -16\,{\rm m\,s^{-1}}$, straightening and sharpening the profile. This figure was taken from Lorimer & Kramer (2005).

orbital acceleration values to try to recover a signal. The acceleration is assumed to be constant over the length of the observation t, so that $v_{\rm los} = a_{\rm los}t$. The time series is corrected for each different acceleration in the grid, and if there is a pulsar with one of those accelerations over the observation interval, its spin period will be found with a Fourier transform.

In order to avoid performing so many FFTs, Ransom et al. (2002) developed the "correlation method" for acceleration searches done entirely in the Fourier domain. The DFT of a signal with varying frequency is a delta function (the ideal response to a constant frequency) convolved with a finite impulse response (FIR) filter that

spreads the power over multiple bins in the Fourier power spectrum. In the Fourier domain, for a constant acceleration throughout the observation, the signal will drift by $\dot{r} = \dot{\nu}_{\rm D} T^2$, where r is the Fourier bin, $\dot{r}$ is its derivative, and T is the total integration time Ransom et al. (2002). By applying the inverse of the FIR filter (which is the complex conjugate of the Fourier response) to the DFT, the power is re-concentrated in a single Fourier bin. If the center frequency of the signal is in Fourier bin r_0, then the Fourier response to the signal can be written as $\mathcal{F}_{k-r_0}$, where $|k - r_0|$is the frequency offset of the $k^{\rm th}$ bin from r_0. The corrected Fourier component, within which the power is contained in a single bin, is then

$$\mathcal{F}_{r_0} = \sum_{k=r_0-m/2}^{k=r_0+m/2} \mathcal{F}_k \mathcal{F}^*_{r_0-k} \tag{5.19}$$

where m is the maximum number of bins over which the signal is assumed to have been spread, and $\mathcal{F}^*_{r_0-k}$ is the complex conjugate of $\mathcal{F}_{r_0-k}$. The latter is composed of a phase rotation term and a set of Fresnel integrals that are functions of r_0 and its derivative, $\dot{r}$. $\mathcal{F}_{r_0}$ is calculated for a range of $\dot{r}$, in the same way that the time series would be corrected for a range of different $a_{\rm los}$ values, and saves computational time because it is not necessary to perform many FFTs—only one FFT per de-dispersed time series is required. Ransom et al. (2001) first used the correlation method to discover the 1.7 h binary pulsar PSR J1807−2459 in the globular cluster NGC 6544.

The correlation method is commonly used for acceleration searches. In PRESTO, an acceleration search can be performed using the `accelsearch` command. The most important parameter for this routine is $z_{\rm max}$; this is the maximum number of Fourier bins by which the highest harmonic may linearly drift in the power spectrum, thus setting k for all the lower harmonics and determining the range of frequency bin offsets to be searched. It is not uncommon to set $z_{\rm max} = 200$ bins, or even higher in some cases, to search for highly accelerated binary pulsars.

It should be noted that over a long observation, a solitary pulsar's intrinsic

frequency derivative may cause the spin frequency to change enough that the Fourier power is contained in more than one frequency bin. It is therefore advisable to always perform an acceleration search, even if only with a small $z_{\max}$ to search for an isolated pulsar.

5.2.5 Identifying and Folding Pulsar Candidates

After the time series has been transformed to the Fourier domain, and acceleration searched if necessary, the Fourier transform must be searched for pulsar-like signals. A pulsar-like signal is one that appears at the same frequency in several time series produced at neighboring DMs, and that is most significant at one of those DM values. A script such as `ACCEL_sift.py`, available with PRESTO, can be used to identify such signals. Once identified, the time series are folded on the pulse period of each pulsar candidate found in that time series, as well as on the period derivative if applicable. The period derivative will be large if, for example, the signal is from a real pulsar that is in a binary system.

The frequency ν of the signal is the rate of change of the signal's phase, where one complete cycle (rotation, if the signal is from a pulsar) occurs through the phase range $0 \leq \phi < 1$. Therefore, $\nu = d\phi/dt$. The signal's phase as a function of time can be expressed as a second-order Taylor series,

$$\phi(t) = \phi_0 + \nu(t - t_0) + \frac{1}{2}\dot{\nu}(t - t_0)^2 \tag{5.20}$$

where, for the case of folding a new pulsar candidate, $\phi_0 = 0$ corresponds to the observation start time t_0, ν is the frequency measured from the Fourier transform, and $\dot{\nu}$ is the frequency derivative measured from the acceleration search, if applicable. To fold the time series on a candidate ν and $\dot{\nu}$, each time bin in the time series is assigned a phase, and all signals in equivalent phase bins are summed to

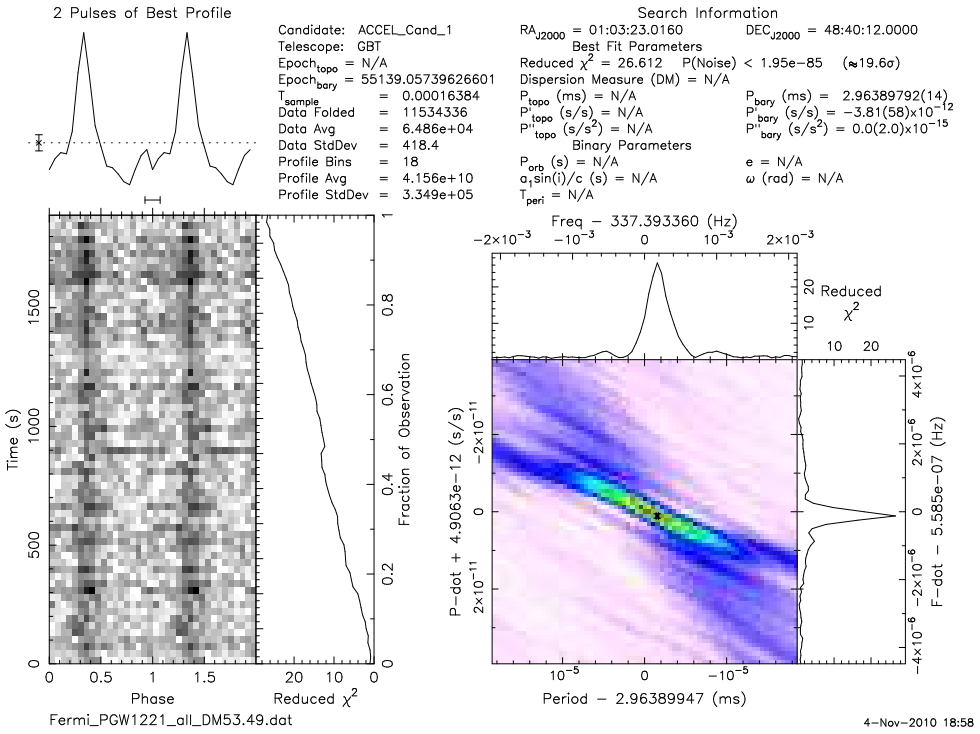

Figure 5.5: The output plot from a DM = 53.5 cm^{-3} pc time series that was folded on a pulsar candidate's ν and $\dot{\nu}$. While some automatic techniques are used by PRESTO to reduce false candidates, they cannot match the eye's ability to pick out likely pulsar candidates, and it is therefore necessary to look through many plots like these as one of the last steps in a pulsar search.

produce a pulse profile. The parameters of any profiles that may be true pulsars—typically identified in the time series folds as a signal that is most significant at a single $(\nu, \dot{\nu})$—are then used to fold the raw data.

Figure 5.5 shows the result of folding a time series, which was de-dispersed at DM = 53.5 cm^{-3} pc, on the frequency and frequency derivative of one pulsar candidate found in an acceleration search. The fold was done using `prepfold` in PRESTO. At the top left, two full cycles of the pulse profile are shown; below the summed profile is the profile over time, showing the stability of the pulse throughout the observation. On the right of the profile is the cumulative χ^2 of the profile; it

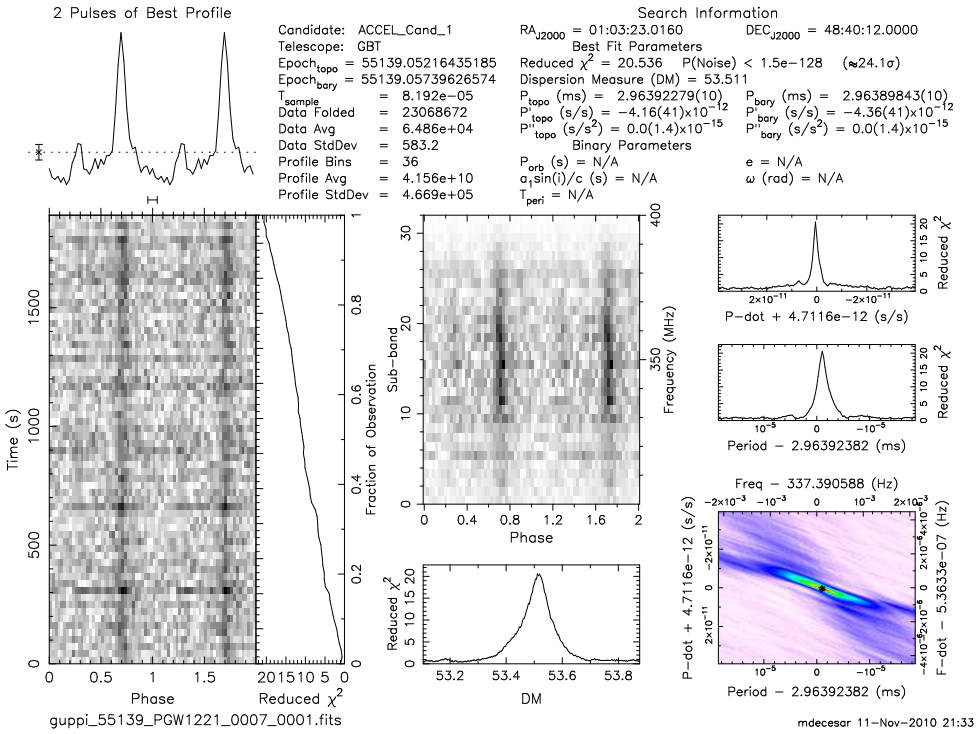

Figure 5.6: The same pulsar candidate's ν, $\dot{\nu}$, and DM from Figure 5.5 were used to fold the raw data, resulting in the detection of a millisecond pulsar, PSR J0102+4839.

increases over the observation, as expected for a steady signal. The plot on the right shows the χ^2 of the signal over a range of ν and $\dot{\nu}$, with the parameters yielding the highest significance located near the center of the plot. (In practice, many plots like those of Figure 5.5 will be output by PRESTO, and need to be searched through by eye.)

The raw data were then folded over a range of ν, $\dot{\nu}$, and DM to produce Figure 5.6. The plots on the right again show $\chi^2(\nu, \dot{\nu})$. The top plot in the center shows the pulse profile over the bandwidth, summed within 32 frequency sub-bands. The bottom center plot shows the χ^2 significance over the range of DM values used in the fold. This highly significant χ^2 over a small range of DM is characteristic of a true pulsar signal. Folding the raw data is necessary in order to inspect the significance

with DM, and results in a more precise DM value than was achieved in the time series folds.

Once a pulsar is found, it is necessary to do a follow-up observation to confirm its detection. After that, a series of observations are done over the course of at least one year in order to obtain a phase-connected timing solution that adequately describes the pulsar's rotation and predicts with high precision the time of each individual pulse of emission. This procedure will be described in Section 5.3.

5.2.6 Pulsar Searching Strategies and Sensitivity Limits

There are two basic strategies for pulsar searches, pulsar surveys and targeted searches. Surveys cover a larger portion of the sky, but with short integration times and relatively low sensitivity. Targeted searches are typically longer, deeper observations that cover only a few sources of interest in which pulsars are expected to lie. An updated catalog of all known pulsars is available at the ATNF website[3], and is described in Manchester et al. (2005).

In any pulsar search, be it survey or targeted, it is important to calculate the search's sensitivity to pulsations. The minimum detectable flux density $S_{\rm min}$, corresponding to a signal-to-noise threshold $({\rm S/N})_{\rm min}$, is calculated using the radiometer equation for pulsed signals (Appendix 1.4 of Lorimer & Kramer (2005)),

$$S_{\rm min} = \beta \, \frac{({\rm S/N})_{\rm min} T_{\rm sys}}{G\sqrt{n_{\rm p} t_{\rm int} \Delta f}} \sqrt{\frac{W}{P-W}} \; . \tag{5.21}$$

System imperfections are accounted for with the correction factor β, with typical values of $\sim 1.05 - 1.25$ (e.g., Ray et al. (2011a)). $T_{\rm sys}$ is the system temperature, which includes the sky temperature, G is the gain, $n_{\rm p}$ is the number of polarizations (typically $n_{\rm p} = 2$), Δf is the bandwidth, P is the pulse period, and W is pulse

[3] `http://www.atnf.csiro.au/people/pulsar/psrcat/`

width in time (such that W/P is the duty cycle). By calculating the sensitivity of an observation to pulsed flux, one can determine the utility of a deeper search, and can place upper limits on the pulsed radio flux for non-detections (e.g., Ray et al. 2011a).

In a pulsar survey, the ground-based radio observatory records high time resolution data from as many points on the sky as possible, given its elevation limits. Some examples are the Parkes Southern Pulsar Survey and the Parkes Multi-beam Pulsar Survey, both performed at the Parkes Observatory in Australia, which respectively discovered 101 Lyne et al. (1998) and 953 Lyne (2008) new pulsars. The latter survey discovered more pulsars than the 822 that were previously known. Reanalysis of this survey using acceleration searches has led to the recent discoveries of 16 new pulsars Eatough et al. (2013). Recent northern-hemisphere surveys include the Pulsar ALFA survey Cordes (2008) at the Arecibo Observatory, and the Green Bank drift scan survey Boyles et al. (2013); Lynch et al. (2013), for which analysis is ongoing. A current survey being done at Parkes is the High Time Resolution Universe survey, the focus of which is millisecond pulsars as well as fast radio transients; 135 new pulsars, including 29 MSPs, have been discovered so far Keith (2013).

While most known pulsars are detected only at radio frequencies, some pulsars have also been found to emit at higher energies, particularly in the X-ray and γ-ray bands. Surveys for high-energy pulsar emission are done with satellite instrumentation, and are therefore performed over the full sky. The EGRET instrument on the Compton Gamma-Ray Observatory (CGRO) detected seven γ-ray pulsars, and its successor, the *Fermi* LAT, has detected more than 120 γ-ray pulsars, 117 of which are included in the Second Fermi LAT Pulsar Catalog The Fermi-LAT Collaboration (2013).

In a targeted search, one identifies and searches locations in which pulsars are

likely to be found. Common locations are globular clusters, which may contain tens to hundreds of MSPs, and supernova remnants, within which isolated pulsars are likely to exist given current understanding of stellar evolution. During the CGRO mission, γ-ray sources were searched for radio pulsations, and this sort of targeted searching is currently being done again in LAT sources that have no associated multi-wavelength counterpart. The reasoning behind these searches is that if a γ-ray source is a pulsar, then radio pulsations may be detected much more easily than γ-ray pulsations, especially for a pulsar in a binary system; folding on the radio ephemeris (timing solution) may, however, yield a detection of γ-ray pulsations as well. These searches have been quite fruitful, especially in discoveries of MSPs, as will be discussed further in Chapter 6. Additionally, of the $\sim$ 120 γ-ray pulsars detected by the LAT, $\sim 1/3$ were discovered in blind γ-ray pulsation searches Abdo et al. (2009a). Targeted radio searches of these pulsars found all but three Camilo et al. (2009); Abdo et al. (2010e) of them to be radio-quiet within current detection limits (The Fermi-LAT Collaboration (2013), and references therein).

In Chapter 6, I describe targeted searches with which I was involved, and through which I discovered two new MSPs. These searches were done using the Green Bank Telescope, in Green Bank, WV, using the Green Bank Ultimate Pulsar Processing Instrument (GUPPI) DuPlain et al. (2008).

5.3 Pulsar Timing

"Pulsar timing" refers to the process by which one calculates the precise arrival time of each pulse of emission from a given pulsar. A phase connected timing solution will accurately predict the time of each pulse, and the exact number of pulses, or neutron star rotations, between two separate observations, over long timescales

(several years, to decades). A timing solution is achieved by fitting measured pulse arrival times to arrival times predicted from a model of the pulsar rotation and orbital motion, if in a binary system. Here I describe the process of pulsar timing. I begin with a description of the physics and mathematics of pulsar timing, largely drawn from Lorimer & Kramer (2005). I then explain the practical procedure of extracting pulse arrival times from a time series and fitting a timing solution to these data points.

5.3.1 Physical Concepts of Pulsar Timing

To accurately predict the arrival time of each pulse, an accurate mathematical description of the pulsar's rotation is required. This is achieved by approximating the unknown function describing the rotation over time with a Taylor series of the time-dependent rotation frequency and frequency derivatives. The spin frequency ν is then expressed as

$$\nu(t) = \nu_0 + \dot{\nu}_0(t - t_0) + \frac{1}{2}\ddot{\nu}_0(t - t_0)^2 + \cdots , \tag{5.22}$$

where $\nu_0 = \nu(t_0)$ at a reference epoch t_0, while $\dot{\nu}_0 = \dot{\nu}(t_0)$ and $\ddot{\nu}_0 = \ddot{\nu}(t_0)$ are its time derivatives. The pulse number N changes at rate ν, so the number of pulses that occur after t_0 is

$$N = N_0 + \nu_0(t - t_0) + \frac{1}{2}\dot{\nu}_0(t - t_0)^2 + \cdots , \tag{5.23}$$

where N_0 is the number of the pulse occurring at t_0. A similar equation, in which phase $0 \leq \phi \leq 1$ rather than pulse number N is used, can be written as

$$\phi = \phi_0 + \nu_0(t - t_0) + \frac{1}{2}\dot{\nu}_0(t - t_0)^2 + \cdots , \tag{5.24}$$

where ϕ_0 is the rotation phase at t_0. To maintain $0 \leq \phi < 1$, one must take the modulus of ϕ with the spin period.

Consider an isolated (non-binary) pulsar that has zero velocity with respect to the Solar System barycenter (SSB), so that the SSB and pulsar share the same inertial reference frame. Imagine further that the interstellar medium (ISM) is a vacuum. In this special case, the pulse arrival times measured at the SSB are equivalent to the pulse emission times, separated only by the constant light propagation time d/c, where d is the distance between the pulsar and the SSB. The number of pulses N counted from t_0 is then directly dependent on the pulsar's rotation, and can be described with Equation 5.23, where each value of t is a measured pulse arrival time. For an unrealistically (and persistently) bright pulsar, individual pulses could be recorded and their arrival times measured, such that N_i and t_i would be known. Then ν and its derivatives could be determined from Equation 5.23.

As one might expect, the situation is quite different in reality. Radio pulsars are very faint sources, and those that are bright enough for individual pulses to be detected display variation in the pulse profile from one pulse to the next. However, averaging several hundred to thousand pulses together produces mean pulse profiles that have been shown to be stable (Lorimer & Kramer 2005, and references therein). Pulse times of arrival, or TOAs, are therefore extracted from mean profiles, and do not represent time stamps of individual pulses.

The TOAs must be corrected for several effects before being used to obtain a timing solution. First, the interstellar medium is not a vacuum, and radio photons are therefore subject to frequency-dependent scattering by free electrons in the ISM. Higher-frequency radio waves will reach the observer sooner than lower-frequency waves, introducing error in the precise pulse arrival time. Second, the TOAs are measured at telescopes on Earth, not at the SSB. The TOAs therefore must be transformed to barycentered TOAs by correcting for the motion of the Earth and other Solar System bodies. The telescope's location on Earth must also be taken

into account through clock corrections, especially when timing a pulsar at different observatories. Third, the SSB is not a perfect inertial frame because the pulsar has some initially unknown velocity relative to the SSB; the transverse component of this velocity can be measured in some cases. Finally, the pulsar may be in a binary system, introducing a varying Doppler shift in the pulse arrival times due to the changing orbital accelerations and requiring additional orbital parameters in the timing solution.

The result of taking these effects into account is that clock, observation frequency, and barycentric corrections are applied to Earth-based TOAs extracted from summed rather than individual pulses. For a solitary pulsar, a barycentric TOA $t^{\rm s}_{\rm SSB}$ is calculated as

$$t^{\rm s}_{\rm SSB} = t_{\rm topo} + t_{\rm clock} - \Delta D/f^2 + \Delta_{\rm R\odot} + \Delta_{\rm S\odot} + \Delta_{\rm E\odot}, \tag{5.25}$$

where $t_{\rm topo}$ are topocentric pulse times of arrival, $t_{\rm clock}$ accounts for clock corrections, $\Delta D/f^2$ is the time difference due to the dispersion measure, and $\Delta_{\rm R\odot}$, $\Delta_{\rm S\odot}$, and $\Delta_{\rm E\odot}$ are the Römer, Shapiro, and Einstein delays experienced by a photon propagating through the Solar System. In Sections 5.3.1.1-5.3.1.4, I describe the process of extracting $t_{\rm topo}$ and each corrective term needed to calculate $t^{\rm s}_{\rm SSB}$. I then describe how the corrected $t^{\rm s}_{\rm SSB}$ and the pulse number N (Equation 5.23) are used to fit for the pulsar's spin frequency, frequency derivatives, position, and other physical parameters (Sections 5.3.1.5-5.3.1.6). Timing of binary pulsars is discussed in Section 5.3.2.

5.3.1.1 Topocentric Pulse Arrival Times from Summed Pulses

Individual pulses are very faint, if detectable at all, and they display small variations in profile shape and time of onset from one rotation to the next. As noted previously, mean profiles composed of several hundreds to thousands of pulses are stable. Therefore, to increase the S/N and stabilize the pulse profile, several hundred consecutive pulses are summed, and TOAs are extracted from these summed profiles. Arrival times are extracted by fitting a template of the pulse profile to each summed profile. The time of the pulse closest to the middle of the interval (which contains several hundred to thousand pulses) is recorded as the TOA. Each TOA refers to the same fiducial point in the profile template, which is ideally chosen such that it coincides with the time at which the pulsar magnetic pole crosses closest to the observer's line of sight. Observations are typically planned so that at least a few TOAs can be extracted (a single observation should be several times longer than the length of the interval from which TOAs are extracted).

The same template must be used to determine each TOA, even those at different observing frequencies, so that the time shift between the profile and the template relates all TOAs to the same fiducial point and starting time. The template can be a high S/N pulse profile from a previous observation, or more ideally, composed of Gaussians to reproduce its shape.

The uncertainty in the TOA measurement, from the radiometer equation, is the ratio of the pulse width to the profile S/N,

$$\sigma_{\rm TOA} \simeq \frac{W}{\rm S/N} \propto \frac{S_{\rm sys}}{\sqrt{t_{\rm obs}\Delta f}} \times \frac{P}{S_{\rm mean}}\,\delta^{3/2}, \tag{5.26}$$

where W is the pulse width, $S_{\rm sys}$ is the system equivalent flux density, $t_{\rm obs}$ is the integration time over which the TOA is extracted, Δf is the observing bandwidth, P is the pulse period, $\delta = W/P$ is the pulse duty cycle, and $S_{\rm mean}$ is the mean pulsar

flux density. The TOA uncertainty is therefore reduced for narrower, brighter pulses, larger bandwidths, lower $S_{\rm sys}$, and shorter periods. The use of summed pulse profiles increases the S/N and stabilizes the profile against variation in shape and onset time, further reducing the uncertainty as $\sigma_{\rm TOA} \propto \sqrt{1/N_{\rm pulses}}$.

5.3.1.2 Clock Corrections to Arrival Times

The second term in Equation 5.25 contains clock corrections that must be applied to each topocentric TOA. The TOA, defined by the time measured at a fiducial point on the summed pulse profile, is determined using hydrogen maser clocks at the observatory. It must ultimately be converted to Terrestrial Time (TT), the idealized geocentric time Seidelmann et al. (1992), defined by the time that would be recorded at the geoid (the equipotential surface coinciding with the mean sea level of Earth). The TT, measured in SI seconds, is on the same timescale as the International Atomic Time (TAI), which is determined by the average of many atomic clocks[4]; the time standards are related by TT = TAI + 32.184 s.

The TAI does not include leap seconds, and is related to the Coordinated Universal Time (UTC) by TAI = UTC + ΔT, where ΔT is the total sum of leap seconds since their adoption. The UTC is maintained by the Global Positioning System (GPS[5]). The TOA measured in local time is converted to UTC, and then to TT.

[4]The clocks are chosen, and their time maintained, by the Bureau International des Poids et Mesures (BIPM).

[5]The UTC is measured by the US National Institute of Standards and Technology (NIST).

5.3.1.3 Radio Frequency Corrections to Arrival Times

As discussed in Section 5.1.1, dispersion by the ISM causes radio pulses to be delayed in a frequency-dependent way, with higher-frequency waves arriving sooner than lower-frequency waves of the same pulse. Pulse arrival times therefore depend on f; in order to allow timing at different observing frequencies, TOAs must be corrected to the arrival time of a pulse with infinitely high f to remove the dispersion delay. The correction applied is the $\Delta D/f^2$ term in Equation 5.25. For f expressed in MHz and DM in $\mathrm{cm}^{-3}\,\mathrm{pc}$, $\Delta D = \mathcal{D} \times \mathrm{DM}$, where $\mathcal{D}$ is the dispersion constant and DM is the dispersion measure.

5.3.1.4 Transformation of Arrival Times to the Barycenter

The arrival times are transformed to the barycenter by correcting for the Römer, Shapiro, and Einstein delays. The Römer delay $\Delta_{R\odot}$ is the classical light travel time between the SSB and the phase center of the Earth-based telescope,

$$\Delta_{R\odot} = -\frac{1}{c}\mathbf{r}\cdot\hat{\mathbf{s}} = -\frac{1}{c}(\mathbf{r}_{\mathrm{SSB}} + \mathbf{r}_{\mathrm{EO}})\cdot\hat{\mathbf{s}}\ . \tag{5.27}$$

The unit vector $\hat{\mathbf{s}}$ points from the SSB to the pulsar position, and $\mathbf{r} = \mathbf{r}_{\mathrm{SSB}} + \mathbf{r}_{\mathrm{EO}}$ is the vector from the SSB and the telescope; $\mathbf{r}_{\mathrm{SSB}}$ points from the SSB to the geocenter, and $\mathbf{r}_{\mathrm{EO}}$ from the geocenter to the phase center of the telescope.

The Shapiro delay $\Delta_{S\odot}$ is a relativistic effect that increases the light travel time due to propagation through the curved spacetime near Solar System objects Shapiro (1964):

$$\Delta_{S\odot} = -2\sum_i \frac{GM_i}{c^3}\log\left[\frac{\hat{\mathbf{s}}\cdot\mathbf{r}_i^{\mathrm{E}} + r_i^{\mathrm{E}}}{\hat{\mathbf{s}}\cdot\mathbf{r}_i^{\mathrm{P}} + r_i^{\mathrm{P}}}\right]. \tag{5.28}$$

M_i is the mass of the i_{th} Solar System body, $\mathbf{r}_i^{\mathrm{P}}$ is the pulsar position relative to the body, and $\mathbf{r}_i^{\mathrm{E}}$ is the position of the telescope relative to the body at the moment when the photon is closest to the body.

As the Earth orbits, the gravitational potential within which it lies, dominated by the Sun, changes due to its elliptical orbit. This results in a gravitational redshift, to which the other Solar System bodies contribute, but to a lesser extent (in general, all bodies but the Sun and Jupiter have negligible contributions). The Einstein delay accounts for these time-varying effects, and is given by

$$\frac{\mathrm{d}\Delta_{E\odot}}{\mathrm{d}t} = \sum_i \frac{GM_i}{c^2 r_i^{\mathrm{E}}} + \frac{v_{\mathrm{E}}^2}{2c^2} - \text{constant}, \tag{5.29}$$

where r_i^{E} is the distance between Earth and body i, and v_{E} is the Earth's velocity relative to the Sun. This sum is over all Solar System bodies except the Earth.

Including these effects in Equation 5.25 is necessary to accurately barycenter the TOAs. They are also used to determine the pulsar position to high accuracy, and to measure proper motion and parallax for some pulsars (Section 5.3.1.6).

5.3.1.5 Finding a Phase-Connected Timing Solution

The goal of pulsar timing is to obtain a solution that accounts for every rotation that occurs between one observation and the next. Such a solution is *phase-connected*. For young pulsars, which have higher spin-down rates, the solution can go out of phase within a few months, so continued monitoring is necessary to maintain phase connection. MSPs are much steadier and have lower spin-down rates; once phase connection over a $>$ 1-yr timescale is achieved for an MSP, several years may go by before another set of TOA measurements is needed to update the solution.

To obtain a timing solution, the corrected TOAs of Equation 5.25 are used to fit for spin parameters (ν and its derivatives), astrometric parameters (e.g., pulsar position), and binary parameters if relevant Lorimer & Kramer (2005). These

parameters are initialized and fit for by minimizing

$$\chi^2 = \sum_i \left(\frac{N(t_i) - n_i}{\sigma_i} \right)^2, \tag{5.30}$$

where the σ_i are computed from Equation 5.26 In this way, the pulse number $N(t_i)$ (Equation 5.23) is matched to the barycentric TOA t_i. The integer nearest to $N(t_i)$ is n_i, and σ_i is the uncertainty in t_i in units of the pulse period, or number of pulsar rotations.

As will be described in the following section, pulsar timing is used to fit for pulsar position and other astrometric observables, in addition to the more obvious spin frequency and spin-down rate. To begin timing a solitary pulsar, the pulsar position is fixed at its discovery position, and all parameters except ν and the reference epoch are held constant; $\dot{\nu}$ is fixed at zero. The frequency is initialized with the value similar to that found in the search observations, and t_0 typically with the time of the first TOA, so the fit is likely to converge. TOAs from a few closely spaced (hours to days) observations are used to establish initial phase connection, and more TOAs from observations that are increasingly separated in time (days, up to ~ 1 month) are added, always being careful to maintain phase connection. Post-fit residuals like those shown in Figure 5.7 are used to test the quality of the fit. For a valid phase-connected timing solution, the post-fit residuals will consistently cluster around zero as a Gaussian distribution with a root mean square comparable to the TOA uncertainty Lorimer & Kramer (2005).

After several months to a year, the error in position will become significant enough that the RA and/or dec can become free parameters in the fit. The error resulting from $\dot{\nu}$ being fixed at zero is usually not separable from positional errors until after a full year of timing, as errors in position cause a 1-year periodicity in the post-fit timing residuals. The effects of incorrectly modeling some typical timing parameters are demonstrated in Figure 5.7.

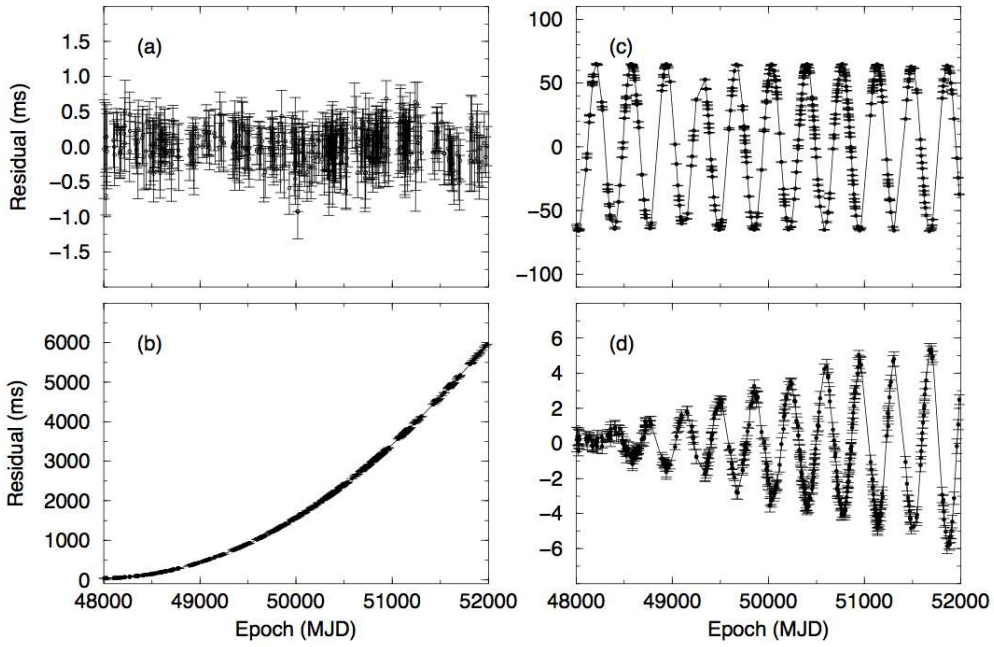

Figure 5.7: Illustration of residual patterns resulting from incorrect parameters, or parameters that have not been included, in the timing solution. (a) Timing residuals of a phase-connected timing solution. (b) Residuals resulting from setting $\dot{\nu} = 0$, thus showing the effect of not including the first frequency derivative. (c) Residuals from timing a pulsar with an inaccurate position. (d) Residuals from proper motion.

Binary timing is more complicated and will be discussed in Section 5.3.2.

5.3.1.6 Timing Position, Proper Motion, and Parallax

As stated above, pulsar timing can lead to improved position measurements, and in some cases to measurements of proper motion and parallax. The position is determined from the variation of the Römer delay, which causes a variation in pulse arrival times with a 1-year periodicity. The maximum amplitude of $\Delta_{\mathrm{R}\odot}$ is

$$\Delta_{\mathrm{R}\odot}^{\mathrm{max}} = \frac{1\mathrm{AU}}{c} \cos\beta \simeq 500 \cos\beta \ \mathrm{s} \tag{5.31}$$

where β is the ecliptic latitude. The position in ecliptic latitude is therefore poorly determined for pulsars lying near the ecliptic plane, and radio interferometric observations, or multi-wavelength observations where applicable (for example, X-ray observations with Chandra), are necessary to determine the position to higher accuracy.

The Römer delay also contributes to the measurement of proper motion, or transverse motion, in which the pulsar's transverse velocity $V_{\rm T}$ relative to the SSB causes a gradual change in $\hat{s}$ (Equation 5.27) and an additional time-dependent delay in Equation 5.25. The proper motion $\mu_{\rm T} = \sqrt{\mu_\alpha^2 + \mu_\delta^2}$, where $\mu_\delta \equiv \dot{\delta}$ is the change in declination and $\mu_\alpha \equiv \dot{\alpha}\cos\delta$ is the change in right ascension. Typical values of $\mu_{\rm T}$ are of order $\sim$few mas yr^{-1}. Measurements of the radial velocity $V_{\rm R}$ are technically possible, but require greater timing sensitivity than is currently available Lorimer & Kramer (2005).

Proper motion also causes the Shklovskii effect Shklovskii (1970) due to the gradual increase over time in the projected distance to the pulsar from the SSB. While the time delay introduced is generally too small to be included in timing analyses, it also increases the observed spin-down rate (and, for a binary pulsar, the rate of change of the orbital period) as

$$\frac{\dot{P}}{P} = \frac{1}{c}\frac{V_{\rm T}^2}{d} = 2.43 \times 10^{-21} \left(\frac{d}{\rm kpc}\right) \left(\frac{\mu_{\rm T}}{\rm mas\,yr^{-1}}\right)^2, \tag{5.32}$$

where P and $\dot{P}$ are the period and period derivative of a given periodicity (spin or orbital). This effect must be taken into account for nearby MSPs in particular—MSPs have small intrinsic spin-down rates, and if the distance is also small, then a significant amount of the measured spindown rate may be due to the Shklovskii effect rather than to intrinsic pulsar properties. Neglecting to account for this effect causes errors in the inferred spindown power $\dot{E}$, ages, and magnetic field strengths of MSPs Camilo et al. (1994). Additionally, in globular clusters where MSPs are prevalent,

the line of sight acceleration $a_{\rm los}$ (caused by the cluster potential) experienced by these MSPs produces an apparent spin period derivative, $\dot{P} = a_{\rm los}P/c$ that can be comparable to or even larger than the intrinsic $\dot{P}$. Some cluster MSPs therefore appear to have negative $\dot{P}$, such that their rotation speeds seem to be increasing rather than decreasing.

For nearby pulsars, the parallax and therefore distance may also be measured. Timing parallax is very different from positional parallax, in that it relies on changes in the curvature of the wavefront of the pulse at different positions in the Earth's orbit. This effect results in a variation of the pulse arrival time with amplitude $l^2 \cos\beta/(2cd)$, where l is the distance from the Earth to the Sun. The delay is very small ($\sim \mu$s), hence parallax and d are measured for only a few MSPs.

5.3.2 Binary Pulsar Timing

A comprehensive description of timing binary pulsars is given in Lorimer & Kramer (2005). In this section, I will cover the aspects that are relevant to this thesis —the Keplerian and post-Keplerian descriptions of binary motion, and neutron star and companion mass measurements.

Binary pulsars display periodic variations in their pulse arrival times, which are used to determine their orbital parameters. The parameters are contained in the Römer, Shapiro, and Einstein delays ($\Delta_{\rm Rb}$, $\Delta_{\rm Sb}$, and $\Delta_{\rm Eb}$, respectively) experienced by photons propagating through the pulsar's orbit, as well as an aberration delay $\Delta_{\rm Ab}$ introduced by the orbital motion. For a binary pulsar, the corrected TOAs are then

$$t^{\rm b}_{\rm SSB} = t^{\rm s}_{\rm SSB} + \Delta_{\rm Rb} + \Delta_{\rm Sb} + \Delta_{\rm Eb} + \Delta_{\rm Ab}, \tag{5.33}$$

where $t^{\rm s}_{\rm SSB}$ is from Equation 5.25. Timing of binary pulsars can be used to constrain or measure the masses of the pulsar and companion, to measure general relativistic

parameters, and to test and constrain general relativity in some cases.

5.3.2.1 Keplerian Orbits

Non-relativistic orbits can be described in terms of Kepler's laws. Five Keplerian parameters enter the TOA correction of Equation 5.33; these are the orbital period $P_{\rm b}$, the projected semimajor axis of the orbit $a_{\rm p} \sin i$ (where i is the inclination of the orbit to the plane of the sky), the orbital eccentricity, $e = b_{\rm p}/a_{\rm p}$ ($b_{\rm p}$ is the semiminor axis), the longitude of periastron, ω, and the epoch of periastron passage, T_0. Figure 5.8 illustrates the orbital parameters. These parameters are combined to define a set of angles present in orbits with $e > 0$, and which help to simplify formulae of effects resulting in arrival time delays. These angles are the mean anomaly M, the eccentric anomaly E, and the true anomaly $A_{\rm T}(E)$:

$$M = \Omega_{\rm b}(t - T_0), \tag{5.34}$$

$$E - e \sin E = \Omega_{\rm b} \left[(t - T_0) - \frac{1}{2} \frac{\dot{P}_{\rm b}}{P_{\rm b}} (t - T_0)^2 \right], \tag{5.35}$$

$$A_{\rm T}(E) = 2 \arctan \left(\sqrt{\frac{1+e}{1-e}} \tan \frac{E}{2} \right), \tag{5.36}$$

$$\omega = \omega_0 + \frac{\dot{\omega}}{\Omega_{\rm b}} A_{\rm T}(E) \, . \tag{5.37}$$

$\Omega_{\rm b} \equiv 2\pi/P_{\rm b}$ is the mean angular velocity of the pulsar in its orbit. For circular orbits ($e = 0$), $M = E = A_{\rm T}(E)$; for orbits that are unchanging with time, such that $\dot{P}_{\rm b}$ and $\dot{\omega}$ are zero, $M = E - e \sin E$. Most MSP orbits are circular and unchanging over the timescales of their monitoring observations, so there is often reference to the mean anomaly rather than the eccentric anomaly. However, as Equations 5.35 and 5.37 indicate, there are effects that can cause a secular change in the orbital period and the longitude of periastron. In Section 5.3.2.3, I will describe some of the effects that are specific to general relativity; these effects are relevant to this

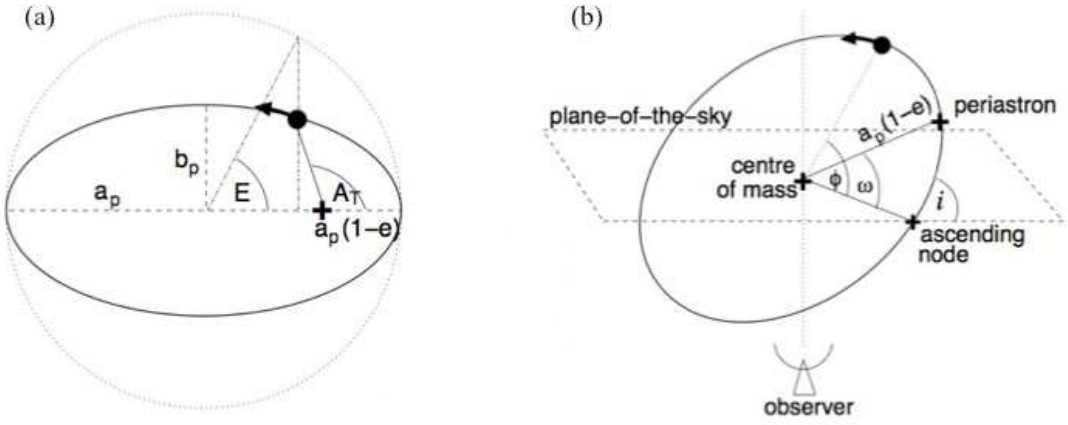

Figure 5.8: Orbital geometry with binary parameters, as described in the text; (a) shows the orbit as viewed face-on, while the orbit in (b) is inclined. This figure was taken from Lorimer & Kramer (2005).

thesis in that they may yield MSP mass measurements. Other effects are described in detail in Lorimer & Kramer (2005).

Provided the number of TOAs is larger than than number of timing parameters, the Keplerian parameters $P_{\rm b}$ (or $\Omega_{\rm b}$), e, $a_{\rm p}$, T_0, and ω_0 are derived using the Römer delay that results from the pulsar's orbital motion Blandford & Teukolsky (1976),

$$\Delta_{\rm Rb} = x(\cos E - e)\sin\omega + x\sin E\sqrt{1-e^2}\cos\omega, \tag{5.38}$$

where $x \equiv a_{\rm p}\sin i$ is commonly used to denote the projected semimajor axis of the orbit. The Römer delay also has a relativistic form, and the Einstein and Shapiro delays only appear as relativistic corrections (Section 5.3.2.3) to the Keplerian orbital description.

5.3.2.2 The Mass Function

Mass measurements are important for constraining the maximum neutron star mass, which gives information on the equation of state of the densest matter known to exist in the universe. A measurement of the total system mass, or, even better, the individual masses, also allows study of binary stellar evolution. GR effects must be measured in order to tightly constrain the masses of the individual pulsar and companion, but useful constraints can be placed on these masses using the *mass function*, derived from Kepler's Third Law. This function is

$$f(m_{\rm p}, m_{\rm c}) = \frac{(m_{\rm c} \sin i)^3}{(m_{\rm p} + m_{\rm c})^2} = \frac{4\pi^2}{G} \frac{(a_{\rm p} \sin i)^3}{P_{\rm b}^2} = \frac{4\pi^2}{T_\odot} \frac{x^3}{P_{\rm b}^2}, \tag{5.39}$$

where $G = 6.67 \times 10^{-8} \mathrm{cm^3\,g^{-1}\,s^{-2}}$ is Newton's gravitational constant, and $T_\odot = GM_\odot/c^3 = 4.925490947\mu$s is a conversion factor used to express masses and the mass function in solar units.

The mass function is used to determine the most likely class of companion (evolved main sequence star, white dwarf, neutron star, or black hole). For example, if the pulsar mass is assumed to be $1.4\,\mathrm{M}\odot$, then a low-mass white dwarf companion ($m_{\rm c} \sim 0.1\,\mathrm{M}\odot$) will yield $f(m_{\rm p}, m_{\rm c}) \leq 0.0004$. The value of $\sin i$ is unknown in most cases, but the minimum mass of the companion is found by setting $i = 90°$, providing another constraint on the object class. In the special case of eclipsing systems, the inclination is known to be $i \sim 90°$, allowing further constraints on the masses in these systems. (Note that for eclipses to imply $i \sim 90°$, the eclipsing system must not be a black widow system, in which the pulsar irradiates its companion and may be eclipsed by the resulting wind. The latter can be identified by observing frequency-dependent eclipse lengths, while the former shows the same length of eclipse at all frequencies.) The individual masses can be determined using the mass function along with two or more parameters from relativistic orbits

(below).

5.3.2.3 Post-Keplerian Parameters for Relativistic Orbits

If a pulsar is in a relativistic orbit, defined by its periastron velocity being a significant fraction of c, then additional parameters are introduced to describe the orbit. These parameters are "post-Keplerian" (PK) corrections to Keplerian orbits, and are derived from general relativity (e.g., Blandford & Teukolsky (1976)):

$$\dot{\omega} = 3T_{\odot}^{2/3}\left(\frac{P_{\rm b}}{2\pi}\right)^{-5/3}\frac{1}{1-e^2}(m_{\rm p}+m_{\rm c})^{2/3}, \tag{5.40}$$

$$\gamma = T_{\odot}^{2/3}\left(\frac{P_{\rm b}}{2\pi}\right)^{1/3} e\frac{m_{\rm c}(m_{\rm p}+2m_{\rm c})}{(m_{\rm p}+m_{\rm c})^{4/3}}, \tag{5.41}$$

$$r = T_{\odot}m_{\rm c}, \tag{5.42}$$

$$s = \sin i = T_{\odot}^{-1/3}\left(\frac{P_{\rm b}}{2\pi}\right)^{-2/3} x\frac{(m_{\rm p}+m_{\rm c})^{2/3}}{m_{\rm c}}, \tag{5.43}$$

$$\dot{P}_{\rm b} = -\frac{192\pi}{5}T_{\odot}^{5/3}\left(\frac{P_{\rm b}}{2\pi}\right)^{-5/3} f(e)\frac{m_{\rm p}m_{\rm c}}{(m_{\rm p}+m_{\rm c})^{1/3}}\ . \tag{5.44}$$

From Equation 5.39, $T_{\odot}$, $m_{\rm p}$, and $m_{\rm c}$ are respectively the solar mass conversion factor, pulsar mass, and companion mass, the latter two being expressed in units of solar mass; the factor

$$f(e) = \frac{1+(73/24)e^2+(37/96)e^4}{(1-e^2)^{7/2}}\ . \tag{5.45}$$

These parameters are dependent only on the unknown pulsar and companion masses. Neutron star masses can be constrained through measurement of one parameter, while measurement of two PK parameters results in the determination of $m_{\rm p}$ and $m_{\rm c}$. These masses are very interesting quantities that are rarely measured independently (see Section 5.3.2.2). If more than two of these parameters can be measured, then the additional measured parameters can be compared with their expected values as a way of testing Einstein's theory of general relativity. As is implied here, it

is difficult to measure even one or two PK parameters. The measurements require very high timing sensitivity, and with current sensitivity, some parameters are only measured in "lucky" circumstances; for example, r and s can only be measured via the PK Shapiro delay if the orbit is highly inclined.

As stated above, the PK parameters are measured using orbit-induced variations in pulse arrival times, for which Equation 5.33 summarizes the correction terms. The first PK parameter, $\dot{\omega}$, is the rate of change of the longitude of periastron; ω changes as the pulsar's orbit undergoes general relativistic precession. The parameter is obtained from the Keplerian Römer delay, $\Delta_{\rm Rb}$—because secular changes in the orbit can occur classically or relativistically, E and $\dot{\omega}$ are already related in Equations 5.34–5.37. The Römer delay also has a relativistic modification,

$$\Delta_{\rm Rb} = x(\cos E - e_{\rm r})\sin\omega + x\sin e\sqrt{1-e_\theta^2}\cos\omega, \tag{5.46}$$

in which two eccentricities appear: $e_{\rm r} = e(1+\delta_{\rm r})$ and $e_\theta = e(1+\delta_\theta)$. The parameters $\delta_{\rm r}$ and δ_θ are additional PK parameters Damour & Deruelle (1986); Damour & Taylor (1992) that describe periodic corrections to Keplerian motion due to relativistic deformations in the pulsar orbit. In practice, $\delta_{\rm r}$ is not measurable; δ_θ has not been measured, but a measurement may be possible after many years of timing a system Lorimer & Kramer (2005). Therefore, the Römer delay of Equation 5.38 is sufficient for measuring $\dot{\omega}$.

For low eccentricity orbits, it is difficult to constrain the value of ω, and therefore $\dot{\omega}$. Accurate measurements of $\dot{\omega}$ are therefore restricted to highly eccentric systems. Such systems are interesting both in terms of their evolutionary histories and in the possibility of measuring the total system mass $m_{\rm p}+m_{\rm c}$, which can lead to constraints on the neutron star mass.

The second PK parameter, γ, is measured from the Einstein delay, $\Delta_{\rm Eb}$, occurring within the pulsar's orbit. For a pulsar in a non-circular orbit, the changes

in gravitational redshift and time dilation experienced by photons passing through the companion's gravitational field cause variations in the pulse arrival time with amplitude γ (measured in seconds). The Einstein delay term is given by

$$\Delta_{\rm Eb} = \gamma \sin E \ . \tag{5.47}$$

The parameters r ("range") and s ("shape") are measured at once using the Shapiro delay, which is caused by an increase in the photons' travel time as they pass through the gravitational field of the companion:

$$\Delta_{\rm Sb} = -2r \ln \left[1 - e\cos E - s\left(\sin\omega(\cos E - e) + \sqrt{1-e^2}\cos\omega \sin E\right)\right] \ . \tag{5.48}$$

Note that $s = \sin i$ is simply a rearrangement of the mass function in Equation 5.39—the Shapiro delay results in a measurement of the orbital inclination, and hence a measurement of the total system mass. The change in the Shapiro delay over the orbits allows r and s to be measured. Because the delay also yields r, the masses $m_{\rm p}$ and $m_{\rm c}$ can be determined individually. The Shapiro delay was used in the mass measurement of the first $M = 2\,M_\odot$ neutron star, the binary pulsar PSR J1614−2230 Demorest et al. (2010).

The maximum Shapiro delay occurs at superior conjunction, when the companion is directly between the observer and the pulsar. The effect increases dramatically with orbital inclination, and is only measurable when the system is nearly edge-on (however, for $i = 90°$, the system will be eclipsing, preventing detection of pulses and hence of the Shapiro delay). Thus, while the Shapiro delay is incredibly useful for obtaining neutron star masses, it is also elusive in that only a small percentage of known binary systems are inclined enough to allow its measurement.

The fifth parameter, $\dot{P}_{\rm b}$, is the rate of change of the binary period due to orbital decay via gravitational radiation. The measurement of $\dot{P}_{\rm b}$ of PSR J1913+16 in the double neutron star binary system Taylor & Weisberg (1982); Weisberg et al. (2010)

matched precisely the GR prediction of orbital decay, and was thus deemed the first indirect detection of gravitational waves. The pulsar was originally discovered by Russell Hulse and Joseph Taylor, who won the 1993 Nobel Prize for their discovery.

The final term in Equation 5.25 accounts for aberration caused by the rotation of the pulsar—$\Delta_{\rm Ab}$ is the difference in pulse arrival times between those expected from radial oscillations and rotational motion. In practice, this effect is typically degenerate with the other PK parameters.

Another effect observed in a few relativistic systems is geodetic precession. The pulsar spin axis precesses around the system's total angular momentum vector, which is dominated by the orbital angular momentum of the system. As the pulsar precesses, the pulse profile changes, indicative of our line of sight crossing over different parts of the emission region and allowing the emission region to be mapped over time (e.g., Kramer (1998)). Geodetic precession is observed in several pulsars, including PSR J1913+16 Weisberg et al. (1989) and the double pulsar system, PSR J0737−3039 Breton et al. (2008).

5.3.3 Pulsar Timing in Practice

The first step in pulsar timing is to have a properly spaced cadence of observations so that an initial phase-connected timing solution may be established. Typically, the pulsar is observed 2-3 times every few hours to every other day, depending on how accelerated it is and on the observatory schedule; 2-3 times over the following week; once per week for 2-3 weeks; and then once per month for at least a year. The densely spaced observations can be taken anytime during that year, but it is best to do them first if possible, as timing can begin as soon as these observations are complete.

To extract TOAs, a pulse template is needed. The template is typically made

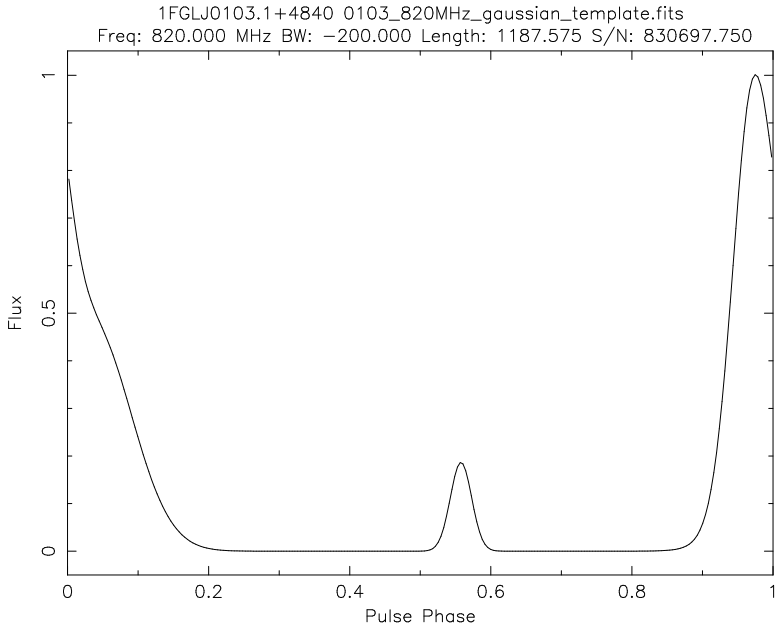

Figure 5.9: Example of a pulse template, constructed from three Gaussians, of PSR J0102+4839 at 820 MHz (the pulsar shown in Figures 5.5 and 5.6).

by fitting one or more Gaussians to the pulse profile of a long observation, such that the profile has a large enough S/N to ensure that the profile components are all included in the template. The template is then cross-correlated with profiles made from each segment of the observation in order to obtain a TOA from eat segment. If the pulse profile $\mathcal{P}(t)$ from the short segment is well represented by the template $\mathcal{T}(t)$ (allowing for re-normalization and shifting in phase), then

$$\mathcal{P}(t) = a + b\mathcal{T}(t - \tau) + \mathcal{N}(t) \tag{5.49}$$

where a is an arbitrary offset in phase, b is a scale factor, and $\mathcal{N}(t)$ is noise in the profile. The time shift τ between the profile and template gives the TOA relative to the zero-point of the template and the observation start time. TOAs can be extracted using the PRESTO script `get_TOAs.py`, or the PSRCHIVE[6] Hotan et al.

[6] `http://psrchive.sourceforge.net`

(2004); van Straten et al. (2012) command `pat`, if the data is archived in this format. The output TOAs are saved in a `.tim` file (e.g., `toas.tim`).

If the pulsar is isolated, fitting the timing model can begin at this stage. The initial conditions for the model parameters are saved in a `.par` file (e.g., `timing.par`), with values for all the relatively well known parameters (ν, DM, right ascension, declination), $\dot{\nu} = 0$ (F1 in a `.par` file), and only ν (F0) free.

If the pulsar is instead in a binary system, the orbital parameters can be estimated in some cases. If the pulsar is accelerated over the course of the observation, then it is reasonable to estimate that the observation was $\sim 20\%$ of the orbital period if the orbit is circular, and the semi-major axis in light seconds is about the orbital period in days. A more precise estimate can be obtained using a method presented by Freire et al. (2001), in which the period and the Doppler-induced period derivative (or ν and $\dot{\nu}_{\rm D}$) are fit to an orbital model. For a line-of-sight velocity $v_{\rm los} << c$, the observed Doppler-shifted pulse period can be approximated as

$$P(A_{\rm T}) \simeq P_0 \left(1 + \frac{v_{\rm los}(A_{\rm T})}{c}\right), \tag{5.50}$$

where P_0 is the pulsar's period in its rest frame. The acceleration $a_{\rm los}$ is found from the Doppler-shifted period derivative, $\dot{P}_{\rm D} = a_{\rm los} P/c$. The velocity $v_{\rm los}$ and acceleration $a_{\rm los} = {\rm d}v_{\rm los}/{\rm d}t$ are then related to the orbital parameters by

$$v_{\rm los}(A_{\rm T}) = \Omega_{\rm b} \frac{a_{\rm p} \sin i}{\sqrt{1-e^2}} [\cos(\omega + A_{\rm T}) + e\cos\omega], \tag{5.51}$$

$$a_{\rm los}(A_{\rm T}) = -\Omega_{\rm b}^2 \frac{a_{\rm p} \sin i}{\sqrt{1-e^2}} (1 + e\cos A_{\rm T})^2 \sin(\omega + A_{\rm T}) \ . \tag{5.52}$$

The orbital parameters can be estimated from $v_{\rm los}$ and $a_{\rm los}$. Figure 5.10 shows how this method can be used to constrain the orbital model, plotting acceleration against pulse period, with observations that are not spaced closely enough to determine the

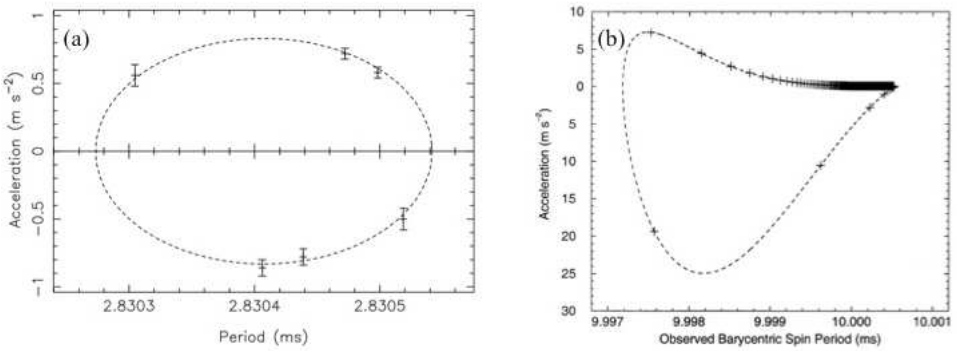

Figure 5.10: (a) The period-acceleration plane from a sparse sampling of the orbit of the globular cluster binary MSP 47 Tuc S. This pulsar has a circular orbit. The dashed line shows the best orbital model that has been fit to the data points. (b) The same plot, this time for a simulated pulsar in an eccentric orbit with $e = 0.9$. The pulsar was "observed" every 10 min, as marked by the '+' signs. Apastron is at the upper right, where $a_{\rm los} \sim 0\,{\rm m\,s^{-2}}$ and the orbit is most densely sampled.

parameters using Tempo[7] or TEMPO2[8] Hobbs et al. (2006).

The orbital, spin, DM, and astrometric parameters are initialized in the `.par` file with their best estimated values, the position and DM are fixed, and the spin frequency derivative is again set to zero. The orbital parameters and ν can be left free, although it may be useful to fix one or more orbital parameters at the best fit value and iterate until the solution is stable, at which point all parameters may be freed.

In the `.tim` file, identify which TOAs should immediately lead to a initial phase-connected solution. For example, the TOAs extracted from a single observation must be phase-connected, and may be connected for observations within a few days of each other. Groups of TOAs that are not expected to be phase-connected are

[7] `http://www.atnf.csiro.au/people/pulsar/tempo/`

[8] `http://www.atnf.csiro.au/research/pulsar/tempo2/`

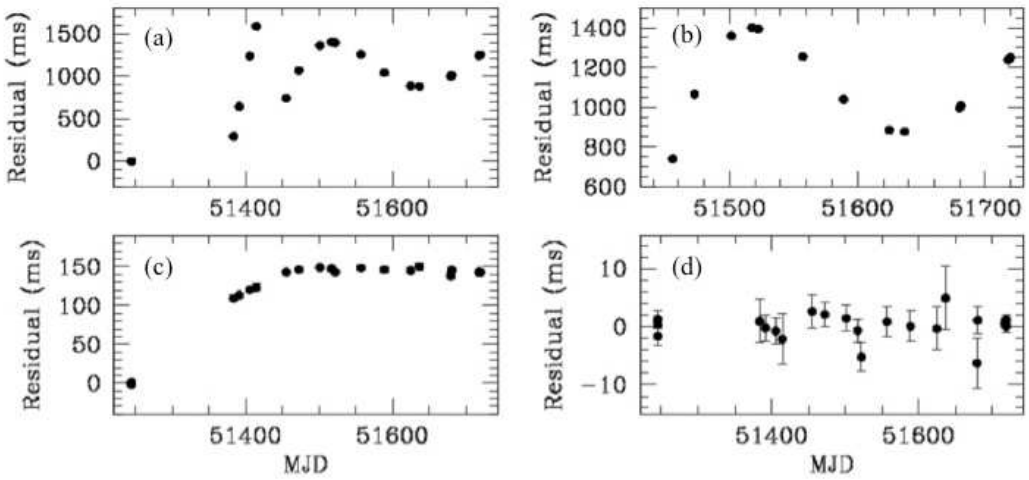

Figure 5.11: Example of timing residuals through the timing sequence, from http://www.cv.nrao.edu/course/astr534/PulsarTiming.html. (a) Phase connection is established between a few observations near MJD 51500. (b) The timing solution is extended until positional errors dominate; one position parameter is free and fit here. (c) The other position parameter is fit. (d) The fit now includes $\dot{\nu}$, flattening the residuals.

separated by typing "JUMP" above and below the TOAs from the disconnected observations. Then Tempo or TEMPO2 is run to fit an initial solution.

To run Tempo, type

```
tempo -f timing.par toas.tim  .
```

The timing residuals are contained in `timing.resid`. It is usually necessary to try different starting points and different combinations of JUMPs until two or more sets of TOAs are connected. From there, JUMPs from neighboring TOAs are gradually removed. After a few months, positional errors typically become significant, so the RA and/or declination parameter(s) can be freed. A year of timing is needed before positional errors and the intrinsic $\dot{\nu}$ become non-degenerate, so after a year $\dot{\nu}$ can be fit reliably. Continued monitoring may yield a parallax, proper motion, or other

interesting parameters, particularly if the pulsar is in a binary system. An example of the steps taken in pulsar timing is shown in Figure 5.11.

More details on pulsar timing are given in Lorimer & Kramer (2005), as well as in the Tempo and TEMPO2 manuals[9].

[9]Manuals for Tempo and TEMPO2 can be found at `http://www.atnf.csiro.au/people/pulsar/tempo/reference_manual.html` and `http://www.atnf.csiro.au/research/pulsar/ppta/tempo2/manual.pdf`

Chapter 6

Radio Pulsar Searches Guided by the LAT

The previous chapters focused on the study of pulsar magnetospheres and high-energy emission through geometrical modeling of their $> 100\,\mathrm{MeV}$ light curves and phase resolved modeling of their spectra. The *Fermi* LAT has advanced this field dramatically due to its high sensitivity, which has resulted in the discoveries of more than 100 new γ-ray pulsars and to excellent statistics, allowing quality light curves and spectra to be obtained for these pulsars. In this chapter, I switch gears to focus on a different aspect of the discovery space that has been opened by *Fermi*—that of targeted searches for, and discoveries of, millisecond pulsars (MSPs). Many LAT sources that previously had no multi-wavelength associations have since been found to be radio-loud γ-ray MSPs. Additionally, fourteen globular clusters have been detected by the LAT, allowing estimates of their MSP populations if the high-energy emission originates in MSP magnetospheres, as well as targets for MSP searches.

In this chapter, I will describe my discoveries of two MSPs, and the subsequent

timing and other analysis that I have done. The first MSP was found in a LAT source in the Galactic field, and was done in collaboration with a group led by Mallory Roberts[1]. The second MSP was discovered in a globular cluster that contained no known MSPs prior to this discovery. This latter pulsar was found as a result of my initiative to propose Green Bank telescope observations of LAT-detected globular clusters, in collaboration with Scott Ransom[2] and Paul Ray[3]. Initial timing has revealed this MSP to be a member of a very interesting and exotic binary system.

Unless otherwise noted, detailed descriptions of all LAT tools used in this work can be found on the Fermi Science Support Center (FSSC) data analysis website[4].

6.1 Radio Searches of Unassociated LAT Sources

Pulsars have been known to be pulsed γ-ray emitters since the detections of the Crab and Vela pulsars in the early 1970s (e.g., Browning et al. 1971; Grindlay et al. 1973b,a; Albats et al. 1974). By the end of the Compton Gamma-Ray Observatory (CGRO) mission, seven γ-ray pulsars had been detected, six of which were seen at $> 100\,\mathrm{MeV}$ with the Energetic Gamma-Ray Experiment Telescope (EGRET) (Thompson 2001, and references therein). It was therefore suspected that some of the unidentified EGRET sources (Hartman et al. 1999) may also be pulsars (Yadigaroglu & Romani 1995; Harding & Muslimov 2005), prompting multi-wavelength observations, in particular radio pulsation searches (e.g., searches of the bright EGRET source 3EG J1835+5918 by Halpern et al. 2002, 2007).

[1]Eureka Scientific

[2]National Radio Astronomy Observatory

[3]Naval Research Lab

[4]`http://fermi.gsfc.nasa.gov/ssc/data/analysis`

The *Fermi* LAT has similarly produced a list of sources that have no associated multi-wavelength counterparts (Ackermann et al. 2012; Nolan et al. 2012). The majority of these sources are blazars or other AGN, which are highly variable in γ-ray flux and have steep γ-ray power law spectra, but pulsars are expected to be a significant fraction of the population as well. Unlike AGN, pulsars show little to no variability, and their spectra are flatter with a cutoff energy $E_{\rm c} \sim$ few GeV. Thus, sources that display pulsar-like characteristics of low variability and high spectral curvature (indicative of a cutoff) were and continue to be preferentially searched for radio pulsations. Similar criteria were used to identify likely pulsar candidates with EGRET, although the spectral curvature was not as well determined due to the poorer statistics.

A major advantage the LAT has over EGRET, in addition to much higher sensitivity, is its much smaller point-spread function (PSF), which is $\sim 1^\circ$ at 1 GeV and decreases with increasing energy (Atwood et al. 2009). This results in a smaller error circle around the best position of a given source than was achievable with EGRET. The typical angular radius of the 95% error circle of an EGRET source was $\sim 0.5^\circ - 1^\circ$ (Hartman et al. 1999); the radio beam of the GBT at 350 MHz is 0.6° across. Several pointings were therefore required to search the full error circle of an EGRET source at low radio frequencies, and many pointings were required at higher frequencies, as the radio beam decreases in size with increasing spectral frequency f. LAT sources, on the other hand, have typical error circles of radius $0.1^\circ - 0.5^\circ$, and can easily be searched with a single radio observation at common frequencies for pulsar observing.

Several different groups, all organized under the Pulsar Search Consortium (PSC) (Ray et al. 2012) associated with *Fermi*, used telescopes around the world to search for radio pulsations from "pulsar-like" unassociated LAT sources, and were quite

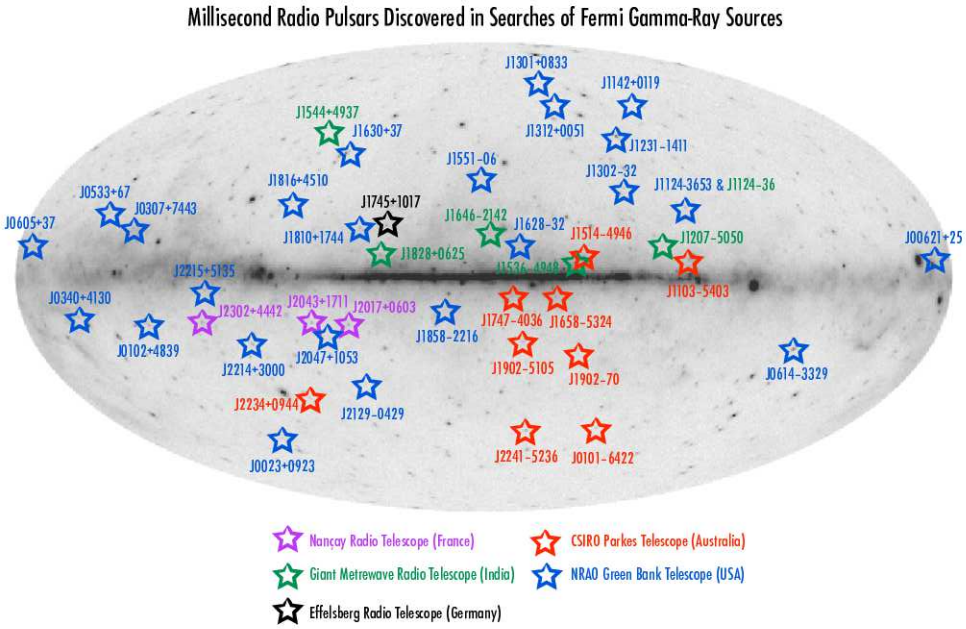

Figure 6.1: The sky positions of many of the MSPs that have been discovered in LAT-guided searches. Figure provided by Paul Ray.

successful. The large majority of the pulsars that have been discovered in this way are millisecond pulsars lying at high galactic latitudes (e.g., Ransom et al. 2011). After confirming their detections, the MSPs are timed for at least a year to establish a phase-connected timing solution that includes a measurement of $\dot{\nu}$. The sky locations of many of these MSPs are shown in Figure 6.1; several more have been found since this figure was made. At the time of writing, 50 new radio MSPs have been discovered in this way, 47 of which are definitely associated with the γ-ray source, and γ-ray pulsations from 34 of these have been detected by folding the γ-rays on the radio timing solution (P. Ray, private communication; The Fermi-LAT Collaboration 2013). Ongoing searches are continuing to find new MSPs.

6.2 PSR J0102+4839: A MSP in the Galactic Field

I contributed to a pulsar search program, led by Mallory Roberts, in which 50 faint LAT sources were searched with the GBT (Hessels et al. 2011). The sources chosen had no obvious blazar associations at other wavelengths, displayed little flux variability, and had pulsar-like γ-ray spectra. All sources lay at high galactic latitude, with $|b| > 5^\circ$, specifically chosen because scattering decreases significantly outside the Galactic plane. Ten MSPs have been discovered in these searches (Hessels et al. 2011). I found one of these MSPs, PSR J0102+4839.

6.2.1 Search Observations and Data Analysis

The unassociated LAT source 1FGL J0103.1+4840 was searched at 350 MHz using the GUPPI pulsar backend at the GBT. The bandwidth was 100 MHz, time resolution was 81.92 μs, and the integration time was 1 h. The 1FGL error circle had a radius $\sim 0.1^\circ$ (Abdo et al. 2010a), and easily fit inside the 350 MHz beam, which has a full-width-at-half-maximum (FWHM) of 0.6°. The beam was centered on the nominal position of the 1FGL source (RA = $1^{\rm h}\,03^{\rm m}\,11^{\rm s}.28$, Dec = $48^\circ\,40'\,15''.6$).

The observation was barycentered and de-dispersed at 8800 DMs from $0 - 105.6\,{\rm cm}^{-3}\,{\rm pc}$, and the Fourier transforms of the time series were processed with acceleration searches using $z_{\rm max} = 50$ (see Sections 5.2.2.1 and 5.2.4). A very strong pulsar candidate was found with barycentric $P = 2.964$ ms and $\dot{P} = -4.4 \times 10^{-12}$ s s^{-1} (Figure 6.2), indicating that it was undergoing acceleration from a binary orbit. The MSP was confirmed in a follow-up observation, and was incorporated into an ongoing timing campaign to measure the spin and binary parameters of

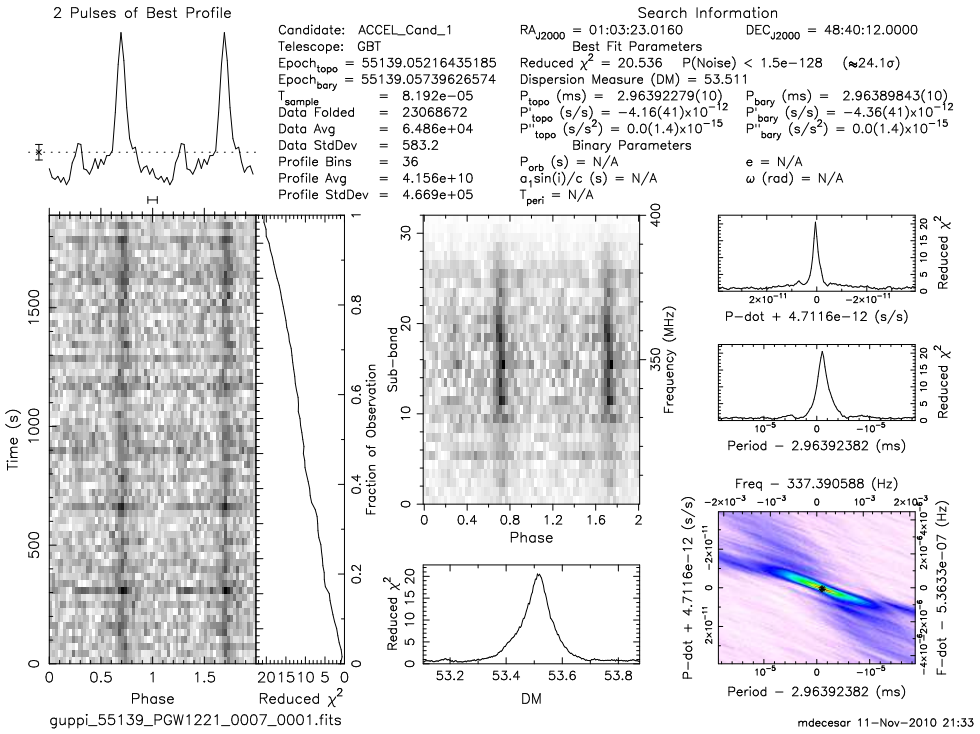

Figure 6.2: The discovery plot of PSR J0102+4839 from PRESTO. *Top left:* Two cycles of the 350 MHz pulse profile. *Left:* Two cycles of the pulse profile with time. *Top center:* Two cycles of the pulse profile over the radio frequency bandwidth of the observation. *Bottom center:* A search over DM yields a peak in DM, a signature of a real pulsar rather than a signal from interference, at DM = 53.5 cm^{-3} pc. *Top right:* The peak in reduced χ^2 is at the best period derivative searched. *Middle right:* The χ^2 peak shows the best pulse period. *Bottom right:* The χ^2 contours in $P - \dot{P}$ space, evaluated at the best DM value, showing the best-fit P and $\dot{P}$.

MSPs discovered in LAT sources.

6.2.2 Timing and Pulse Profiles

Timing observations of PSR J0102+4839 were taken between MJD 55514.7–56093.2 (2010 November 14 to 2012 June 15) by my collaborators and me. The observations were all performed with the GBT and GUPPI, with the majority of the data taken at

820 MHz with 200 MHz of bandwidth; a few observations were also taken at 350 and 1500 MHz (with bandwidths of 100 and 800 MHz, respectively). Observing at two or more radio frequencies allows for a more accurate determination of the DM, as it may then be fit along with the binary and spin parameters in the timing solution.

The pulse template was made by fitting three Gaussians to a long observation at 820 MHz. This template matched the pulse profile at 1500 MHz fairly well, but was different enough from the profile at 350 MHz that we chose to only use TOAs extracted from observations at the higher two radio frequencies. PSRCHIVE[5] (van Straten et al. 2012) was used to archive the data files and extract the TOAs, and Tempo[6] was used to time the pulsar as in Section 5.3.3.

Initial timing using the Tempo binary model `BT` found that the MSP has a very low eccentricity $e \sim 10^{-6}$ (nearly circular), which led to difficulty in locating the periastron using the Römer delay given in Equation 5.38. For low eccentricity orbits, the longitude of periastron, ω, and epoch of periastron passage, T_0, are highly correlated, leading to large uncertainties in their values. The `ELL1` binary model (Lange et al. 2001) in Tempo was therefore used to describe the MSP's orbit and complete the timing solution. This binary model provides an alternative description of Keplerian orbital motion by parameterizing e, T_0, and ω with the epoch of ascending node $T_{\rm asc}$ and the first and second Laplace-Lagrange parameters ϵ_1 and ϵ_2:

$$T_{\rm asc} = T_0 - \omega/\Omega_{\rm b}, \tag{6.1}$$

$$\epsilon_1 = e \sin\omega, \tag{6.2}$$

$$\epsilon_2 = e \cos\omega \ . \tag{6.3}$$

[5] `http://psrchive.sourceforge.net`

[6] `http://www.atnf.csiro.au/people/pulsar/tempo/`

Table 6.1. PSR J0102+4839 Timing Parameters

Timing Parameter	GBT Solution	LAT+GBT Solution
Start Time (MJD)	55514.7415	54729.7521
End Time (MJD)	56093.1598	56093.1598
$N_{\rm TOAs}$	298	314
Right ascension	$1^{\rm h}\,02^{\rm m}\,50^{\rm s}.6688(1)$	$1^{\rm h}\,02^{\rm m}\,50^{\rm s}.66898(9)$
Declination	$48^\circ\,39'\,42''.7635(6)$	$48^\circ\,39'\,42''.7625(6)$
Dispersion measure ($\rm cm^{-3}\,pc$)	53.5036(7)	53.5036[a]
Spin period, P (ms)	2.9641124215896(7)	2.9641124215878(3)
Spindown rate, $\dot{P}$ ($\rm s\,s^{-1}$)	$1.136(3) \times 10^{-20}$	$1.143(2) \times 10^{-20}$
Orbital period, $P_{\rm b}$ (days)	1.672149563(2)	1.672149565(2)
Projected semimajor axis, x (lt-s)	1.8558827(8)	1.8558824(8)
Epoch of ascending node, $T_{\rm asc}$ (MJD)	55514.5773301(2)	55514.5773300(2)
Laplace-Lagrange parameter, ϵ_1	$(2.2 \pm 0.7) \times 10^{-6}$	$(2.2 \pm 0.7) \times 10^{-6}$
Laplace-Lagrange parameter, ϵ_2	$(1.6 \pm 9.9) \times 10^{-7}$	$(-5.7 \pm 9.9) \times 10^{-7}$
Eccentricity, e	$(2.2 \pm 0.7) \times 10^{-6}$	$(2.3 \pm 0.8) \times 10^{-6}$
Epoch of periastron, T_0 (MJD)	55514.976 ± 0.123	55515.061 ± 0.113
Longitude of periastron, ω (degrees)	85.84 ± 26.42	104.23 ± 24.40

Note. — The best-fit timing solution parameters obtained with TOAs from the GBT only (center column) and from the GBT and LAT (right column). Sixteen TOAs were extracted from the LAT pulsations over the course of $\sim 3.75\,$yr. Because the pulsar was discovered after the beginning of the *Fermi* mission, the LAT TOAs are used to extend the timing solution backward to an earlier start time. The `ELL1` binary model parameters are $T_{\rm asc}$, ϵ_1, and ϵ_2; from these parameters, e, T_0, and ω were calculated using Equations 6.4–6.6. [a]The DM cannot be fit using LAT TOAs, so it was fixed at its best value from the radio timing solution.

The original parameters can then be calculated by

$$e = \sqrt{\epsilon_1^2 + \epsilon_2^2}, \tag{6.4}$$

$$\omega = \arctan\left(\epsilon_1/\epsilon_2\right), \tag{6.5}$$

$$T_0 = T_{\rm asc} + \frac{P_{\rm b}}{2\pi} \arctan\left(\epsilon_1/\epsilon_2\right) . \tag{6.6}$$

The radio timing solution given in Table 6.1 was found using 298 TOAs measured

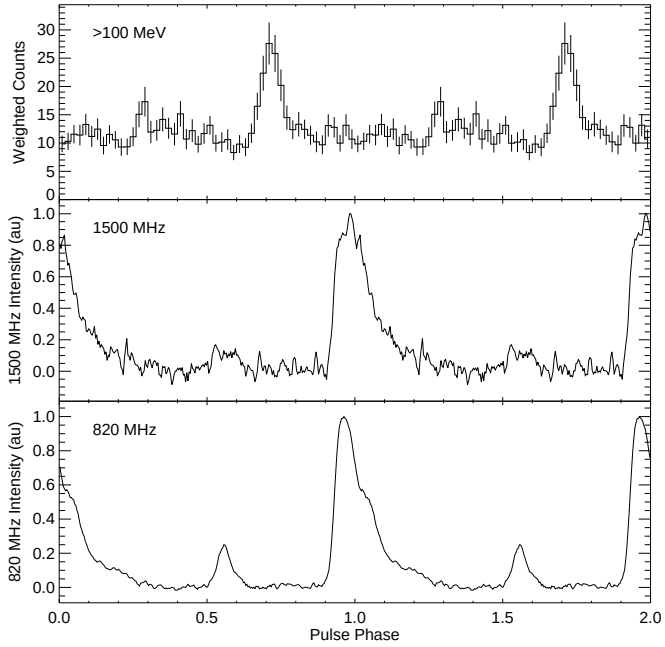

Figure 6.3: The light curves of PSR J0102+4839 at $E > 100\,\mathrm{MeV}$ (top), $f = 1500\,\mathrm{MHz}$ (middle), and $f = 820\,\mathrm{MHz}$ (bottom), made by folding the LAT and GBT observations on the best LAT+GBT timing solution. The radio light curve units are arbitrary. The LAT light curve is in units of LAT counts, or events, that have been weighted by the probability that the event originated from PSR J0102+4839. This probability was calculated with the LAT tool `gtsrcprob` using the pulsar's best fit spectral model from The Fermi-LAT Collaboration (2013).

between MJD 55514.74–56093.16. Using this timing solution, the LAT counts were folded, resulting in the detection of pulsed γ-rays from this MSP. The LAT pulse profile was then used to make a γ-ray template, extract 16 additional TOAs from the LAT counts, and extend the timing solution backward to the beginning of the *Fermi* mission. This solution, obtained using radio and LAT TOAs together, is also given in Table 6.1. The RMS residual for the radio solution is $8.436\,\mu$s (0.0028 in phase), and for the LAT+GBT solution is $8.881\,\mu$s (0.0030 in phase). The 820 MHz, 1500 MHz, and $> 100\,\mathrm{GeV}$ pulse profiles (light curves) are shown in Figure 6.3.

These profiles were made using the LAT+radio timing solution, and are available publicly through the Second LAT Pulsar Catalog (The Fermi-LAT Collaboration 2013).

The mass function (Equation 5.39) derived from the timing solution is $f(m_{\rm p}, m_{\rm c}) = 0.0024546(6)\,{\rm M}_\odot$, resulting in minimum, median, and maximum companion masses of $0.1790\,{\rm M}_\odot$, $0.2095\,{\rm M}_\odot$, and $0.4595\,{\rm M}_\odot$, assuming a pulsar mass of $1.4\,{\rm M}_\odot$. The characteristic age $\tau_{\rm c} \sim 4.1\,{\rm Gyr}$, and the surface magnetic field $B_{\rm S} \sim 1.86 \times 10^8\,{\rm G}$ (Equation 1.5).

The distance of PSR J0102+4839, estimated from its DM using the NE2001 model (Cordes & Lazio 2002, also see Section 5.1.1), is $d \sim 2.3\,{\rm kpc}$. At this distance, it may be possible to detect the MSP's proper motion. An attempt to measure the proper motion using pulsar timing resulted in unconstrained measurements of motion in both right ascension and declination. Further timing of this pulsar over several years may yield a proper motion measurement.

6.2.3 Polarization Analysis

Once the timing solution was well-established, an observation of PSR J0102+4839 was taken at 820 MHz in full-Stokes mode to allow for an analysis of the MSP's polarized emission, resulting in the polarized profile shown in Figure 6.4 (the profile has been rotated by an arbitrary phase shift in order to show the profile clearly). The rotation measure (RM, which is a measure of the pulse delay in terms of phase rotations due to Faraday rotation; see Section 4.1.2 of Lorimer & Kramer 2005) was fit to the polarized data, yielding ${\rm RM} = -86.3 \pm 0.8\,{\rm rad\,m^{-2}}$. Calibrating the polarized profile gave an average flux density of $S_{820} = 0.541 \pm 0.005\,{\rm mJy}$.

The 820 MHz profile in Figure 6.4 is mostly linearly polarized (red), with a hint of negative circular polarization through the main peak. The main peak is asymmet-

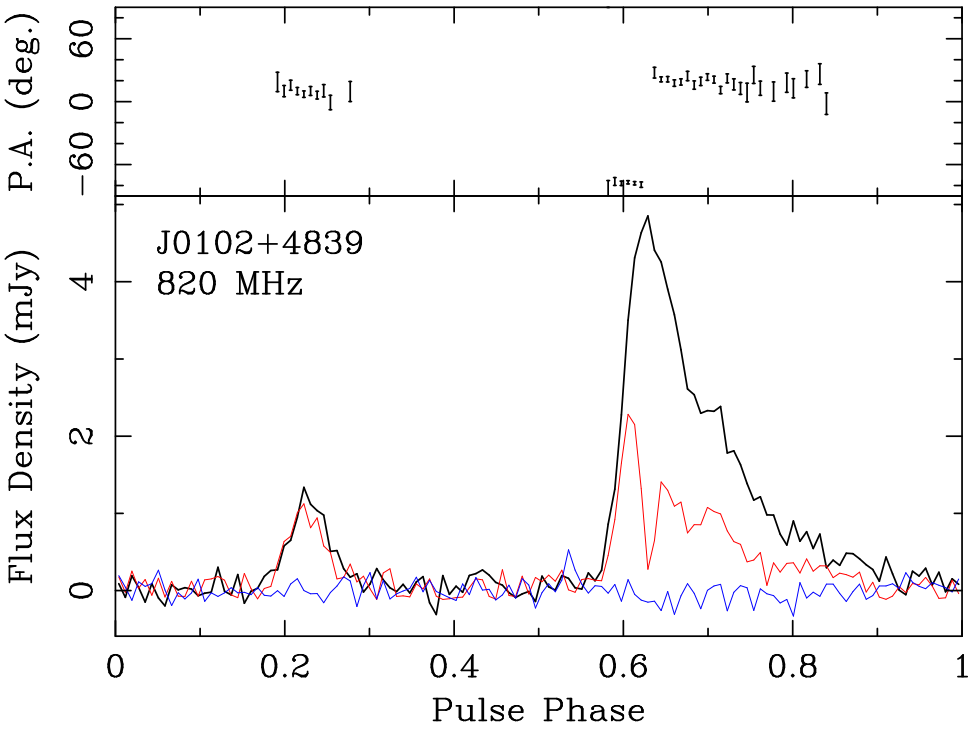

Figure 6.4: The 820 MHz polarized profiles of PSR J0102+4839. In the bottom panel, the linearly polarized emission is shown with the red line, circularly polarized with the blue line, and total intensity with the black line. The P.A. (top panel) is plotted for all bins in which the linear polarization S/N > 2.5. The P.A. has been corrected for Faraday rotation, so that the P.A. is what it would be in the pulsar's frame rather than at the Earth.

rically shaped, and it appears to contain at least two linearly polarized components, with a possible third component in the tail of the peak. This is consistent with the averaged profile (black, and also shown in Figure 6.3), in which the tail of the main peak seems to be a separate emission component.

The position angle (P.A.) in the top panel of the figure has been corrected for Faraday rotation, such that the P.A. is that of the pulsar's rest frame rather than what is observed at Earth, and is plotted at all phases in which its S/N > 2.5. The P.A. is maximum at the center of the main peak, and decreases gradually through the tail of the peak before the S/N of the polarized emission drops below

the threshold. It becomes measurable again within the smaller peak, and could be connected with a single line to the P.A. values in the tail of the main peak. In the rise of the main peak, the P.A. $\sim -80°$; it rises to $\sim 10°$ at the highest point of the main peak. Thus, there appears to be a 90° P.A. jump, indicative of the onset of an orthogonal polarization mode. This mode change occurs at the same phase as the onset of the second linearly polarized feature in the main peak, providing additional evidence for separate emission components within this peak.

Flat P.A. swings and orthogonal modes are fairly common in MSP polarization data, as evidenced by the polarized profiles compiled by, e.g., Ord et al. (2004) and Yan et al. (2011). The P.A. swings of MSPs are often difficult to reconcile with the traditional model of pulsar polarization, the Rotating Vector Model (RVM; Radhakrishnan & Cooke 1969a), in which the radio emission is assumed to originate at or near the polar cap surface. Fitting the P.A. swing with a modified version of the RVM (e.g., Blaskiewicz et al. 1991) may constrain $\beta = |\alpha - \zeta|$, and might constrain α as well as the radio emission altitude. A RVM fit was not done for this thesis.

6.2.4 Gamma-ray Spectrum

The phase averaged spectrum of PSR J0102+4839 was modeled over the energy range 0.1–300 GeV using four years of data from the *Fermi* LAT. Only counts in the "Source" event class (in the LAT `gtselect` tool, `evclass`= 1) were used to fit the spectrum. With the `gtmktime` tool, the counts were filtered using a ROI-based zenith cut in which counts originating from a zenith angle $z > 100°$ from the LAT zenith were not included in the dataset. Good time intervals were determined using the filter expression "`DATA_QUAL==1 && LAT_CONFIG==1 && ABS(ROCK_ANGLE)<52`", also using the `gtmktime` tool.

Spectral analysis of PSR J0102+4839 was performed with the LAT likelihood analysis tool `gtlike`, run within *python*. The fit was done within a $20^\circ \times 20^\circ$ Region of Interest (ROI) centered on the timing position of PSR J0102+4839, using 34 logarithmically spaced energy bins with 10 bins per logarithmic decade in energy. The spectral+spatial model, contained in an XML file, included sources within a 20° radius of the central pulsar. All spectral parameters of sources lying within a 10° degree radius of PSR J0102+4839 were left free, while all parameters of source outside this radius were fixed at their 2FGL (Nolan et al. 2012) values.

The spectrum was fit with three different spectral models: a simple power law,

$$\frac{dN}{dE} = K_0 \left(\frac{E}{E_0} \right)^{\Gamma}, \tag{6.7}$$

a broken power law (BPL),

$$\frac{dN}{dE} = K_0 \times \begin{cases} (E/E_\mathrm{b})^{\Gamma_1} & \text{if } E \leq E_\mathrm{b} \\ (E/E_\mathrm{b})^{\Gamma_2} & \text{otherwise} \end{cases}, \tag{6.8}$$

and a power law with an exponential cutoff (ECPL),

$$\frac{dN}{dE} = K_0 \left(\frac{E}{E_0} \right)^{\Gamma} \exp\left[\left(\frac{E}{E_\mathrm{c}} \right)^{b} \right]. \tag{6.9}$$

In each model, K_0 is the differential flux prefactor. E_0 in the PL and ECPL models is a scale factor, for which the 2FGL value of the pivot energy is used; this value is $E_0 = 1.372\,\mathrm{GeV}$ for PSR J0102+4839. Γ in the PL and ECPL represents the spectral index; in the BPL model, Γ_1 is the spectral index at energies lower than the break energy E_b, while Γ_2 is the spectral index at $E > E_\mathrm{b}$. In the ECPL, b determines whether the roll-off above the cutoff energy E_c is exponential ($b = 1$), sub-exponential ($b < 1$), or super-exponential ($b > 1$). Pulsars with high count rates, for example bright pulsars like Vela and the Crab, all show $b < 1$, caused by significant variation in E_cutoff with rotation phase.

The test statistic, or TS, is used as a measure of the significance of a source in a model, or of a parameter in the spectral model of an individual source. It is defined as

$$TS = -2\ln(\mathcal{L}_1/\mathcal{L}_2) \ . \tag{6.10}$$

In the case of testing whether or not a source should be included in the model of the region, $\mathcal{L}_\in$ is the likelihood of a model that includes the source in question, and $\mathcal{L}_\infty$ is the likelihood of a model that does not include the source. Sources with extremely low TS, especially $TS < 0$, are likely not true sources but rather poorly modeled fluctuations in the diffuse background that were bright enough to be considered as sources in the Second LAT Catalog (Nolan et al. 2012). Such sources can alter a spectral fit, and may result in pockets of significantly negative residuals when differencing the model and counts map. It is therefore undesirable to include very low-TS sources in a spectral model. For example, in the Second Pulsar Catalog (The Fermi-LAT Collaboration 2013), sources with $TS < 2$ were removed from the spectral models before obtaining a final spectrum.

In this work, a more conservative value of $TS = 0.5$ was used as the threshold for whether or not to include a source in the spectral model. After an initial fit to an absolute tolerance in likelihood $\mathcal{L}$ of 0.01, sources with $TS < 0.5$ were removed from the fit. This step was done simultaneously for all spectral models, so that the same sources were removed from each model, hence preserving the ability to statistically compare the models. A source was therefore removed only if it met the criterion $TS < 0.5$ in each of the model fits, or if its $TS < 0$ in one or more of the fits. After removing these low-TS sources, the fits were repeated to an absolute tolerance in $\mathcal{L}$ of 0.001. The spectral parameters are given in Table 6.2.

Pulsars that are bright in γ-rays, and therefore have high count rates, show a sub-exponential cutoff ($b < 1$) rather than a purely exponential cutoff ($b = 1$)

Table 6.2. Spectral Model Parameters and Comparison

Model Parameter	PL	ECPL ($b = 1$)	BPL
K_0	0.947 ± 0.084	2.232 ± 0.463	0.941 ± 0.390
Γ	-2.148 ± 0.054	-1.307 ± 0.238	$\cdots$
$E_{\rm c}$	$\cdots$	2.828 ± 0.826	$\cdots$
Γ_1	$\cdots$	$\cdots$	-1.358 ± 0.277
Γ_2	$\cdots$	$\cdots$	-3.113 ± 0.258
$E_{\rm b}$	$\cdots$	$\cdots$	1.950 ± 0.342
F_{100}	2.289 ± 0.295	1.218 ± 0.306	1.058 ± 0.336
G_{100}	1.233 ± 0.118	0.811 ± 0.091	0.795 ± 0.097
TS	276.6	308.9	307.2
Model Comparison			
$-\ln\mathcal{L}$	492812.4	492792.6	492791.2
ΔTS	$\cdots$	39.8	42.4
$N_{\rm free}$	36	37	38
AIC	985696.8	985659.1	985658.4

Note. — The top part of the table lists the best-fit spectral parameters, as well as the source fluxes and TS, for each of the three models considered (Equations 6.7–6.9). F_{100} and G_{100} are respectively the 0.1–300 GeV photon flux and energy flux calculated from each model. K_0 is given in units of $10^{-12}\,{\rm cm}^{-2}\,{\rm s}^{-1}\,{\rm MeV}^{-1}$; energies $E_{\rm c}$ and $E_{\rm b}$ are measured in GeV; the 0.1–300 GeV photon flux F_{100} is in units of $10^{-8}\,{\rm photons\,cm}^{-2}\,{\rm s}^{-1}$; and the 0.1–300 GeV energy flux is given in $10^{-11}{\rm erg\,cm}^{-2}\,{\rm s}^{-1}$. The bottom part of the table provides the values that were used to compare the models' goodness of fit. The likelihood $-\ln\mathcal{L}$ was calculated from `gtlike`. ΔTS is the change in TS between the ECPL and BPL models, as compared to the PL model, and can be thought of as the TS of the cutoff or break energy, respectively. $N_{\rm free}$ is the number of model parameters that were left free in each fit, and the AIC is the Akaike Information Criterion, used to measure the *relative* goodness of fit of the three models.

in their phase-averaged spectra. I therefore fit the spectrum of PSR J0102+4839 with the ECPL model again, this time allowing the b parameter to be free. The improvement to the fit, as compared to the ECPL model with $b = 1$ fixed, was insignificant, with $\Delta TS(b < 1, b = 1) = 1.9$. I therefore only included the best-fit parameters obtained with the ECPL ($b = 1$) model in Table 6.2.

I used two methods to test the goodness of fit of the models. The first is the likelihood ratio test, which can be used to compare nested models. This test calculates the test statistic as previously given in Equation 6.10,

$$TS = -2\ln(\mathcal{L}_1/\mathcal{L}_2) \tag{6.11}$$

where, in this case, $\mathcal{L}_1$ is the likelihood of the simpler model (with fewer parameters) computed by `gtlike`, and $\mathcal{L}_2$ is the likelihood of the more complex model. The significance of the improvement of model 2 over model 1 is $\sigma \approx \sqrt{TS}$. We use the TS to test, for example, the significance of the cutoff in the ECPL model, compared to the lack of a cutoff in the power law model.

The second test is a Bayesian test, the Akaike Information Criterion (AIC), which determines the relative goodness of fit between different models,

$$AIC = 2N_{\rm free} - 2\ln\mathcal{L} \tag{6.12}$$

where $N_{\rm free}$ is the number of free parameters in the fit, and $\mathcal{L}$ is the resulting likelihood from the fit. The model yielding the lowest AIC is the best of the models considered.

Because the AIC and TS measure relative goodness of fit, they cannot be used to determine whether the best fit model actually gives a good fit to the data. That the fit is satisfactory is determined 1) by comparing the full energy range fit with the spectral energy distribution (SED); and 2) by using the best fit model to reconstruct the ROI, and then calculating a residual map in units of σ, where

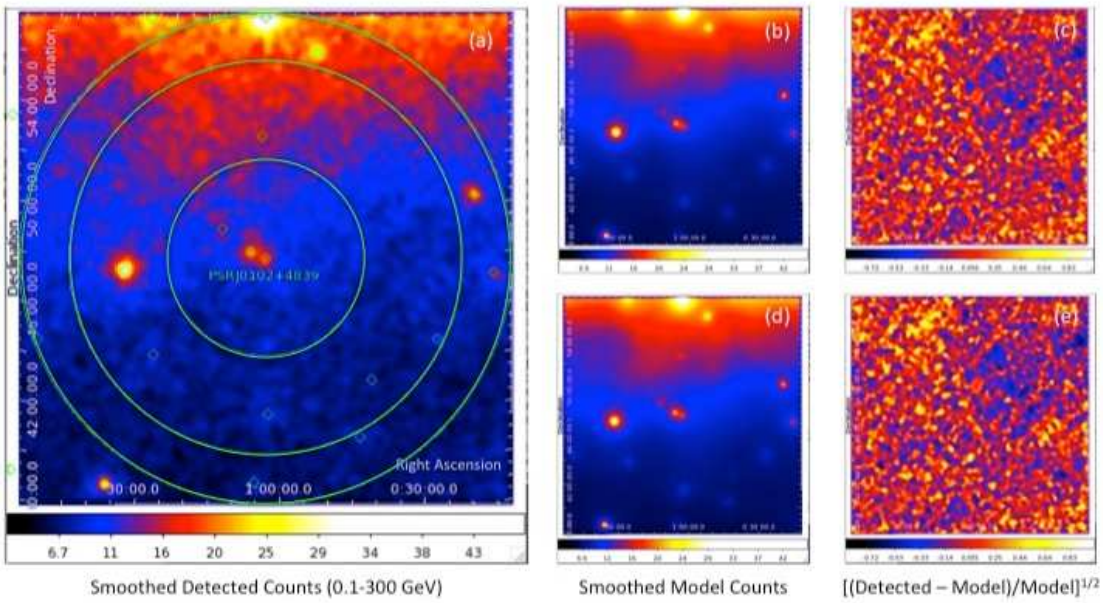

Figure 6.5: The LAT counts map, model maps, and residual maps of the region of interest centered on PSR J0102+4839, which are used to test that the ECPL and BPL spectral models gave satisfactory fits to the $> 100\,\mathrm{MeV}$ spectrum of this pulsar. (a) The counts map of the $20^\circ \times 20^\circ$ region in which the likelihood analysis was performed. PSR J0102+4839 is at the center of the map. Other sources are marked with green diamonds. The green reference circles mark radial distance of 4°, 8°, and 10° from the center of the map. (b) A model map of the region, made using the best-fit BPL spectral parameters of PSR J0102+4839 and surrounding sources. The colors represent zero counts (black) to 42 counts (white) in panels (b) and (c). (c) A model map of the region, this time made using the best-fit ECPL parameters. (d) The (counts − model)/model) residual map obtained from the BPL model map and the counts map. The colors represent $\sigma = 0$ (black) to 0.83 (white) in panels (d) and (e). (e) The residual map obtained with the ECPL model map.

$\sigma = [(\text{detected counts} - \text{model counts})/(\text{model counts})]^{1/2}$ to ensure that the pulsar has been removed (fluctuations are all at the level of the background, $\leq 1\sigma$). The latter is done using the LAT tools `gtbin` and `gtmodel`, and `ftpixcalc` from NASA's HEASARC FTOOLS[7].

[7] `https://heasarc.gsfc.nasa.gov/ftools/`

Both steps were taken to ensure that the fit parameters presented here are valid. The counts map, model maps, and residual maps are shown in Figure 6.5 for the ECPL and BPL models. Each map was smoothed with a Gaussian kernel with a 3-pixel radius, where 1 pixel is 0.1° across. Figure 6.5(a) shows the counts map centered on PSR J0102+4839. The sources used in the spectral fit are marked with diamonds (but not labeled to avoid over-crowding the image). The circles are of radius 4°, 8°, and 10°. In panels (b) and (d), the model maps made from the best-fit spectral parameters of the sources are shown for the BPL and ECPL models, respectively. The residuals between the counts map and model maps of the BPL and ECPL models are shown respectively in panels (c) and (e), and are in units of $\sigma = [(\text{detected counts} - \text{model counts})/(\text{model counts})]^{1/2}$. The highest $\sigma \sim 4$ in the residuals prior to smoothing; in the residual maps shown here, smoothing has reduced the maximum σ to ~ 0.8. Continuing to smooth with larger kernels results in the residuals flattening to $\sigma \sim 0.03$ across the region of the ROI where PSR J0102+4839 lies. The fact that there is no significant source remaining at the MSP's location in the residual maps suggests that both spectral fits are acceptable.

To make SEDs with `bdlikeSED.py`[8], the counts were divided into six energy bands spaced logarithmically between 0.1–300 GeV. The spectrum within each band was fit with a simple power law, from which the flux was calculated. For these individual band fits, the normalization factors (e.g., K_0) of all sources within 8° were left free, while the other parameters (e.g., spectral indices and cutoff or break energies) were fixed at their best-fit values from the fit over the full energy range. Outside 8°, all parameters were fixed. The radius of 8° was chosen to be consistent with the analysis in the LAT Second Pulsar Catalog (The Fermi-LAT Collaboration

[8] `http://fermi.gsfc.nasa.gov/ssc/data/analysis/user/likeSEDmacros_UsageNotes_v13.pdf`

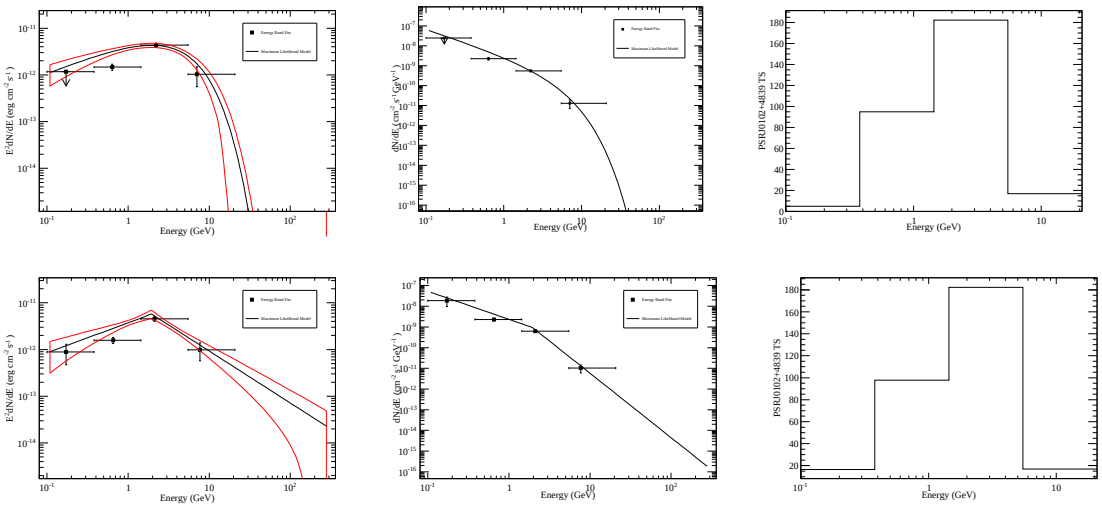

Figure 6.6: *Top:* From left to right are shown the SED, counts spectrum, and energy band TS of PSR J0102+4839, fit with the ECPL model. *(Bottom)* The SED, counts spectrum, and energy band TS from the BPL model.

2013).

The SEDs for the ECPL and BPL models are shown in Figure 6.6. The spectral points are similar, but not identical, between the two models. This is because the parameters of the pulsar and background were based on the best fit parameters for each type of model, and most of the parameters were fixed in order to fit the SED. This means the model in each energy band will be different depending on the model parameters of the other background sources in the ROI. No flux points are shown above 10 GeV, presumably because the lack of counts above this energy prevented the spectral fit from converging.

I therefore find that for PSR J0102+4839, both the ECPL ($b = 1$) and BPL spectral models describe the pulsar's γ-ray spectrum adequately well. Calculating the TS and AIC for both models, I find that neither is strongly preferred over the other. However, it is expected that a sub-exponentially cut-off power law (ECPL

with $b < 1$) will fit the spectrum best, as has been seen for very bright pulsars. With improved statistics, it should eventually be possible to differentiate between the two models, as well as to fit the ECPL model with a free $b < 1$.

6.2.5 Discussion

PSR J0102+4839 is a ~ 3 ms MSP that was discovered in an unassociated LAT source. The radio timing solution yielded a detection of γ-ray pulsations, making it a new γ-ray MSP. Its radio emission is significantly linearly polarized at 820 MHz. Its γ-ray spectrum is well fit by an exponentially cut-off power law or a broken power law. As the *Fermi* mission continues, the detected counts will increase, and it may be possible to differentiate between these two models, as well as to fit the spectrum with a sub-exponentially cut-off power law. A measurement of proper motion was not possible from the current timing solution. However, with continued timing at radio frequencies, this measurement may become possible in the future.

To date, the primary goal of LAT-guided radio pulsar searches has been to find and time more pulsars, especially MSPs, and to subsequently increase the number of known γ-ray pulsars by folding the LAT counts on the radio timing solution. Beyond cataloguing these new pulsars, there is much science to be done with these MSPs, including PSR J0102+4839. The vast majority of the pulsars found in these searches are MSPs. Continued timing of these MSPs can potentially lead to measurements of proper motion, mass, and other physical quantities of interest. Several of them have been found to have very stable timing solutions, meaning that timing them over years to decades will result in nanosecond-scale timing residuals. The NANOGrav collaboration is therefore continuing to time a subset of these recently discovered MSPs, with the goal of a direct detection of gravitational radiation using a pulsar timing array. Another subset of MSPs found in these searches is composed of "black

widow" (BW) and "redback" (RB) pulsars that are evaporating their companions. Prior to the *Fermi* mission, only three such systems were known; the LAT-guided searches led to the discoveries of 19 new BW/RB systems (Roberts 2013, and references therein), allowing the study of a larger sample of these objects. The increased number of radio and γ-ray MSPs will also allow a study of MSP emission geometry: the position angle of linearly polarized pulsar emission can be used to constrain the radio emission geometry and emission altitude (e.g., Radhakrishnan & Cooke 1969b; Blaskiewicz et al. 1991; Craig & Romani 2012), and γ-ray light curve modeling can also be used to constrain the emission geometry and the γ-ray emission mechanism.

6.3 PSR J1835−3259: A New Globular Cluster MSP in NGC 6652

The LAT has guided successful searches for MSPs in the Galactic field, as described in the previous section. It has also led to the discovery of a new globular cluster MSP, through the detection of γ-ray emission from globular clusters. Initial timing of this MSP indicates that its orbit is highly eccentric, and that its companion is unusually massive, suggesting that this binary system may be very interesting for constraining the pulsar mass and studying globular cluster binary evolution.

6.3.1 LAT Detections of Globular Clusters

Venter & de Jager (2008) predicted that globular clusters (GCs) would be detected at γ-ray energies if MSPs were γ-ray emitters; MSPs were confirmed to be pulsed γ-ray sources in the months following *Fermi*'s launch (Abdo et al. 2009b). The shape of the GC γ-ray spectrum was predicted to be a sub-exponentially cutoff power law,

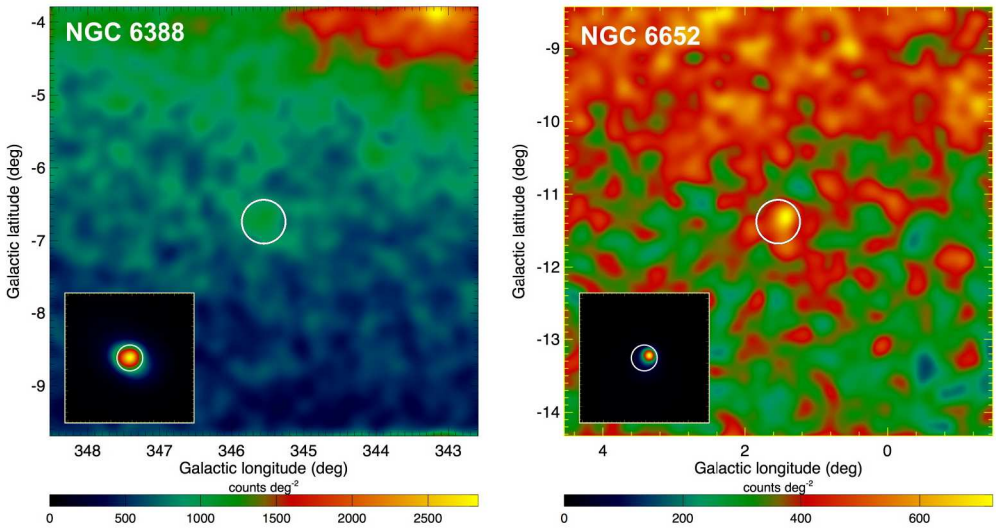

Figure 6.7: The > 100 MeV LAT counts maps of the globular clusters NGC 6388 and NGC 6652, from Abdo et al. (2010f). The large maps show the diffuse emission of the Galactic plane; the faintest emission is dark blue, and the brightest emission from the central region of the plane is yellow. The white circles mark the locations of the clusters in the maps. The insets show maps of the TS of the cluster emission, which can be thought of as background-subtracted maps of the clusters, made by fitting a spatial and spectral model to the data shown in the large images. Both clusters are detected with high significance, and lie within $\sim 10^{\circ}$ of the Galactic plane.

due to the combined spectra of its MSPs (Venter & de Jager 2008). 47 Tuc and Terzan 5, the two GCs with the highest number of known MSPs (Ransom et al. 2005; Camilo & Rasio 2005), were detected by the LAT early in the *Fermi* mission. Later, six more GCs were detected, and three marginally detected, in γ-rays by Abdo et al. (2010f). Two of the latter clusters were then detected with higher significance by Tam et al. (2011), who also detected γ-ray emission from an additional four clusters. The spectra of those with high enough counts were fit better with a cutoff power law than a simple power law, consistent with expectations from a population of MSPs.

Of the detected and marginally detected GCs reported in Abdo et al. (2010f),

four contained no known MSPs: Omega Cen, NGC 6388, NGC 6541, and NGC 6652. While these clusters had been searched for MSPs in the past, recent technological advances in radio pulsar searches (for example, the implementation of the GUPPI spectrometer backend at the GBT) led to significant increases in sensitivity, making another search of these sources worthwhile. I led a search for MSPs in two of these clusters, NGC 6388 and NGC 6652, which are within the GBT sky and were significantly detected by the LAT.

The LAT counts maps of these clusters from (Abdo et al. 2010f) are shown in Figure 6.7. Both clusters had significant detections, with high enough counts to measure a spectral cutoff energy. The spectral parameters, photon and flux energies, distances, γ-ray luminosities, and number of MSPs predicted by Abdo et al. (2010f) are given in Table 6.3. $N_{\rm MSP}$ was derived from the L_γ. Note that the L_γ measured for NGC 6388 is similar to that of Terzan 5, yielding the same $N_{\rm MSP}$ (Abdo et al. 2010f). This is consistent with the fact that NGC 6388 is the most compact cluster known in the Galaxy—the more compact a cluster is, the higher the stellar encounter rate, and the more likely it is that a cluster pulsar will obtain a new companion from which it can accrete and be recycled. The fact that no MSPs have been found in NGC 6388 can be explained by its large distance, which makes faint MSPs harder to detect and also leads to more scattering due to a higher DM. A similar argument can be made for NGC 6652, but fewer MSPs are expected to reside in this cluster.

6.3.2 Observations and Analysis

NGC 6388 and NGC 6652 were observed at S-band (2 GHz) with the GBT and GUPPI backend between 2010 October 19 and 2011 May 6 (MJD 55488–55687). GUPPI recorded the signal with a time resolution of 40.96 μs, using 800 MHz (2048 frequency channels) of bandwidth centered on frequency $f = 2$ GHz. The data were

Table 6.3. Physical Parameters of Globular Clusters

NGC	Γ	E_c	TS	F_{100}	G_{100}	d	L_γ	$N_{\rm MSP}$
6388	1.4 ± 0.2	$2.2^{+0.8}_{-0.5}$	86.6	$1.6^{+1.0}_{-0.6}$	1.6 ± 0.3	11.6 ± 2.0	$25.8^{+14.0}_{-10.6}$	180^{+120}_{-100}
6652	$1.0^{+0.6}_{-0.5}$	$1.8^{+1.2}_{-0.6}$	54.8	$0.7^{+0.5}_{-0.3}$	$0.8^{+0.2}_{-0.1}$	9.0 ± 0.9	$7.8^{+2.5}_{-2.1}$	54^{+27}_{-25}

Note. — Physical characteristics of the two globular clusters that were searched for radio pulsations. The columns are, from left to right: (1) The globular cluster NGC name, (2) the spectral index of the cluster's γ-ray spectrum, fit with an exponentially cutoff power law, (3) the cutoff energy in GeV, (4) the TS of the LAT source, (5) the $> 100\,\mathrm{MeV}$ photon flux, in units of $10^{-8}\,\mathrm{photons\,cm^{-2}\,s^{-1}}$, (6) the $> 100\,\mathrm{MeV}$ energy flux, in units of $10^{-11}\,\mathrm{erg\,cm^{-2}\,s^{-1}}$, (7) the cluster's distance from Earth, (8) the γ-ray luminosity, calculated from G_{100} and d, and (9) the number of MSPs predicted to lie in each cluster. These values are taken from (Abdo et al. 2010f); only statistical errors are included. The distance measurements for NGC 6388 and NGC 6652 are originally from Moretti et al. (2009) and Chaboyer et al. (2000).

taken in coherent search mode, in which the incoming signal is dedispersed in real time at a pre-determined dispersion measure (DM) to minimize pulse broadening (see Section 5.2.2.2 for details); we note that these observations also served to test the coherent dedispersion system on the GUPPI backend. The DM at which the channels were coherently de-dispersed, as well as the coordinates of the beam center, are given for each cluster in Table 6.4; the DM was estimated using the NE2001 model (Cordes & Lazio 2002).

These globular clusters are located at low declinations, $-45°$ and $-33°$ respectively for NGC 6388 and NGC 6652, while the GBT is unable to observe at declinations below $\sim 46°$[9] NGC 6388 is therefore observable for only 3 hr per day from the GBT, while NGC 6652 is observable for 6.5 hr; each cluster was approved by the GBT Time Allocation Committee (TAC) for ≤ 3 hr pointings at a time. NGC 6388 was observed a total of 8 times, with individual observations lasting between

[9]GBT guide, `https://science.nrao.edu/facilities/gbt/proposing/GBTpg.pdf`.

Table 6.4. Globular Cluster Observations

NGC	RA	Dec	l	b	$\mathrm{DM_{obs}}$
6388	$17^{\mathrm{h}}\,36^{\mathrm{m}}\,18^{\mathrm{s}}.1440$	$-44^\circ\,44'\,0''.2400$	$345^\circ\,33'\,34''.9$	$-6^\circ\,44'\,20''.1$	340
6652	$18^{\mathrm{h}}\,35^{\mathrm{m}}\,44^{\mathrm{s}}.8560$	$-32^\circ\,59'\,25''.0800$	$1^\circ\,31'\,59''.2$	$-11^\circ\,22'\,27''.1$	190

Note. — The coordinates and dispersion measure used to observe the globular clusters in coherent de-dispersion mode. Galactic coordinates are included to show the clusters' locations relative to the Galactic plane. The observations took place between 2010 October 19 and 2011 May 6.

1.5–2.5 hr, while NGC 6652 was observed 6 times for 2–3 hr each. The observations for each source were clustered within $\sim$2 week intervals. The sensitivity of each observation, given by the radiometer equation for a pulsed signal (Equation 5.21), was limited by its integration time. For the longest observations ($\sim$ 3 hr), the sensitivity to a pulsed signal with a duty cycle of 0.1 is $S_2 \sim 20\,\mu$Jy for NGC 6388, and $S_2 \sim 18\,\mu$Jy for NGC 6652, where S_2 is the flux density at 2 GHz. Converting to the 2 GHz pseudo-luminosity $L_2 \equiv S_2 d^2$, where d is the distance to the cluster, yields $L_2 = 2.7$ and 1.5 mJy kpc^2 for NGC 6388 and NGC 6652, respectively. For comparison, the pulsar with the faintest pseudo-luminosity measured is Pulsar "R" in Terzan 5, with $L_2 \sim 0.4\,\mu$Jy kpc^2 (Ransom et al. 2005).

The pulsar search analysis was done using PRESTO, as described in Section 5.2. The data sets were dedispersed at $\sim$ 5000 DMs between 0 and 800 cm^{-3} pc to ensure the true cluster DM was included in the range. Acceleration searches with $z_{\mathrm{max}} = 50$ and 200 were performed on each dedispersed time series; as described in Section 5.2.4, acceleration searches are usually necessary to detect MSPs in binary orbits because of Doppler smearing.

6.3.3 Discovery of PSR J1835−3259

One MSP was discovered in these searches—PSR J1835−3259, in NGC 6652. (This MSP may also be referred to as PSR J1835−3259A or NGC 6652A, as more MSPs likely exist in this cluster and will eventually be found.) The discovery plot is shown in Figure 6.8. On the right side of the figure, the χ^2 of a null detection is shown at the spin periods and Doppler-induced period derivatives over which the pulsar search was performed; the χ^2 peaks at the P and $\dot{P}$ giving the best (most significant) pulse profile. The bottom right plot shows P and $\dot{P}$ plotted together, with the brighter central region representing the values that correspond to the most significant signal. Two cycles of the best pulse profile are shown at the top left of the plot, and the pulses are shown with integration time in the plot below the profiles. On the right side of the phase vs. time plot, the steady increase in the cumulative χ^2 with integration time is shown, an indication of persistence of the pulsing source (as opposed to a burst of radio frequency interference, or RFI, which would cause a sudden increase and subsequent flattening in the cumulative χ^2). The middle panel shows the strength of the pulses in 32 frequency sub-bands. The bottom middle plot again shows χ^2, this time against the DM; χ^2 peaks at the pulsar DM. From this plot, we see that $P \sim 3.889\,\mathrm{ms}$, and the DM $\sim 63.35\,\mathrm{cm}^{-3}\,\mathrm{pc}$.

The DM is very different from the expected value of $\sim 190\,\mathrm{cm}^{-3}\,\mathrm{pc}$, and initially led my collaborators and me to question the pulsar's association with the cluster. However, given that there are many more stars contained within the cluster than along our line of sight to the cluster, a chance coincidence is highly unlikely. The DM of NGC 6652 is therefore $\sim 63.35\,\mathrm{cm}^{-3}\,\mathrm{pc}$, and the fact that it is so much lower than expected can be explained by the large error in the NE2001 model of free electron density (Cordes & Lazio 2002).

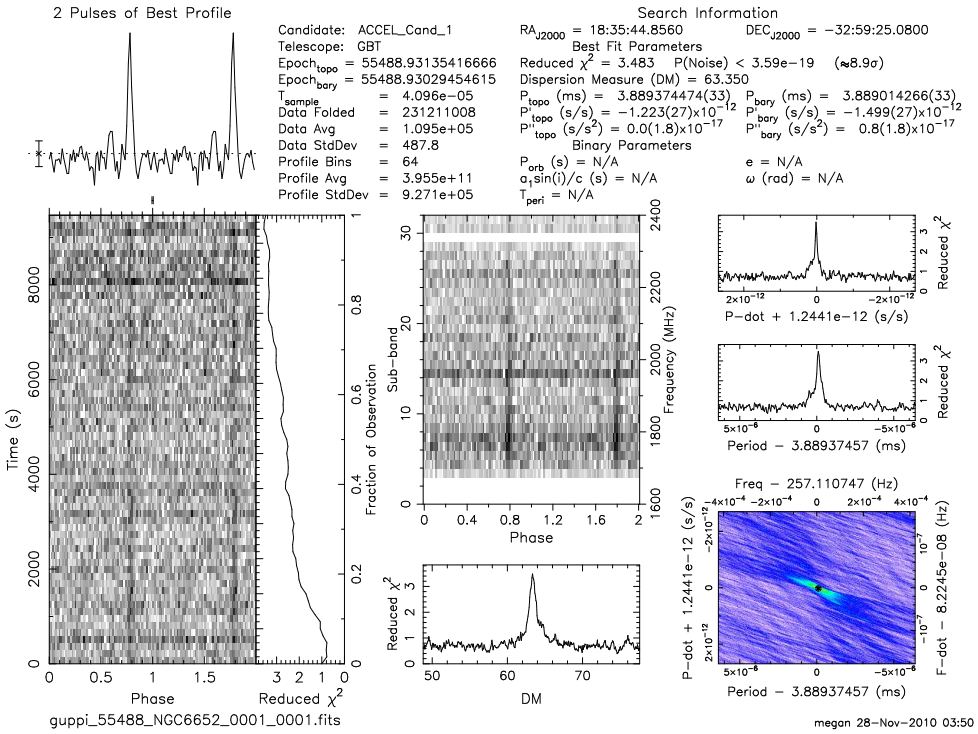

Figure 6.8: The discovery plot of PSR J1835−3259 from PRESTO. *Top left:* Two cycles of the 2 GHz pulse profile. *Left:* Two cycles of the pulse profile with time. *Top center:* Two cycles of the pulse profile over the radio frequency bandwidth of the observation. *Bottom center:* A search over DM yields a peak in DM, a signature of a real pulsar rather than a signal from interference. *Top right:* The peak in reduced χ^2 is at the best period derivative searched. *Middle right:* The χ^2 peak shows the best pulse period. *Bottom right:* The χ^2 contours in $P - \dot{P}$ space, evaluated at the best DM value, showing the best-fit P and $\dot{P}$.

6.3.4 Individual Detections

The MSP was detected through the standard acceleration search procedure in five of the six observations of NGC 6652. It did not appear initially in the observation on 2011 Oct 23, but after folding the data on values of P and $\dot{P}$ intermediate between Oct 22 and 24 with `prepfold` in PRESTO, the pulsar signal emerged from the data. Details of the observations are given in Table 6.5, which lists the observation

Table 6.5. Details of PSR J1835−3259 Detections

Observation Date	P (ms)	$\dot{P}$ (10^{-12} s s^{-1})	Best DM (cm^{-3} pc)
2011-10-19	3.88901426(3)	-1.499 ± 0.027	63.350
2011-10-21	3.88879649(3)	-1.164 ± 0.023	63.385
2011-10-22	3.88869546(3)	-1.183 ± 0.028	63.300
2011-10-23	3.888581(1)	-1.57 ± 2.09	63.250
2011-10-24	3.88844125(5)	-2.146 ± 0.060	63.300
2011-10-29	3.8888233(1)	-1.190 ± 0.286	63.300

Note. — The dates of the observations of NGC 6652, and the best values of the spin period, Doppler-induced period derivative, and dispersion measure found for PSR J1835−3259 in each observation. The P and $\dot{P}$ given are the barycentered values. The number in parentheses in the second column is the error on the last quoted digit of the spin period.

dates, the values of $z_{\max}$ used in each of the acceleration searches, the measured spin period P, the measured (Doppler-dominated) spin period derivative $\dot{P}$, and the best measured DM. For the spin period, the quoted value shows the number of confidently measured digits, with the error on the last digit given in parentheses; for example, for the observation on 2011-10-19, $P = 3.88937447\,\mathrm{ms} \pm 3 \times 10^{-8}\,\mathrm{ms}$. The best P, $\dot{P}$, and DM are the values which yielded the highest χ^2 from a grid search over these parameters in `prepfold`.

Two interesting characteristics of these observations stand out in Table 6.5. The first is that the $\dot{P}$ is negative in every observation, meaning that every time the pulsar was observed, its spin period was observed to be instantaneously decreasing. This effect is caused by a negative velocity between the pulsar and Earth (i.e., the pulsar's motion is toward Earth). In a circular orbit with nonzero inclination to the plane of the sky, the measured $\dot{P}$ will be negative for half the orbit and positive for

the other half. Finding $\dot{P} < 0$ in every observation can be explained by observing a similar orbital phase each time. This would be possible if the pulsar had an orbital period $P_{\rm orb} \sim 1\,{\rm day}$ or (or if it completed a small $\sim$ integer number of orbits each day) because the observations were taken at the same time each day. The orbit, if circular, cannot be much longer than this, as the value of $\dot{P}$ shows that the MSP is highly accelerated. An alternative explanation is that the orbit has a longer period and is eccentric—quite possible in a GC due to stellar interactions that can perturb the orbit— such that the MSP spends the majority of the orbit being accelerated toward the observer.

Second, the optimal DM changes with each observation, varying between 63.250 and $63.385\,{\rm cm^{-3}\,pc}$. This small variation may be due to error in the DM measurement; a rough estimate of the DM error from the individual observations is $\sim 0.025\,{\rm pc\,cm^{-3}}$. It is therefore not possible to tell from these observations whether or not the DM variation is real. If it is physical, then it could mean that there is gas in the system, such that a different column density of free electrons is being sampled at different orbital phases. Note that if the changing DM is physical, it does not support the hypothesis that the MSP is in a circular orbit and is being observed at the same orbital phase each day. Timing the system at two or more wavelengths is necessary to measure the precise DM and its error, and to determine whether or not it is varying over the pulsar's orbit.

6.3.5 Timing Analysis Yields a Highly Eccentric Orbit

Because PSR J1835−3259 is a weak pulsar, $\sim 2\,{\rm h}$ of integration time are required in order to detect it with high enough S/N to obtain a set of quality TOAs. A total of $\sim 50\,{\rm h}$ of observations are needed to time it over the course of one year, an amount of time that has not been granted by the GBT TAC. I therefore attempted to find

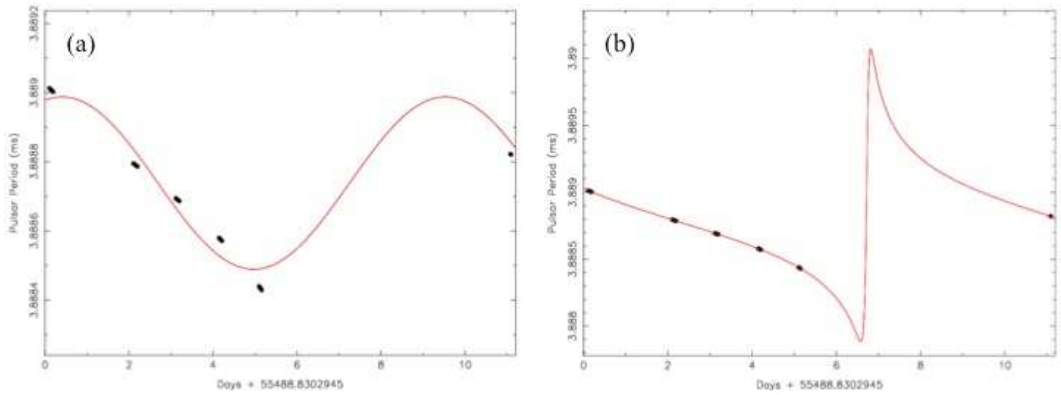

Figure 6.9: (a) A circular orbit, with optimal parameters $x \sim 8$ lt-s and $P_{\rm b} \sim 9.1$ d, was fit to the measured periods and period derivatives of PSR J1835−3259 listed in Table 6.5. The circular orbit clearly does not fit well. (b) P and $\dot{P}$ fit to a highly eccentric orbit. A family of solutions with $e > 0.4$ gave an acceptable fit. The solution shown here has $x \sim 17$ lt-s, $e \sim 0.88$, $P_{\rm b} \sim 9.24$ d.

an initial timing solution by constraining the orbit in the period-acceleration plane with a method developed by Freire et al. (2001) and described in Section 5.3.3. I used a script that was originally written by Scott Ransom and later modified to account for non-zero eccentricity by Ryan Lynch.

Most MSPs are in circular orbits. I therefore began by fitting a circular orbit model to the measured (Doppler-affected) period and period derivatives (which are related to the line-of-sight velocities and accelerations by Equations 5.51-5.52) from each observation. The circular orbit model is shown in Figure 6.9(a).

The circular orbit model did not fit well, suggesting that the orbit is eccentric. I fit P and $\dot{P}$ with a number of different orbital parameters, and found that the orbital model was able to reproduce the observed P and $\dot{P}$ for an eccentricity $e > 0.4$. Figure 6.9(b) shows the orbital model for $e \sim 0.88$, $x \sim 17$ lt-s, $P_{\rm b} \sim 9.24$ d, $T_0 \sim$ MJD55486.3, and $\omega \sim 280°$.

Fitting the orbit in this way resulted in determination of the orbital parameters

with enough accuracy that the fit could be done using Tempo. Because this MSP has a very eccentric orbit, the `BT` binary model was used (rather than the `ELL1` model of the previous section). The `BT` model has as parameters the semi-major axis, x, in light seconds (A1 in the model), orbital period $P_{\rm b}$ (PB), eccentricity e (E), epoch of periastron passage T_0 (T0), and the longitude of periastron, ω (OM).

I began the fit in Tempo with an orbital model in which the longitude of periastron was fixed at $\omega = 283.465$ and the eccentricity was set to $e = 0.914$. I allowed e to be free. The other free fit parameters were the spin frequency ν (Tempo parameter F0), x, $P_{\rm b}$, and T_0; these were set to the best values obtained from the method of Freire et al. (2001). The spin-down frequency $\dot{\nu}$ (F1) was fixed to zero. Fitting this model resulted in a small change in the free parameters, in particular e. After fitting, I altered the value of ω very slightly and fit again.

I stepped through values of ω with step sizes between 0.001 and 0.0001, each time running Tempo and making sure the fit had converged. When it did not converge, I would return to the previous orbital model and make the step size smaller. I automated this procedure when it became clear that it would take thousands of steps to reach a good solution. I gradually removed "JUMP"s from the `.tim` file that contained the TOAs, allowing multiple observations to be phase-connected. Eventually, all six observations were phase connected, and ω was freed to obtain a final timing solution. The parameters of this solution are given in Table 6.6, and the timing residuals are shown in Figure 6.10. This best fit solution has a reduced χ^2 of $368.3/35 = 10.5$; such a high χ^2 is not surprising, given that only one orbit was sampled. Further timing will decrease the scatter in the residuals, and hence χ^2, as the solution becomes more accurate. It is important to note that although χ^2 is large, the fact that the solution has converged even to this level suggests that the spin and orbital parameters are close to correct. Tempo is very sensitive, and

Table 6.6. NGC 6652A timing solution

Timing Parameter	Value
Right Ascension	$18^{\rm h}\,35^{\rm m}\,44^{\rm s}.856$
Declination	$-32^\circ\,59'\,25''.08$
Dispersion Measure ($\rm cm^{-3}\,pc$)	63.35
Spin period, P (ms)	3.8888289774(4)
Spindown rate, $\dot{P}$ ($\rm s\,s^{-1}$)	0
Orbital period, $P_{\rm b}$ (days)	9.2459 ± 0.0005
Projected semimajor axis, x (lt-s)	19.092 ± 0.054
Eccentricity, e	0.9498 ± 0.0013
Epoch of periastron passage, T_0 (MJD)	55477.0400 ± 0.0006
Longitude of periastron, ω (degrees)	289.24 ± 0.23

Note. — The spin and orbital parameters of PSR J1835−3259 obtained from an initial timing solution, for which the six observations are phase-connected. The coordinates were fixed to those used in the searches, while the DM is fixed to its best value from the discovery. The spindown rate was fixed at zero; timing over the course of at least one year is needed in order to measure this parameter.

χ^2 will blow up with incorrect parameters; I find this timing solution to be stable, and for this reason, I believe the timing parameters I have obtained are valid.

The best timing solution obtained from these 6 observations, which spanned 11 days (just over one orbital period of 9.24 days), requires $e \sim 0.95$. This must be confirmed with further timing observations, but if it is accurate, then this binary MSP is the most eccentric one known.

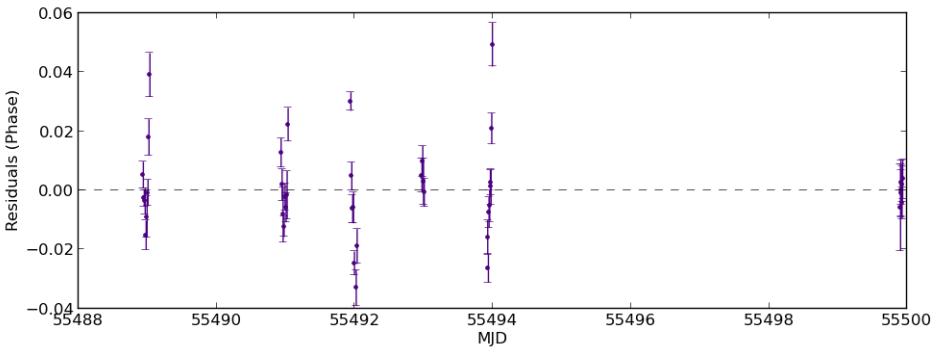

Figure 6.10: Timing residuals from the best-fit solution given in Table 6.6. The reduced $\chi^2 = 10.5$, but the solution is stable and the parameters are likely close to their true values (see the text).

6.3.6 Mass Function and Future Mass Constraints

Using the timing parameters in Table 6.6, Equation 5.39 yields the mass function $f(m_{\rm p}, m_{\rm c}) = 0.087378$. For $\sin i = 90°$, the minimum companion mass is $0.736\,{\rm M}_\odot$, assuming $m_{\rm p} = 1.4\,{\rm M}_\odot$. (The mass function is solved using the cubic equation.) Note that a larger pulsar mass leads to a larger minimum companion mass—for example, if $m_{\rm p} = 2\,{\rm M}_\odot$, the minimum mass of the companion increases to $0.903\,{\rm M}_\odot$—and that it is quite possible that this MSP is more massive than $1.4\,{\rm M}_\odot$ due to gaining mass in its accretion and spin-up phase. The maximum mass can be constrained to the 90% confidence level using $i \leq 26°$ (Lorimer & Kramer 2005), and is $\sim 3\,{\rm M}_\odot$ if $m_{\rm p} = 1.4\,{\rm M}_\odot$. This range of $m_{\rm c}$ indicates a true companion mass that is much higher than the typical low-mass white dwarf (WD) companion, and raises the possibility that the companion is a massive WD, a NS, or possibly a black hole. Another possibility is that it is a main sequence star with a mass similar to that of the Sun, near the cluster turn-off age of $11.7 \pm 1.6\,{\rm Gyr}$ (Chaboyer et al. 2000).

Because the binary is highly eccentric, it will be possible to detect the relativistic

precession of its orbit and hence to measure $\dot{\omega}$ with a timing campaign. As discussed in Section 5.3.2.3, a measurement of $\dot{\omega}$ yields the total system mass (Equation 5.40). This means that by timing the MSP, it will be possible to constrain the mass of the pulsar and its companion. If one or more other post-Keplerian parameters (Equations 5.40–5.44) are measured, then the individual masses will be known.

6.3.7 Discussion

PSR J1835−3259 is a highly eccentric binary MSP that has the potential to be an extremely interesting system. Its rather long orbital period of ~ 9 days is consistent with the MSP lying in a low-density globular cluster (Camilo & Rasio 2005). If the eccentricity of $e \sim 0.95$ obtained from initial timing is correct, then it is the most eccentric binary MSP known; the highest eccentricity of a binary MSP currently known is PSR J0514−4002A in NGC 1851, with $e = 0.89$. The high eccentricity allows a precise measurement of the longitude of periastron ω. Thus, continued timing will yield a measurement of the rate of periastron advance, $\dot{\omega}$, and hence a measurement of the total system mass and constraints on the pulsar mass. If one or more other relativistic parameters can be measured from timing, then the pulsar mass will be known and may potentially contribute to constraints on the neutron star equation of state.

The MSP's orbital eccentricity suggests that the MSP's original orbit was extremely perturbed by an encounter with a third body, or alternatively that its original companion was ejected and the third body was obtained as a new companion. The high eccentricity implies that the latter scenario is more likely; it is even possible that multiple companion exchanges took place (Camilo & Rasio 2005, and references therein). Stellar encounters are highly likely in globular clusters, and can result in exchange interactions (e.g. Sigurdsson & Phinney 1993). If the MSP ex-

perienced a companion exchange, then its new companion may be "exotic" in that it could be a type of star or compact object that rarely or never partakes in binary evolution. The high minimum mass of the companion lends additional support to this possibility, and suggests that the companion is a high-mass white dwarf, a main sequence star, another neutron star, or even a black hole. To date, no neutron star-black hole binaries have been found; if such binaries exist, they are expected to be found in globular clusters because of the high stellar encounter rate. The discovery of such a system may allow for tests of strong gravity, for example by measuring the orbital decay rate over years to decades (this test can also be done for compact white dwarf-neutron star and double neutron star systems), and would provide constraints on the maximum neutron star mass and minimum black hole mass. In the case of a pulsar-black hole binary, pulsar timing can also be used to measure the spin of the black hole (Barker & O'Connell 1975; Wex & Kopeikin 1999). Interestingly, high-eccentricity orbits resulting from multiple companion exchanges are more likely to be associated with very massive neutron stars, and their companions are more likely to be massive compact objects than those of neutron stars that have experienced fewer exchanges (Phinney & Sigurdsson 1991; Sigurdsson 2003).

In addition to potentially yielding a mass measurement, a phase-connected timing solution is needed in order to fold the γ-ray counts and search for high-energy pulsations. This raises the question of whether we might expect to detect γ-ray pulsations from this MSP, which lies in a cluster at $\sim 9\,\mathrm{kpc}$ from Earth. A reasonable range of $\dot{P}$ values for which detection of γ-ray pulsations is feasible can be obtained through order-of-magnitude estimates using the measured γ-ray luminosity of NGC 6652, $L_\gamma^{\mathrm{GC}} \sim 8 \times 10^{34}\,\mathrm{erg\,s^{-1}}$.

The lowest TS of a γ-ray MSP in the Second LAT Pulsar Catalog (The Fermi-LAT Collaboration 2013), obtained from a likelihood analysis with `gtlike`, is $TS =$

23; I therefore assume $TS \sim 10$ or higher is needed in order to detect γ-ray pulsations from a MSP with the LAT. The TS of NGC 6652, with 1.5 yr of LAT data, was 54.8 (Abdo et al. 2010f); the TS scales $\sim$ linearly with improved statistics, so after 4 yr of data collection (which is the amount of data used in the pulsar catalog), the TS would be $\sim$ 150. If PSR J1835−3259 has $TS \geq 10$, then its luminosity $L_\gamma^{\rm MSP} \geq L_\gamma^{\rm GC} \times 10/150 \sim 5 \times 10^{33}\,{\rm erg\,s^{-1}}$. Assuming the efficiency of converting the rotational spin-down energy into γ-ray luminosity is $\eta = 0.1$, then $\dot{E} = L_\gamma^{\rm MSP}/\eta \geq 5 \times 10^{34}\,{\rm erg\,s^{-1}}$, and $\dot{P} \geq 10^{-21}\,{\rm s\ s^{-1}}$. These lower limits on $\dot{E}$ and $\dot{P}$ are quite reasonable for MSPs, and are consistent with the values measured for the γ-ray MSPs in The Fermi-LAT Collaboration (2013).

An estimate of the upper limit on $\dot{P}$ can again be obtained using $L_\gamma^{\rm GC}$, this time considering that the entire γ-ray luminosity originates from PSR J1835−3259. This is not an unreasonable assumption: one of only two γ-ray cluster MSPs detected to date, PSR J1823−3021A, is apparently responsible for the entire L_γ of NGC 6624 (Freire et al. 2011). Again assuming $\eta = 0.1$, the spindown energy is now $\dot{E} \sim 8 \times 10^{35}\,{\rm erg\,s^{-1}}$, and $\dot{P} \sim 10^{-18}\,{\rm s\ s^{-1}}$. A larger value of η will decrease $\dot{E}$ and $\dot{P}$. While these values are quite high for MSPs, they are consistent with those of the highly energetic γ-ray MSPs PSR J1823−3021A, for which $\dot{E} = 8.3 \times 10^{35}\,{\rm erg\,s^{-1}}$ and $\dot{P} = 3.4 \times 10^{-18}\,{\rm s\ s^{-1}}$ (The Fermi-LAT Collaboration 2013), and PSR B1821−24 in M28 ($\dot{E} = 2.2 \times 10^{36}\,{\rm erg\,s^{-1}}$ and $\dot{P} = 1.6 \times 10^{-18}\,{\rm s\ s^{-1}}$). While the gravitational potential of the cluster can artificially enhance $\dot{P}$, the observed values of $\dot{P}$ have been found to be mostly intrinsic for both pulsars (Freire et al. 2011; Phinney 1993). It is therefore feasible that γ-ray pulsations could be detected from PSR J1835−3259.

Much remains to be done with PSR J1835−3259. The MSP must be timed over the course of at least one year in order to obtain a phase-connected timing solution and to measure its position and $\dot{P}$ accurately. Scheduling timing observations has

proven to be a challenge. Because the MSP is faint, 1–2 hr integrations at L- or S-band (1.4 or 2 GHz) with the GBT are needed to detect the MSP with high enough S/N that quality TOAs may be extracted. The total observing time needed, including a dense set of observations to establish initial phase connection, is ~ 50 hr in one year, too large a request for the GBT. The Giant Metre-wave Radio Telescope (GMRT) in India is a good alternative; if the MSP is detected by the GMRT at 610 MHz in upcoming observations, this telescope will instead be used for the timing campaign. Once a precise position has been determined, it may be possible to identify its optical companion (if the companion is a WD or MS star) and determine its spectral type, for example through imaging and spectroscopy with the Hubble Space Telescope.

Finally, MSPs certainly must exist in NGC 6388, and there are likely more MSPs in NGC 6652. The fact that no MSPs were detected in NGC 6388 despite its large stellar encounter rate and γray luminosity may be due to its projected proximity to the Galactic plane and its large distance. This combination results in much more pulse scattering than is experienced by MSPs in NGC 6652—the NE2001 model predicts $\tau_{\rm scatt} \sim 3\,\mu$s for NGC 6388, but only $\sim 0.08\,\mu$s for NGC 6652—making MSPs in NGC 6388 more difficult to detect. There are, however, more search techniques that can be used on the existing datasets presented here. The observations can be searched further using shorter integration times and higher $z_{\rm max}$ values to be more sensitive to more highly accelerated binary MSPs, and by stacking the Fourier series from each time series to search for periodic signals that may have too low a S/N to be detected in a single observation. When the timing campaign of NGC 6652 begins, each of the search mode timing observations will also be searched for pulsations with the goal of finding more MSPs in this cluster. Because the true DM is now known, the use of coherent de-dispersion will be especially beneficial in

recovering faint signals. A natural extension of this work is to search for radio MSPs in more γ-ray-detected globular clusters. Perhaps *Fermi* will lead the way to the discoveries of many more exotic pulsar systems.

Chapter 7

Summary and Conclusions

The excellent sensitivity and resolution (in time, energy, and sky position) of the LAT together make it an orders-of-magnitude better instrument for high-energy γ-ray pulsar studies than any previous γ-ray mission. It has provided a rich dataset of γ-ray emission from over 120 pulsars, with which there is an endless list of possible pulsar studies to be done. The LAT has uncovered three distinct populations of γ-ray pulsars—young radio loud, young radio quiet, and millisecond—from which clues to the underlying emission mechanism or mechanisms can be drawn. The LAT also provides targets for pulsar searches in the form of non-variable, unassociated sources with pulsar-like emission spectra. At the time of writing, 50 new millisecond pulsars have been found by searching for radio pulsations in these unassociated γ-ray sources.

7.1 Millisecond Pulsar Discoveries in GeV Sources

In this thesis, the Green Bank Telescope discoveries of two millisecond pulsars were presented. The first, PSR J0102+4839, was discovered in a faint, high-latitude LAT source that had no multi-wavelength counterparts (i.e., was an unassociated source) and displayed a pulsar-like spectrum at GeV energies. The pulsar was timed with the GBT over $\sim 1.5\,\mathrm{yr}$, after which γ-ray pulsations were detected by assigning rotation phases to the LAT events with the radio timing solution. The LAT was then used to extend the timing solution back to the start of the *Fermi* mission.

PSR J0102+4839 has spin period $P = 2.964\,\mathrm{ms}$, period derivative $\dot{P} = 1.136 \times 10^{-20}\,\mathrm{s\,s^{-1}}$, and spindown power $\dot{E} = 1.722 \times 10^{34}\,\mathrm{erg\,s^{-1}}$. At a distance of $\sim 2.3\,\mathrm{kpc}$, derived from the NE2001 model of free electrons in the ISM, its γ-ray flux of $\sim 0.8 \times 10^{-11}\,\mathrm{erg\,cm^{-2}\,s^{-1}}$ corresponds to a γ-ray luminosity of $L_\gamma \sim 5 \times 10^{33}\,\mathrm{erg\,s^{-1}}$. This implies a large efficiency η_γ of converting the spindown energy into electromagnetic radiation, $\eta_\gamma = L_\gamma/\dot{E} \sim 0.3$. However, using the NE2001 model can lead to errors of up to a factor of ~ 2 in distance derived from DM; η_γ may be as low as ~ 0.08 if the distance to PSR J0102+4839 is half that estimated with NE2001.

The spectrum of PSR J0102+4839 was modeled with a power law, a broken power law, and an exponentially cut-off power law. The simple power law resulted in the worst fit, as expected. Because the pulsar is faint, the statistics are too poor to differentiate between a broken or cut-off power law, nor between an exponential or sub-exponential cutoff, so for simplicity the cut-off power law was modeled with a pure exponential cutoff ($b = 1$ in Equation 6.9). The phase-averaged spectra of bright pulsars are well fit by the sub-exponentially cut-off power law ($b < 1$), so as the γ-ray statistics improve over the lifetime of the *Fermi* mission, it is reasonable to expect that this spectral model will be best for PSR J0102+4839 as well.

The radio emission of this MSP has significant linear polarization, and is almost 100% linearly polarized across the smaller of the two peaks in its 820 MHz profile. The position angle is fairly flat, and displays an orthogonal mode jump at the highest point of the larger peak. The linearly polarized emission in this peak is suggestive of radiation being observed from multiple radio cones. Analysis of the position angle of the polarized emission across the full rotation phase with models like the Rotating Vector Model (Radhakrishnan & Cooke 1969a) may yield constraints on the emission and viewing geometries; additional constraints can also be placed on the geometry through modeling of the γ-ray light curve as in Chapter 3, and may allow estimation of the radio emission altitude when combined with the polarization constraints.

The second pulsar discovered, PSR J1835−3259, was found in NGC 6652, which is one of two globular clusters that were searched for radio MSPs with the GBT following the clusters' detections at GeV energies by the LAT. This MSP has turned out to be quite interesting, as preliminary timing efforts have shown that its orbit is highly eccentric, with $e \sim 0.95$. The initial phase-connected timing solution yields $P = 3.889\,\mathrm{ms}$; a timing campaign over the course of a full year is needed in order to establish the rest of the timing parameters with certainty. With a timing solution that is phase-connected on long timescales $\geq 1\,\mathrm{yr}$, we can measure the intrinsic $\dot{P}$ and fold the LAT events detected from NGC 6652 with the MSP's spin and orbital parameters to search for γ-ray pulsations. We calculate that, despite its distance, it is feasible to detect γ-ray pulsations from this pulsar, especially if the total GeV luminosity originates from a small population of cluster MSPs.

Using the timing solution derived over 11 d of search observations, we constrain the companion's mass to be $0.7\,M_\odot < m_\mathrm{c} < 3\,M_\odot$ (for pulsar mass $1.4\,M_\odot$), much larger than typical inferred minimum companion masses of $\sim 0.1\,M_\odot$. The high

companion mass and the extremely eccentric orbit together point to a colorful past for PSR J1835−3259. It has almost certainly experienced at least one companion exchange, possibly several, as a result of the dense stellar environment of the cluster, and it may have an exotic binary companion. Possible companion types include a massive white dwarf, an evolved main sequence star, another neutron star, or even a black hole. The MSP experienced at least one accretion phase, during which it was spun up to millisecond periods, and may have experienced several if it underwent multiple companion exchanges. The MSP may therefore be very massive like, e.g., the $2\,M_\odot$ neutron star PSR J1614−2230, due to mass gained during accretion. Because the orbit is highly eccentric, its precession, reflected in the rate of change of the longitude of periastron, $\dot{\omega}$, will be detectable. From the post-Keplerian parameters of Equations 5.40–5.44, a measurement of $\dot{\omega}$ yields the total system mass, which can be used to constrain the pulsar mass. Thus, through pulsar timing, we will constrain the masses of the MSP and its companion, which will give information about the companion's stellar type and the past binary evolution of PSR J1835−3259.

7.2 Emission and Field Geometry Constraints

Particles that are accelerated to extremely high Lorentz factors in pulsar magnetospheres radiate at γ-ray energies. The dominant emission process at these energies is likely curvature radiation. The emission seen by the LAT originates at high altitudes (e.g., Abdo et al. 2010d). The effects of the light travel time from different emission altitudes and the relativistic aberration of photon propagation direction together result in caustic emission patterns that are seen as peaks in the pulsar light curves.

The pulsar magnetosphere is largely force-free, with $E_\parallel = 0$ (Goldreich & Julian

1969), and acceleration is confined to narrow gaps along the last open magnetic field lines within which $E_{\|} \neq 0$. The slot gap accelerator extends from the neutron star surface out to the light cylinder, resulting in acceleration and radiation from this full range of altitudes. In contrast, the outer gap accelerator is located only at altitudes above the intersection between the null charge surface and the boundary of the closed field line region. The presence or absence of low-altitude emission has a significant effect on the light curve features, in particular on the level of magnetospheric emission at off-peak rotational phases. The polar cap offset that naturally results from magnetic field line sweepback introduces an asymmetry in $E_{||}$ around the polar cap rim, enhancing the ratio of peak to off-peak emission levels in the slot gap light curves.

Under the assumption that the geometry of the emission region within the pulsar magnetosphere, and with respect to the observer's line of sight, is solely responsible for the observed shapes of high-energy pulsar light curves, we modeled the light curves of four bright γ-ray pulsars using light curves simulated from the slot gap and outer gap geometries. We considered two approximations to the true pulsar magnetic field: the analytic solution of the vacuum retarded dipole field (Deutsch 1955) and the numerical solution of the force-free magnetic field (Kalapotharakos & Contopoulos 2009). The light curves are affected by the choice of magnetic field, which determines the direction of light propagation due to the assumption (valid for $v \approx c$) that photons are emitted tangent to $\mathbf{B}$. Therefore, light curve modeling can potentially constrain both the emission and magnetic field geometries.

It is important to point out here that simulations of light curves within the force-free geometry are relatively new, as the force-free field solution was found numerically less than a decade ago (Spitkovsky 2006) and evolved to a steady-state solution only in the past few years (Kalapotharakos & Contopoulos 2009). The

light curve modeling in this work is the first to use the full force-free solution. Additionally, because of the excellent statistics and incredible detail in the LAT light curves, it is possible to constrain the gap width and maximum emission radius as well as the traditional geometrical parameters α and ζ. Thus, we fit for these parameters rather than fixing them as in previous studies (e.g., Romani & Watters 2010), and find the best fit parameters with a Markov chain Monte Carlo routine.

We found that for most combinations of emission and field geometry, the qualitative features of each of the observed light curves could be reproduced. For the Crab and Vela pulsars, the simulations that best reproduced the qualitative light curve shapes had ζ values that were consistent with ζ measured from the pulsars' X-ray pulsar wind nebula torii (Ng & Romani 2008), as well as small $\beta = |\alpha - \zeta|$ as expected for radio-loud pulsars. For the Crab, this was especially true in the FF field, suggesting its true field may be close to force-free. There are no strong multi-wavelength constraints on α, ζ, or β for Geminga (it is unknown whether its lack of radio emission is intrinsic or results from viewing angle), except for $\zeta > 60$ estimated from its velocity vector. All the fits to its light curve were statistically and qualitatively similar, so no meaningful constraints could be placed on its geometry. For PSR J0007+7303, a radio quiet pulsar, we find large values of β, in line with expectations. No particular geometry stood out as being best overall, and we found that the vacuum field was preferred over force-free for PSR J0007+7303. These results were somewhat surprising, as we expected that either the slot gap or outer gap geometry would consistently yield the best fit, and we expected the physically motivated force-free field to improve the light curves in all cases.

The phase resolved spectra of Vela, Crab, and Geminga were modeled with an exponentially cut-off power law ($b = 1$ fixed) in order to measure the spectral index Γ and cutoff energy $E_{\rm c}$ as they vary with rotation phase. We identified "dips"

in both spectral parameters at phases corresponding to the light curve peaks in Geminga and Crab, and possibly PSR J0007+7303 (for which the phase resolved spectral parameters were taken from Abdo et al. 2012). The origin of these features is not known, and will be the subject of further investigation. Another interesting feature was that of the very high value of, and error on, $E_{\rm c}$ in the Crab's second peak. The large error on the measurement is suggestive of either a very rapid rise and fall in $E_{\rm c}$ across the phase bin, which cannot be resolved with current statistics, or of instantaneous spectral blending from curvature radiation over a broad range of altitudes and therefore field line radii of curvature.

To further investigate the field geometry, we assumed (1) that the dominant $> 100\,\mathrm{MeV}$ emission process in pulsar magnetospheres is curvature radiation in the radiation reaction limit from a population of monoenergetic electrons, so that the measured phase resolved $E_{\rm c}$ are equivalent to the curvature radiation cutoff energy $E_{\rm CR}$, and (2) that the best fit geometrical parameters of each emission and field geometry combination, found from light curve modeling, are representative of the true system geometry. We then calculated $E_{\parallel} \propto E_{\rm c}^{4/3} \rho_{\rm c}^{-2/3}$ for curvature radiation reaction (Equation 4.6). Here it is important to state that such a calculation of $E_{\parallel}$, with the use of real measured quantities from pulsar observations, has not been done previously (except, of course, in order-of-magnitude estimates of $E_{\parallel}$, given the pulsar's surface field and rotation speed).

For all the pulsars, $E_{\parallel}$ is slowly varying over emission radius, for the radii probed by the models, with a scatter of ~ 1 order of magnitude. We compared the minimum values calculated for $E_{\parallel}(r)$ with the maximum local field strength $B(r)$. In general, $E_{\parallel}$ exceeds the local B in the vacuum field, confirming that the vacuum retarded dipole is not a physically realistic approximation to the pulsar magnetic field. In the force-free field, $E_{\parallel}/B \leq 1$, a result of the increased $B(r)$ and $\rho_{\rm c}$ compared to

those of the vacuum case.

There are analytic expressions for $E_{\parallel}$ of the slot gap and outer gap models. We found that our measured $E_{\parallel}$ was orders of magnitude larger than the predicted values, except for the Crab in the force-free field. The Crab light curves were also qualitatively best in the force-free field, especially in that they find ζ consistent with that of Ng & Romani (2008).

From these results, we conclude the following.

1. The combination of emission and field geometries yielding the best fit light curve is not consistent from one pulsar to the next, and in some cases all combinations yield comparably good fits. This suggests that some pulsars may have an outer gap and others a slot gap; or, alternatively, that both a slot gap and outer gap may exist simultaneously in the pulsar magnetosphere.

2. Following from the first point, the field geometry of some pulsars may be closer to force-free than others.

3. The force-free field tends to lower $E_{\parallel}/B$ to physical or near-physical values due to the straightening of field lines from current loading, which results in larger $\rho_{\rm c}$ and $B(r)$ compared to the vacuum field. The vacuum field instead has $E_{\parallel}/B > 1$ in most cases. This shows that, for our assumptions of curvature radiation reaction and emission geometry, the vacuum field is not a physical approximation of the true pulsar field.

4. Narrow gap models predict an $E_{\parallel}$ that is orders of magnitude below the values we have calculated. The exception is the force-free $E_{\parallel}$ of the Crab. The agreement in $E_{\parallel}$, combined with the qualitatively good light curve fits and ζ constraints obtained in the force-free field, points to the Crab having a magnetic field structure that is close to force-free. Because of the agreement in

$E_\parallel$, we suggest that the Crab may be the only pulsar of the four considered for which the assumption of curvature radiation reaction is valid. This hypothesis is consistent with the result from Breed et al. (2013, in preparation) that Vela cannot reach curvature radiation reaction. Alternatively, or additionally, it may be that the Crab is the only pulsar of these four for which narrow gap models are adequate to describe the magnetospheric emission region.

7.3 Looking Forward

Following from this work, the immediate next step is to model the LAT light curves of a larger population of young γ-ray pulsars. An interesting test of the emission models can be done by correcting the γ-ray luminosities L_γ of known pulsars with the beaming factor, f_Ω, that results from the emission geometry, and then fitting a relationship between L_γ and $\dot{E}$. This has been done recently by Pierbattista et al. (in preparation) for the vacuum models, and should be repeated in the force-free field. GeV emission from pulsar magnetospheres with screened $E_\parallel$ have $L_\gamma \propto \dot{E}^{1/2}$, while for magnetospheres without screening, $L_\gamma \propto \dot{E}$ (Harding & Muslimov 2002). The calculation of $E_\parallel$ can also be done for a larger number of pulsars, especially as the *Fermi* mission progresses and the statistics improve. Additionally, there is increasing evidence that the radio emission from millisecond pulsars is produced at relatively high altitudes compared to normal pulsars. Light curve modeling of the now many LAT-detected millisecond pulsars (e.g., Venter et al. 2012; Johnson 2012) can be combined with modeling of their radio polarization properties to constrain both the emission geometry and radio emission altitude.

Models for magnetospheres intermediate between the vacuum and force-free fields have been developed recently (Kalapotharakos et al. 2012b; Li et al. 2012).

Light curve modeling within these magnetospheres (e.g., Kalapotharakos et al. 2012a) may lead to improved constraints on the emission geometry. Another important step toward understanding pulsar emission will be to model the emission using a full radiation code, such that the emissivity can vary with emission radius and both photon energy and intensity can be calculated with rotation phase. Then, both the light curves and phase resolved spectra can be modeled.

The *Fermi* LAT has provided an incredible opportunity to improve our understanding of the pulsar population and of the physics occurring in pulsar magnetospheres. With continuing pulsar discoveries guided by *Fermi*, several new pulsar surveys and/or survey instruments coming online, the accumulation of GeV photon statistics over time by the LAT, and improvements in theoretical understanding of pulsar physics, the field of pulsar astronomy will be producing exciting science for years to come.

Appendix A

List of Abbreviations and Symbols

Table A.1. List of Abbreviations and Symbols

Abbreviation	Meaning
1FGL	First *Fermi* LAT source catalog
2FGL	Second *Fermi* LAT source catalog
ACD	Anti-Coincidence Detector
AGN	Active Galactic Nucleus
AIC	Aitoff Information Criterion
aSG	Asymmetric Slot Gap
$B_{\rm LC}$	Magnetic field strength at the light cylinder
BPL	Broken Power Law
$B_{\rm s}$	Magnetic field strength at the neutron star surface
BW	Black Widow pulsar
CF	Co-rotating Frame
CGRO	*Compton* Gamma-Ray Observatory
CR	Curvature Radiation
CRR	Curvature Radiation Reaction
CTA	Cherenkov Telescope Array
DFT	Discrete Fourier Transform
DM	Dispersion Measure
$\dot{E}$	Spindown energy, or spindown luminosity
$E_{\parallel}$	Electric field component parallel to the magnetic field
E_c	Spectral cutoff energy
ECPL	Exponentially Cut-off Power Law
EGRET	Energetic Gamma-Ray Experiment Telescope
FDTD	Finite-Difference Time Domain
FF	Force-Free
FFE	Force-Free Electrodynamics
FFT	Fast Fourier Transform
GBM	Gamma-ray Burst Monitor
GC	Globular Cluster
GeV	Giga-electronVolt
GHz	Gigahertz
GRB	Gamma-Ray Burst
GUPPI	Green Bank Ultimate Pulsar Processing Instrument
Gyr	Gigayear
HE	High Energy
Hz	Hertz
IC	Inverse Compton

Table A.1 (cont'd)

Abbreviation	Meaning
IOF	Inertial Observer Frame
IRF	Instrument Response Function
ISM	Interstellar Medium
keV	kilo-electronVolt
LAT	Large Area Telescope
MAGIC	Major Atmospheric Gamma-ray Imaging Cherenkov telescopes
MCMC	Markov Chain Monte Carlo
MeV	Mega-electronVolt
MHz	Megahertz
MJD	Modified Julian Day
MSP	Millisecond Pulsar
Myr	Megayear
NCS	Null Charge Surface
NS	Neutron Star
OG	Outer Gap
P	Pulsar period
$\dot{P}$	Time derivative of pulsar period (spindown rate)
P1	Peak 1 in light curve
P2	Peak 2 in light curve
P3	Peak 3 (inner peak) in light curve
PC	Polar Cap
PFF	Pair Formation Front
PK	Post-Keplerian
PL	Power Law
PRESTO	PulsaR Exploration and Search TOolkit
PSF	Point Spread Function
PSR	Pulsar
PWN	Pulsar Wind Nebula
RB	Redback pulsar
RFI	Radio Frequency Interference
RL	Radio-loud
$R_{\rm LC}$	Light cylinder radius
RM	Rotation Measure
$R_{\rm NS}$	Neutron star radius
ROI	Region of Interest
RQ	Radio-quiet

Table A.1 (cont'd)

Abbreviation	Meaning
SCLF	Space-Charge Limited Flow
SED	Spectral Energy Distribution
SG	Slot Gap
SNR	Supernova Remnant
SSB	Solar System Barycenter
SSD	Silicon Strip Detector
sSG	Symmetric Slot Gap
TAC	Time Allocation Committee
TAI	International Atomic Time
TeV	Tera electron Volt
TOA	Time of Arrival
TPC	Two-Pole Caustic
TS	Test Statistic
TT	Terrestrial Time
UTC	Coordinated Universal Time
VERITAS	Very Energetic Radiation Imaging Telescope Array System
VHE	Very High Energy
VRD	Vacuum Retarded Dipole
WD	White Dwarf

Appendix B

Atlas of Simulated Light Curves

This appendix contains an "atlas" of simulated pulsar light curves. I have included plots of light curves in (α, ζ) space for twelve combinations of w and r. For all geometries, $w = [0.01, 0.05, 0.1, 0.2]$; for the outer gap geometry, $r = [0.9, 1.2, 1.7]\, R_{\rm LC}$, while for the slot gap geometries, $r = [0.7, 1.0, 1.5]\, R_{\rm LC}$. This allows the reader to compare the light curve shapes for different geometrical parameters, without plotting every combination of (α, ζ, w, r). In each plot, the x-axis is the rotation phase from 0 to 1, and the y-axis is the dimensionless intensity of the simulated emission.

B.1 Light Curves in the Vacuum Outer Gap Geometry

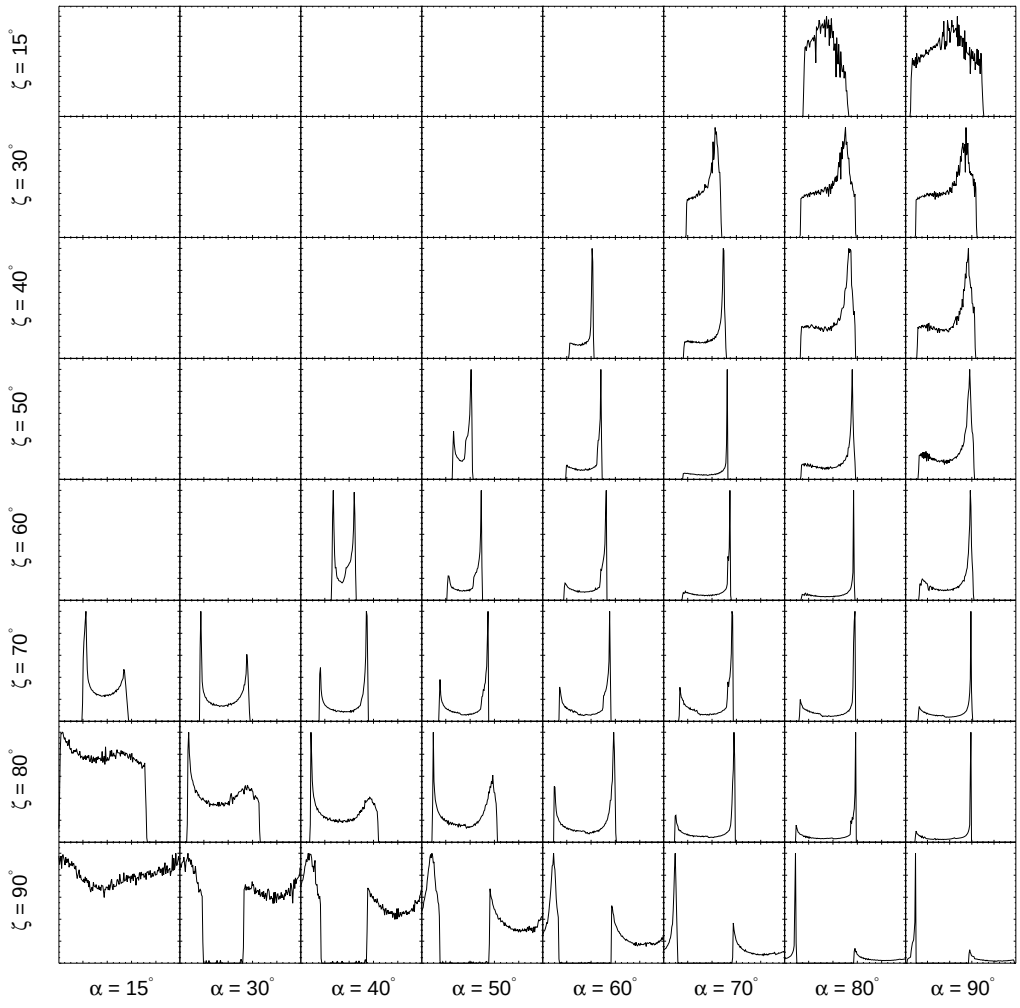

Figure B.1: Light curves from the outer gap geometry in the vacuum retarded dipole field geometry, with $w = 0.01$ and $r = 0.9\,R_{\rm LC}$.

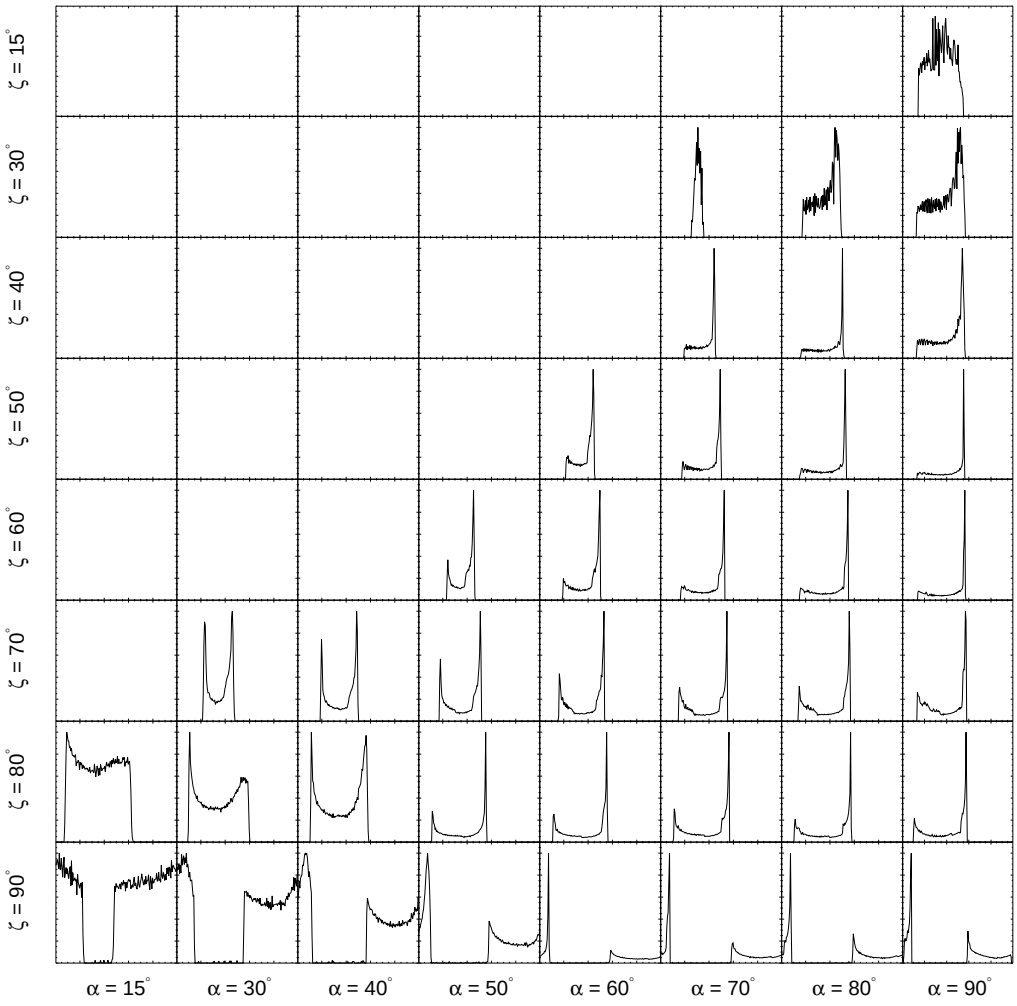

Figure B.2: Light curves from the outer gap geometry in the vacuum retarded dipole field, with $w = 0.05$ and $r = 0.9\,R_{\rm LC}$.

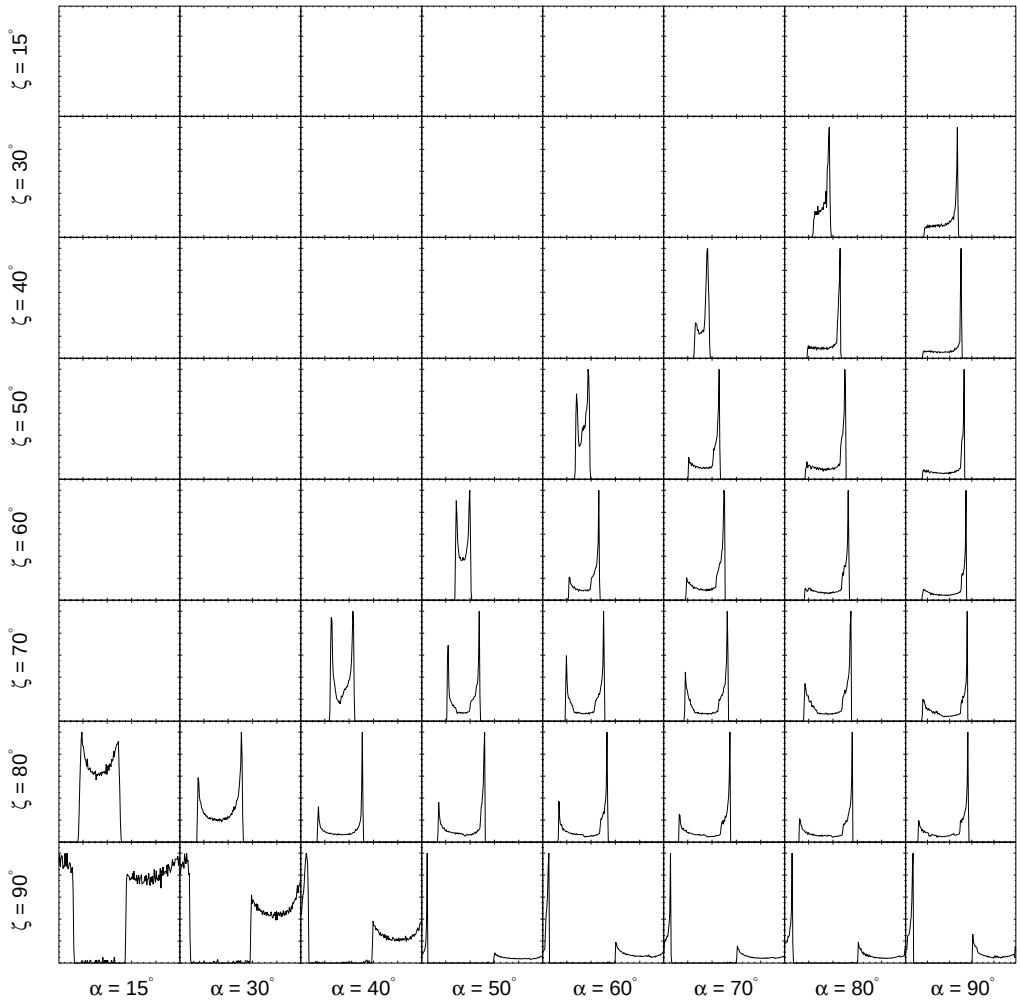

Figure B.3: Light curves from the outer gap geometry in the vacuum retarded dipole field geometry, with $w = 0.10$ and $r = 0.9\,R_{\rm LC}$.

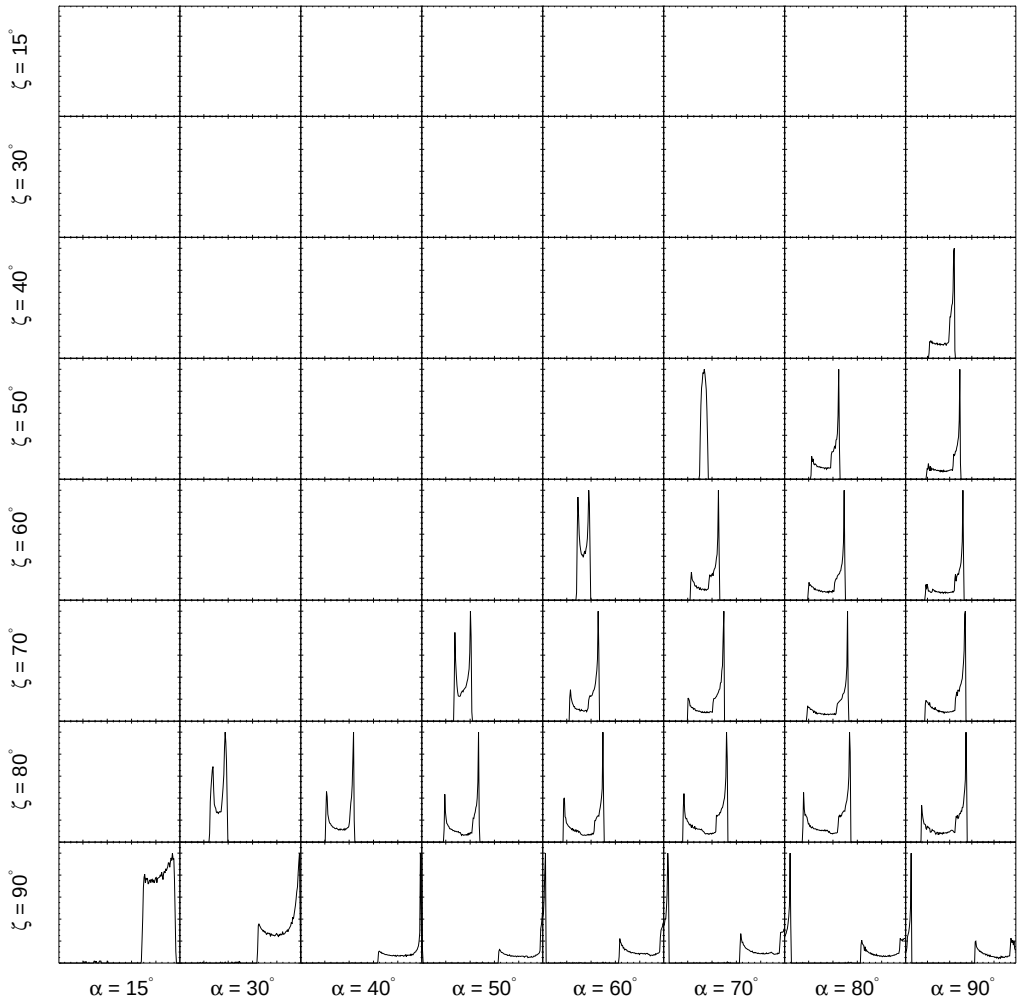

Figure B.4: Light curves from the outer gap geometry in the vacuum retarded dipole field geometry, with $w = 0.20$ and $r = 0.9\,R_{\rm LC}$.

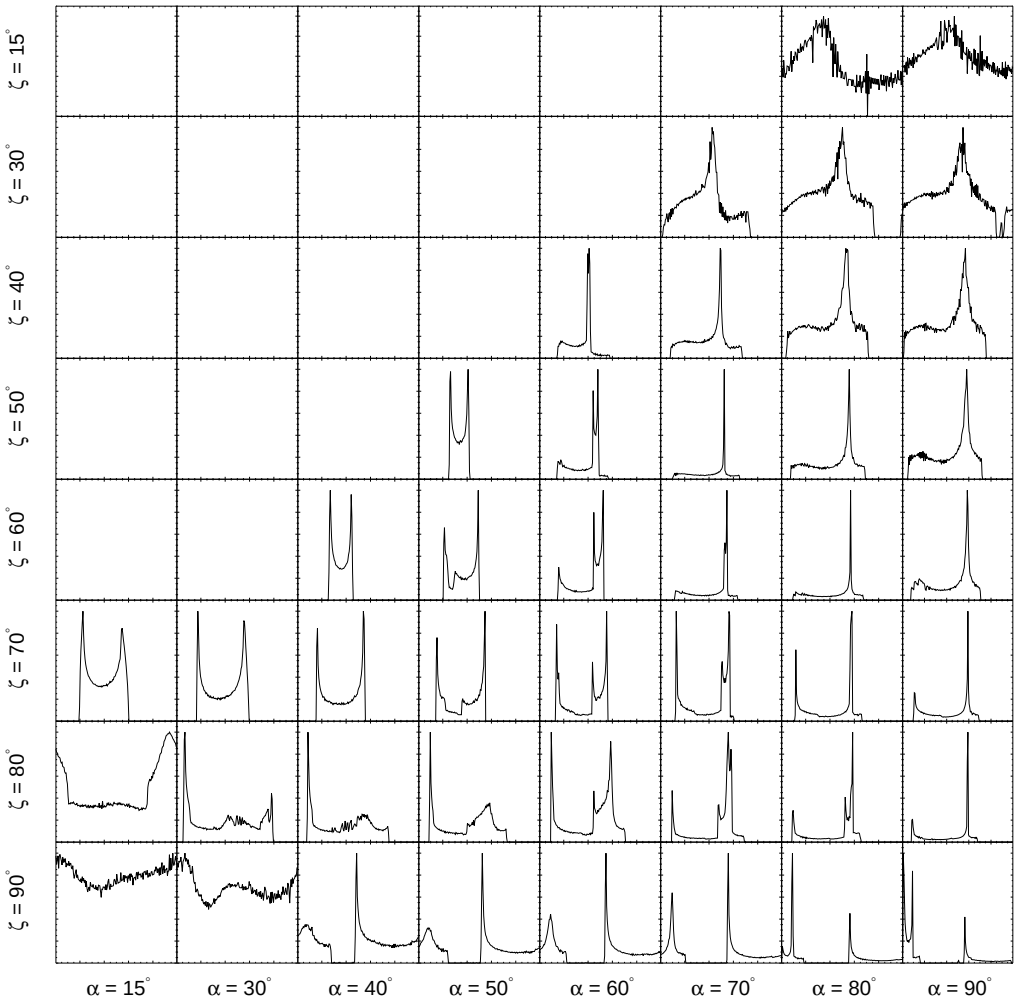

Figure B.5: Light curves from the outer gap geometry in the vacuum retarded dipole field geometry, with $w = 0.01$ and $r = 1.2\,R_{\rm LC}$.

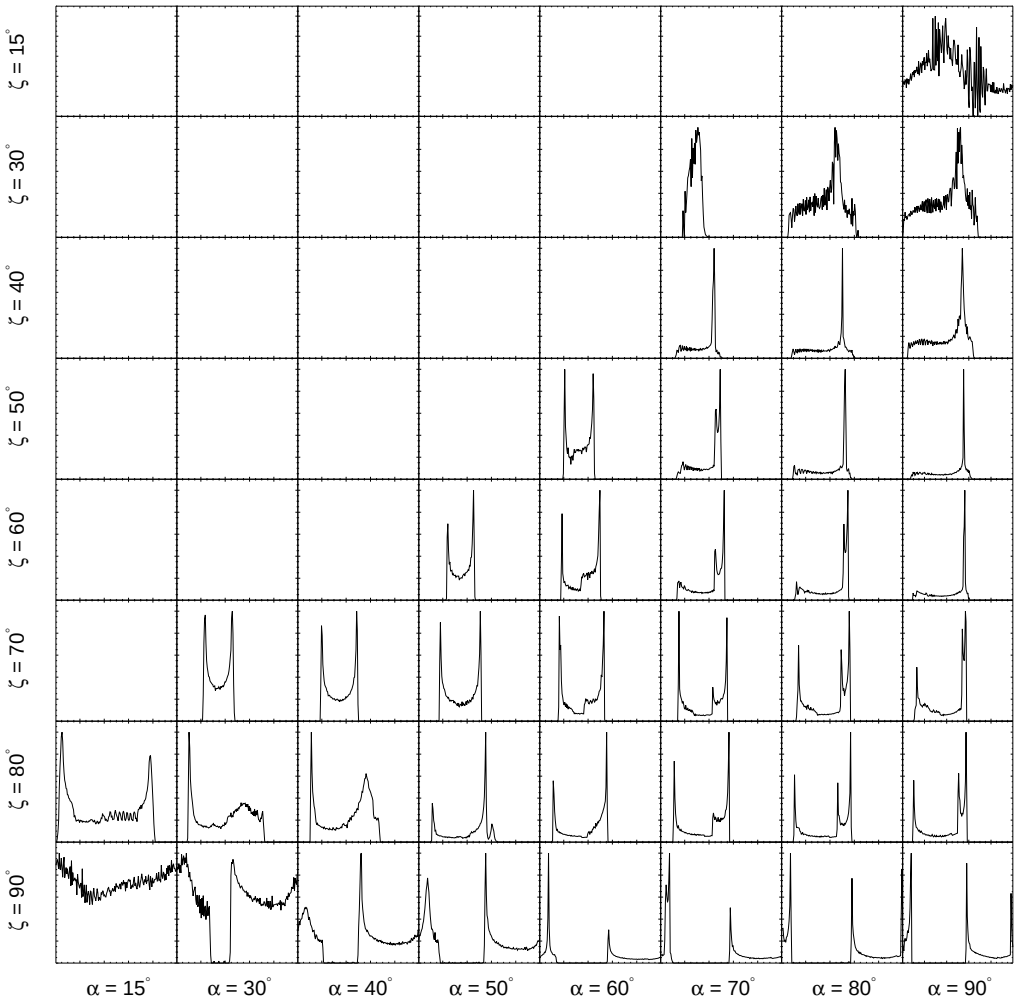

Figure B.6: Light curves from the outer gap geometry in the vacuum retarded dipole field geometry, with $w = 0.05$ and $r = 1.2\,R_{\rm LC}$.

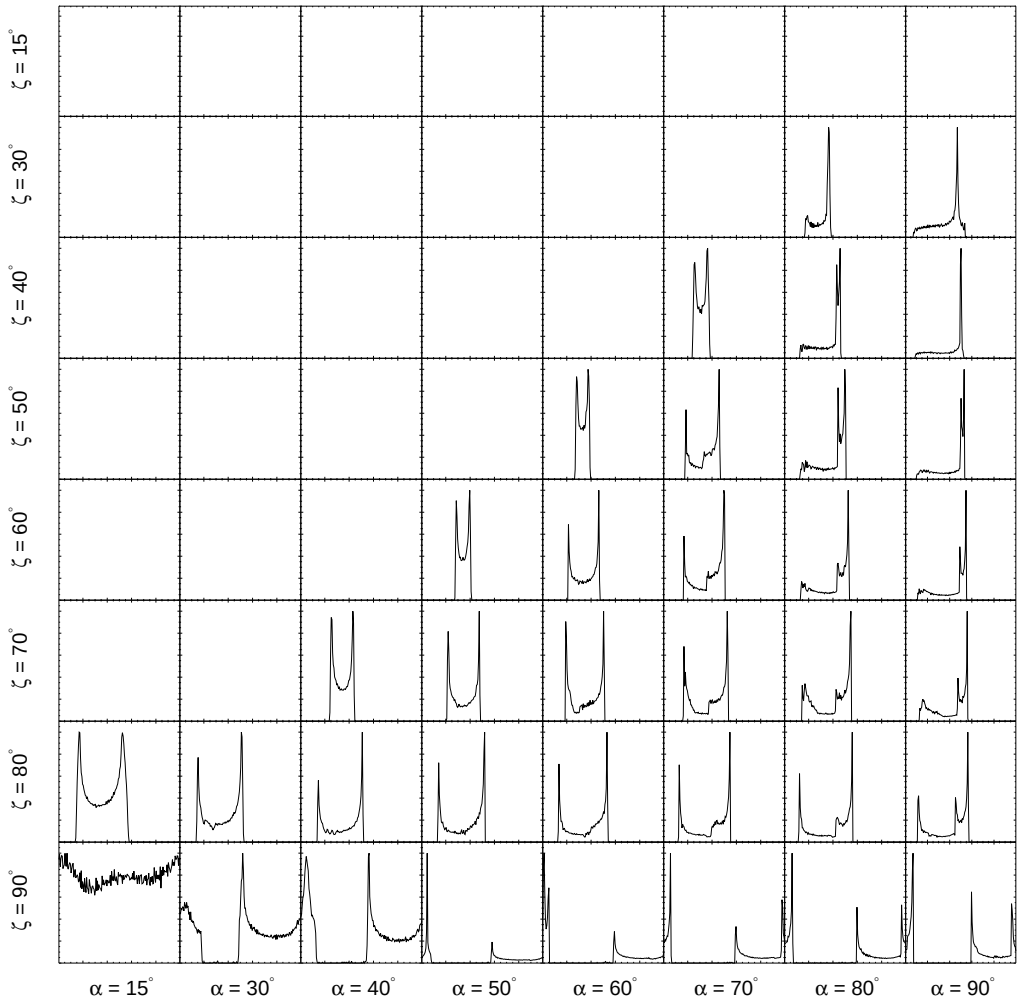

Figure B.7: Light curves from the outer gap geometry in the vacuum retarded dipole field geometry, with $w = 0.10$ and $r = 1.2\,R_{\rm LC}$.

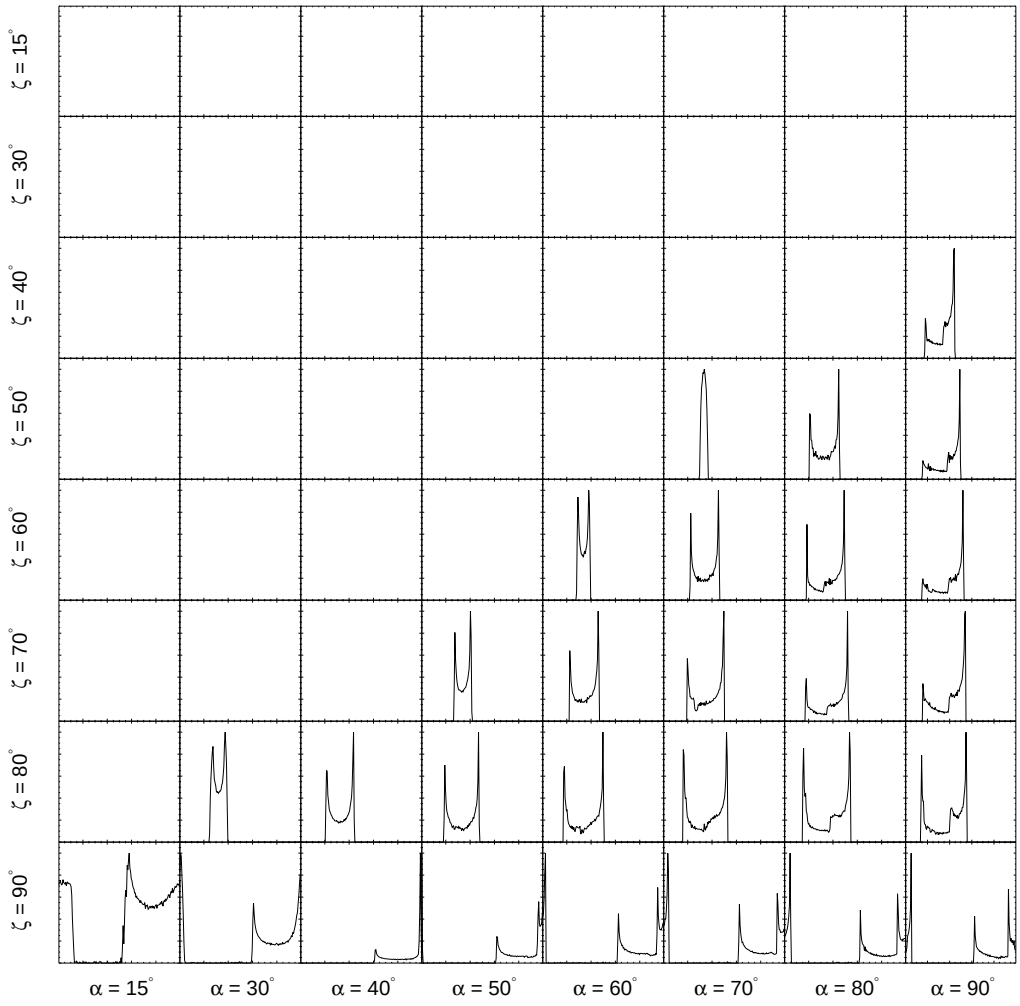

Figure B.8: Light curves from the outer gap geometry in the vacuum retarded dipole field geometry, with $w = 0.20$ and $r = 1.2\,R_{\rm LC}$.

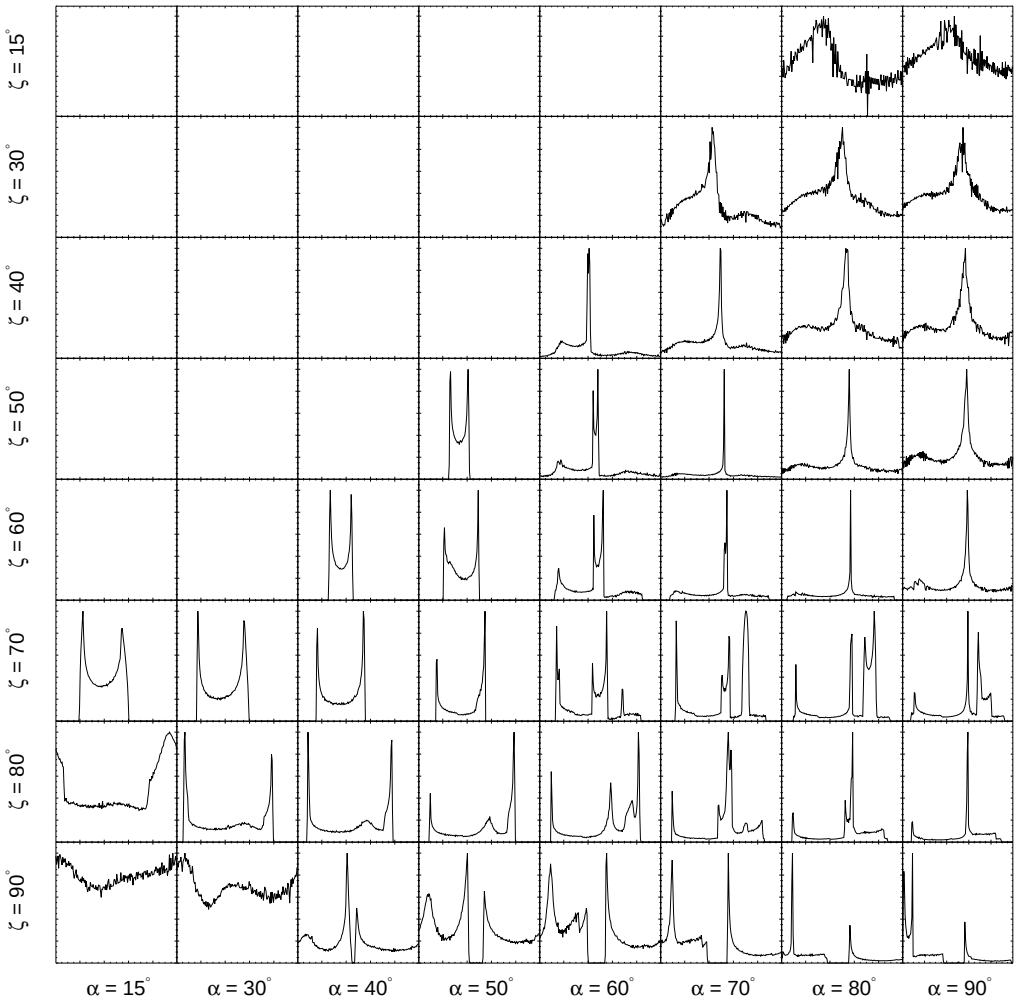

Figure B.9: Light curves from the outer gap geometry in the vacuum retarded dipole field geometry, with $w = 0.01$ and $r = 1.7\,R_{\rm LC}$.

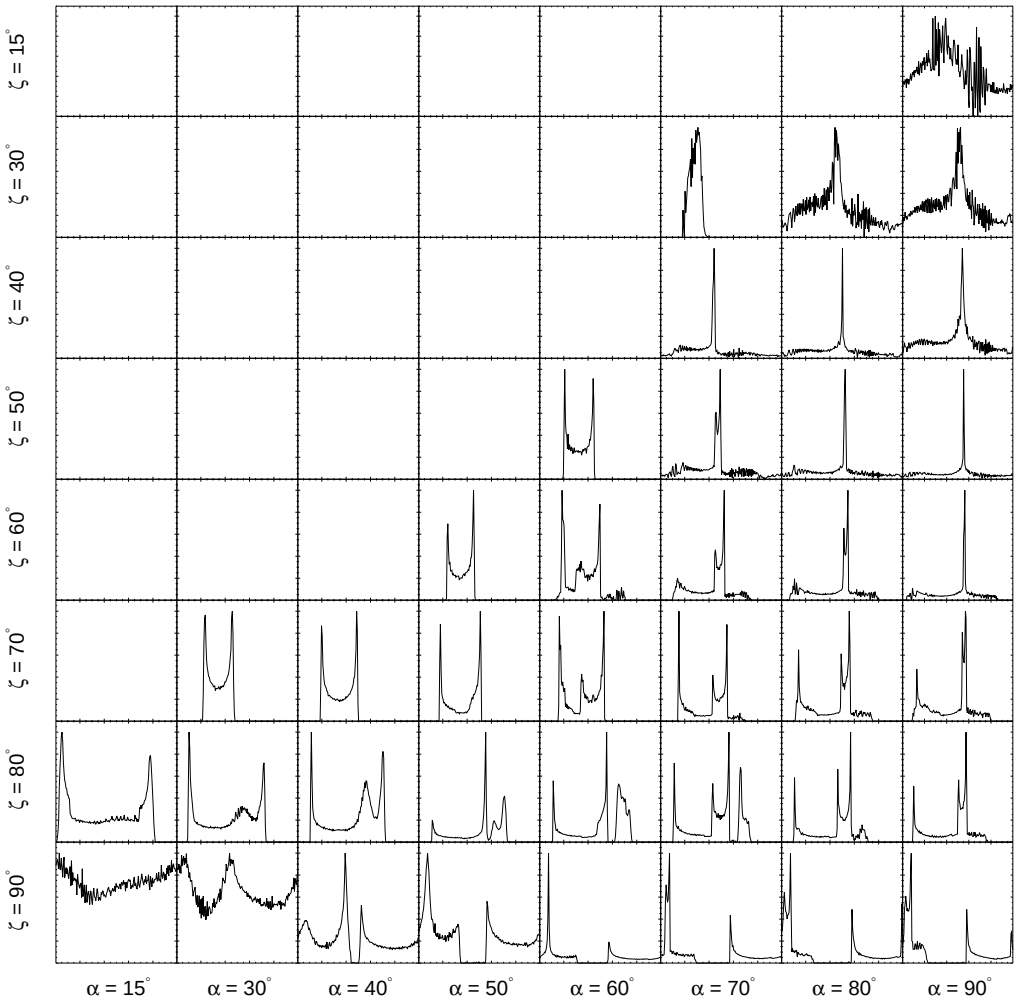

Figure B.10: Light curves from the outer gap geometry in the vacuum retarded dipole field geometry, with $w = 0.05$ and $r = 1.7\,R_{\rm LC}$.

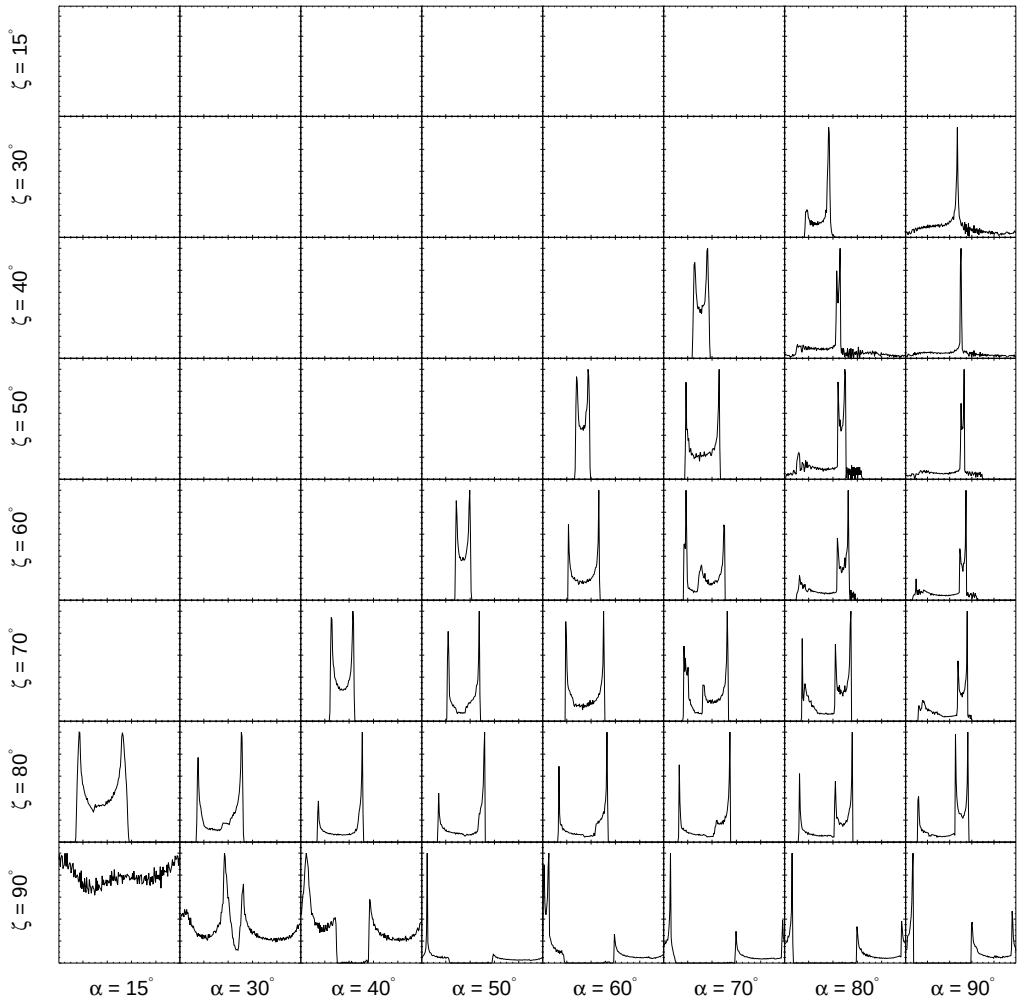

Figure B.11: Light curves from the outer gap geometry in the vacuum retarded dipole field geometry, with $w = 0.10$ and $r = 1.7\,R_{\rm LC}$.

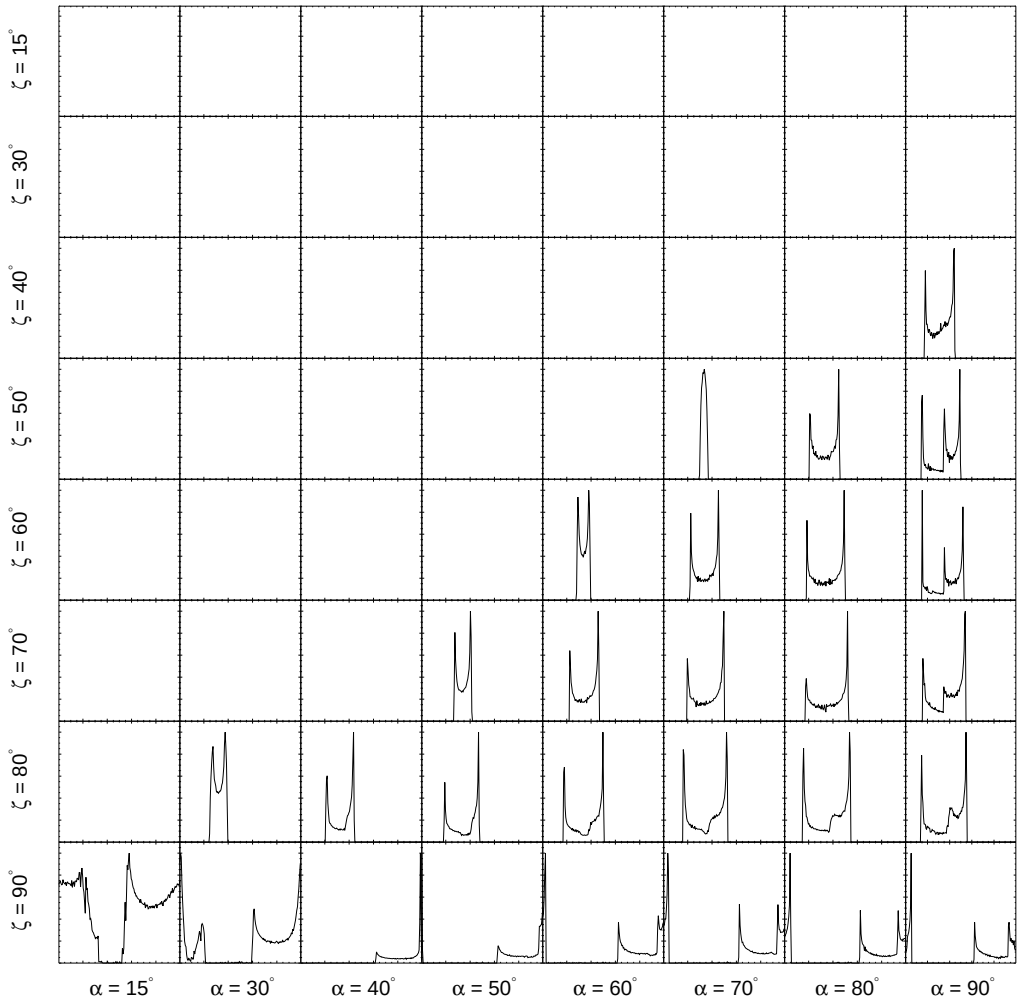

Figure B.12: Light curves from the outer gap geometry in the vacuum retarded dipole field geometry, with $w = 0.20$ and $r = 1.7\,R_{\rm LC}$.

B.2 Light Curves in the Vacuum Symmetric Slot Gap Geometry

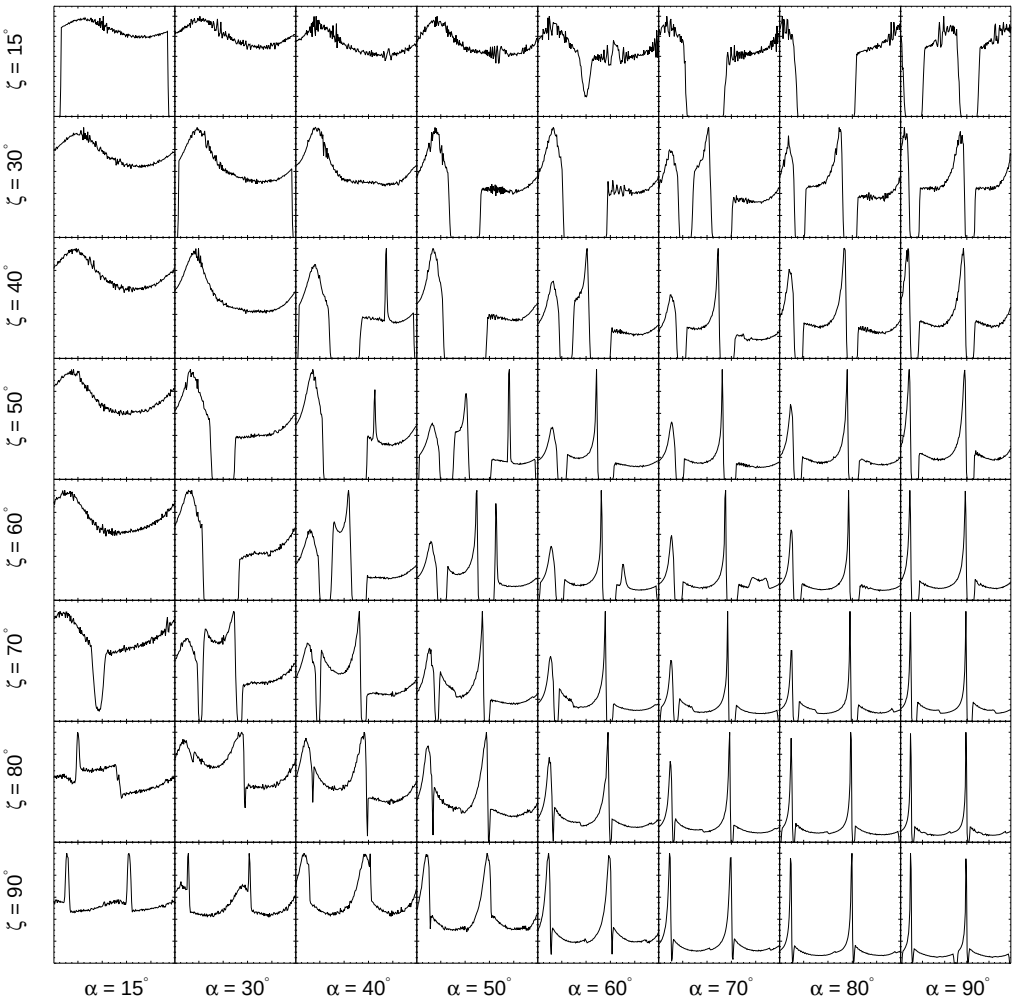

Figure B.13: Light curves from the symmetric slot gap geometry in the vacuum retarded dipole field geometry, with $w = 0.01$ and $r = 0.7\,R_{\rm LC}$.

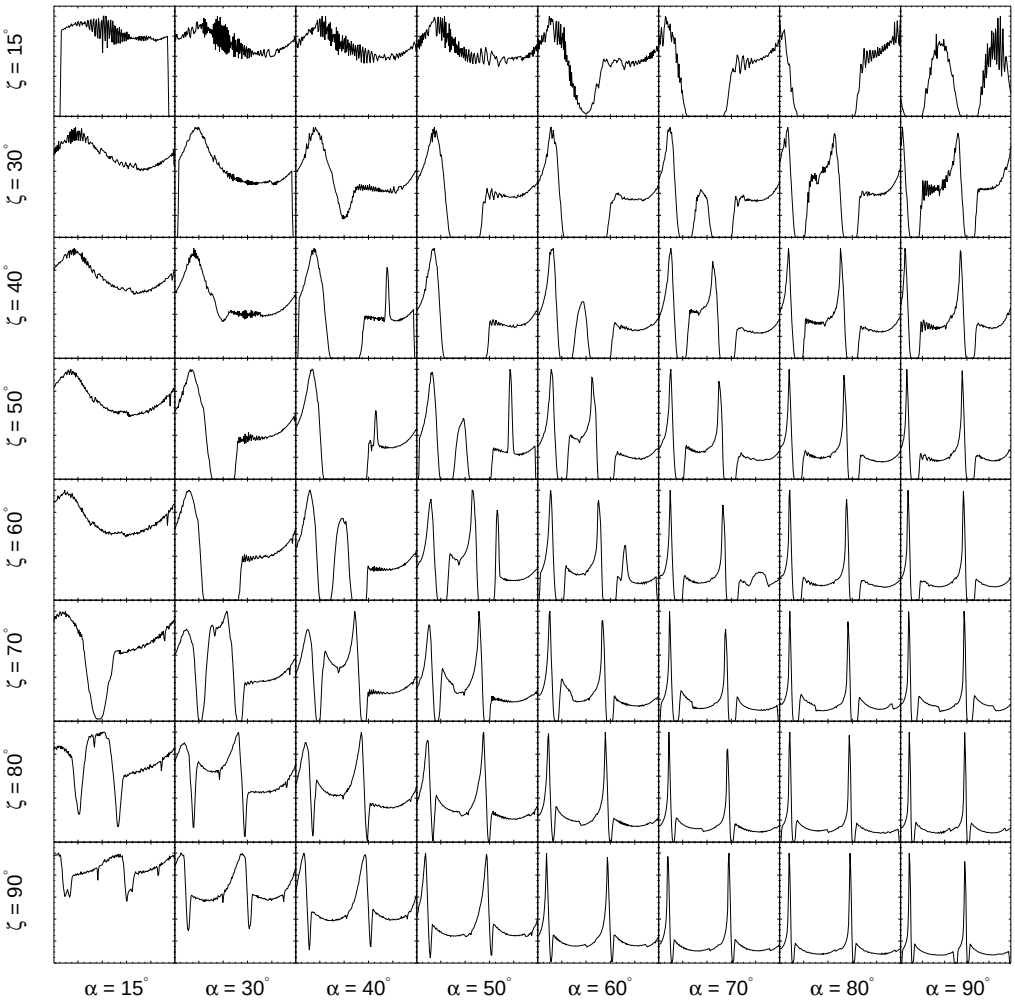

Figure B.14: Light curves from the symmetric slot gap geometry in the vacuum retarded dipole field, with $w = 0.05$ and $r = 0.7\,R_{\rm LC}$.

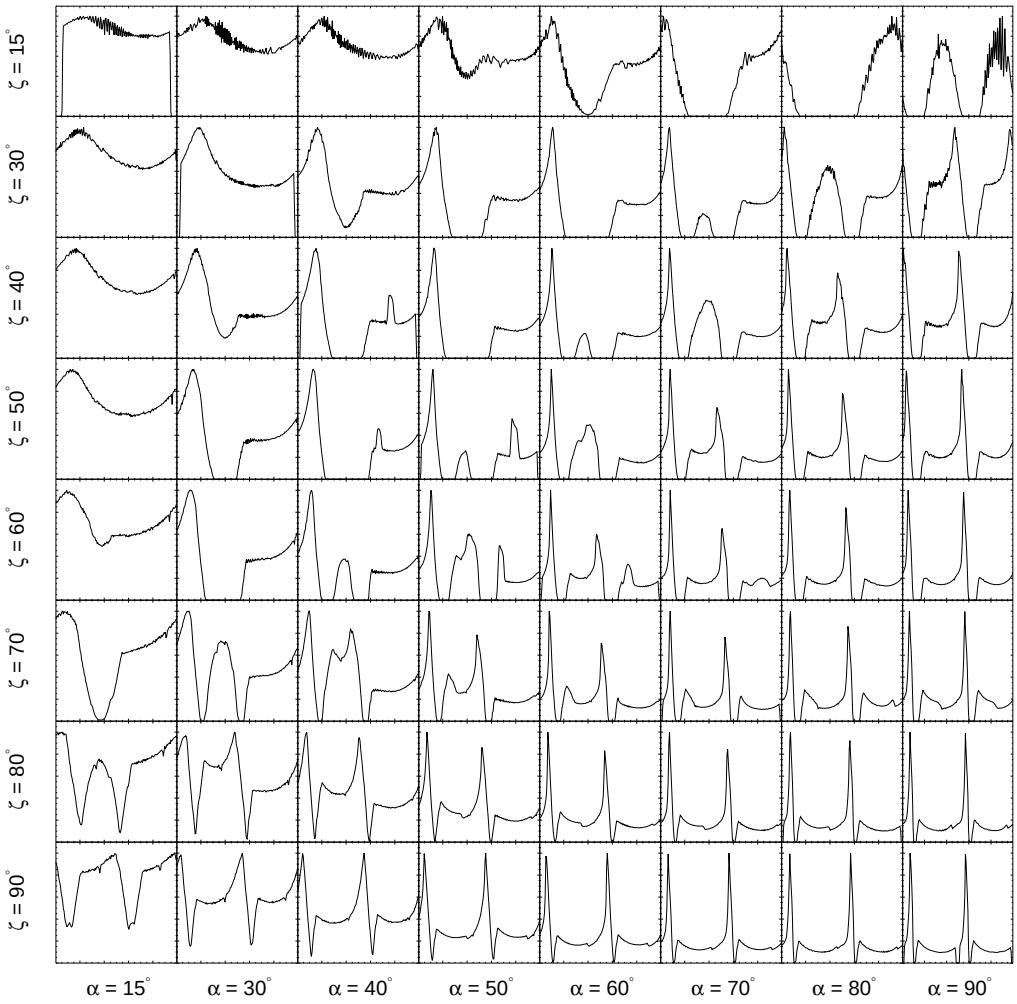

Figure B.15: Light curves from the symmetric slot gap geometry in the vacuum retarded dipole field geometry, with $w = 0.10$ and $r = 0.7\,R_{\rm LC}$.

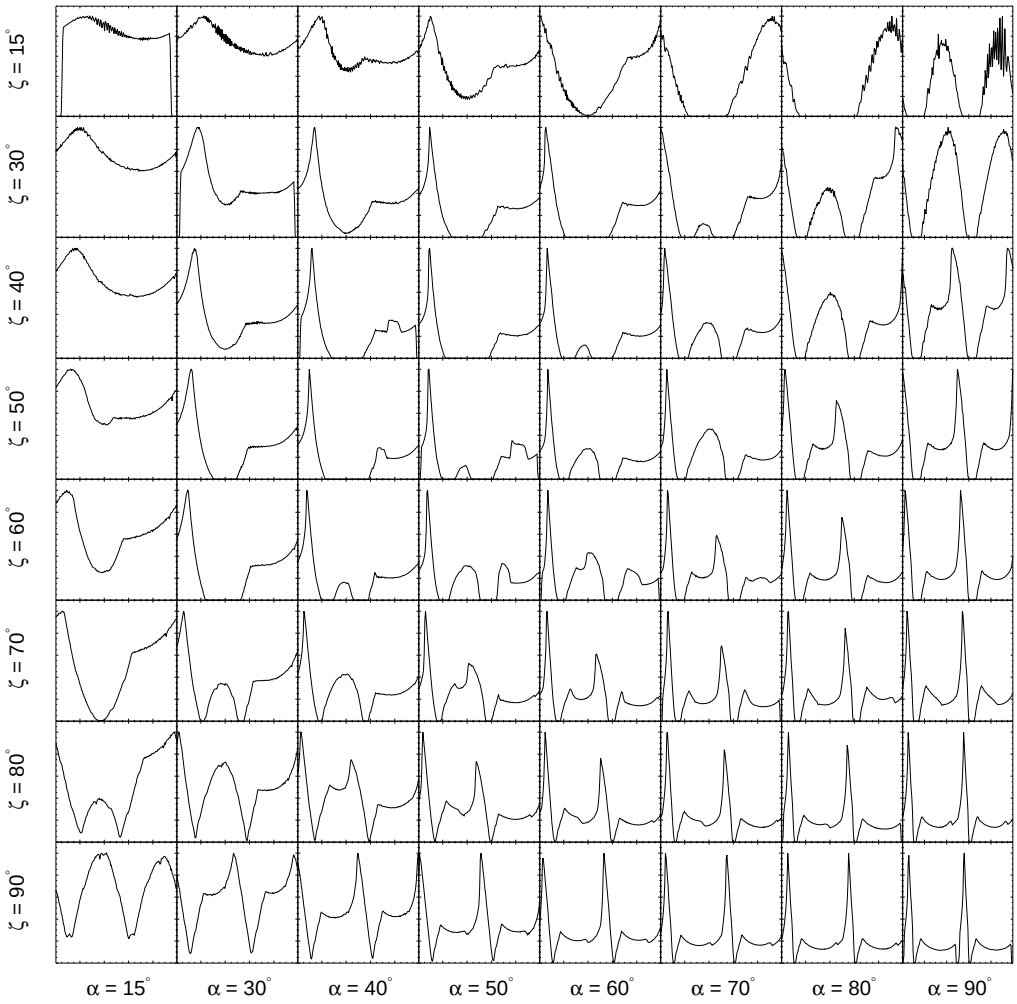

Figure B.16: Light curves from the symmetric slot gap geometry in the vacuum retarded dipole field geometry, with $w = 0.20$ and $r = 0.7\,R_{\rm LC}$.

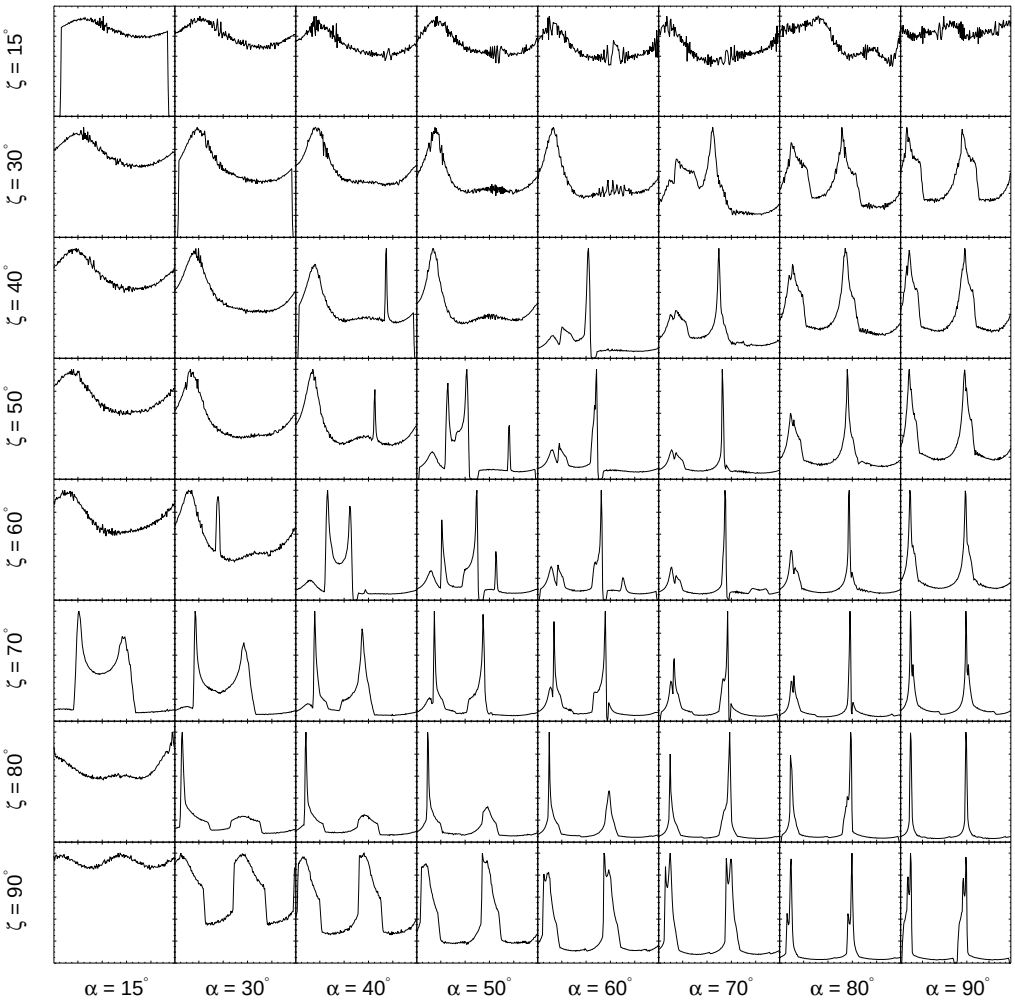

Figure B.17: Light curves from the symmetric slot gap geometry in the vacuum retarded dipole field geometry, with $w = 0.01$ and $r = 1.0\,R_{\rm LC}$.

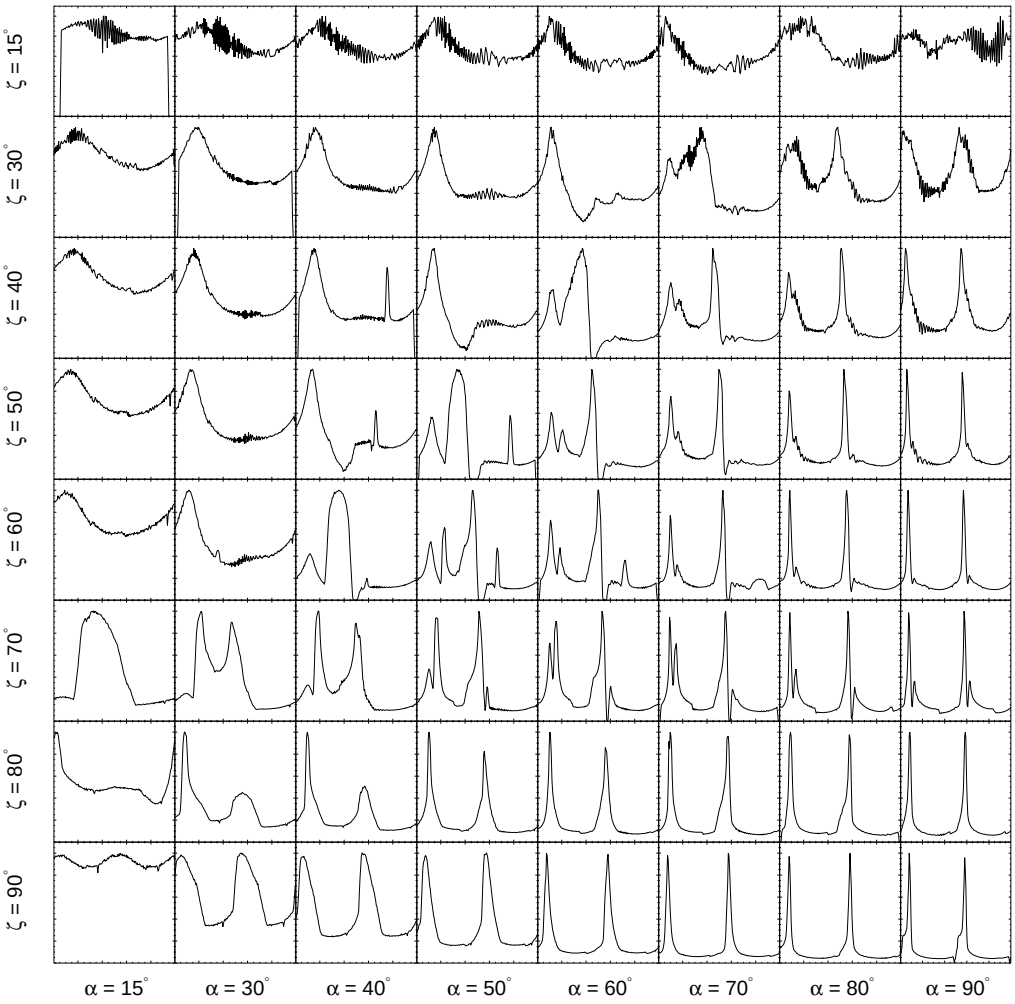

Figure B.18: Light curves from the symmetric slot gap geometry in the vacuum retarded dipole field geometry, with $w = 0.05$ and $r = 1.0\,R_{\rm LC}$.

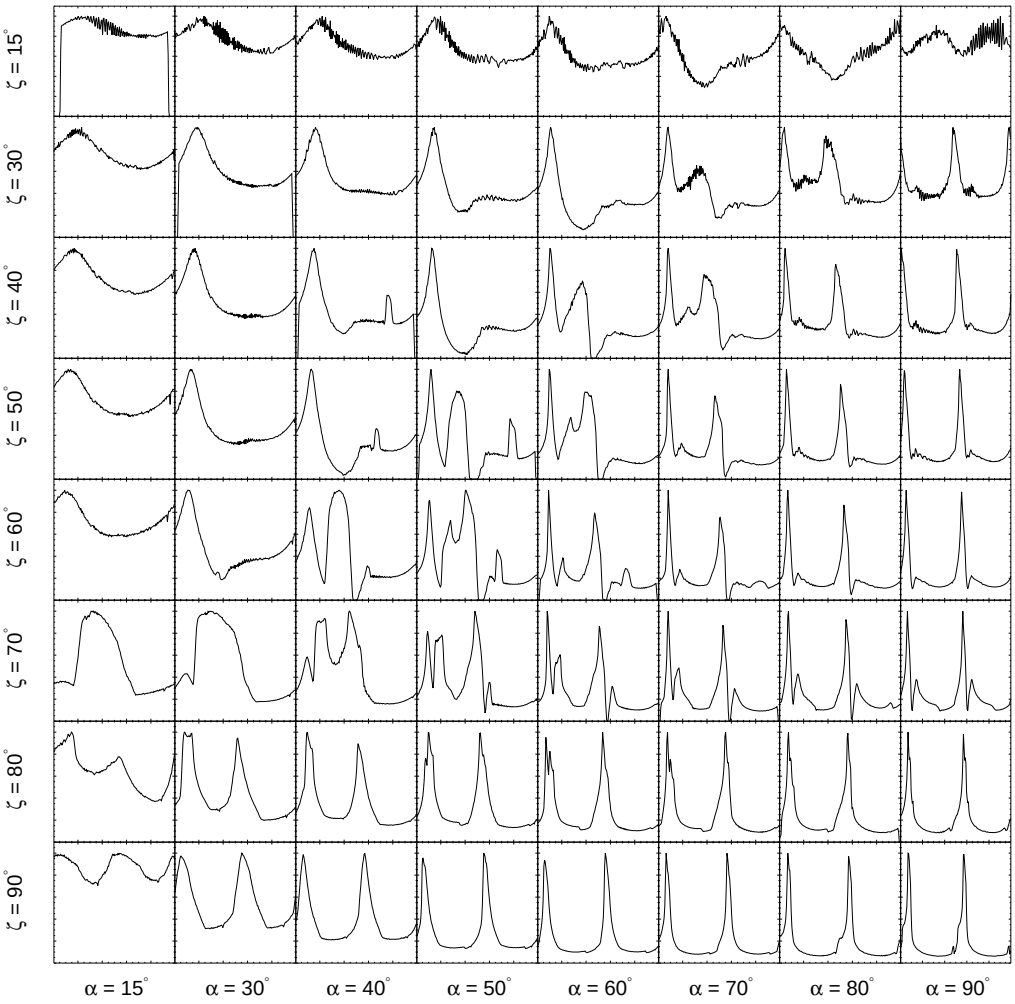

Figure B.19: Light curves from the symmetric slot gap geometry in the vacuum retarded dipole field geometry, with $w = 0.10$ and $r = 1.0\,R_{\rm LC}$.

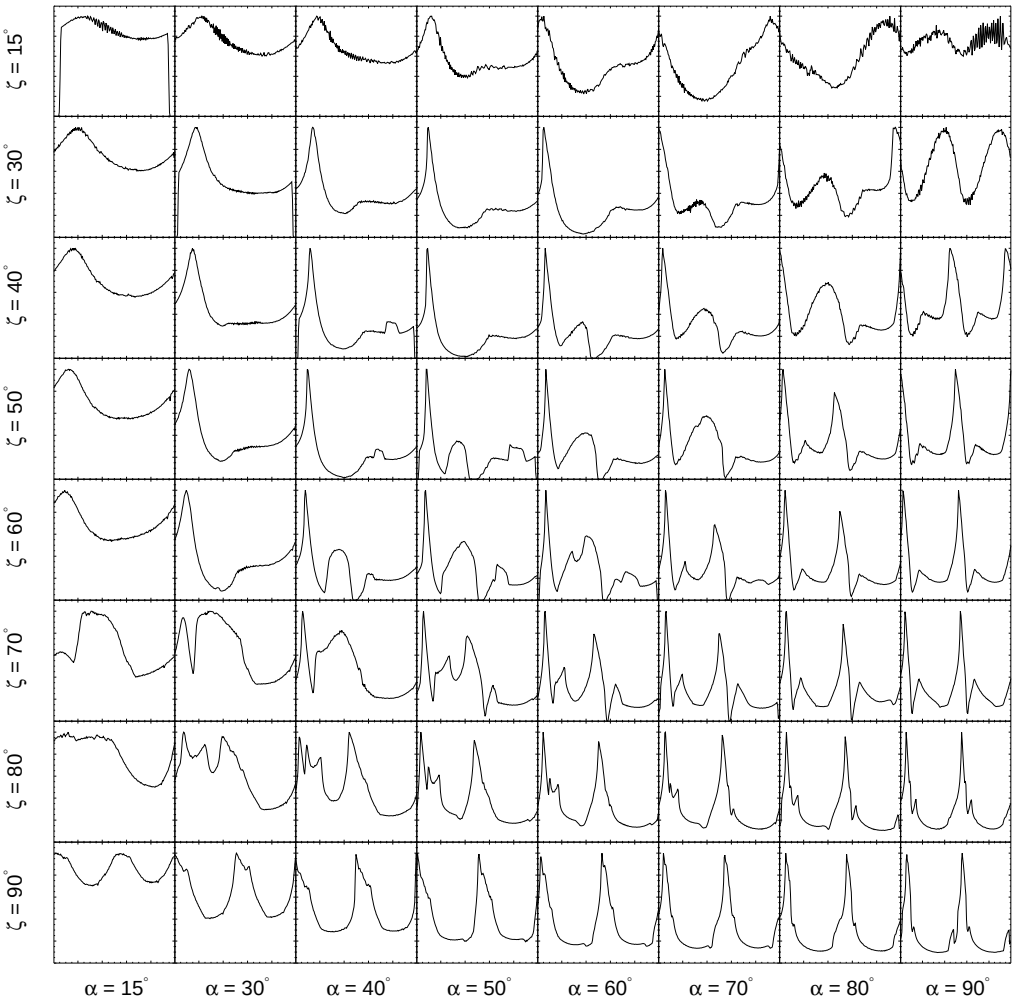

Figure B.20: Light curves from the symmetric slot gap geometry in the vacuum retarded dipole field geometry, with $w = 0.20$ and $r = 1.0\,R_{\rm LC}$.

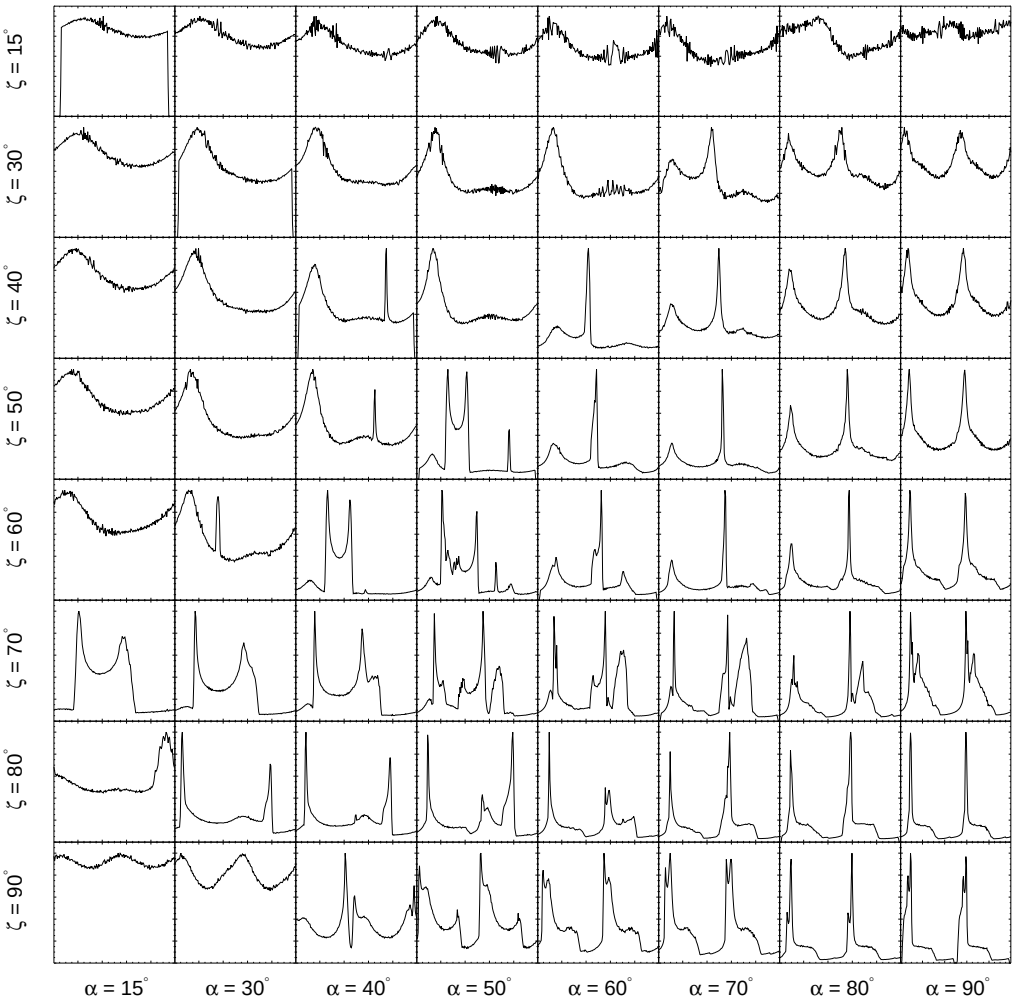

Figure B.21: Light curves from the symmetric slot gap geometry in the vacuum retarded dipole field geometry, with $w = 0.01$ and $r = 1.2\,R_{\rm LC}$.

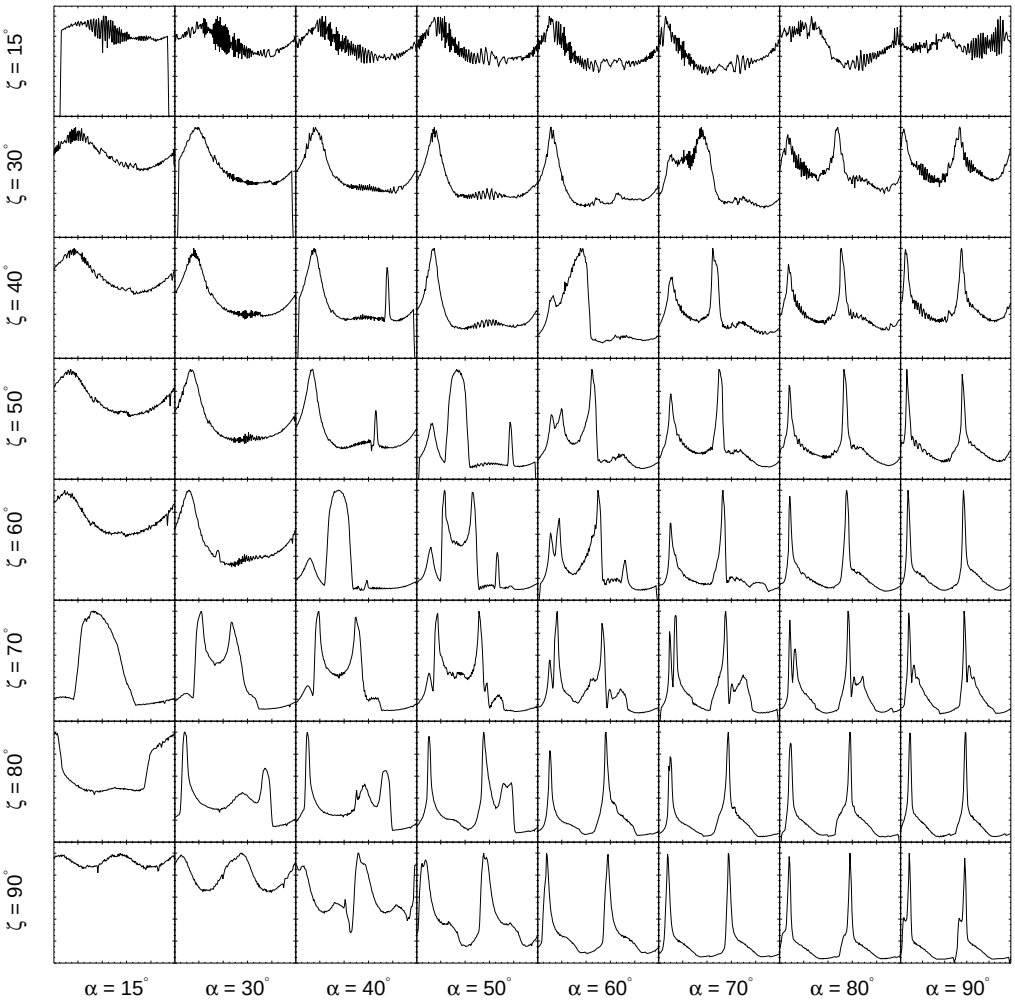

Figure B.22: Light curves from the symmetric slot gap geometry in the vacuum retarded dipole field geometry, with $w = 0.05$ and $r = 1.2\,R_{\rm LC}$.

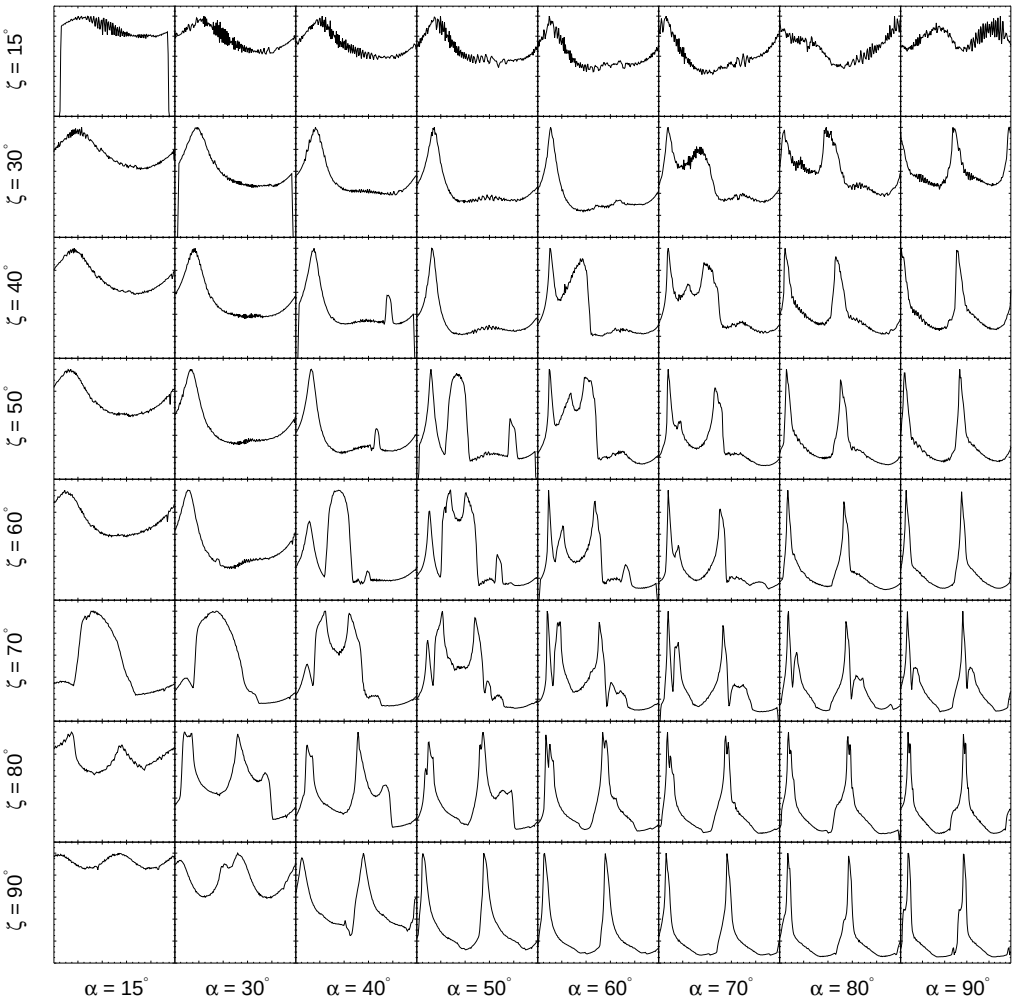

Figure B.23: Light curves from the symmetric slot gap geometry in the vacuum retarded dipole field geometry, with $w = 0.10$ and $r = 1.2\,R_{\rm LC}$.

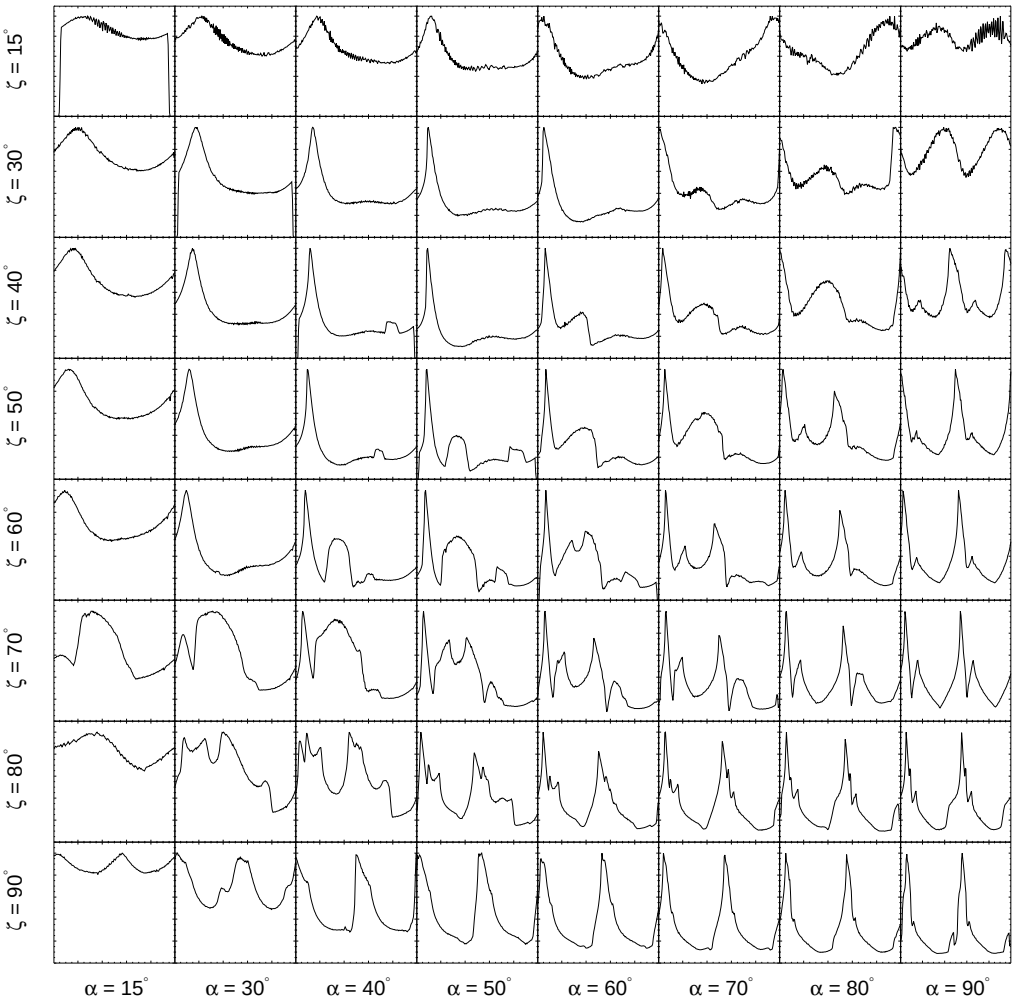

Figure B.24: Light curves from the symmetric slot gap geometry in the vacuum retarded dipole field geometry, with $w = 0.20$ and $r = 1.2\,R_{\rm LC}$.

B.3 Light Curves in the Vacuum Asymmetric Slot Gap Geometry

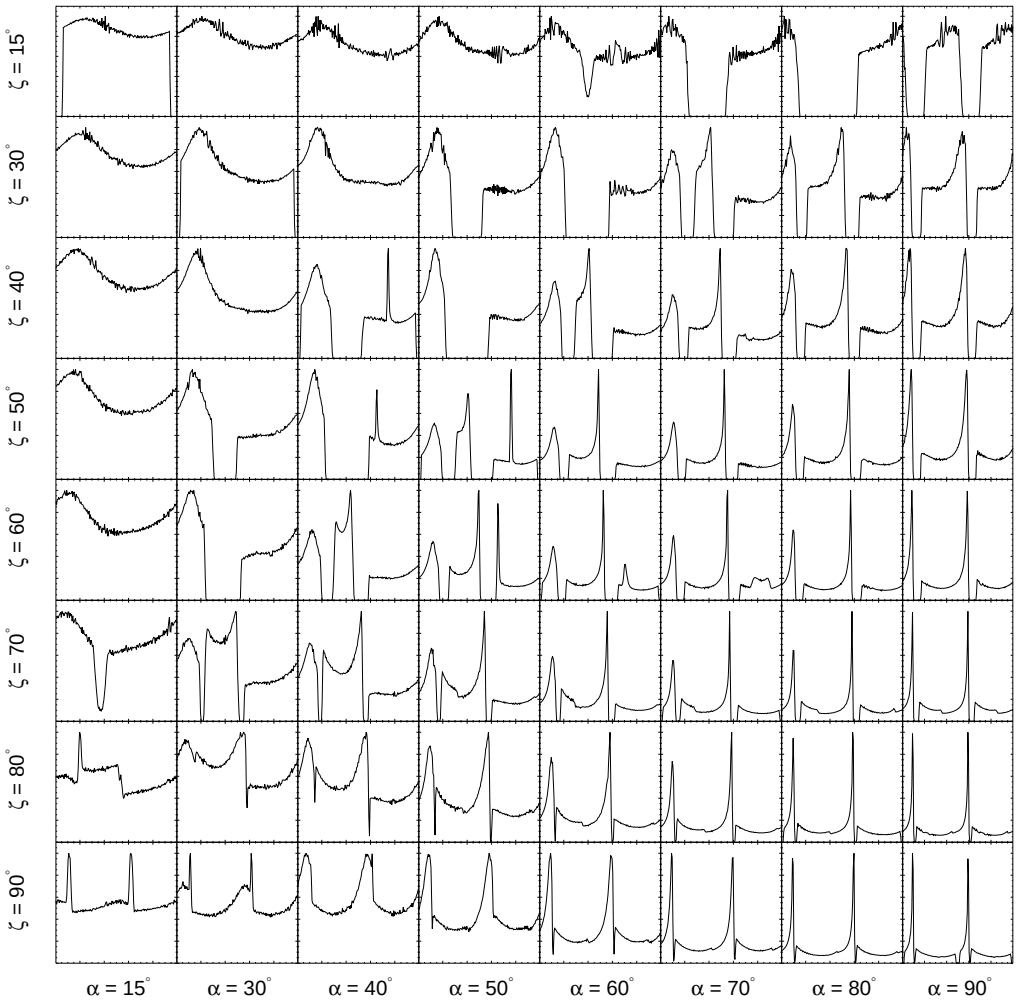

Figure B.25: Light curves from the asymmetric slot gap geometry in the vacuum retarded dipole field geometry, with $w = 0.01$ and $r = 0.7\,R_{\rm LC}$.

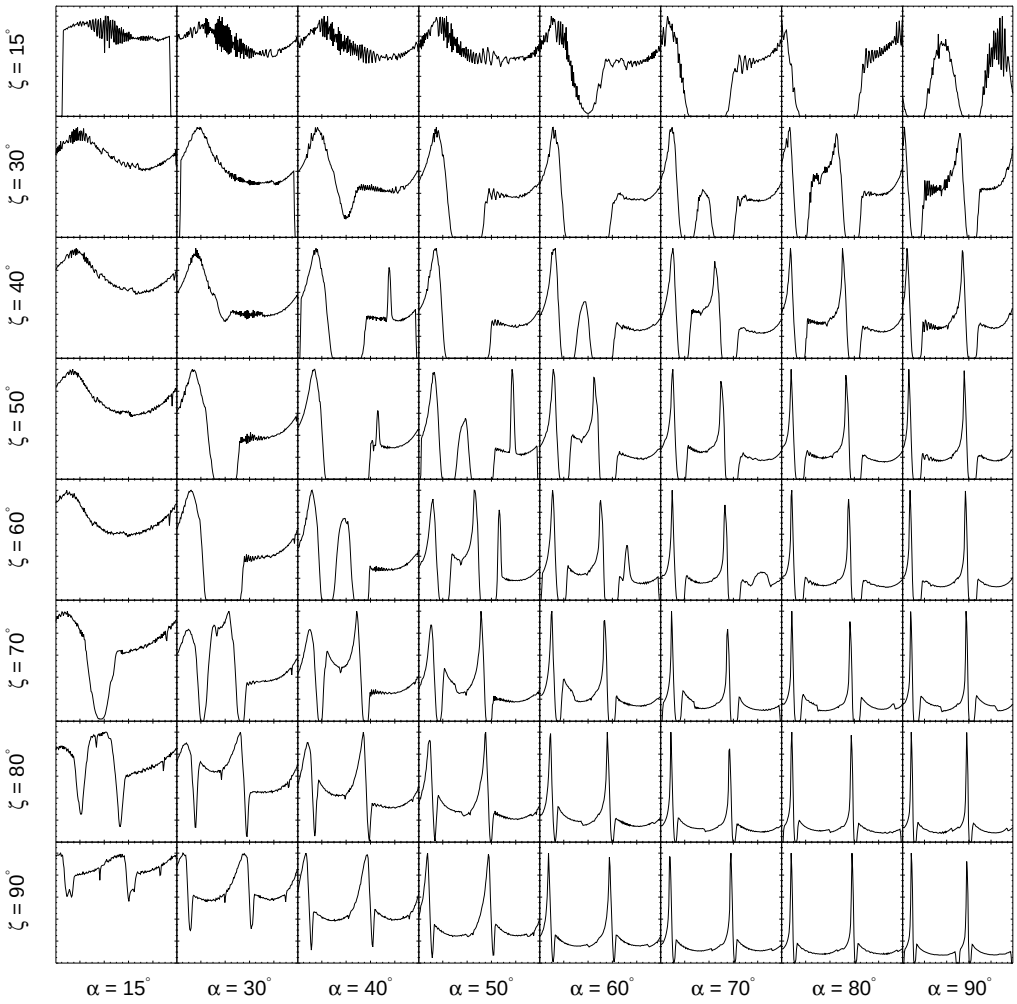

Figure B.26: Light curves from the asymmetric slot gap geometry in the vacuum retarded dipole field geometry, with $w = 0.05$ and $r = 0.7\,R_{\rm LC}$.

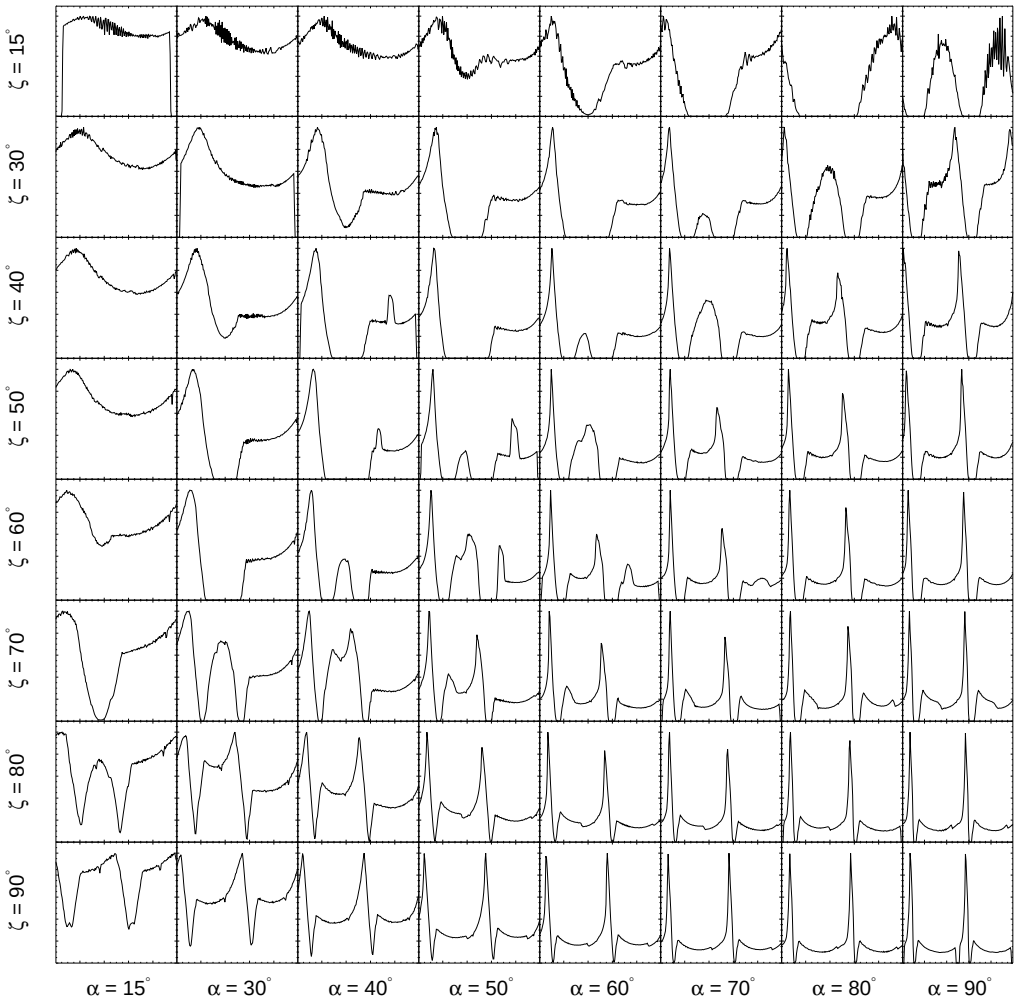

Figure B.27: Light curves from the asymmetric slot gap geometry in the vacuum retarded dipole field geometry, with $w = 0.10$ and $r = 0.7\,R_{\rm LC}$.

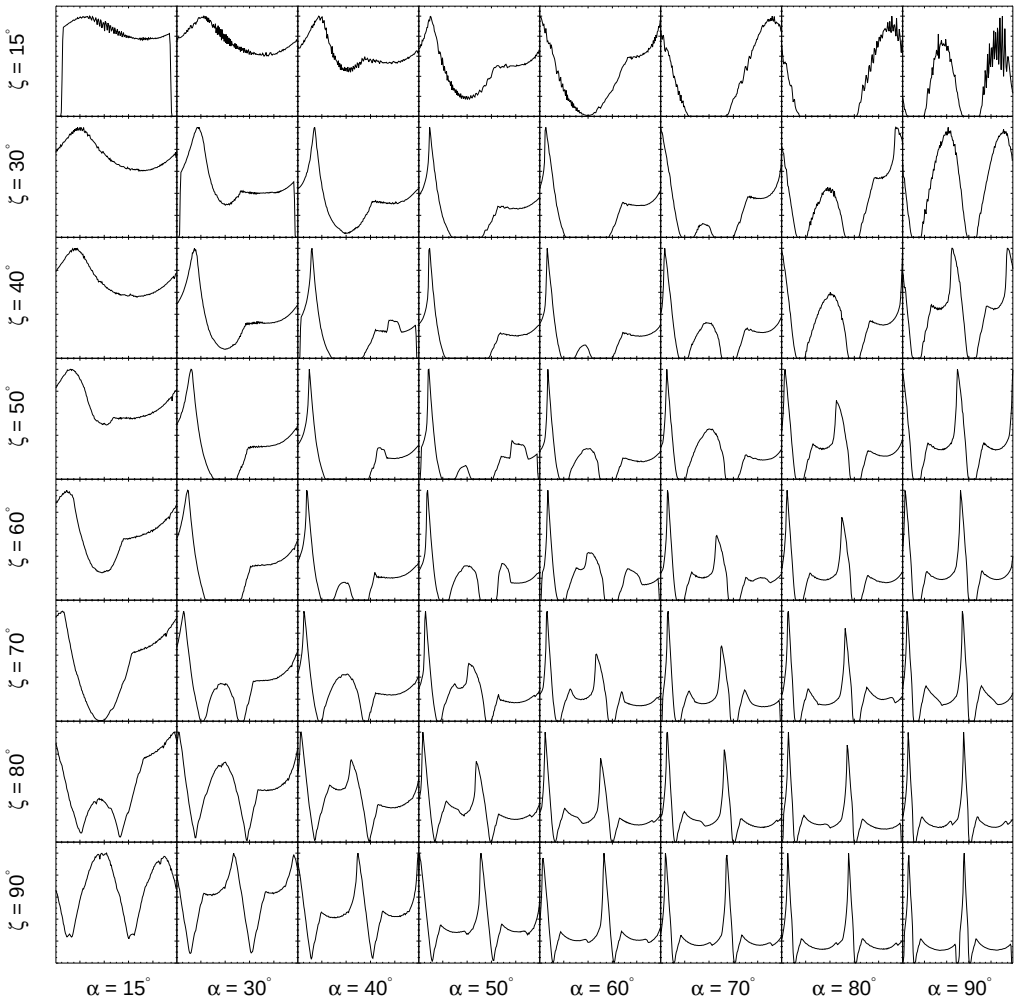

Figure B.28: Light curves from the asymmetric slot gap geometry in the vacuum retarded dipole field geometry, with $w = 0.20$ and $r = 0.7\,R_{\rm LC}$.

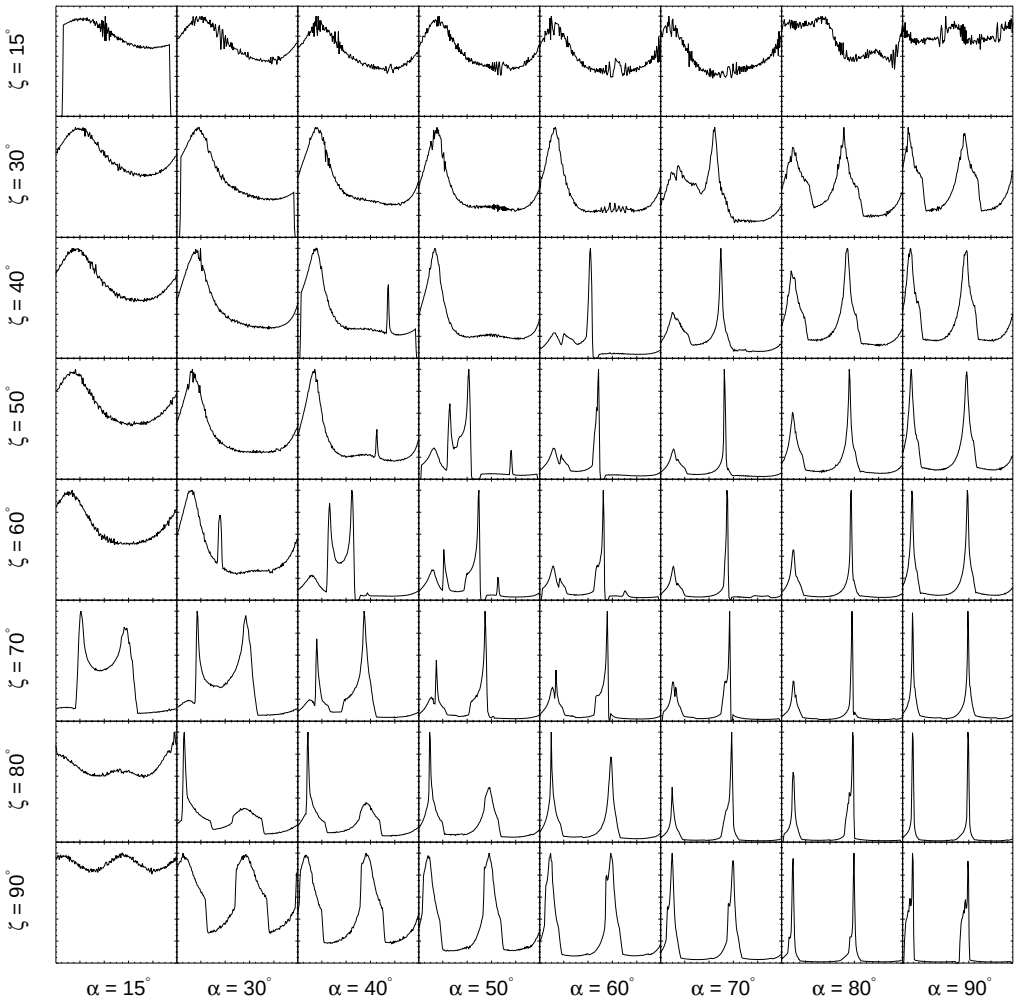

Figure B.29: Light curves from the asymmetric slot gap geometry in the vacuum retarded dipole field geometry, with $w = 0.01$ and $r = 1.0\,R_{\rm LC}$.

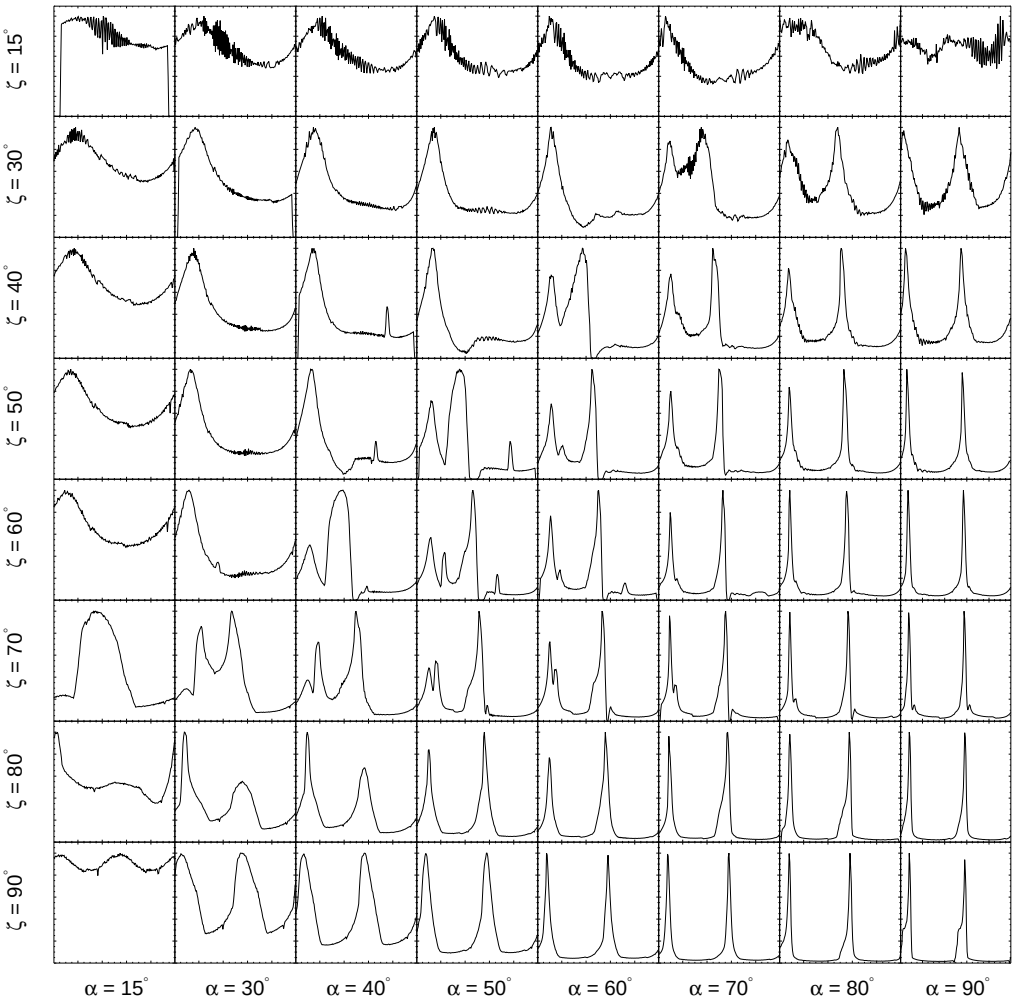

Figure B.30: Light curves from the asymmetric slot gap geometry in the vacuum retarded dipole field geometry, with $w = 0.05$ and $r = 1.0\,R_{\rm LC}$.

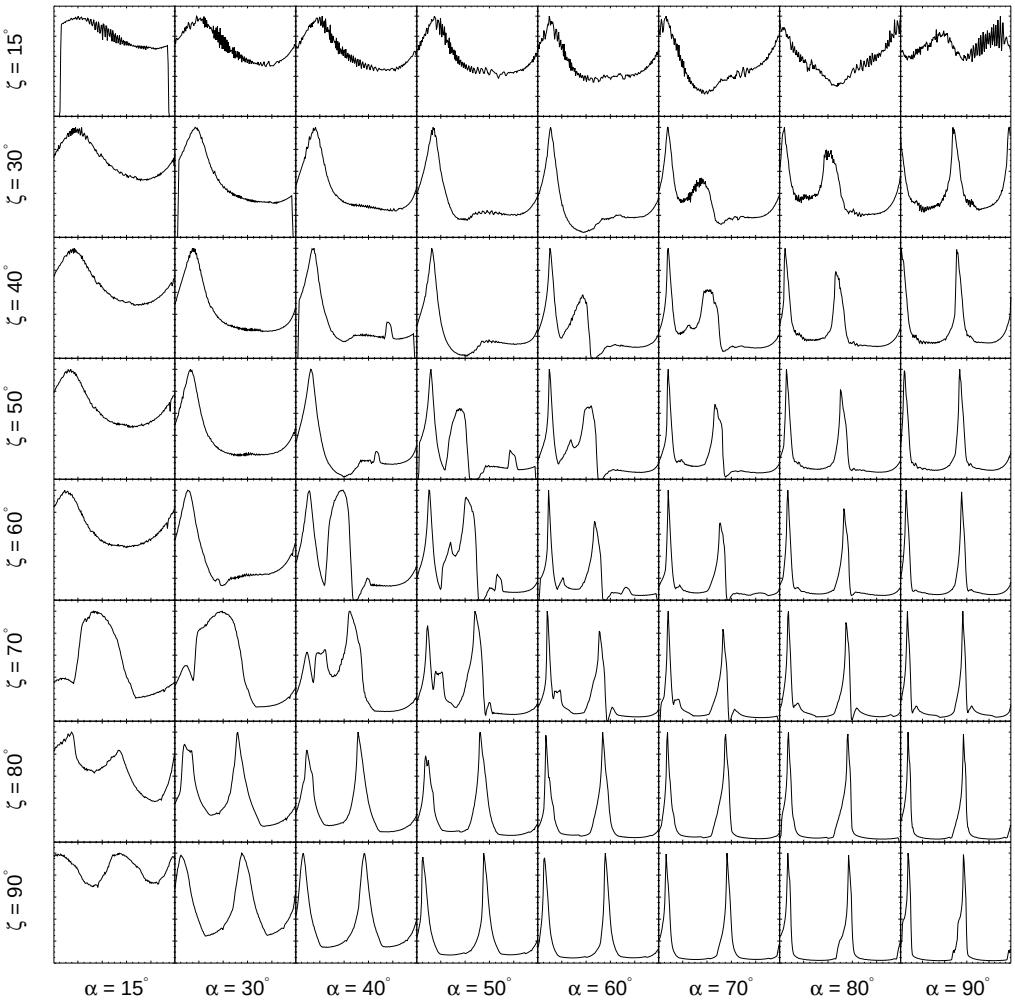

Figure B.31: Light curves from the asymmetric slot gap geometry in the vacuum retarded dipole field geometry, with $w = 0.10$ and $r = 1.0\,R_{\rm LC}$.

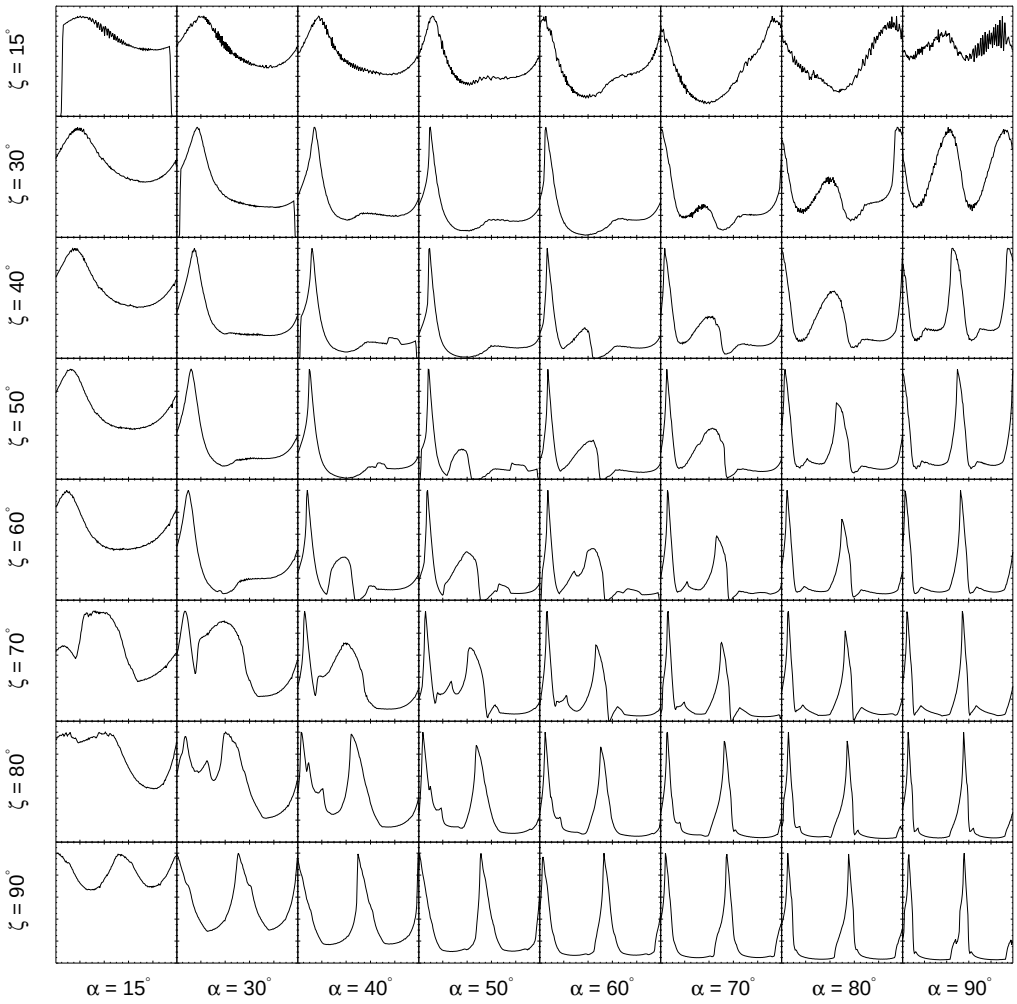

Figure B.32: Light curves from the asymmetric slot gap geometry in the vacuum retarded dipole field geometry, with $w = 0.20$ and $r = 1.0\,R_{\rm LC}$.

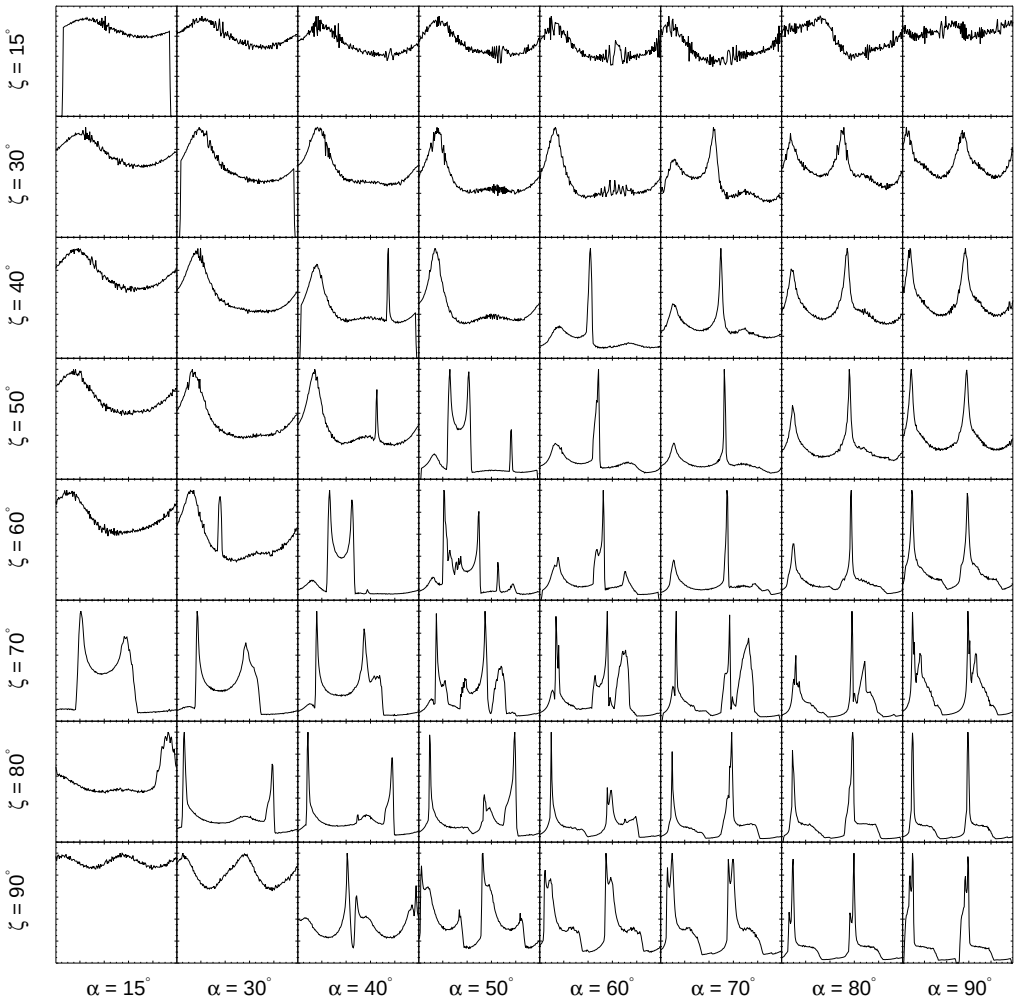

Figure B.33: Light curves from the asymmetric slot gap geometry in the vacuum retarded dipole field geometry, with $w = 0.01$ and $r = 1.5\,R_{\rm LC}$.

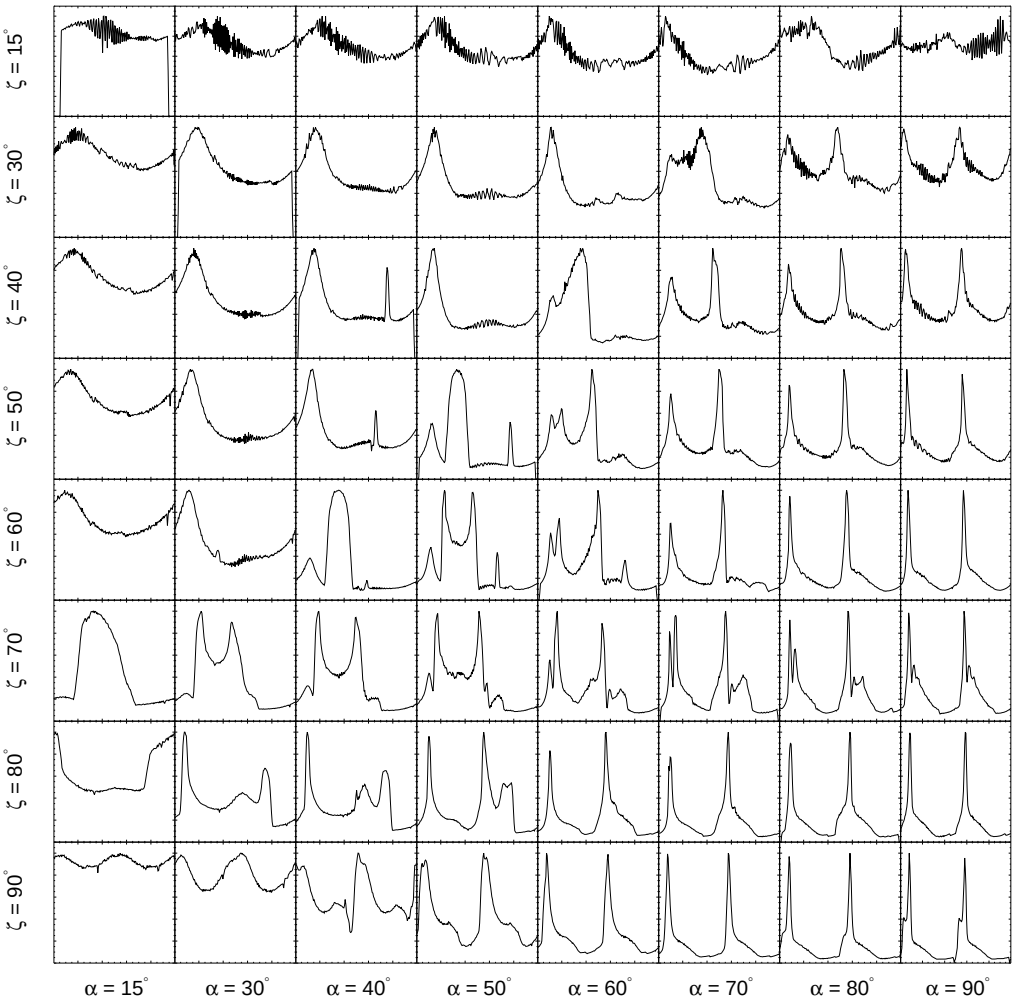

Figure B.34: Light curves from the asymmetric slot gap geometry in the vacuum retarded dipole field geometry, with $w = 0.05$ and $r = 1.5\,R_{\rm LC}$.

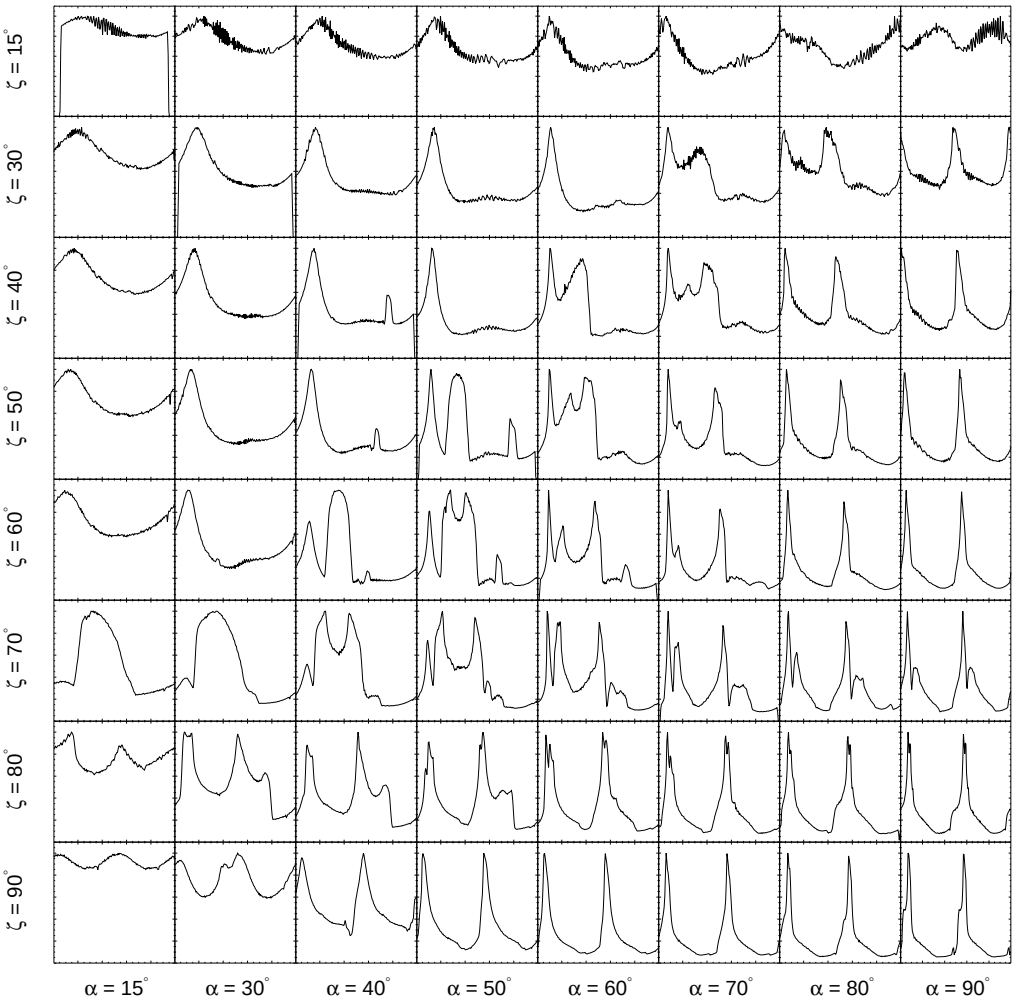

Figure B.35: Light curves from the asymmetric slot gap geometry in the vacuum retarded dipole field geometry, with $w = 0.10$ and $r = 1.5\,R_{\rm LC}$.

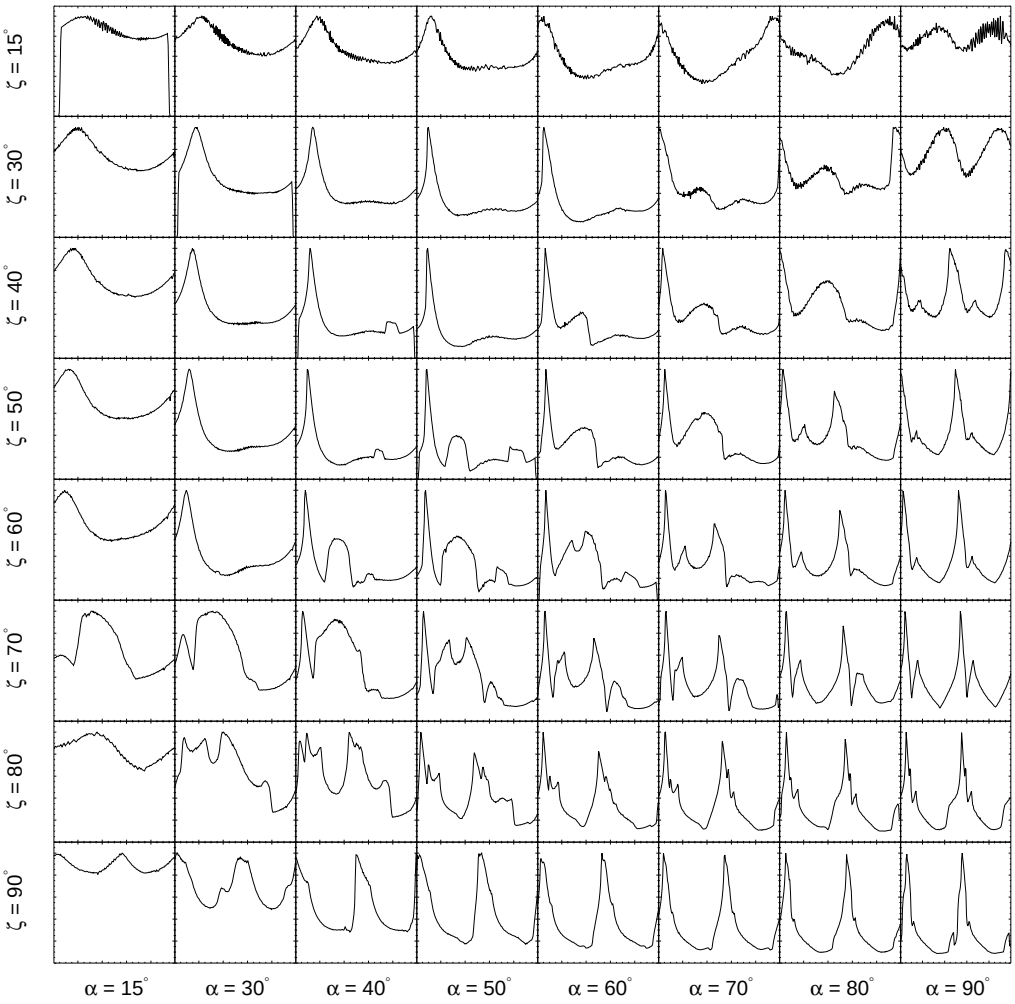

Figure B.36: Light curves from the asymmetric slot gap geometry in the vacuum retarded dipole field geometry, with $w = 0.20$ and $r = 1.5\,R_{\rm LC}$.

B.4 Light Curves in the Force-free Outer Gap Geometry

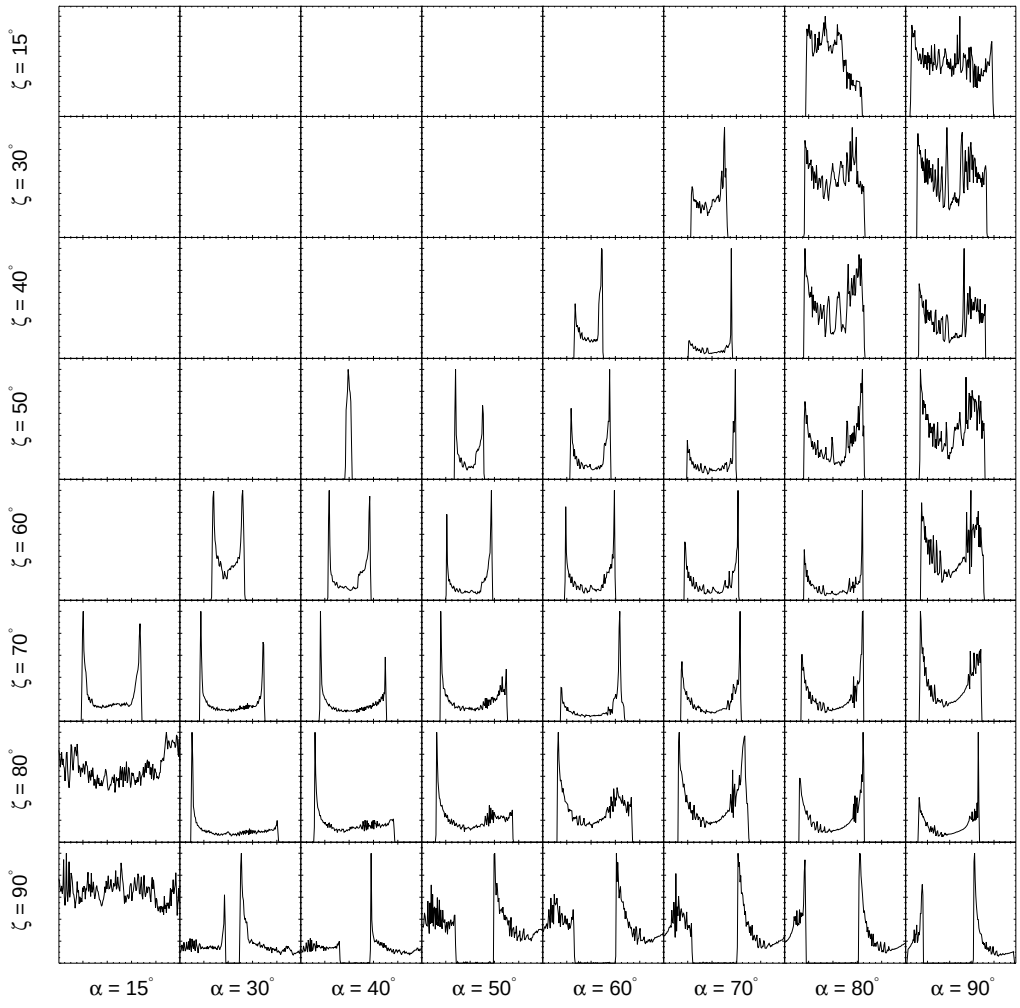

Figure B.37: Light curves from the outer gap geometry in the force-free field geometry, with $w = 0.01$ and $r = 0.9\,R_{\rm LC}$.

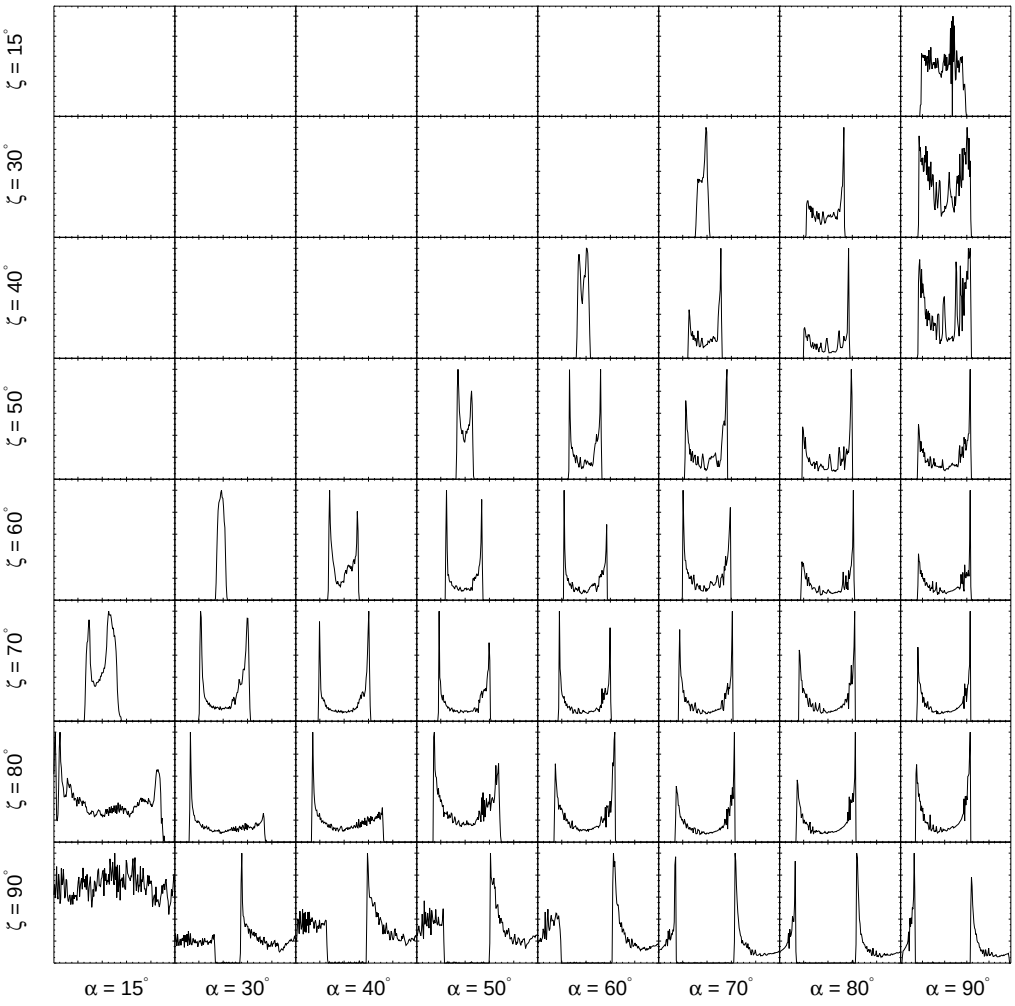

Figure B.38: Light curves from the outer gap geometry in the force-free field geometry, with $w = 0.05$ and $r = 0.9\,R_{\rm LC}$.

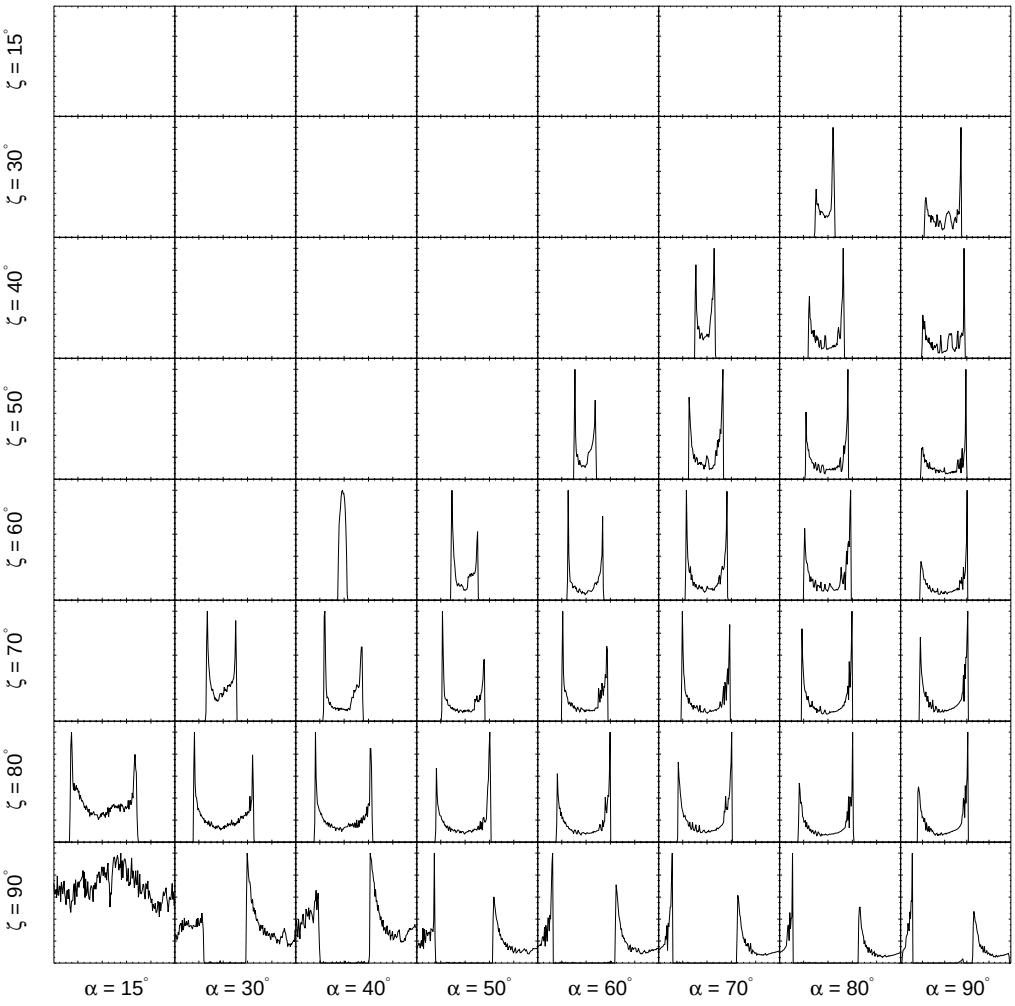

Figure B.39: Light curves from the outer gap geometry in the force-free field geometry, with $w = 0.10$ and $r = 0.9\,R_{\rm LC}$.

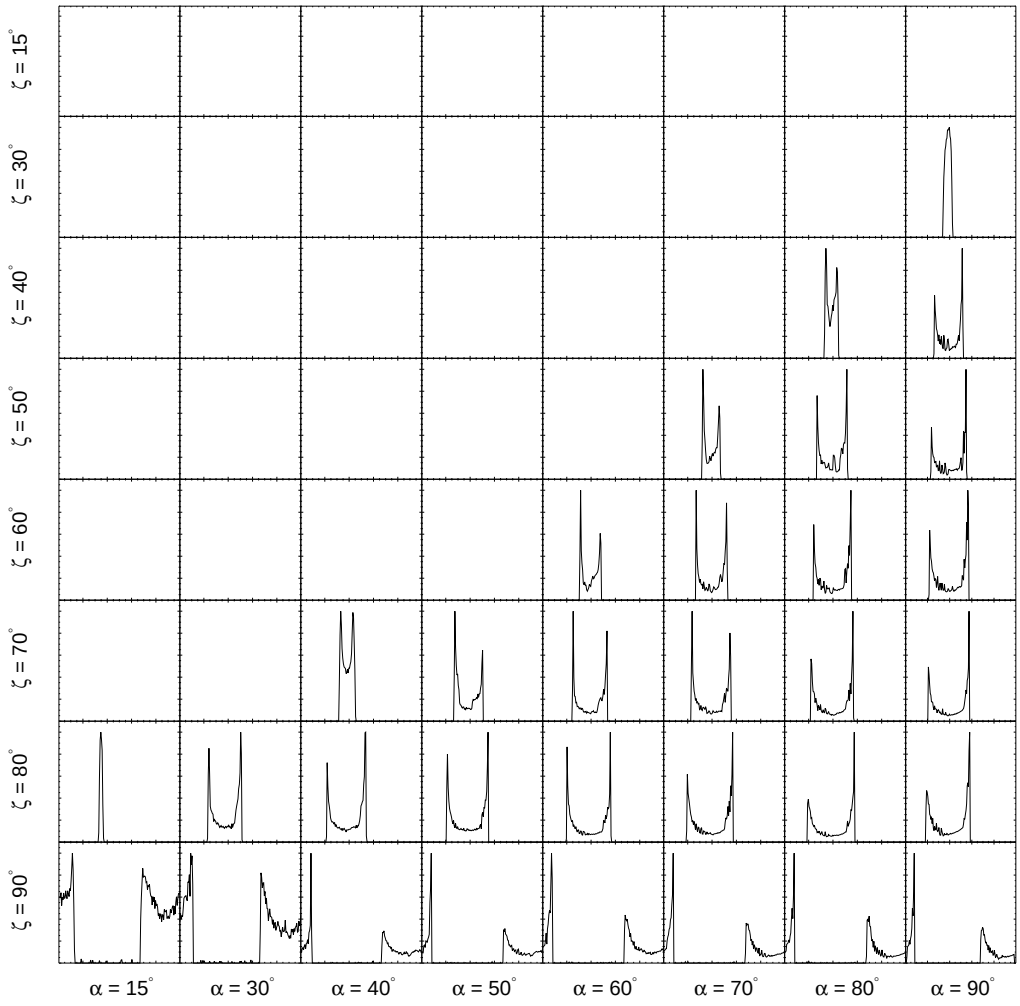

Figure B.40: Light curves from the outer gap geometry in the force-free field geometry, with $w = 0.20$ and $r = 0.9\,R_{\rm LC}$.

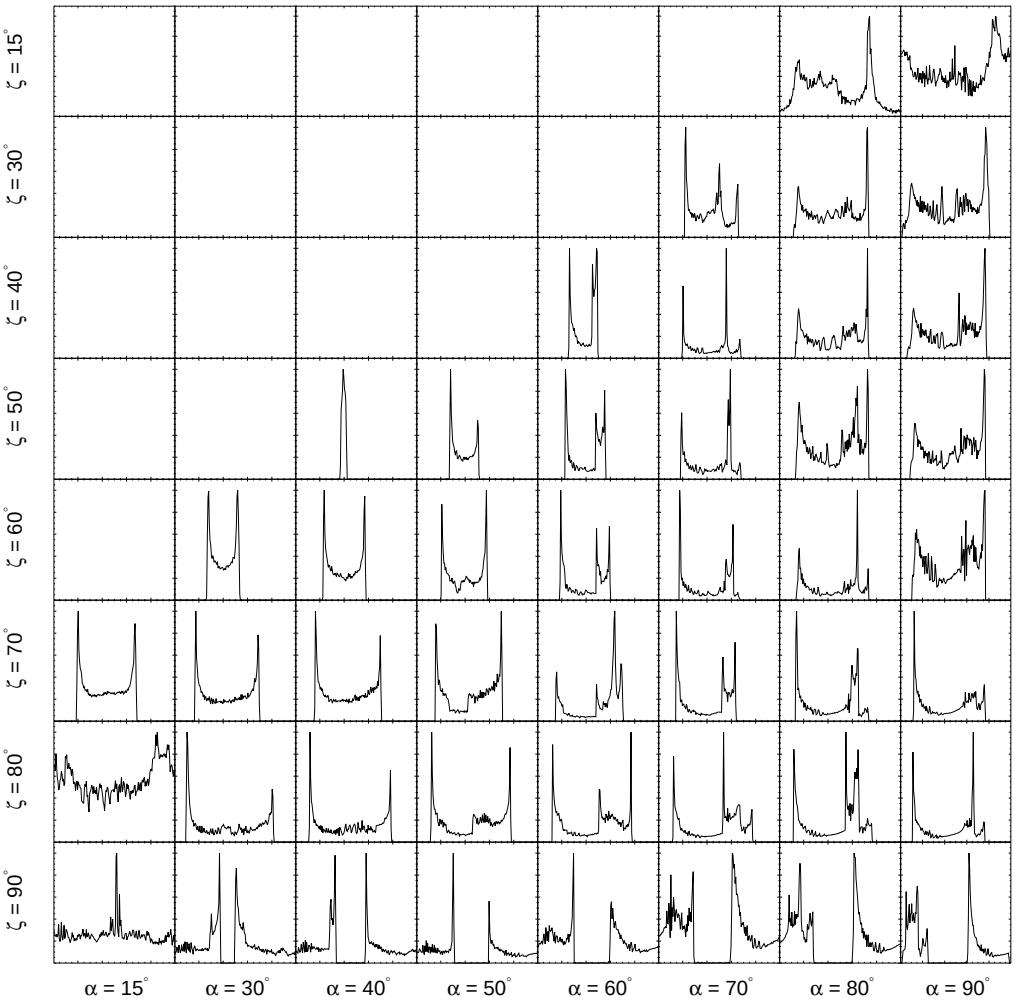

Figure B.41: Light curves from the outer gap geometry in the force-free field geometry, with $w = 0.01$ and $r = 1.2\,R_{\rm LC}$.

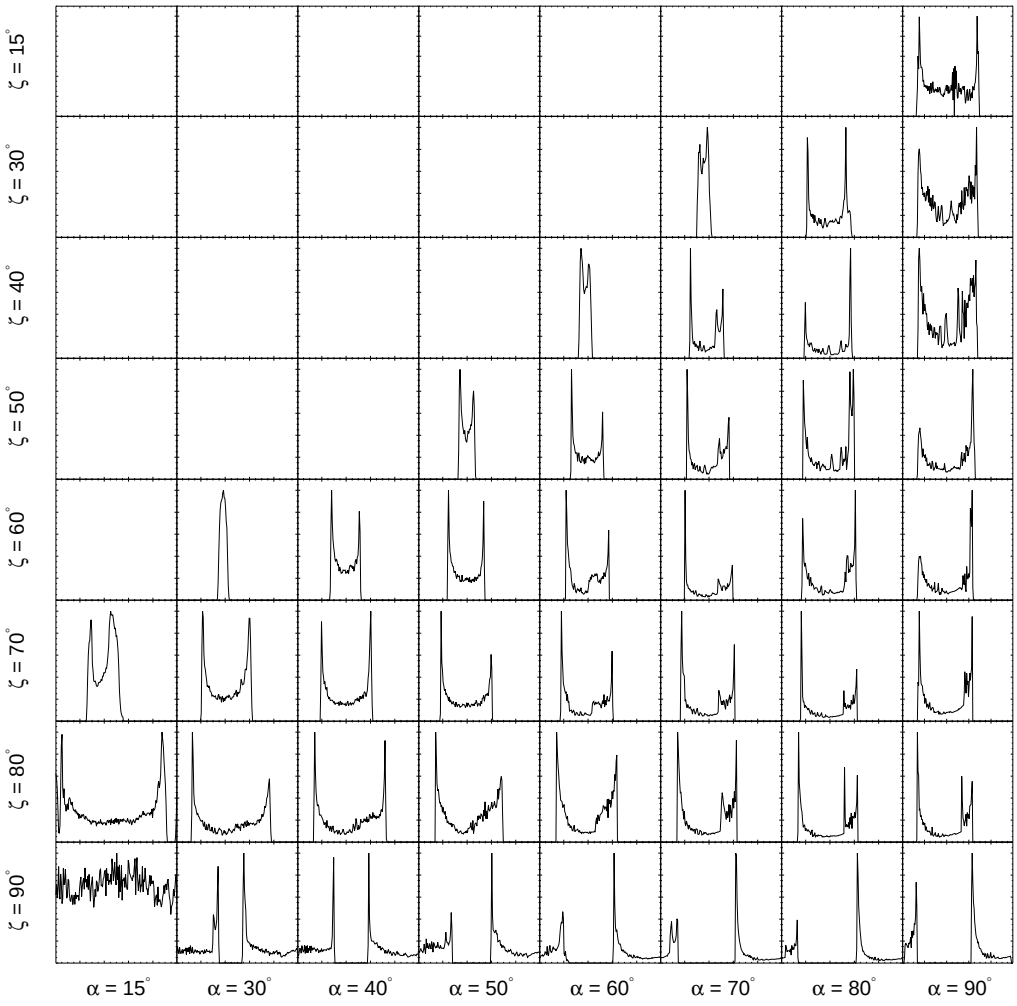

Figure B.42: Light curves from the outer gap geometry in the force-free field geometry, with $w = 0.05$ and $r = 1.2\,R_{\rm LC}$.

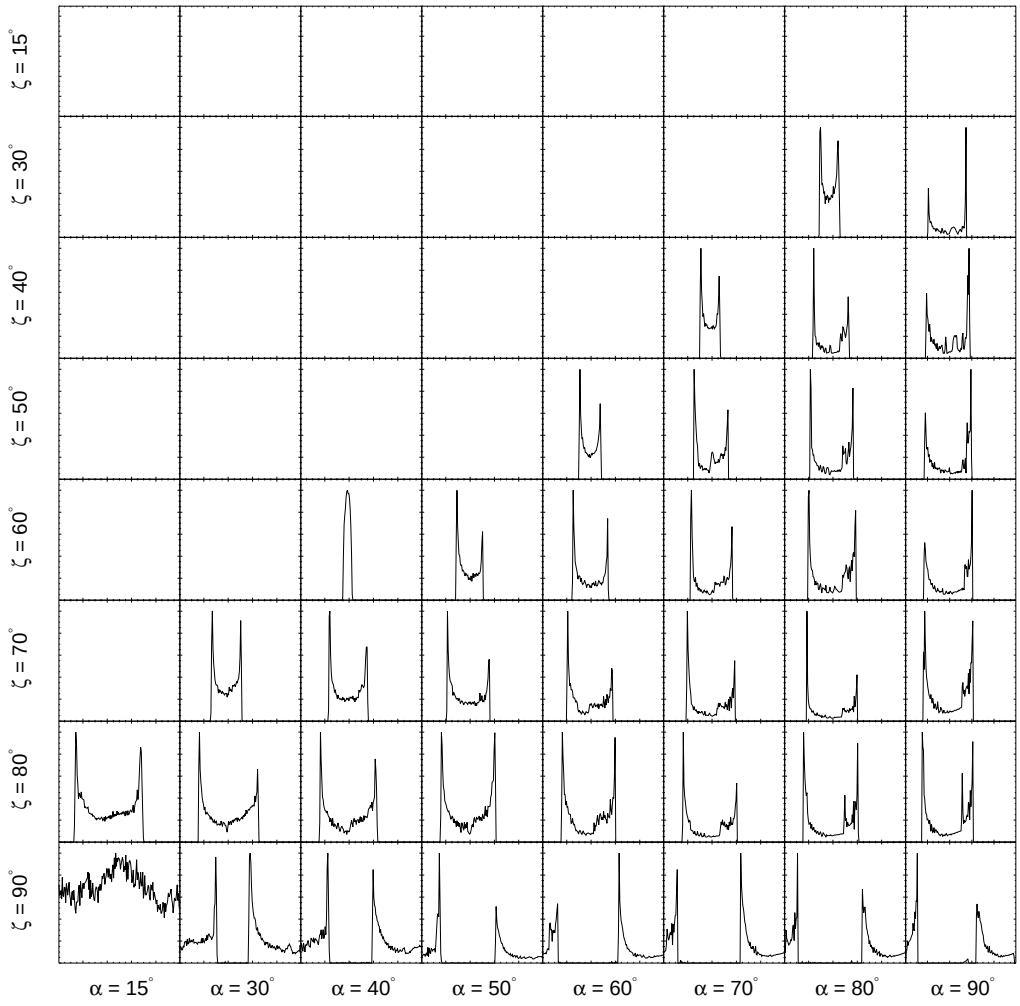

Figure B.43: Light curves from the outer gap geometry in the force-free field geometry, with $w = 0.10$ and $r = 1.2\,R_{\rm LC}$.

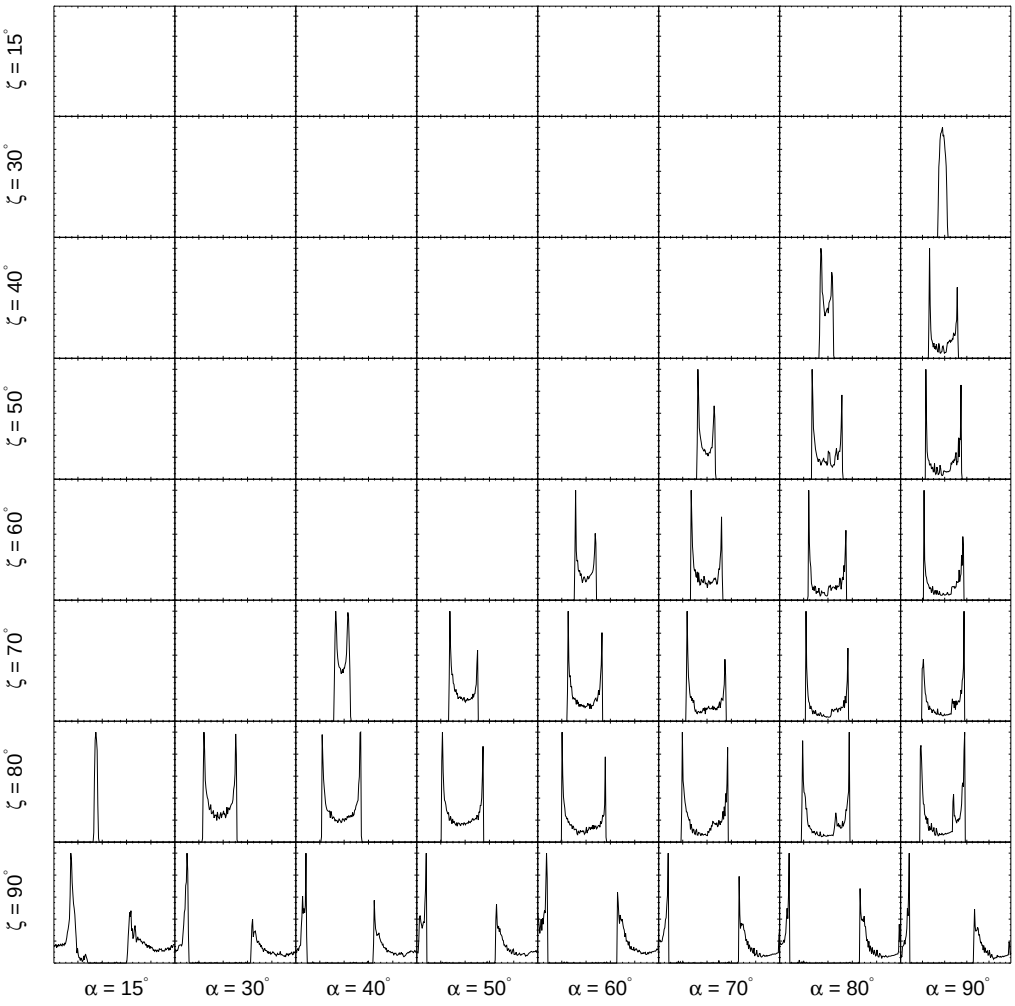

Figure B.44: Light curves from the outer gap geometry in the force-free field geometry, with $w = 0.20$ and $r = 1.2\,R_{\rm LC}$.

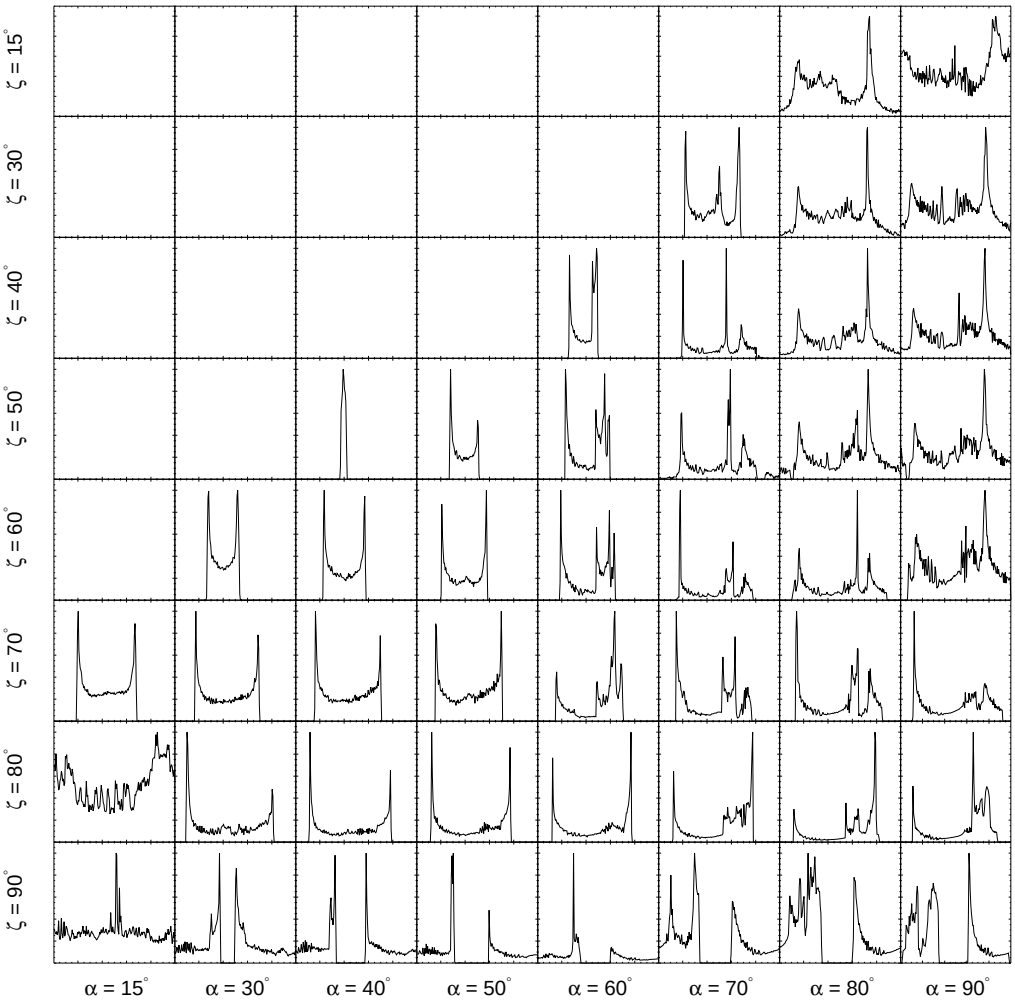

Figure B.45: Light curves from the outer gap geometry in the force-free field geometry, with $w = 0.01$ and $r = 1.7\,R_{\rm LC}$.

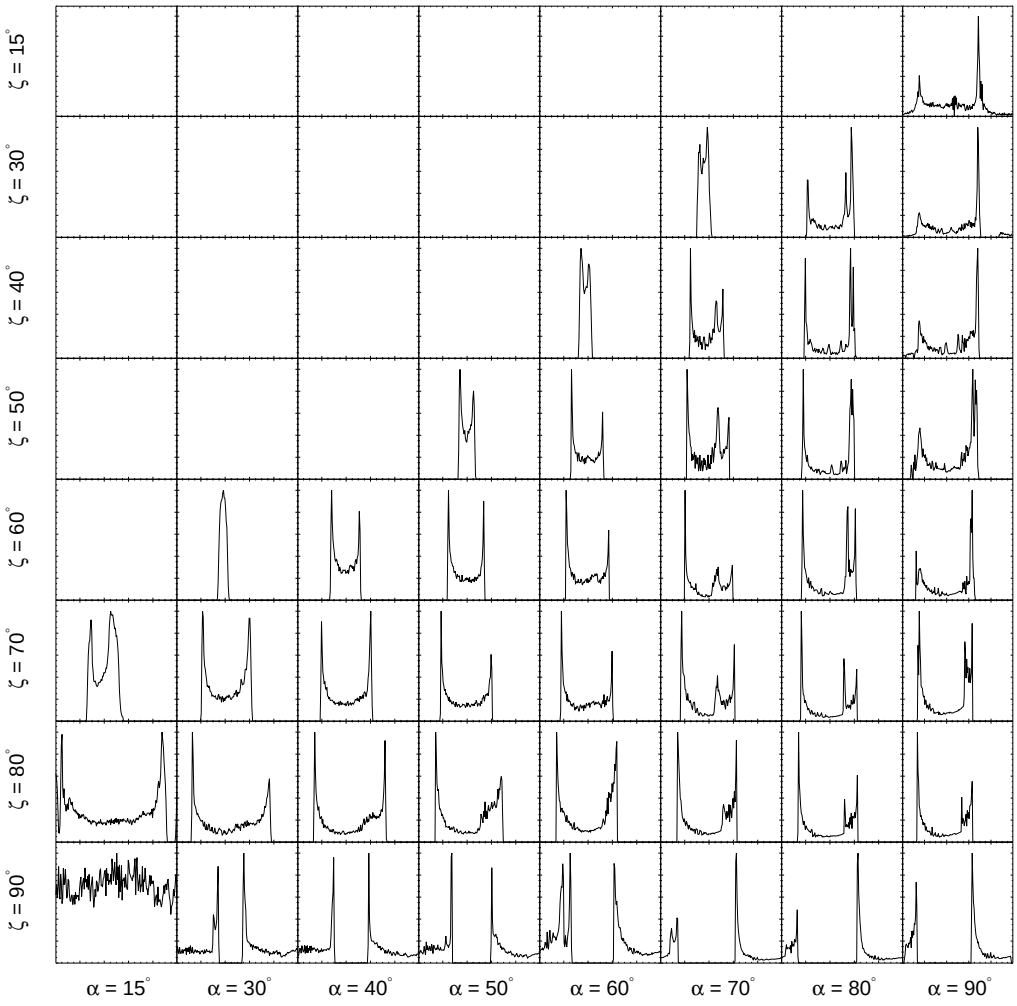

Figure B.46: Light curves from the outer gap geometry in the force-free field geometry, with $w = 0.05$ and $r = 1.7\,R_{\rm LC}$.

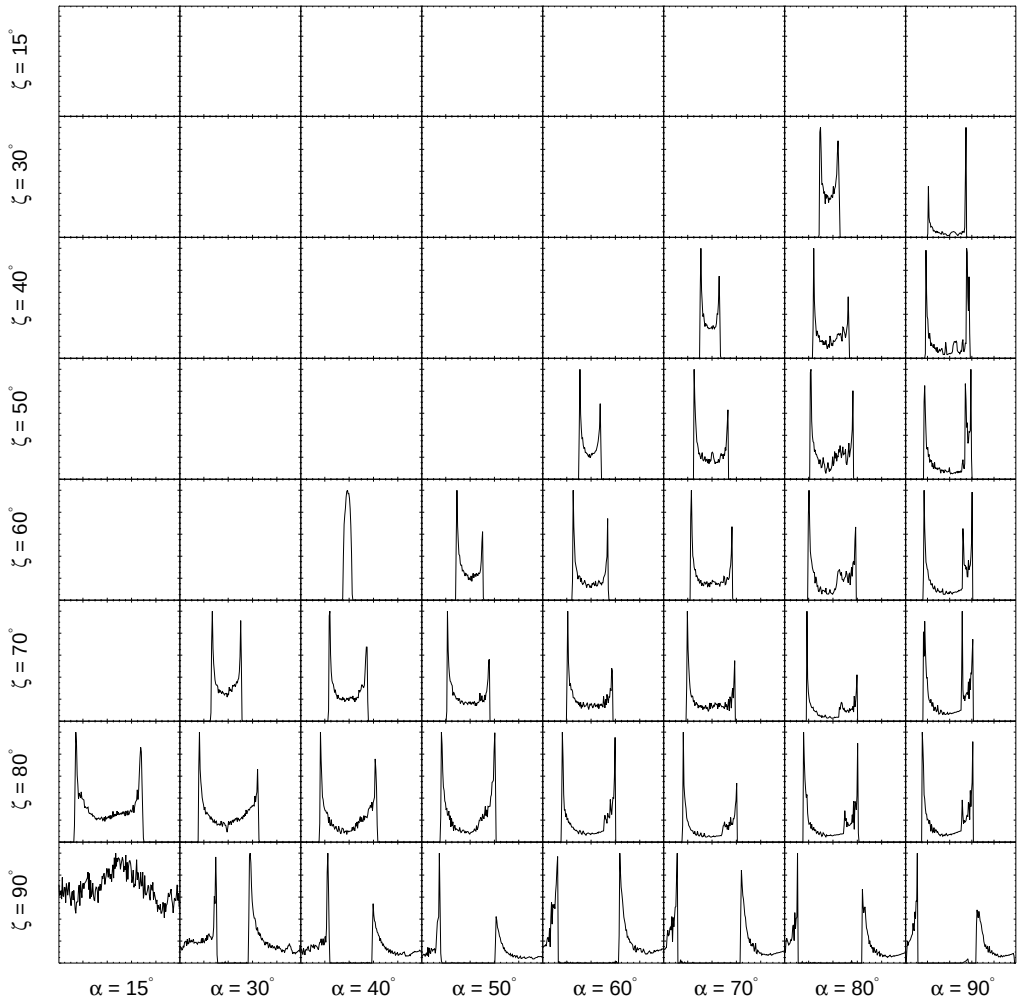

Figure B.47: Light curves from the outer gap geometry in the force-free field geometry, with $w = 0.10$ and $r = 1.7\,R_{\rm LC}$.

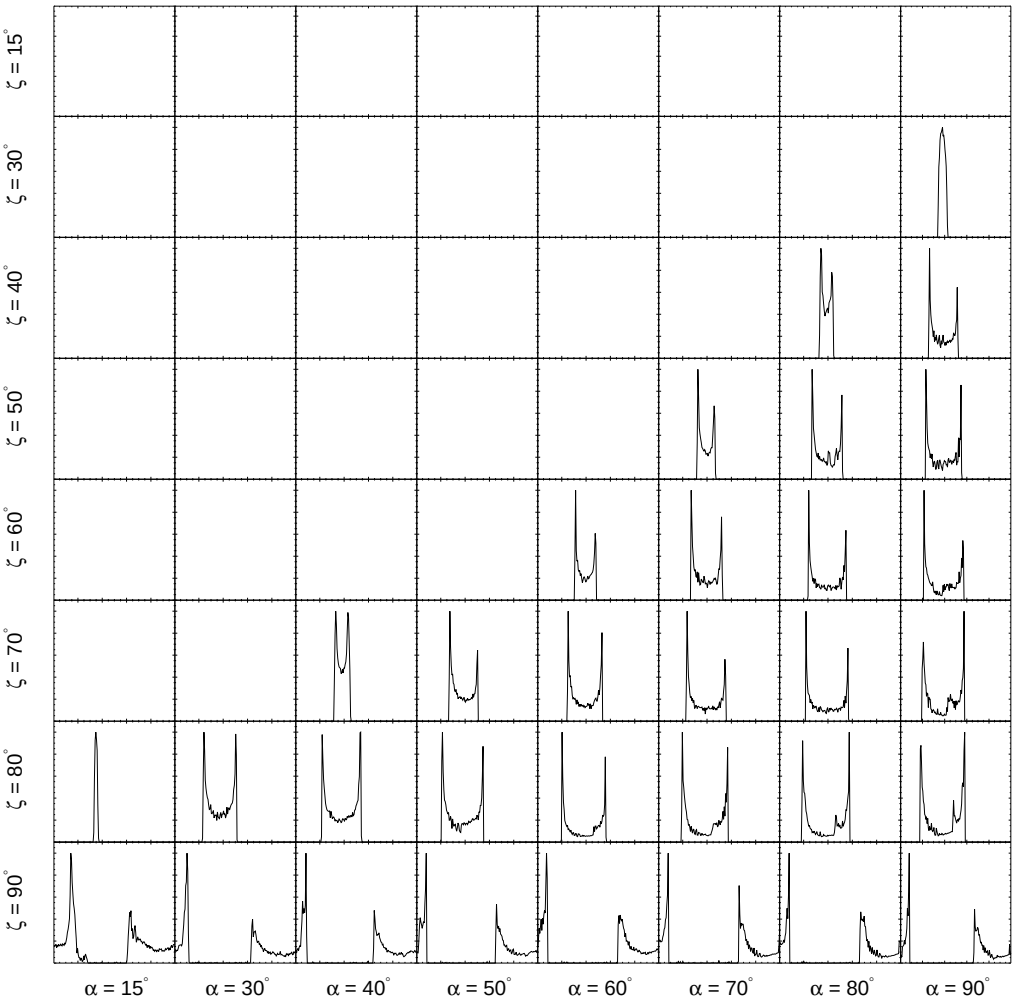

Figure B.48: Light curves from the outer gap geometry in the force-free field geometry, with $w = 0.20$ and $r = 1.7\,R_{\rm LC}$.

B.5 Light Curves in the Force-free Symmetric Slot Gap Geometry

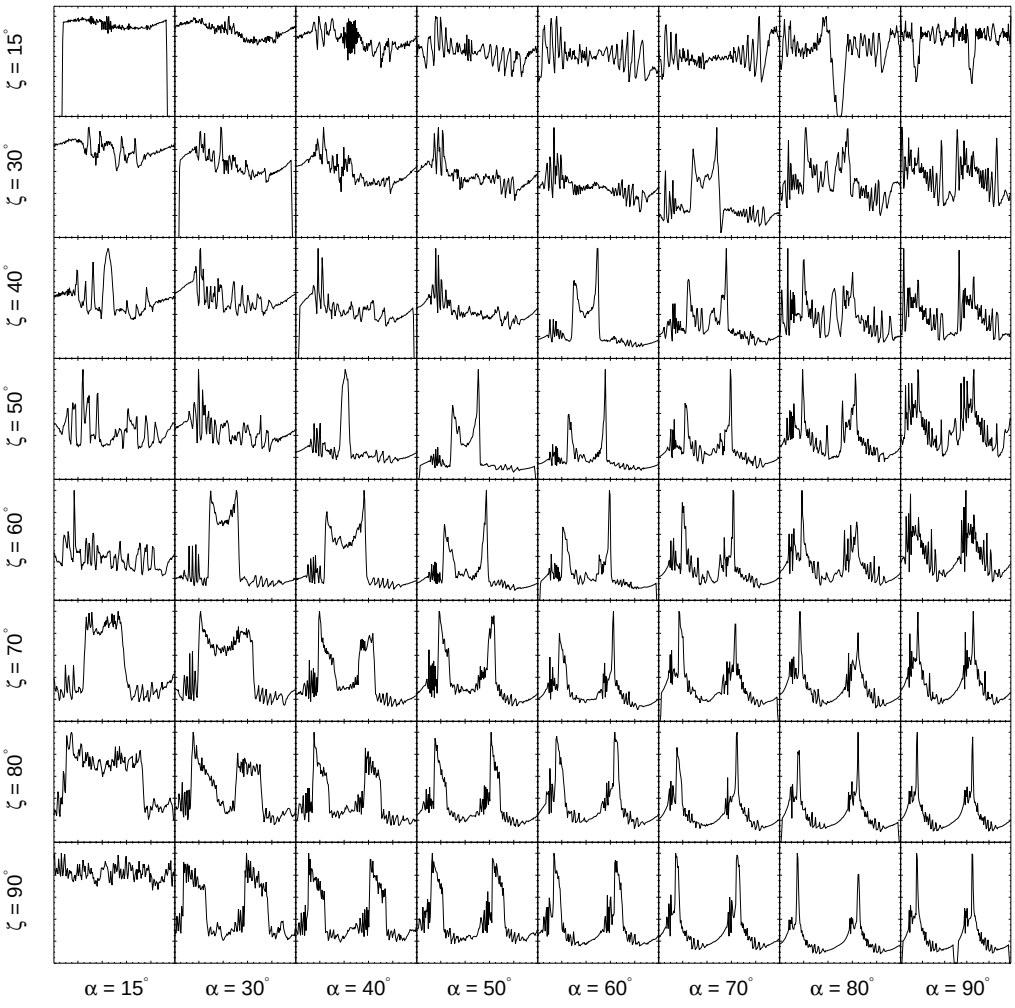

Figure B.49: Light curves from the symmetric slot gap geometry in the force-free field geometry, with $w = 0.01$ and $r = 0.7\,R_{\rm LC}$.

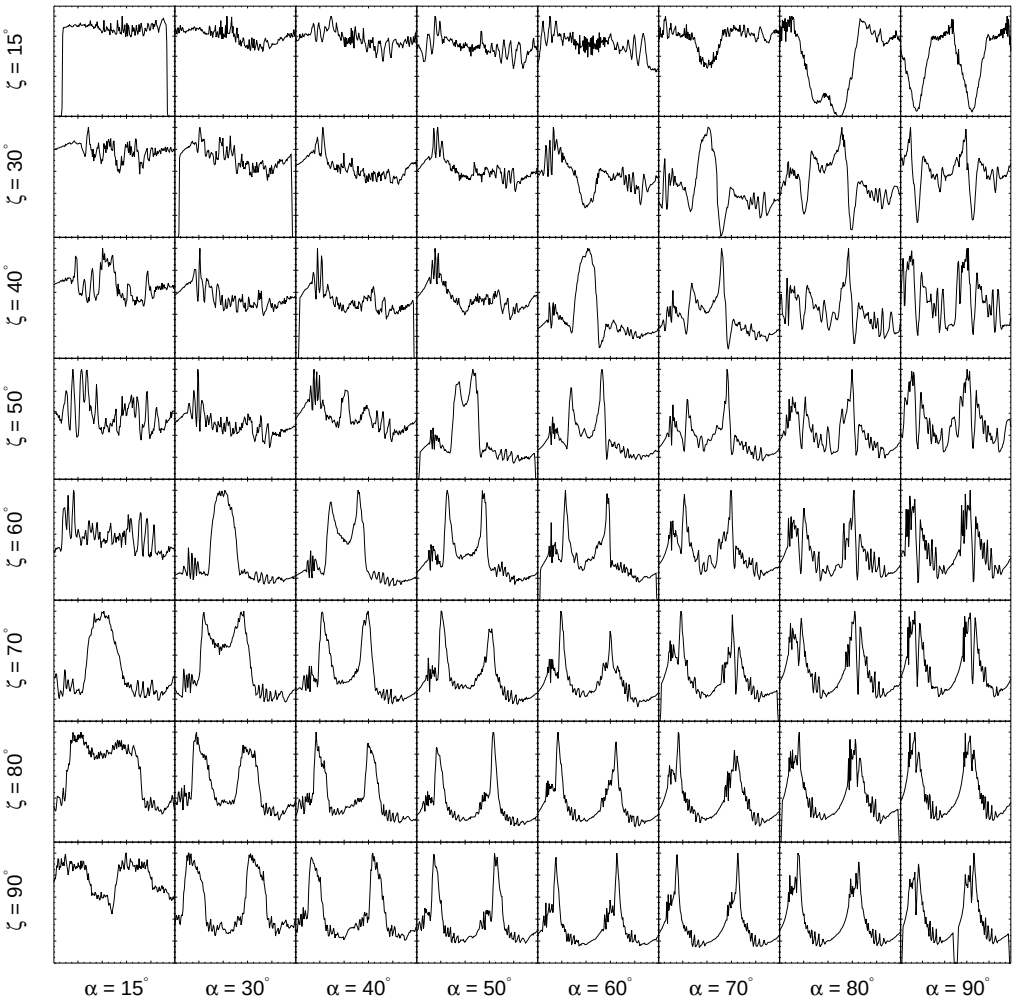

Figure B.50: Light curves from the symmetric slot gap geometry in the force-free field geometry, with $w = 0.05$ and $r = 0.7\,R_{\rm LC}$.

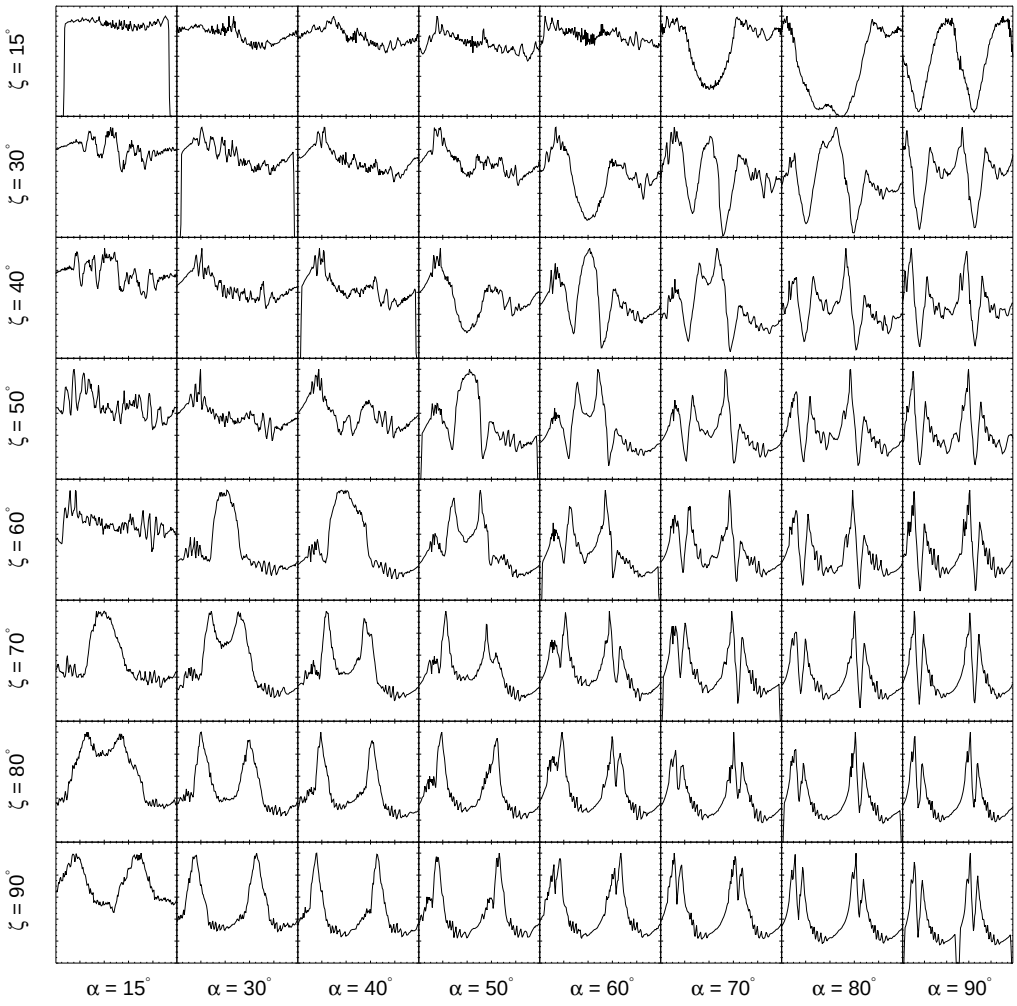

Figure B.51: Light curves from the symmetric slot gap geometry in the force-free field geometry, with $w = 0.10$ and $r = 0.7\,R_{\rm LC}$.

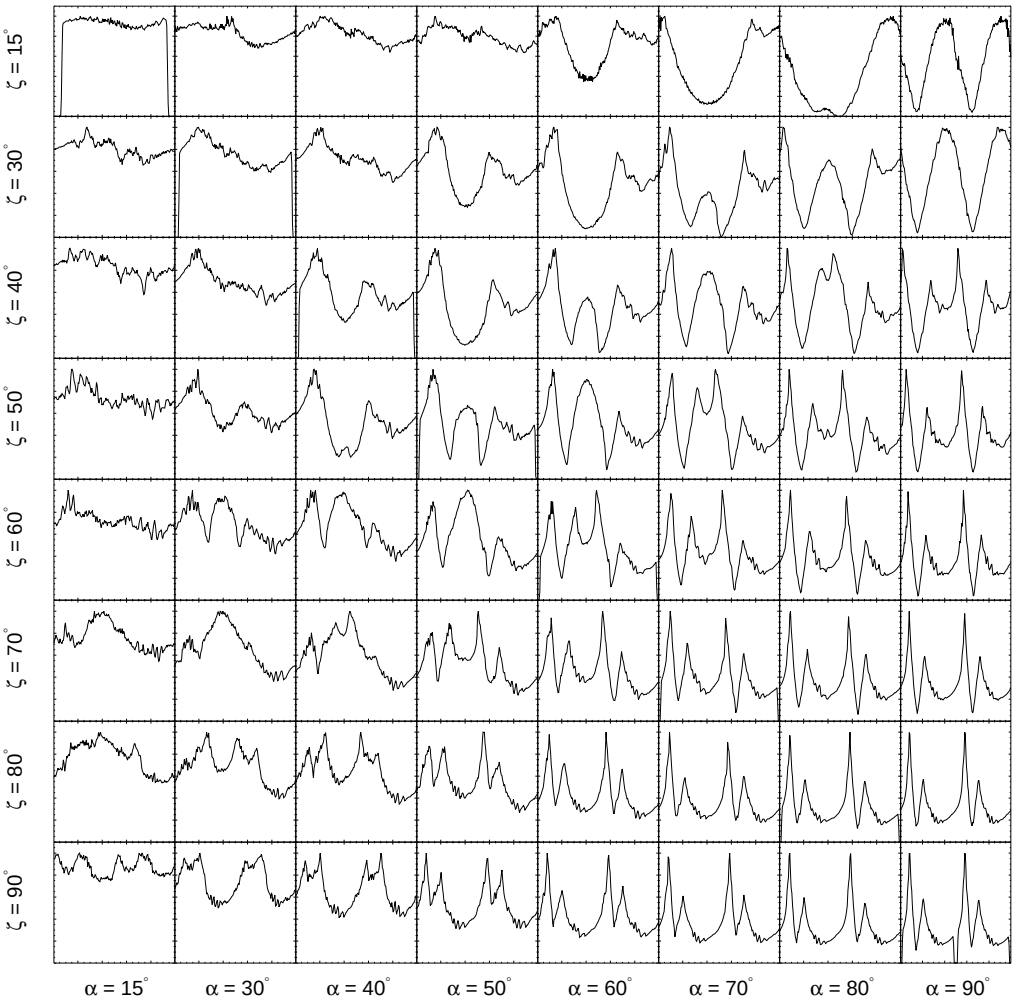

Figure B.52: Light curves from the symmetric slot gap geometry in the force-free field geometry, with $w = 0.20$ and $r = 0.7\,R_{\rm LC}$.

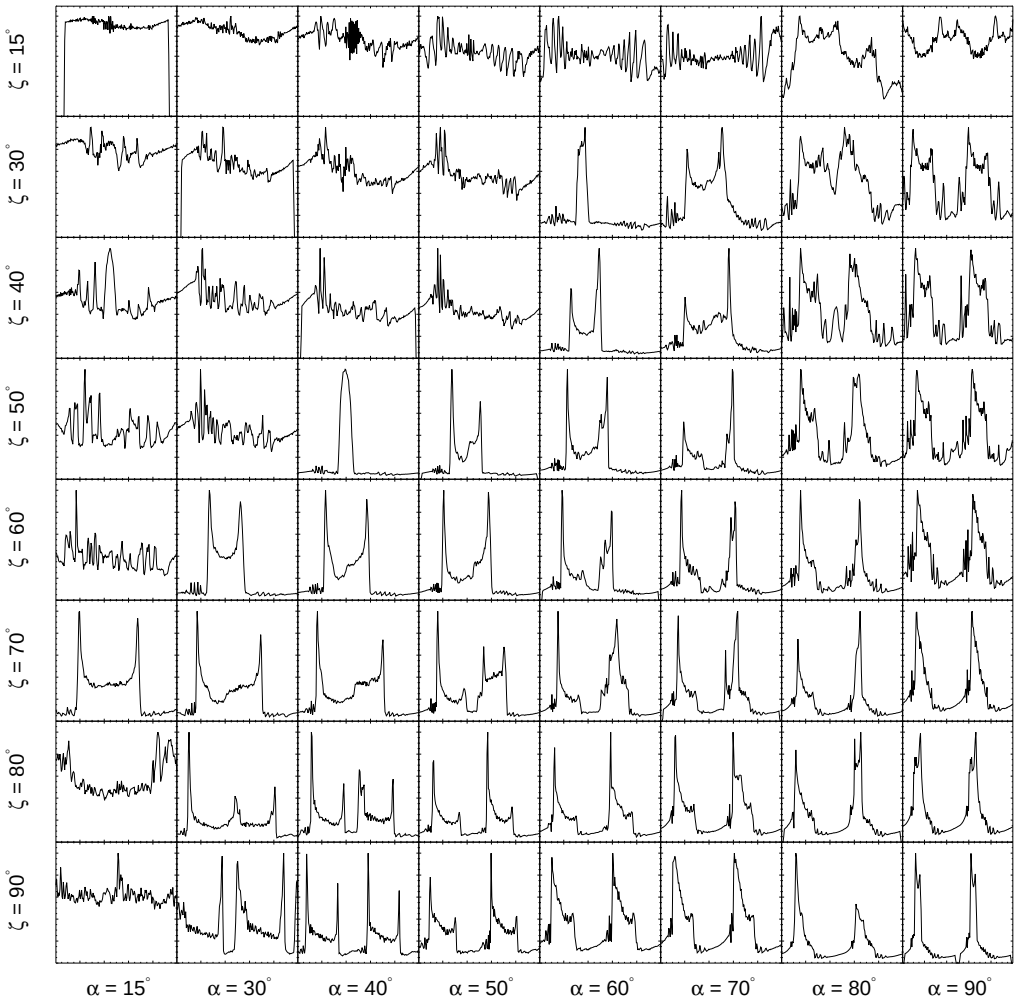

Figure B.53: Light curves from the symmetric slot gap geometry in the force-free field geometry, with $w = 0.01$ and $r = 1.0\,R_{\rm LC}$.

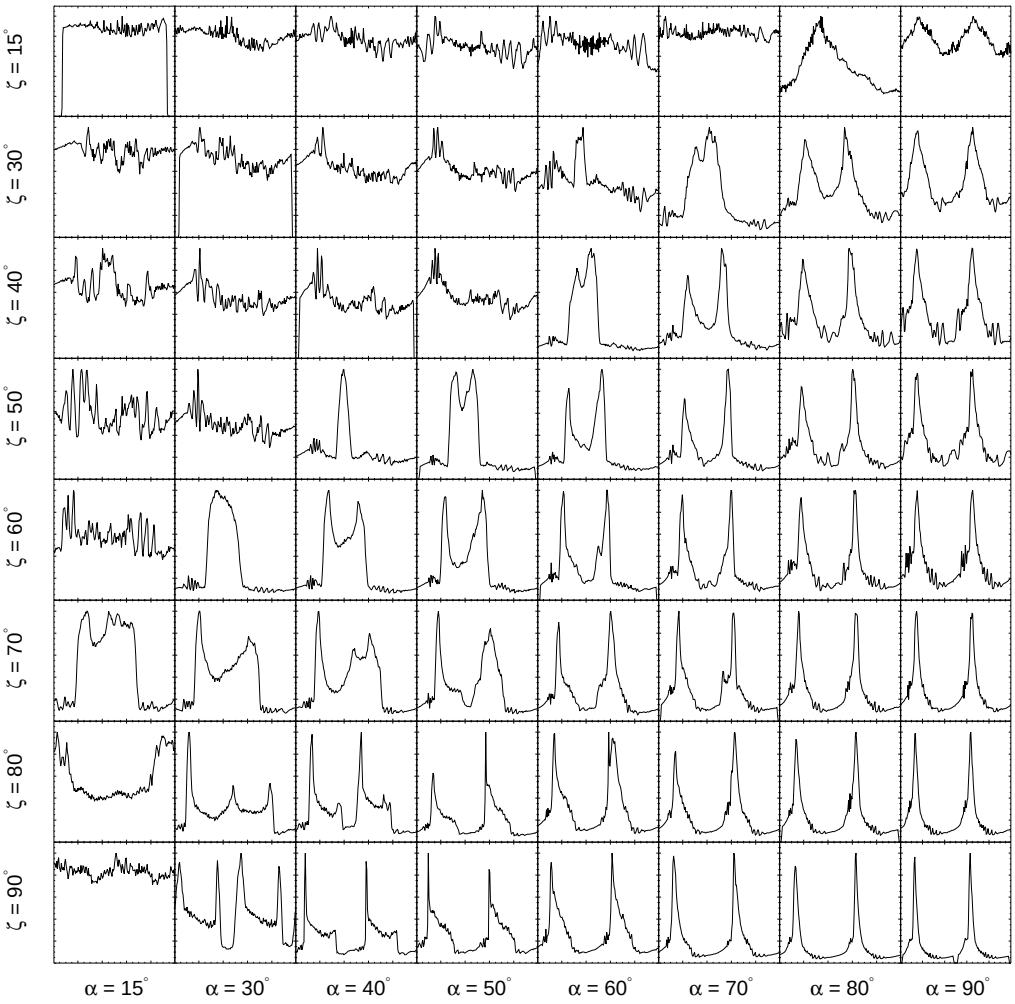

Figure B.54: Light curves from the symmetric slot gap geometry in the force-free field geometry, with $w = 0.05$ and $r = 1.0\,R_{\rm LC}$.

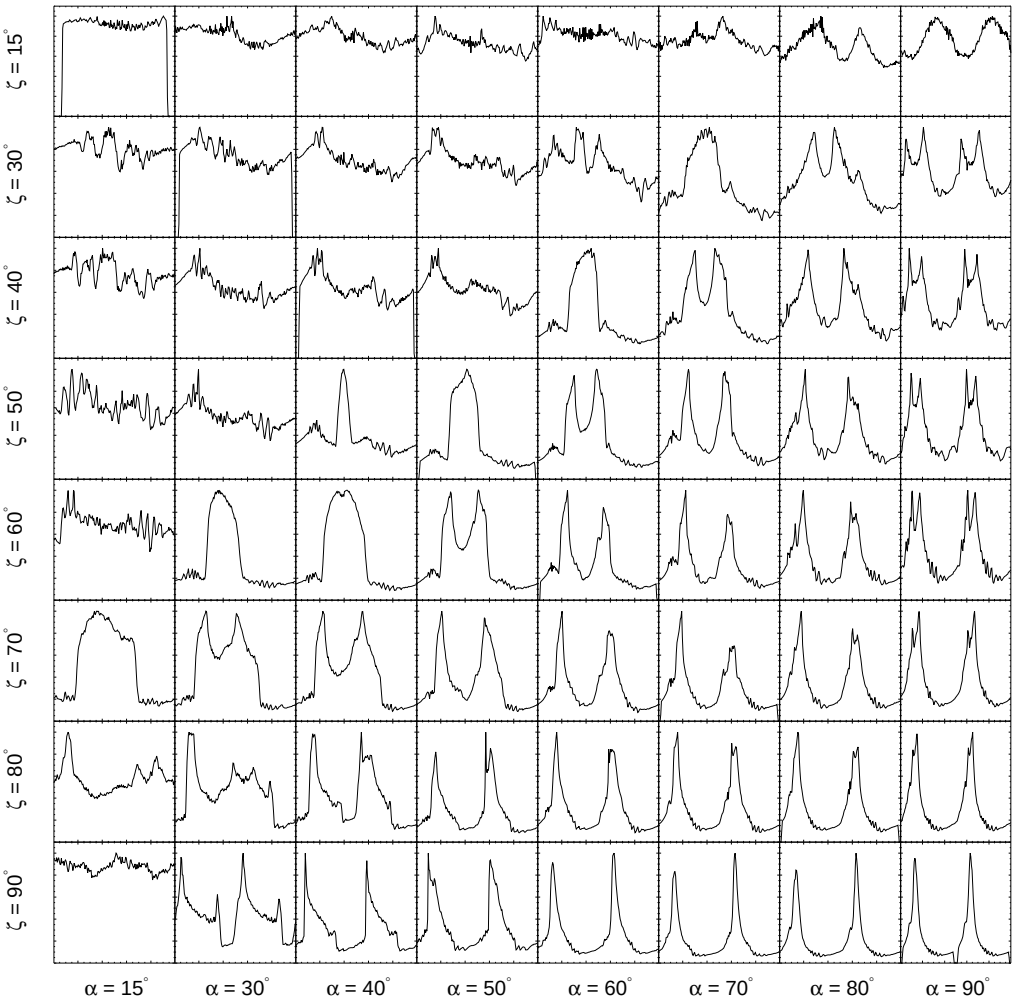

Figure B.55: Light curves from the symmetric slot gap geometry in the force-free field geometry, with $w = 0.10$ and $r = 1.0\,R_{\rm LC}$.

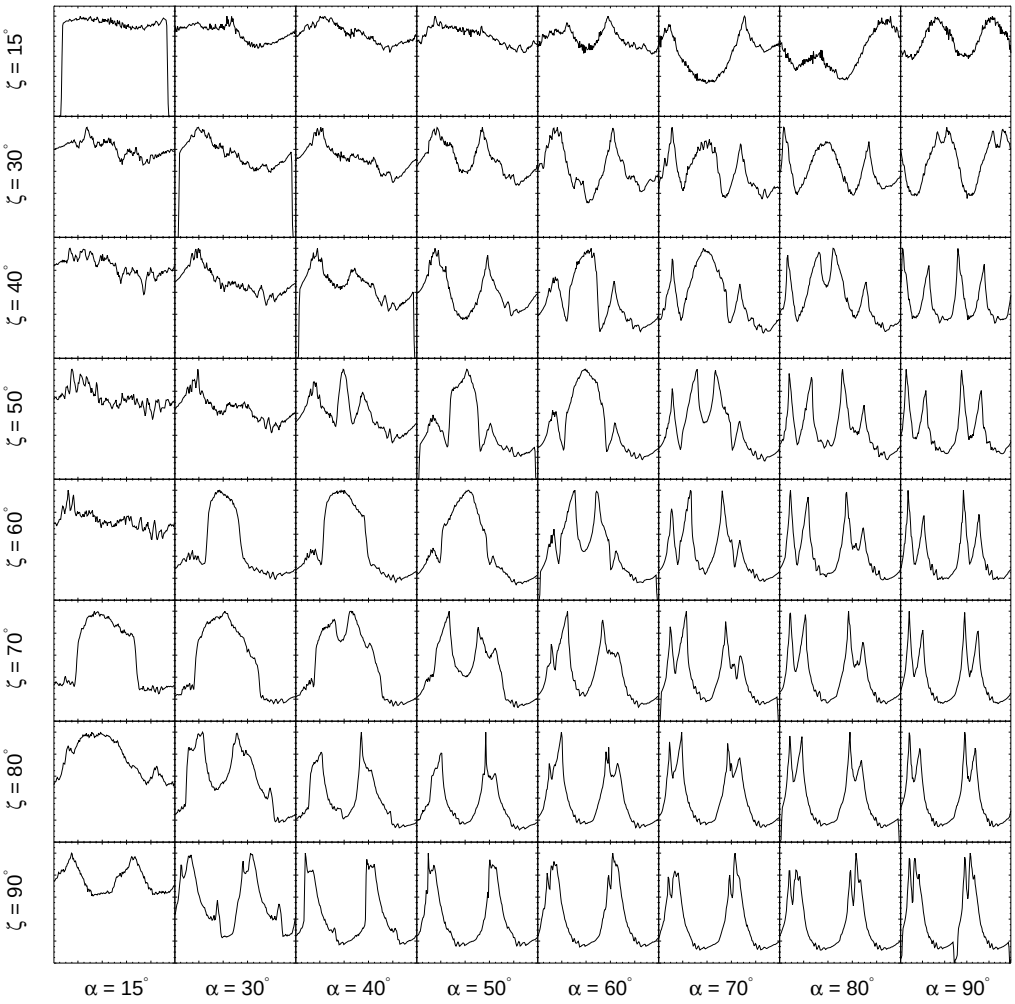

Figure B.56: Light curves from the symmetric slot gap geometry in the force-free field geometry, with $w = 0.20$ and $r = 1.0\,R_{\rm LC}$.

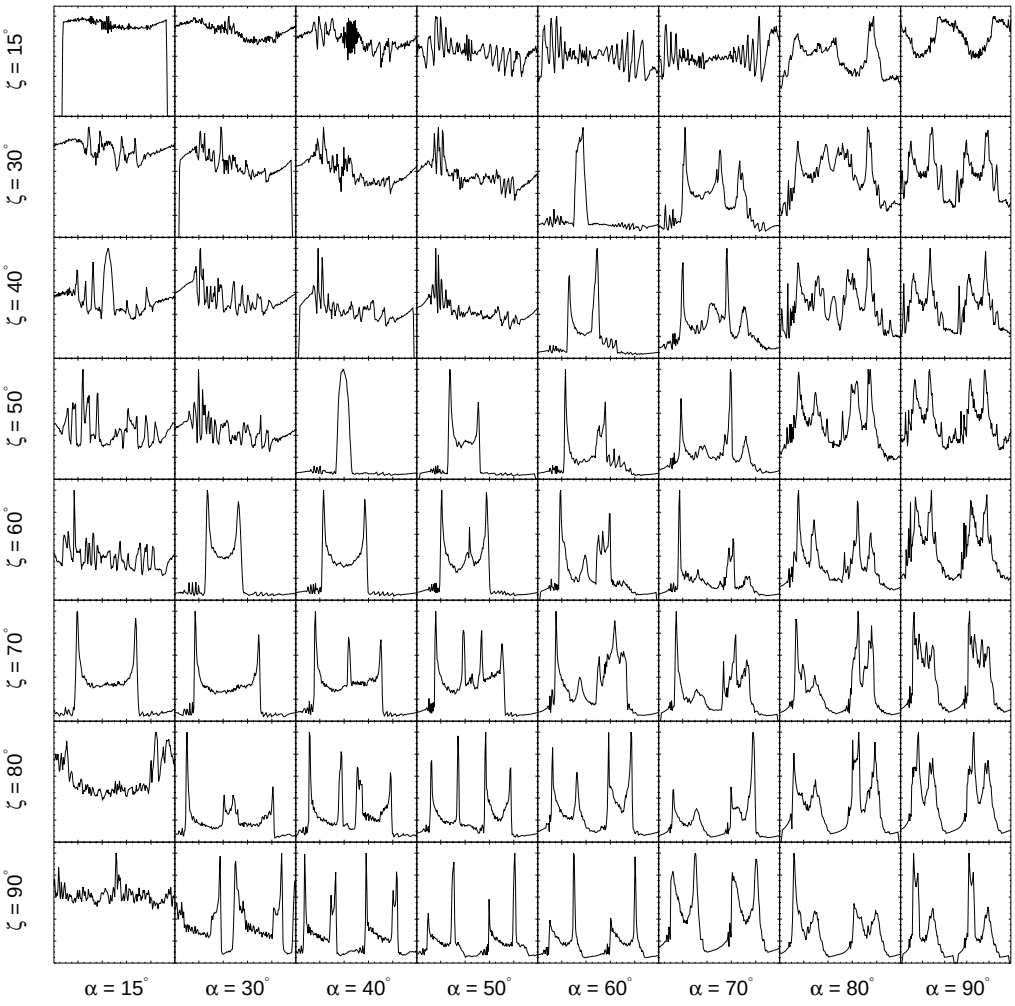

Figure B.57: Light curves from the symmetric slot gap geometry in the force-free field geometry, with $w = 0.01$ and $r = 1.2\,R_{\rm LC}$.

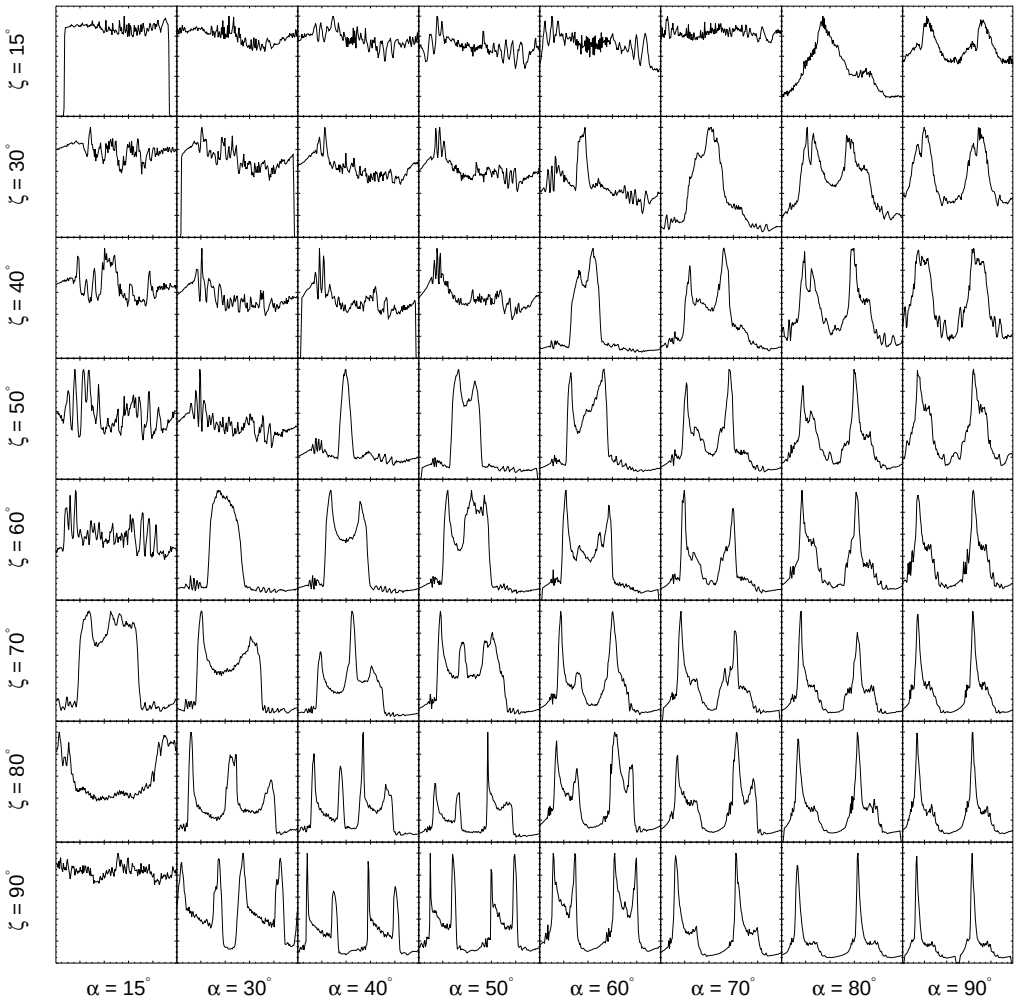

Figure B.58: Light curves from the symmetric slot gap geometry in the force-free field geometry, with $w = 0.05$ and $r = 1.2\,R_{\rm LC}$.

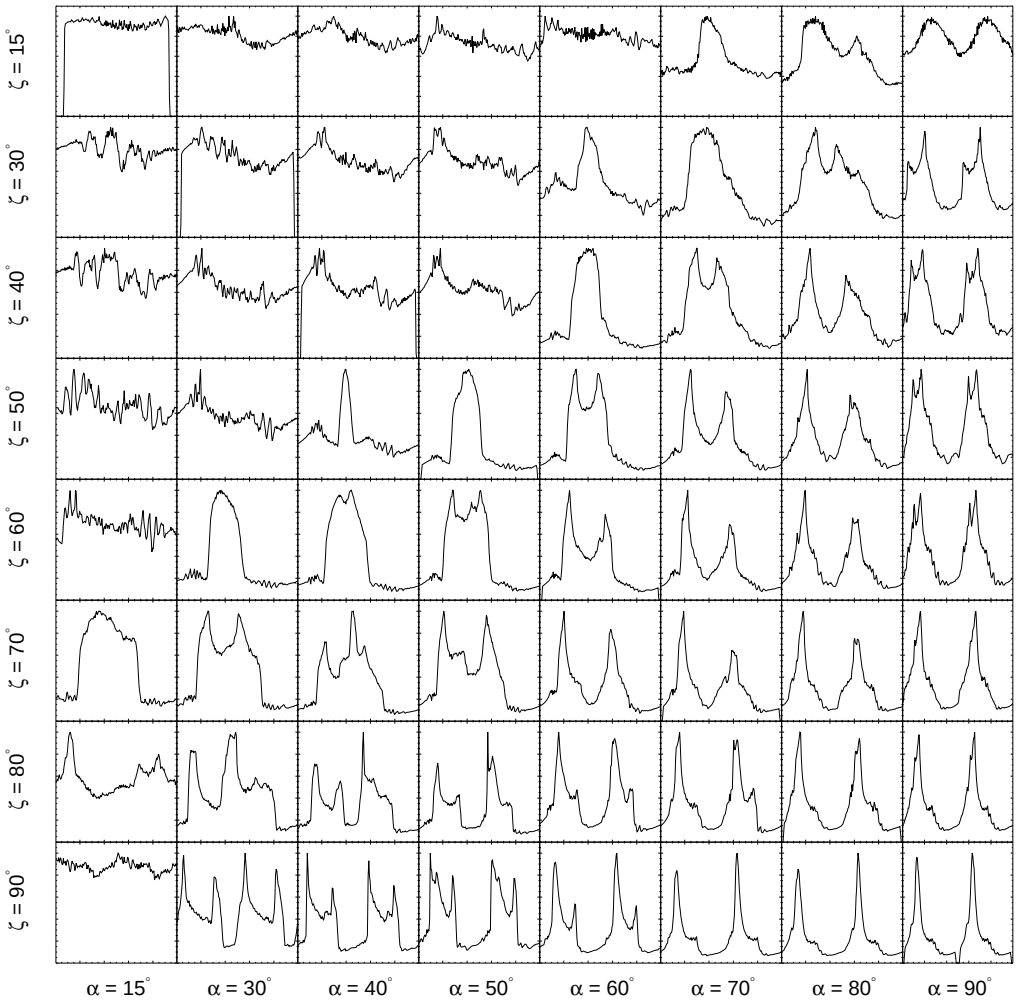

Figure B.59: Light curves from the symmetric slot gap geometry in the force-free field geometry, with $w = 0.10$ and $r = 1.2\,R_{\rm LC}$.

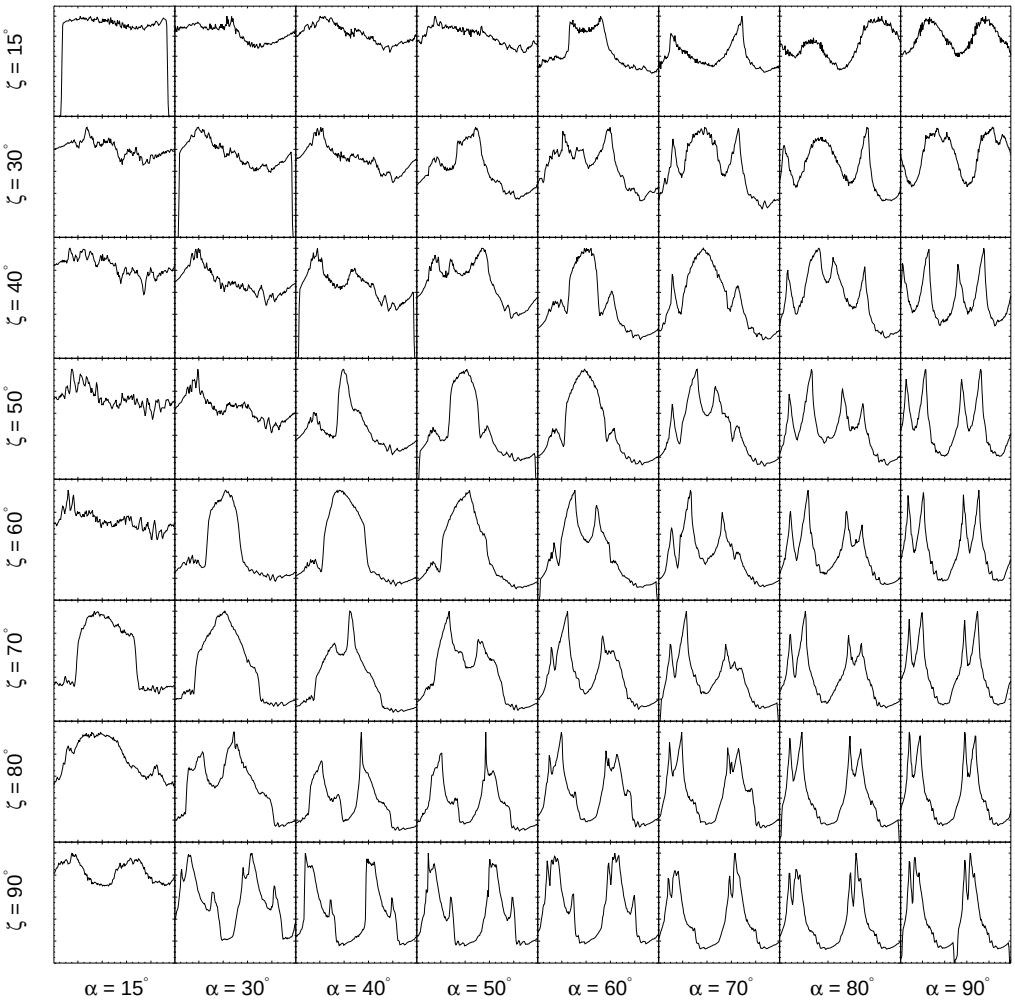

Figure B.60: Light curves from the symmetric slot gap geometry in the force-free field geometry, with $w = 0.20$ and $r = 1.2\,R_{\rm LC}$.

B.6 Light Curves in the Force-free Asymmetric Slot Gap Geometry

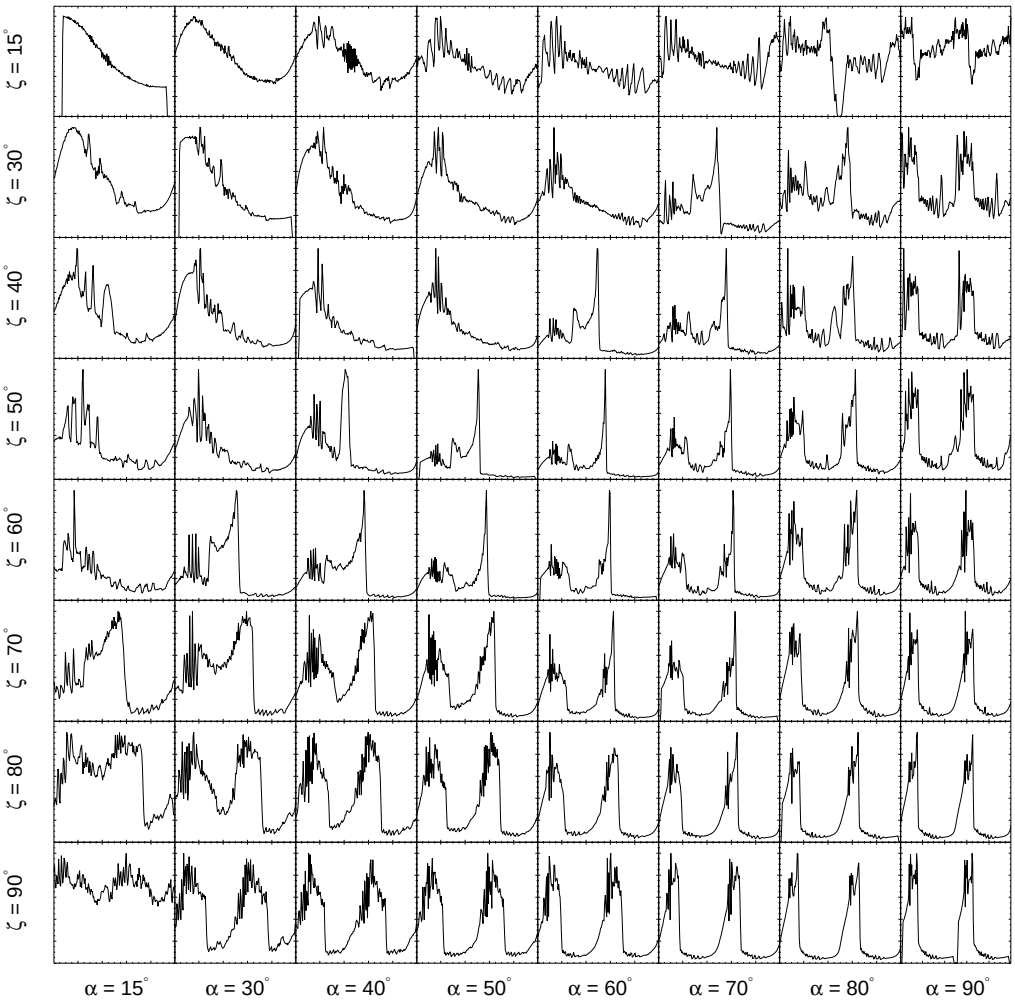

Figure B.61: Light curves from the asymmetric slot gap geometry in the force-free field geometry, with $w = 0.01$ and $r = 0.7\,R_{\rm LC}$.

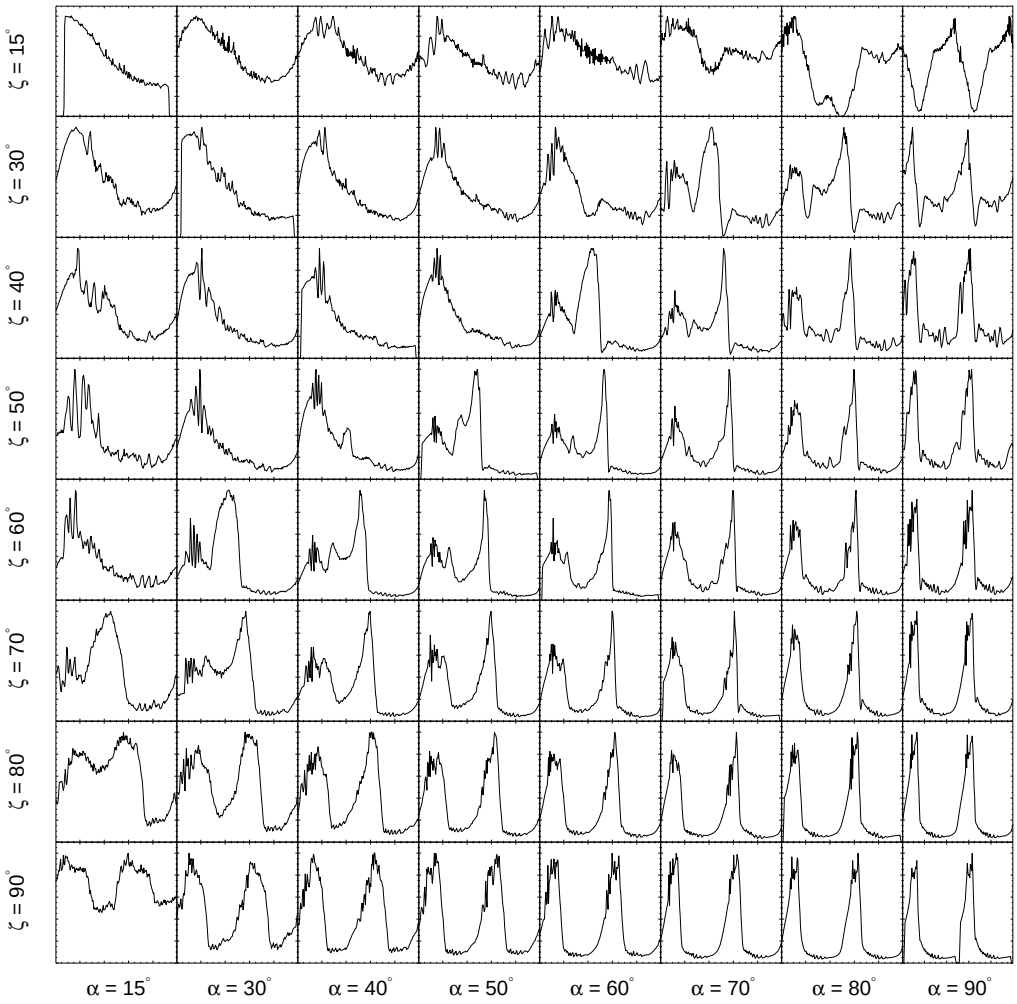

Figure B.62: Light curves from the asymmetric slot gap geometry in the force-free field geometry, with $w = 0.05$ and $r = 0.7\,R_{\rm LC}$.

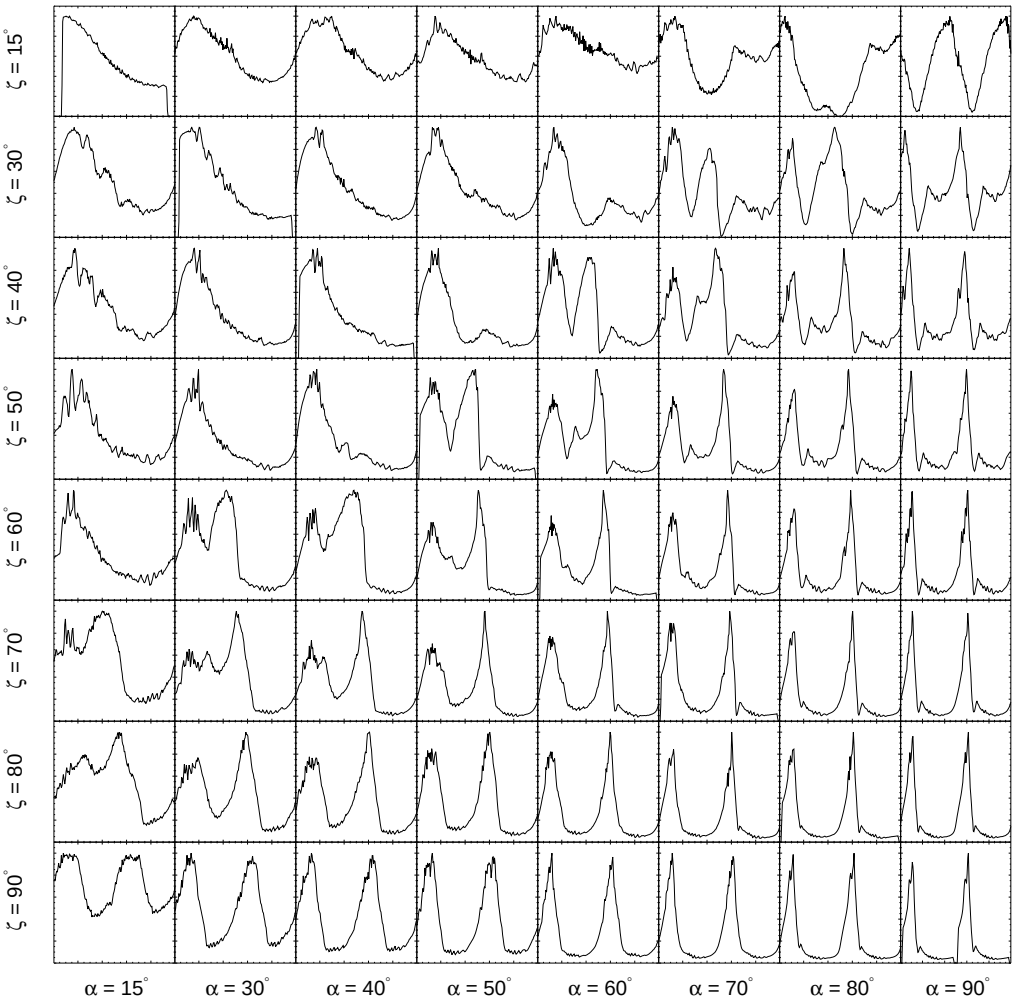

Figure B.63: Light curves from the asymmetric slot gap geometry in the force-free field geometry, with $w = 0.10$ and $r = 0.7\,R_{\rm LC}$.

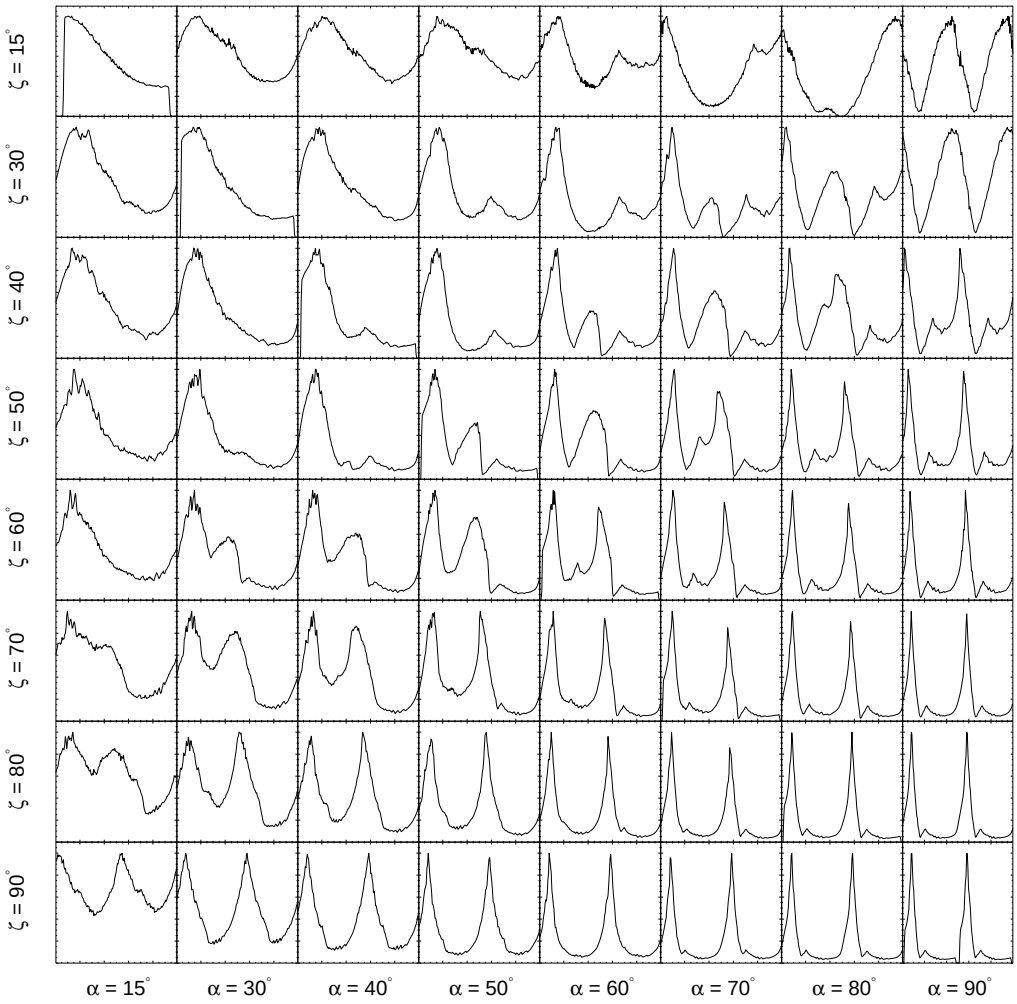

Figure B.64: Light curves from the asymmetric slot gap geometry in the force-free field geometry, with $w = 0.20$ and $r = 0.7\,R_{\rm LC}$.

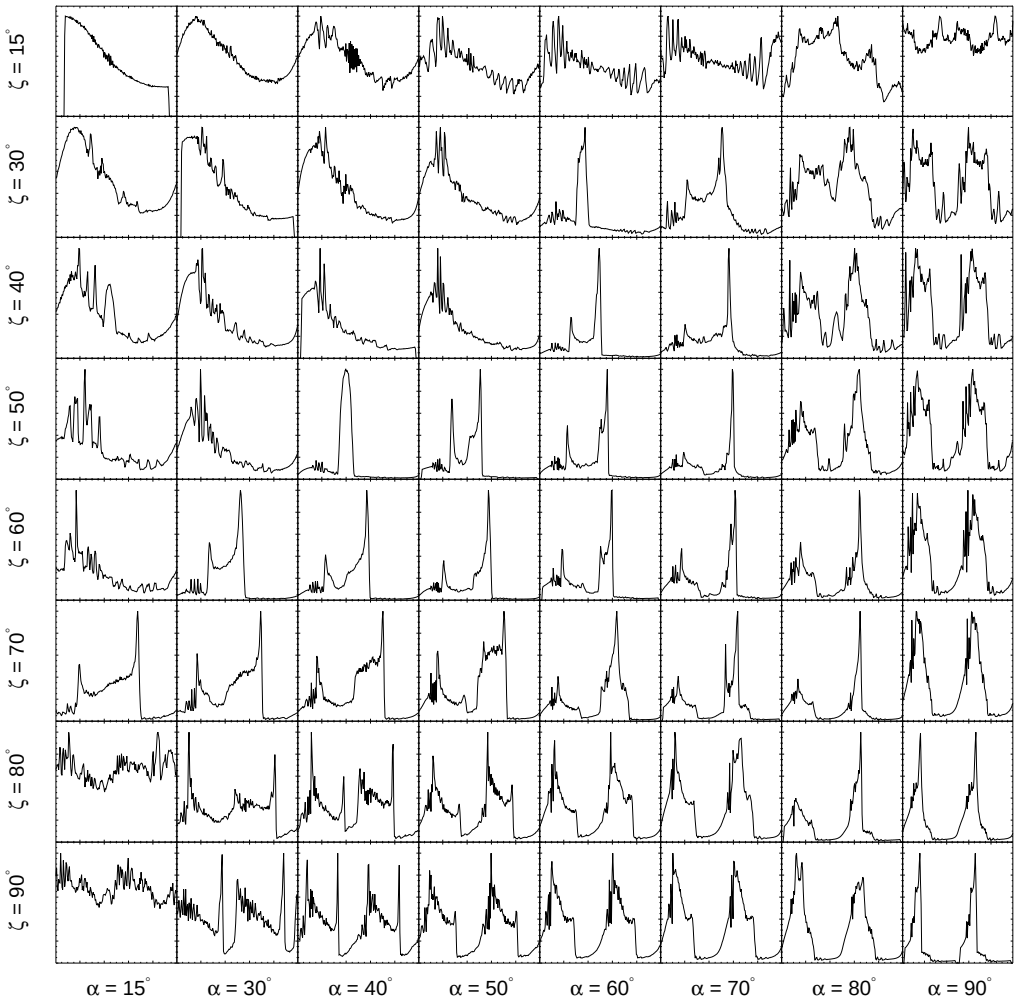

Figure B.65: Light curves from the asymmetric slot gap geometry in the force-free field geometry, with $w = 0.01$ and $r = 1.0\,R_{\rm LC}$.

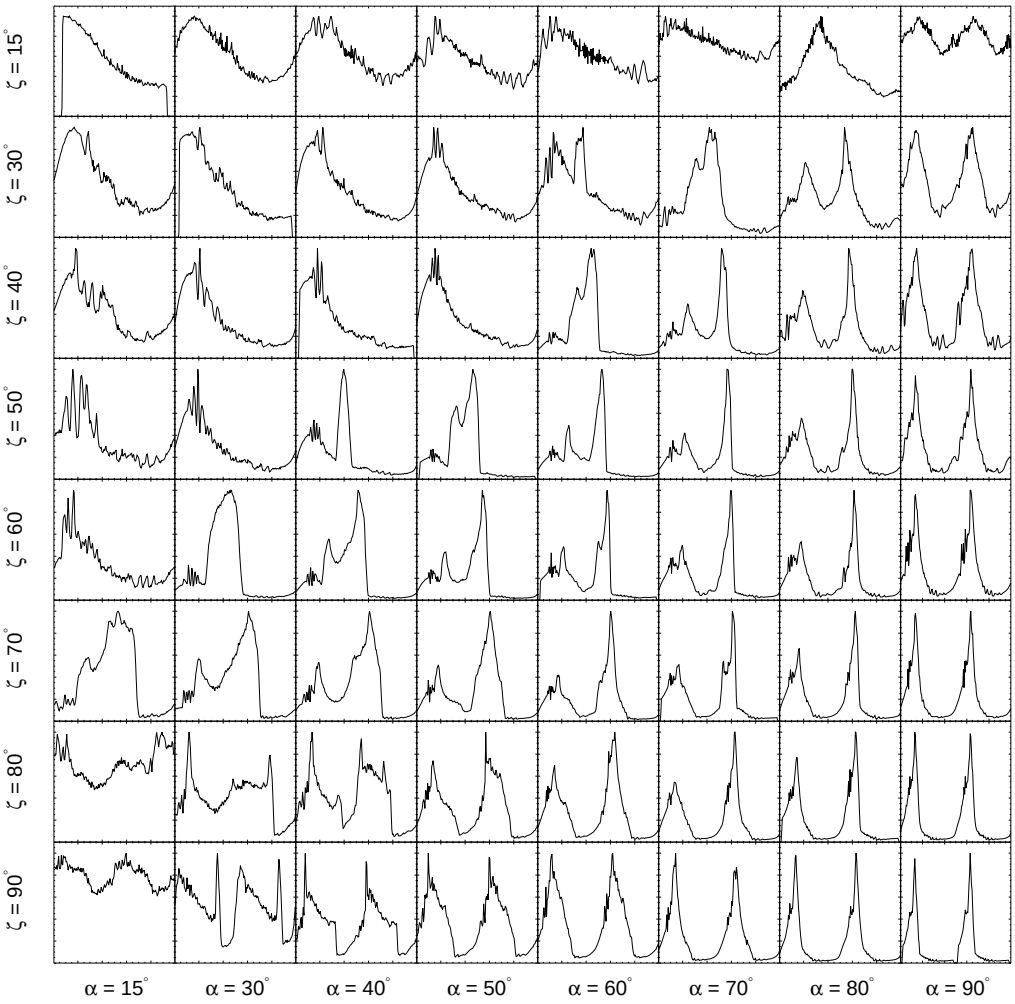

Figure B.66: Light curves from the asymmetric slot gap geometry in the force-free field geometry, with $w = 0.05$ and $r = 1.0\,R_{\rm LC}$.

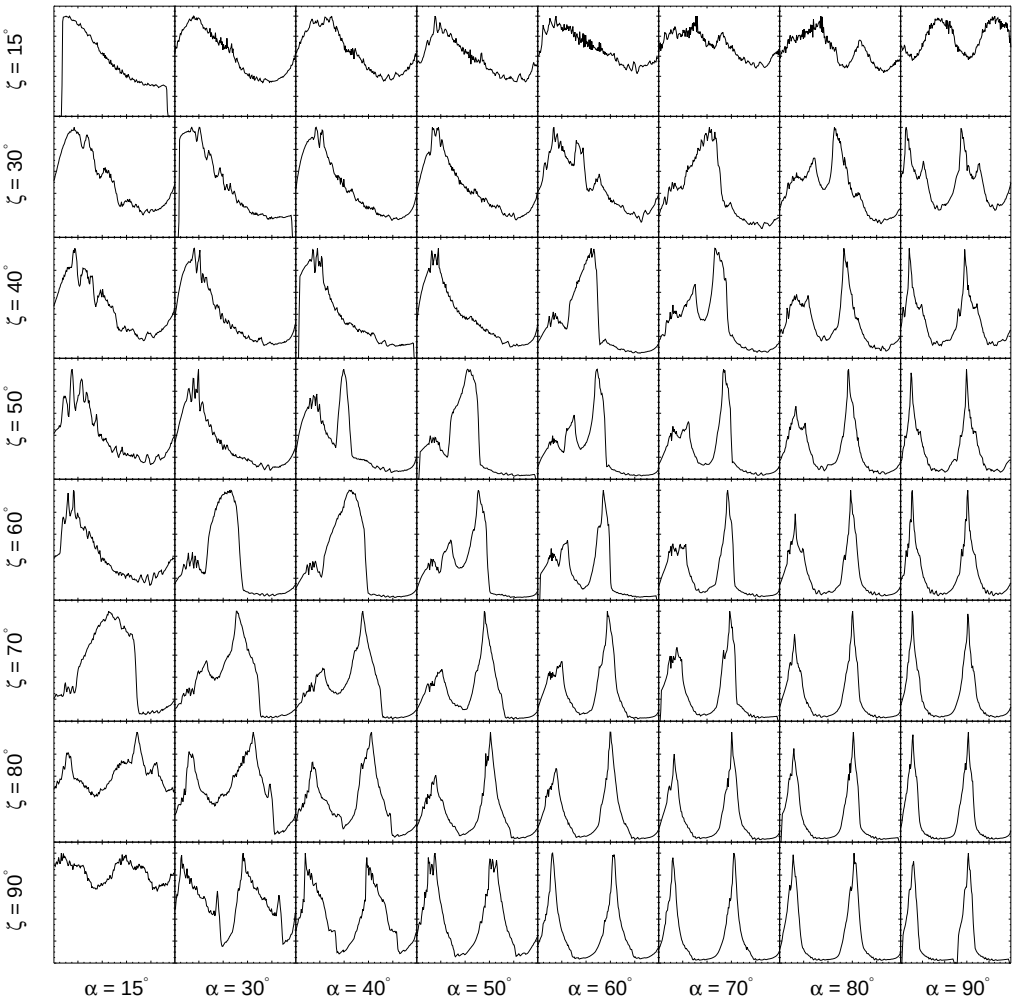

Figure B.67: Light curves from the asymmetric slot gap geometry in the force-free field geometry, with $w = 0.10$ and $r = 1.0\,R_{\rm LC}$.

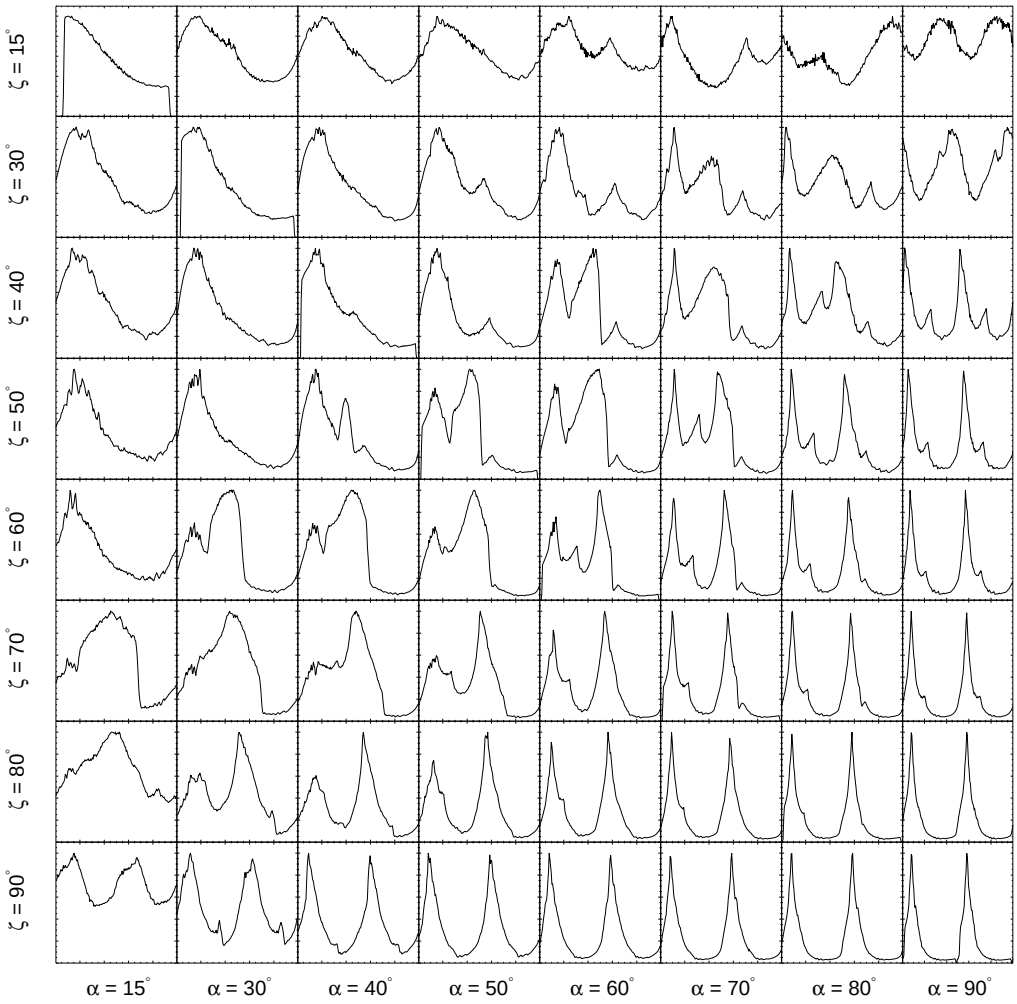

Figure B.68: Light curves from the asymmetric slot gap geometry in the force-free field geometry, with $w = 0.20$ and $r = 1.0\,R_{\rm LC}$.

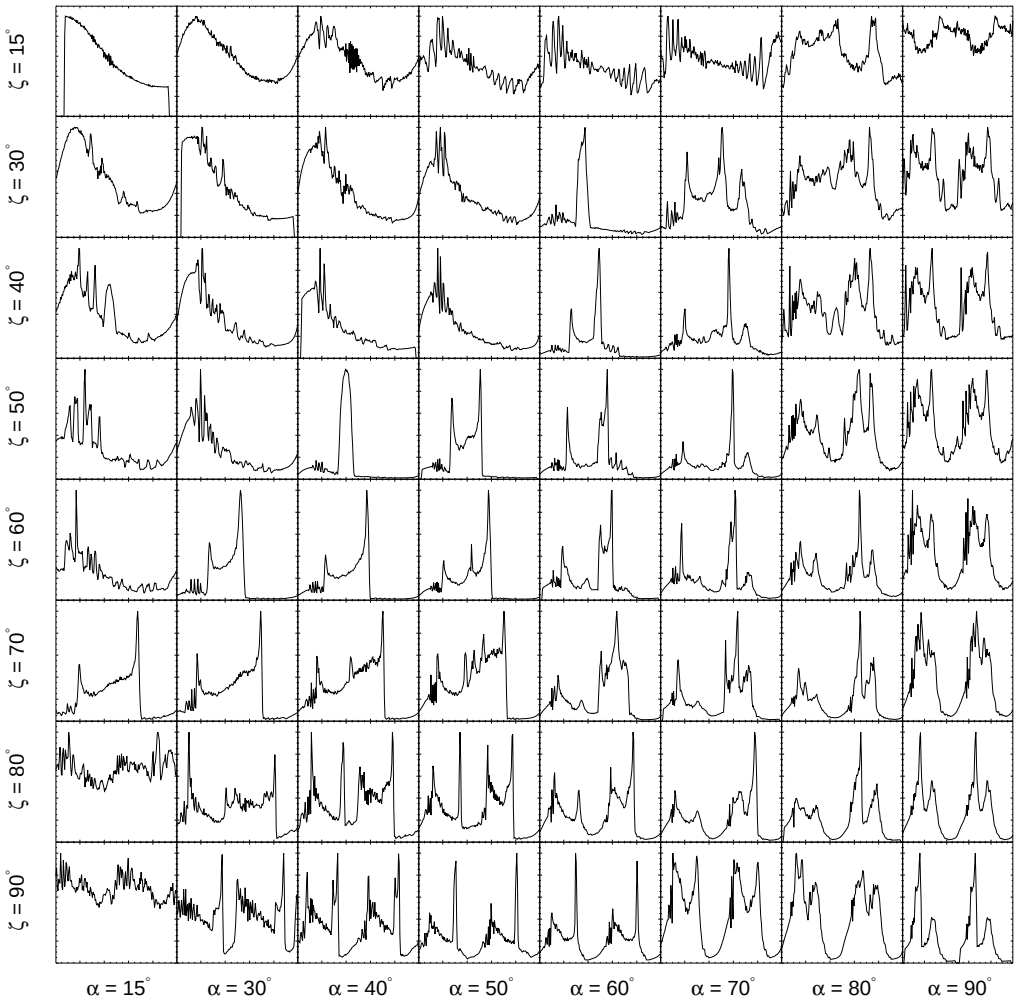

Figure B.69: Light curves from the asymmetric slot gap geometry in the force-free field geometry, with $w = 0.01$ and $r = 1.5\,R_{\rm LC}$.

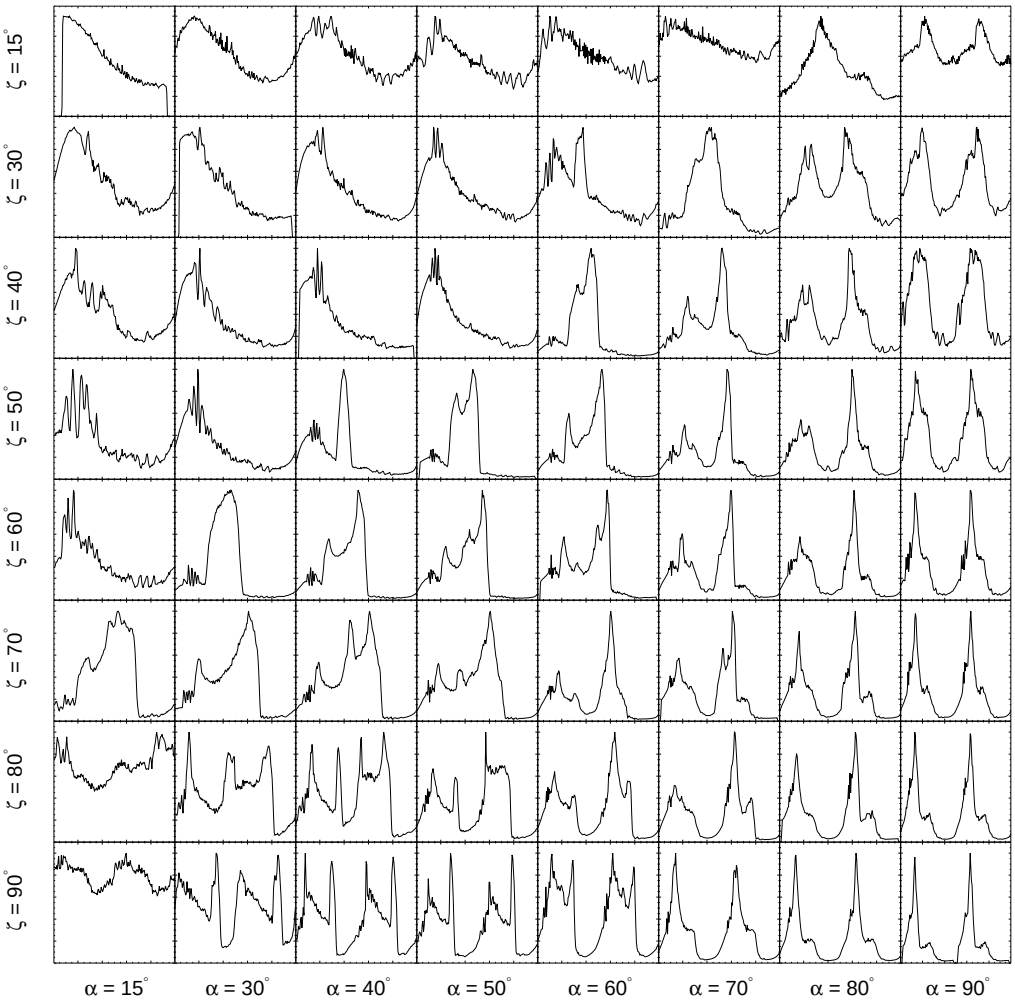

Figure B.70: Light curves from the asymmetric slot gap geometry in the force-free field geometry, with $w = 0.05$ and $r = 1.5\,R_{\rm LC}$.

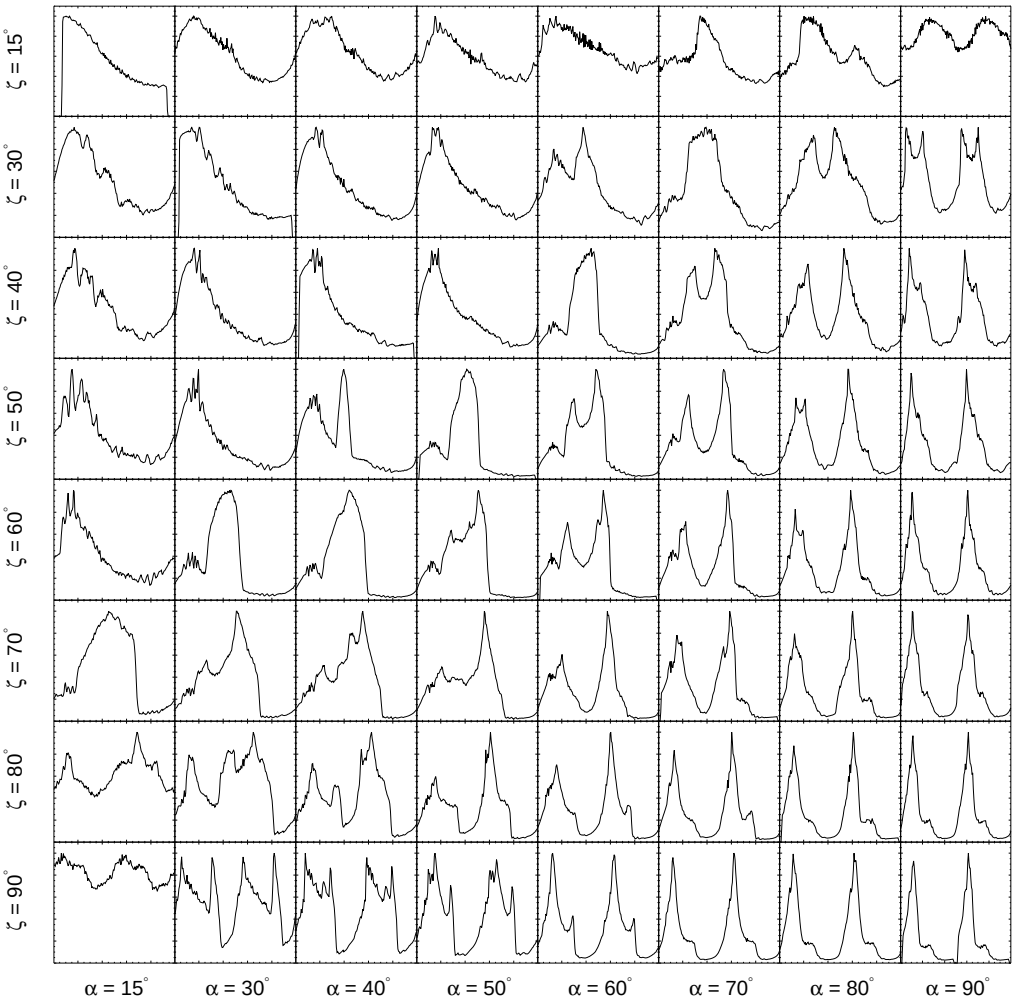

Figure B.71: Light curves from the asymmetric slot gap geometry in the force-free field geometry, with $w = 0.10$ and $r = 1.5\,R_{\rm LC}$.

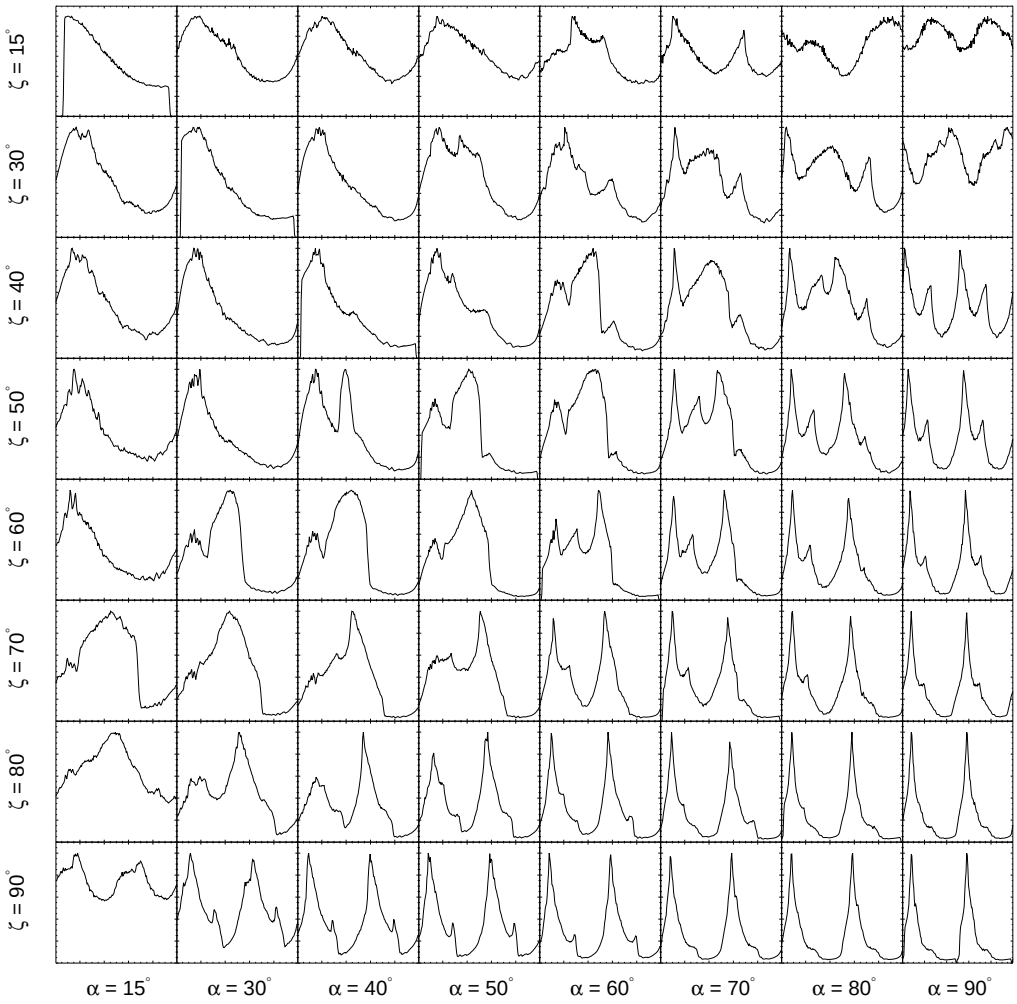

Figure B.72: Light curves from the asymmetric slot gap geometry in the force-free field geometry, with $w = 0.20$ and $r = 1.5\,R_{\rm LC}$.

Appendix C

Proof of Wilks' Theorem

Wilks' Theorem (Wilks 1938) can be used to relate the difference in the natural logarithms of the likelihoods of two models with the difference in χ^2 between those models, for the case of data that has Gaussian errors. This theorem was used in the light curve modeling of Chapter 3. The pulsars studied are bright at γ-ray energies, and therefore their LAT light curves contained sufficient numbers of counts to have Gaussian rather than Poisson errors. Here I provide the proof of Wilks' Theorem, for completeness.

The likelihood is defined as

$$\mathcal{L} = \prod_i p_i \tag{C.1}$$

For a Gaussian probability distribution,

$$p_i = \frac{1}{\sqrt{2\pi}\sigma_i} \exp\left[-\frac{(C_i - M_i)^2}{2\sigma_i^2}\right] \tag{C.2}$$

where C_i are the data points, in the case the number of counts in light curve bin i, and M_i is the number of counts expected from a model. Substituting the expression for p_i and taking the logarithm,

$$\ln \mathcal{L} = -\sum_i \frac{(C_i - M_i)^2}{2\sigma_i^2} + \sum_i \ln\left(\frac{1}{\sqrt{2\pi}\sigma_i}\right) \tag{C.3}$$

Note that the second term is model-independent and will not contribute to model comparison or parameter estimation through use of the likelihood ratio test.

Imagine we are performing the likelihood ratio test between models 1 and 2, which have likelihoods $\mathcal{L}_1$ and $\mathcal{L}_2$. In logarithm space, the likelihood ratio is a subtraction:

$$\ln \mathcal{L}_2/\mathcal{L}_1 = \ln \mathcal{L}_2 - \ln \mathcal{L}_1 \tag{C.4a}$$

$$\begin{aligned} &= -\sum_i \frac{(C_i - M_{i,2})^2}{2\sigma_i^2} + \sum_i \ln\left(\frac{1}{\sqrt{2\pi}\sigma_i}\right) \\ &\quad + \sum_i \frac{(C_i - M_{i,1})^2}{2\sigma_i^2} - \sum_i \ln\left(\frac{1}{\sqrt{2\pi}\sigma_i}\right) \end{aligned} \tag{C.4b}$$

$$= -\frac{1}{2}\left[\sum_i \frac{(C_i - M_{i,2})^2}{\sigma_i^2} - \sum_i \frac{(C_i - M_{i,1})^2}{\sigma_i^2}\right] \tag{C.4c}$$

Equation C.4c is simply the difference of two χ^2 values. Therefore,

$$\Delta\mathcal{L} = -\frac{1}{2}\Delta\chi^2 \tag{C.5}$$

Equation C.5 is Wilks' Theorem.

Appendix D

Phase Resolved Spectral Parameters

This appendix contains the phase-resolved spectral parameters, photon and energy fluxes, and test statistics of the Vela, Crab, and Geminga pulsars. The corresponding values for PSR J0007+7303 can be found in Abdo et al. (2012).

Table D.1. Phase Resolved Spectral Parameters of the Vela Pulsar

Phase Bin	N_0	Γ	E_c	Photon Flux	Energy Flux	TS
0.000–0.035	0.00 ± 0.00	...	...	...	...	< 1
0.035–0.068	0.47 ± 0.27	0.00 ± 0.00	0.29 ± 0.07	0.10 ± 0.03	0.04 ± 0.01	16.78
0.068–0.088	1.99 ± 0.25	1.54 ± 0.13	0.94 ± 0.18	1.94 ± 0.10	0.63 ± 0.03	1196.87
0.088–0.098	6.07 ± 0.43	1.64 ± 0.07	1.19 ± 0.15	6.76 ± 0.21	2.23 ± 0.07	3957.05
0.098–0.105	9.30 ± 0.55	1.73 ± 0.06	1.51 ± 0.19	11.56 ± 0.31	3.88 ± 0.10	6644.76
0.105–0.110	13.08 ± 0.66	1.77 ± 0.05	1.68 ± 0.20	17.07 ± 0.41	5.75 ± 0.14	9024.37
0.110–0.114	18.62 ± 0.97	1.67 ± 0.05	1.38 ± 0.14	21.82 ± 0.51	7.46 ± 0.18	8490.54
0.114–0.117	21.24 ± 1.09	1.79 ± 0.05	1.65 ± 0.20	28.01 ± 0.64	9.22 ± 0.22	8922.43
0.117–0.120	26.76 ± 1.35	1.74 ± 0.05	1.53 ± 0.17	33.52 ± 0.77	11.24 ± 0.26	9538.06
0.120–0.122	34.10 ± 1.67	1.65 ± 0.05	1.42 ± 0.14	39.90 ± 0.89	13.99 ± 0.32	10282.50
0.122–0.124	35.00 ± 1.53	1.76 ± 0.04	2.10 ± 0.25	47.26 ± 0.99	17.27 ± 0.41	11023.81
0.124–0.126	39.61 ± 1.55	1.75 ± 0.04	2.16 ± 0.24	53.63 ± 1.10	19.85 ± 0.46	11692.64
0.126–0.128	44.89 ± 1.78	1.75 ± 0.04	2.03 ± 0.21	59.79 ± 1.21	21.86 ± 0.50	12068.10
0.128–0.129	50.64 ± 3.09	1.76 ± 0.03	1.90 ± 0.15	67.25 ± 6.02	23.78 ± 2.19	12075.34
0.129–0.130	54.45 ± 2.12	1.75 ± 0.04	2.16 ± 0.23	73.44 ± 1.46	27.33 ± 0.63	12297.86
0.130–0.131	61.92 ± 2.46	1.67 ± 0.04	1.88 ± 0.18	77.87 ± 1.63	29.69 ± 0.68	12238.39
0.131–0.132	62.10 ± 2.37	1.71 ± 0.04	2.24 ± 0.24	82.61 ± 1.71	32.20 ± 0.76	12999.07
0.132–0.134	66.51 ± 2.57	1.67 ± 0.04	2.09 ± 0.21	85.38 ± 1.77	33.84 ± 0.79	13192.18
0.134–0.135	65.96 ± 2.33	1.65 ± 0.04	2.27 ± 0.22	85.23 ± 1.78	35.43 ± 0.84	13062.81
0.135–0.136	64.78 ± 2.06	1.70 ± 0.03	2.85 ± 0.29	89.03 ± 1.77	38.24 ± 0.92	13747.02
0.136–0.137	62.10 ± 2.05	1.66 ± 0.04	2.97 ± 0.33	84.34 ± 1.70	38.27 ± 0.95	13710.03
0.137–0.138	62.81 ± 1.98	1.64 ± 0.03	2.68 ± 0.26	83.17 ± 1.68	37.18 ± 0.89	13890.72
0.138–0.139	58.41 ± 1.84	1.63 ± 0.03	2.83 ± 0.28	77.94 ± 1.61	35.67 ± 0.88	13403.09
0.139–0.140	54.96 ± 1.80	1.62 ± 0.04	2.59 ± 0.25	71.86 ± 1.47	32.17 ± 0.78	13378.40
0.140–0.141	50.96 ± 1.64	1.61 ± 0.04	2.69 ± 0.26	66.73 ± 1.47	30.72 ± 0.76	13447.10
0.141–0.143	46.45 ± 1.54	1.60 ± 0.04	2.45 ± 0.23	59.67 ± 1.31	26.68 ± 0.65	12665.19
0.143–0.144	39.27 ± 1.24	1.67 ± 0.04	3.05 ± 0.32	53.83 ± 1.14	24.37 ± 0.61	12622.72
0.144–0.146	35.09 ± 1.17	1.65 ± 0.04	2.63 ± 0.27	46.58 ± 1.04	20.41 ± 0.50	12292.77
0.146–0.148	32.68 ± 1.09	1.65 ± 0.04	2.60 ± 0.26	43.22 ± 0.92	18.92 ± 0.46	12065.20
0.148–0.151	27.66 ± 0.94	1.64 ± 0.04	2.63 ± 0.27	36.49 ± 0.80	16.23 ± 0.41	11300.46
0.151–0.153	26.12 ± 0.92	1.55 ± 0.04	2.31 ± 0.22	32.39 ± 0.74	14.96 ± 0.37	11561.92
0.153–0.156	22.08 ± 0.75	1.62 ± 0.04	2.66 ± 0.27	28.93 ± 0.66	13.17 ± 0.34	10910.74
0.156–0.159	21.24 ± 0.73	1.61 ± 0.04	2.73 ± 0.30	27.92 ± 0.65	12.89 ± 0.34	10767.29
0.159–0.162	18.71 ± 0.65	1.55 ± 0.04	2.44 ± 0.24	23.47 ± 0.55	11.09 ± 0.29	10363.20
0.162–0.166	17.57 ± 0.61	1.57 ± 0.04	2.52 ± 0.25	22.39 ± 0.53	10.43 ± 0.27	10069.48
0.166–0.170	17.74 ± 0.64	1.51 ± 0.04	2.19 ± 0.21	21.48 ± 0.50	10.03 ± 0.25	10157.45
0.170–0.173	18.21 ± 0.66	1.47 ± 0.04	2.08 ± 0.19	21.49 ± 0.50	10.23 ± 0.26	10379.80
0.173–0.177	16.86 ± 0.60	1.49 ± 0.04	2.11 ± 0.19	20.02 ± 0.47	9.48 ± 0.24	10039.14
0.177–0.181	16.73 ± 0.62	1.47 ± 0.04	1.97 ± 0.18	19.44 ± 0.46	9.06 ± 0.23	9818.21
0.181–0.185	16.17 ± 0.57	1.54 ± 0.04	2.34 ± 0.22	20.09 ± 0.49	9.36 ± 0.24	11112.76
0.185–0.189	17.06 ± 0.65	1.50 ± 0.04	1.95 ± 0.18	19.99 ± 0.49	9.04 ± 0.23	9726.57
0.189–0.193	17.43 ± 0.67	1.45 ± 0.04	1.80 ± 0.16	19.70 ± 0.48	8.95 ± 0.22	9838.44
0.193–0.197	15.92 ± 0.59	1.47 ± 0.04	1.98 ± 0.18	18.53 ± 0.47	8.64 ± 0.22	9743.81
0.197–0.201	17.05 ± 0.64	1.49 ± 0.04	1.94 ± 0.18	19.94 ± 0.48	9.03 ± 0.23	11403.17
0.201–0.205	18.01 ± 0.70	1.41 ± 0.05	1.74 ± 0.15	19.88 ± 0.49	9.24 ± 0.23	9847.27
0.205–0.209	19.95 ± 0.82	1.36 ± 0.05	1.44 ± 0.12	20.44 ± 0.48	9.10 ± 0.22	9970.88
0.209–0.212	17.61 ± 0.68	1.43 ± 0.04	1.78 ± 0.16	19.69 ± 0.48	9.11 ± 0.23	9933.58
0.212–0.216	18.05 ± 0.73	1.41 ± 0.05	1.61 ± 0.14	19.48 ± 0.47	8.79 ± 0.22	9445.05
0.216–0.220	18.73 ± 0.73	1.31 ± 0.05	1.56 ± 0.13	19.35 ± 0.46	9.39 ± 0.23	10513.55
0.220–0.224	18.63 ± 0.75	1.29 ± 0.05	1.46 ± 0.11	18.68 ± 0.46	8.93 ± 0.22	9846.00
0.224–0.228	18.33 ± 0.69	1.24 ± 0.05	1.51 ± 0.11	18.35 ± 0.43	9.33 ± 0.23	10387.36
0.228–0.232	15.48 ± 0.54	1.39 ± 0.04	2.14 ± 0.19	17.85 ± 0.44	9.41 ± 0.25	10046.84
0.232–0.236	17.47 ± 0.64	1.25 ± 0.05	1.69 ± 0.13	18.18 ± 0.45	9.70 ± 0.24	10682.38
0.236–0.240	17.63 ± 0.62	1.14 ± 0.05	1.57 ± 0.11	17.43 ± 0.42	9.96 ± 0.25	11228.63
0.240–0.244	16.79 ± 0.60	1.17 ± 0.05	1.65 ± 0.12	16.99 ± 0.43	9.72 ± 0.24	10890.01
0.244–0.249	16.20 ± 0.57	1.17 ± 0.05	1.67 ± 0.12	16.50 ± 0.42	9.48 ± 0.24	10838.68
0.249–0.253	15.61 ± 0.51	1.20 ± 0.04	1.92 ± 0.14	16.72 ± 0.42	10.17 ± 0.26	11132.45

Table D.1 (cont'd)

Phase Bin	N_0	Γ	E_c	Photon Flux	Energy Flux	TS
0.253–0.257	15.41 ± 0.52	1.19 ± 0.04	1.86 ± 0.14	16.29 ± 0.41	9.83 ± 0.25	11125.26
0.257–0.261	14.64 ± 0.45	1.20 ± 0.04	2.18 ± 0.16	16.30 ± 0.41	10.65 ± 0.28	11884.67
0.261–0.266	13.14 ± 0.40	1.19 ± 0.04	2.34 ± 0.17	14.93 ± 0.38	10.23 ± 0.27	11511.90
0.266–0.270	13.10 ± 0.40	1.20 ± 0.04	2.32 ± 0.17	14.86 ± 0.38	10.06 ± 0.27	11515.75
0.270–0.275	13.08 ± 0.39	1.17 ± 0.04	2.27 ± 0.17	14.69 ± 0.35	10.15 ± 0.27	11917.72
0.275–0.279	12.43 ± 0.37	1.18 ± 0.04	2.47 ± 0.18	14.33 ± 0.35	10.28 ± 0.27	11961.96
0.279–0.284	11.76 ± 0.36	1.18 ± 0.04	2.32 ± 0.17	13.31 ± 0.34	9.25 ± 0.25	11424.86
0.284–0.289	11.26 ± 0.33	1.18 ± 0.04	2.63 ± 0.19	13.23 ± 0.33	9.84 ± 0.27	12603.24
0.289–0.294	11.46 ± 0.34	1.14 ± 0.04	2.27 ± 0.16	12.85 ± 0.32	9.23 ± 0.24	12326.24
0.294–0.299	10.89 ± 0.33	1.11 ± 0.04	2.29 ± 0.17	12.22 ± 0.32	9.13 ± 0.24	12353.90
0.299–0.305	9.96 ± 0.30	1.20 ± 0.04	2.61 ± 0.20	11.67 ± 0.31	8.47 ± 0.23	11715.40
0.305–0.311	8.99 ± 0.27	1.19 ± 0.04	2.77 ± 0.21	10.72 ± 0.29	8.14 ± 0.23	11658.98
0.311–0.316	9.03 ± 0.27	1.21 ± 0.04	2.91 ± 0.23	10.91 ± 0.29	8.35 ± 0.24	11575.39
0.316–0.322	8.34 ± 0.25	1.19 ± 0.04	2.91 ± 0.22	10.07 ± 0.27	7.87 ± 0.22	11233.13
0.322–0.329	7.78 ± 0.22	1.29 ± 0.04	3.58 ± 0.30	9.91 ± 0.26	7.69 ± 0.22	11304.79
0.329–0.336	7.01 ± 0.21	1.26 ± 0.04	3.14 ± 0.26	8.66 ± 0.24	6.51 ± 0.19	10294.66
0.336–0.343	7.32 ± 0.23	1.13 ± 0.04	2.52 ± 0.19	8.47 ± 0.24	6.52 ± 0.18	10626.17
0.343–0.350	6.88 ± 0.21	1.26 ± 0.04	3.23 ± 0.28	8.56 ± 0.23	6.53 ± 0.19	10385.35
0.350–0.357	6.74 ± 0.20	1.21 ± 0.04	3.32 ± 0.27	8.43 ± 0.24	6.97 ± 0.21	10684.03
0.357–0.364	6.48 ± 0.20	1.17 ± 0.04	2.93 ± 0.24	7.84 ± 0.23	6.28 ± 0.18	9934.34
0.364–0.372	6.50 ± 0.20	1.20 ± 0.04	2.76 ± 0.23	7.74 ± 0.22	5.75 ± 0.17	9850.76
0.372–0.380	5.80 ± 0.18	1.29 ± 0.04	3.44 ± 0.31	7.33 ± 0.21	5.55 ± 0.17	8998.66
0.380–0.388	6.30 ± 0.21	1.20 ± 0.05	2.72 ± 0.24	7.48 ± 0.22	5.53 ± 0.16	9271.32
0.388–0.396	5.53 ± 0.18	1.26 ± 0.04	2.76 ± 0.24	6.62 ± 0.20	4.62 ± 0.14	8324.35
0.396–0.405	5.95 ± 0.20	1.29 ± 0.04	2.61 ± 0.23	7.05 ± 0.21	4.58 ± 0.13	8027.01
0.405–0.413	5.94 ± 0.20	1.24 ± 0.05	2.46 ± 0.21	6.88 ± 0.20	4.57 ± 0.13	8285.46
0.413–0.422	6.14 ± 0.22	1.21 ± 0.05	2.03 ± 0.18	6.70 ± 0.20	4.13 ± 0.12	7684.75
0.422–0.431	5.95 ± 0.22	1.31 ± 0.05	2.18 ± 0.21	6.76 ± 0.20	3.92 ± 0.11	7356.77
0.431–0.440	5.91 ± 0.22	1.33 ± 0.05	2.21 ± 0.20	6.78 ± 0.20	3.84 ± 0.11	7200.14
0.440–0.449	6.12 ± 0.23	1.20 ± 0.05	1.84 ± 0.16	6.46 ± 0.20	3.84 ± 0.11	7434.24
0.449–0.457	5.55 ± 0.19	1.34 ± 0.04	2.75 ± 0.26	6.71 ± 0.20	4.23 ± 0.13	7689.20
0.457–0.465	6.24 ± 0.21	1.25 ± 0.05	2.42 ± 0.21	7.21 ± 0.21	4.74 ± 0.14	8245.50
0.465–0.473	6.63 ± 0.21	1.38 ± 0.04	3.13 ± 0.31	8.31 ± 0.24	5.34 ± 0.16	8856.89
0.473–0.480	7.55 ± 0.25	1.28 ± 0.04	2.58 ± 0.22	8.91 ± 0.25	5.83 ± 0.17	9234.69
0.480–0.486	8.67 ± 0.26	1.40 ± 0.04	3.10 ± 0.29	10.89 ± 0.29	6.79 ± 0.19	10205.42
0.486–0.492	9.43 ± 0.28	1.43 ± 0.04	3.31 ± 0.31	12.09 ± 0.31	7.48 ± 0.21	10477.47
0.492–0.497	10.62 ± 0.33	1.45 ± 0.04	3.39 ± 0.34	13.74 ± 0.36	8.36 ± 0.24	10522.67
0.497–0.502	11.24 ± 0.33	1.38 ± 0.04	3.17 ± 0.28	14.13 ± 0.37	9.15 ± 0.26	10275.03
0.502–0.506	12.50 ± 0.37	1.51 ± 0.04	3.99 ± 0.45	16.84 ± 0.43	10.31 ± 0.31	11507.52
0.506–0.510	13.49 ± 0.37	1.50 ± 0.03	3.82 ± 0.37	18.04 ± 0.43	10.89 ± 0.30	11015.86
0.510–0.514	14.34 ± 0.40	1.54 ± 0.03	3.85 ± 0.38	19.38 ± 0.46	11.24 ± 0.31	11057.86
0.514–0.517	16.81 ± 0.49	1.44 ± 0.04	2.99 ± 0.27	21.17 ± 0.50	12.35 ± 0.33	11556.53
0.517–0.521	17.35 ± 0.48	1.49 ± 0.03	3.57 ± 0.33	22.84 ± 0.55	13.69 ± 0.37	11935.73
0.521–0.524	18.65 ± 0.53	1.50 ± 0.03	3.54 ± 0.33	24.63 ± 0.58	14.39 ± 0.39	11756.06
0.524–0.527	21.47 ± 0.64	1.43 ± 0.04	2.81 ± 0.25	26.66 ± 0.62	15.19 ± 0.40	12352.19
0.527–0.529	21.98 ± 0.62	1.54 ± 0.03	3.44 ± 0.33	29.22 ± 0.64	16.08 ± 0.43	12236.11
0.529–0.532	24.52 ± 0.69	1.52 ± 0.03	3.40 ± 0.33	32.37 ± 0.71	18.11 ± 0.48	12618.92
0.532–0.534	25.45 ± 0.74	1.51 ± 0.04	3.02 ± 0.28	32.74 ± 0.73	17.76 ± 0.46	12595.98
0.534–0.536	26.03 ± 0.74	1.56 ± 0.03	3.93 ± 0.42	35.56 ± 0.80	20.12 ± 0.56	12604.58
0.536–0.539	27.86 ± 0.74	1.58 ± 0.03	4.10 ± 0.41	38.56 ± 0.83	21.59 ± 0.58	13327.79
0.539–0.541	29.83 ± 0.81	1.54 ± 0.03	3.87 ± 0.38	40.42 ± 0.89	23.32 ± 0.63	13282.40
0.541–0.542	31.68 ± 0.91	1.52 ± 0.03	3.23 ± 0.31	41.43 ± 0.89	22.73 ± 0.59	13296.00
0.542–0.544	33.44 ± 0.91	1.45 ± 0.03	3.27 ± 0.28	42.98 ± 0.94	25.73 ± 0.67	14133.66
0.544–0.546	36.13 ± 1.05	1.56 ± 0.03	3.42 ± 0.34	48.22 ± 1.05	25.95 ± 0.68	13359.93
0.546–0.548	39.08 ± 1.13	1.53 ± 0.03	3.07 ± 0.28	50.87 ± 1.08	26.84 ± 0.68	13496.81
0.548–0.549	40.24 ± 1.11	1.52 ± 0.03	3.33 ± 0.30	52.96 ± 1.13	29.29 ± 0.75	14317.84
0.549–0.551	40.08 ± 1.09	1.57 ± 0.03	3.85 ± 0.37	54.65 ± 1.21	30.53 ± 0.81	13781.17

Table D.1 (cont'd)

Phase Bin	N_0	Γ	E_c	Photon Flux	Energy Flux	TS
0.551–0.552	44.46 ± 1.25	1.51 ± 0.03	3.15 ± 0.28	57.61 ± 1.22	31.77 ± 0.81	14435.51
0.552–0.553	44.95 ± 1.20	1.55 ± 0.03	3.83 ± 0.37	60.97 ± 1.29	34.60 ± 0.92	14705.16
0.553–0.555	45.34 ± 1.23	1.54 ± 0.03	3.62 ± 0.34	60.84 ± 1.29	34.01 ± 0.89	14469.76
0.555–0.556	43.49 ± 1.13	1.62 ± 0.03	5.42 ± 0.62	63.01 ± 1.39	37.58 ± 1.10	13482.62
0.556–0.557	47.86 ± 1.22	1.56 ± 0.03	4.22 ± 0.40	65.92 ± 1.37	38.76 ± 1.04	14637.14
0.557–0.558	50.06 ± 1.31	1.53 ± 0.03	3.85 ± 0.36	67.49 ± 1.43	39.54 ± 1.05	15405.91
0.558–0.560	50.99 ± 1.31	1.51 ± 0.03	3.96 ± 0.36	68.68 ± 1.44	41.69 ± 1.11	14954.51
0.560–0.561	52.58 ± 1.36	1.51 ± 0.03	3.67 ± 0.33	69.93 ± 1.45	41.28 ± 1.07	15286.55
0.561–0.562	54.27 ± 1.36	1.51 ± 0.03	4.07 ± 0.37	73.47 ± 1.51	45.12 ± 1.21	15375.52
0.562–0.563	51.20 ± 1.28	1.55 ± 0.03	4.66 ± 0.46	71.42 ± 1.46	43.97 ± 1.22	14933.11
0.563–0.564	52.74 ± 1.29	1.51 ± 0.03	4.53 ± 0.42	72.41 ± 1.52	46.99 ± 1.28	15275.66
0.564–0.565	51.87 ± 1.28	1.49 ± 0.03	4.32 ± 0.39	70.47 ± 1.46	45.65 ± 1.24	15389.57
0.565–0.566	53.16 ± 1.28	1.53 ± 0.03	4.86 ± 0.47	74.11 ± 1.53	48.04 ± 1.33	15895.18
0.566–0.567	54.20 ± 1.39	1.46 ± 0.03	3.72 ± 0.32	71.46 ± 1.47	44.86 ± 1.18	15649.29
0.567–0.568	51.92 ± 1.31	1.54 ± 0.03	4.37 ± 0.41	71.57 ± 1.49	43.50 ± 1.17	14962.50
0.568–0.570	51.77 ± 1.30	1.50 ± 0.03	3.75 ± 0.33	68.87 ± 1.41	41.71 ± 1.08	15957.11
0.570–0.571	49.08 ± 1.27	1.52 ± 0.03	3.96 ± 0.37	66.34 ± 1.39	39.61 ± 1.05	15032.66
0.571–0.572	44.73 ± 1.15	1.57 ± 0.03	4.50 ± 0.45	62.35 ± 1.38	37.16 ± 1.02	14611.36
0.572–0.574	41.11 ± 1.11	1.57 ± 0.03	3.96 ± 0.39	56.35 ± 1.21	31.71 ± 0.85	14080.98
0.574–0.575	37.61 ± 1.09	1.55 ± 0.03	3.22 ± 0.30	49.56 ± 1.11	26.35 ± 0.68	13131.56
0.575–0.577	36.17 ± 1.15	1.52 ± 0.04	2.69 ± 0.26	45.72 ± 0.98	23.27 ± 0.59	13284.69
0.577–0.579	32.78 ± 1.14	1.51 ± 0.04	2.14 ± 0.19	39.50 ± 0.87	18.27 ± 0.44	12224.55
0.579–0.582	24.55 ± 0.81	1.62 ± 0.04	2.76 ± 0.28	32.47 ± 0.74	14.86 ± 0.38	11363.83
0.582–0.585	22.46 ± 0.84	1.58 ± 0.04	2.16 ± 0.21	27.91 ± 0.63	12.13 ± 0.30	10486.68
0.585–0.588	19.20 ± 0.82	1.64 ± 0.05	1.94 ± 0.21	23.91 ± 0.54	9.48 ± 0.23	9664.85
0.588–0.593	15.16 ± 0.73	1.64 ± 0.05	1.75 ± 0.20	18.56 ± 0.46	7.05 ± 0.18	9766.56
0.593–0.598	12.36 ± 0.64	1.66 ± 0.05	1.53 ± 0.17	14.80 ± 0.39	5.29 ± 0.14	8013.27
0.598–0.605	8.02 ± 0.43	1.77 ± 0.05	1.80 ± 0.24	10.57 ± 0.29	3.66 ± 0.10	6364.90
0.605–0.616	4.95 ± 0.29	1.86 ± 0.06	1.87 ± 0.28	6.95 ± 0.21	2.26 ± 0.07	4080.93
0.616–0.630	3.79 ± 0.36	1.66 ± 0.09	0.98 ± 0.14	4.02 ± 0.15	1.22 ± 0.04	2428.43
0.630–0.650	1.88 ± 0.25	1.83 ± 0.12	0.98 ± 0.21	2.25 ± 0.11	0.62 ± 0.03	1152.10
0.650–0.675	1.03 ± 0.23	1.81 ± 0.20	0.81 ± 0.25	1.13 ± 0.09	0.30 ± 0.02	417.22
0.675–0.704	1.29 ± 0.80	1.32 ± 0.49	0.33 ± 0.13	0.63 ± 0.08	0.15 ± 0.01	156.91
0.704–0.733	0.88 ± 1.49	1.54 ± 1.08	0.26 ± 0.26	0.43 ± 0.07	0.09 ± 0.01	56.63
0.733–0.764	0.43 ± 0.37	1.95 ± 0.64	0.58 ± 0.55	0.47 ± 0.07	0.11 ± 0.01	80.19
0.764–0.795	0.69 ± 1.12	0.00 ± 0.02	0.22 ± 0.14	0.10 ± 0.07	0.03 ± 0.01	10.45
0.795–0.828	0.07 ± 0.09	0.00 ± 0.04	0.41 ± 0.20	0.02 ± 0.02	0.01 ± 0.01	2.05
0.828–0.863	0.01 ± 0.01	0.00 ± 0.02	1.46 ± 0.75	0.01 ± 0.01	0.01 ± 0.01	4.76
0.863–0.896	0.00 ± 0.00	···	···	···	···	< 1
0.896–0.929	0.31 ± 4.23	···	···	···	···	< 1
0.929–0.965	0.00 ± 0.00	···	···	···	···	< 1
0.965–1.000	0.00 ± 0.10	···	···	···	···	< 1

Note. — An exponentially cutoff power law with $b = 1$ was used to fit the spectrum in each fixed-count phase bin of the Vela light curve. The differential flux prefactor N_0 is given in units of $10^{-9}\,\mathrm{cm}^{-2}\,\mathrm{s}^{-1}\,\mathrm{MeV}^{-1}$; cutoff energy E_c in GeV; photon flux in $10^{-6}\,\mathrm{cm}^{-2}\,\mathrm{s}^{-1}$; and energy flux in $10^{-9}\,\mathrm{erg}\,\mathrm{cm}^{-2}\,\mathrm{s}^{-1}$. The phase bins without data had $TS < 1$; the spectral parameters at these phases were unconstrained.

Table D.2. Phase Resolved Spectral Parameters of the Crab Pulsar

Phase Bin	N_0	Γ	E_c	Photon Flux	Energy Flux	TS
0.000–0.006	7.06 ± 0.28	1.90 ± 0.04	4.20 ± 0.72	13.94 ± 0.35	5.46 ± 0.15	9784.82
0.006–0.014	4.99 ± 0.21	1.82 ± 0.04	3.54 ± 0.58	9.20 ± 0.24	3.74 ± 0.11	7964.76
0.014–0.028	2.71 ± 0.10	1.81 ± 0.04	4.42 ± 0.72	5.09 ± 0.15	2.22 ± 0.07	5162.01
0.028–0.049	1.27 ± 0.06	1.76 ± 0.06	4.71 ± 1.06	2.32 ± 0.09	1.10 ± 0.05	2857.48
0.049–0.080	0.60 ± 0.03	1.66 ± 0.07	6.01 ± 1.57	1.08 ± 0.06	0.63 ± 0.04	1417.46
0.080–0.118	0.28 ± 0.02	1.49 ± 0.10	7.63 ± 2.46	0.49 ± 0.05	0.42 ± 0.04	668.25
0.118–0.158	0.24 ± 0.02	1.36 ± 0.13	4.92 ± 1.69	0.38 ± 0.04	0.32 ± 0.03	559.41
0.158–0.200	0.22 ± 0.02	1.27 ± 0.13	4.06 ± 1.09	0.33 ± 0.04	0.28 ± 0.02	467.04
0.200–0.237	0.32 ± 0.02	1.35 ± 0.10	5.04 ± 1.30	0.51 ± 0.04	0.44 ± 0.03	846.06
0.237–0.269	0.51 ± 0.03	1.47 ± 0.08	5.61 ± 1.26	0.85 ± 0.05	0.64 ± 0.04	1390.03
0.269–0.296	0.81 ± 0.04	1.56 ± 0.07	4.94 ± 1.12	1.35 ± 0.07	0.84 ± 0.04	2057.75
0.296–0.319	1.41 ± 0.07	1.52 ± 0.06	2.67 ± 0.41	2.11 ± 0.09	1.07 ± 0.04	3024.79
0.319–0.336	1.91 ± 0.09	1.72 ± 0.05	3.37 ± 0.58	3.30 ± 0.11	1.47 ± 0.05	3828.25
0.336–0.351	2.33 ± 0.10	1.76 ± 0.05	4.18 ± 0.73	4.23 ± 0.14	1.92 ± 0.07	4759.82
0.351–0.364	2.93 ± 0.12	1.82 ± 0.04	4.33 ± 0.77	5.53 ± 0.16	2.37 ± 0.08	5412.18
0.364–0.375	3.23 ± 0.13	1.91 ± 0.04	5.09 ± 1.09	6.55 ± 0.19	2.66 ± 0.09	5732.17
0.375–0.385	3.32 ± 0.11	1.99 ± 0.04	10.84 ± 3.08	7.43 ± 0.20	3.24 ± 0.12	6284.64
0.385–0.396	3.38 ± 0.12	1.92 ± 0.04	5.61 ± 1.02	6.93 ± 0.19	2.86 ± 0.09	6066.75
0.396–0.409	2.70 ± 0.12	2.00 ± 0.05	5.08 ± 1.20	5.82 ± 0.17	2.14 ± 0.07	5074.27
0.409–0.428	1.68 ± 0.11	1.97 ± 0.07	3.29 ± 0.91	3.42 ± 0.12	1.17 ± 0.04	3235.65
0.428–0.455	0.90 ± 0.09	2.04 ± 0.09	2.24 ± 0.67	1.86 ± 0.08	0.55 ± 0.02	1524.70
0.455–0.493	0.24 ± 0.03	2.29 ± 0.13	9.88 ± 14.29	0.69 ± 0.06	0.21 ± 0.02	320.64
0.493–0.540	0.13 ± 0.12	2.30 ± 0.67	0.94 ± 1.50	0.28 ± 0.05	0.06 ± 0.01	55.51
0.540–0.590	0.29 ± 0.23	0.00 ± 0.01	0.25 ± 0.08	0.05 ± 0.02	0.02 ± 0.01	8.63
0.590–0.641	0.00 ± 0.01	···	···	···	···	< 1
0.641–0.691	0.00 ± 0.00	0.00 ± 0.00	6.27 ± 3.17	0.00 ± 0.00	0.02 ± 0.02	1.69
0.691–0.743	0.00 ± 0.01	···	···	···	···	< 1
0.743–0.795	0.00 ± 0.08	···	···	···	···	< 1
0.795–0.848	0.00 ± 0.00	···	···	···	···	< 1
0.848–0.896	0.10 ± 0.10	0.99 ± 1.18	0.81 ± 1.09	0.08 ± 0.04	0.04 ± 0.01	24.23
0.896–0.927	0.90 ± 0.13	1.67 ± 0.14	1.08 ± 0.25	1.19 ± 0.07	0.37 ± 0.02	993.66
0.927–0.945	2.34 ± 0.25	1.89 ± 0.09	1.18 ± 0.23	3.77 ± 0.13	1.06 ± 0.03	3065.68
0.945–0.957	4.06 ± 0.29	1.91 ± 0.06	1.47 ± 0.21	6.98 ± 0.19	2.05 ± 0.05	5240.73
0.957–0.965	5.81 ± 0.34	1.89 ± 0.05	1.66 ± 0.22	10.08 ± 0.26	3.09 ± 0.08	7323.93
0.965–0.972	7.38 ± 0.37	1.91 ± 0.05	2.21 ± 0.31	13.65 ± 0.32	4.45 ± 0.11	9270.31
0.972–0.977	8.63 ± 0.40	1.94 ± 0.04	2.82 ± 0.43	16.89 ± 0.39	5.72 ± 0.14	10490.96
0.977–0.982	9.89 ± 0.41	1.88 ± 0.04	2.88 ± 0.39	18.57 ± 0.42	6.67 ± 0.16	11152.40
0.982–0.986	11.14 ± 0.49	1.83 ± 0.04	2.54 ± 0.34	19.92 ± 0.45	7.22 ± 0.17	11526.16
0.986–0.991	10.98 ± 0.45	1.85 ± 0.04	2.91 ± 0.40	20.13 ± 0.46	7.51 ± 0.19	11994.34
0.991–0.995	10.71 ± 0.41	1.90 ± 0.04	3.65 ± 0.54	20.97 ± 0.47	7.87 ± 0.20	12279.38
0.995–1.000	8.67 ± 0.31	1.91 ± 0.04	4.41 ± 0.69	17.37 ± 0.41	6.80 ± 0.18	10059.25

Note. — An exponentially cutoff power law with $b = 1$ was used to fit the spectrum in each fixed-count phase bin of the Crab light curve. The differential flux prefactor N_0 is given in units of $10^{-9}\,\mathrm{cm}^{-2}\,\mathrm{s}^{-1}\,\mathrm{MeV}^{-1}$; cutoff energy E_c in GeV; photon flux in $10^{-6}\,\mathrm{cm}^{-2}\,\mathrm{s}^{-1}$; and energy flux in $10^{-9}\,\mathrm{erg\,cm}^{-2}\,\mathrm{s}^{-1}$. The phase bins without data had $TS < 1$; the spectral parameters in these bins were unconstrained. In phases 0.641–0.691, $TS > 1$ and $\Gamma = 0$, and there appears to be a constrained measurement of $E_c \sim 6\,\mathrm{GeV}$. This spectral fit is consistent with being part of a flat background with few photons above $\sim 6\,\mathrm{GeV}$, and is not representative of pulsed emission from the Crab.

Table D.3. Phase Resolved Spectral Parameters of the Geminga Pulsar

Phase Bin	N_0	Γ	E_c	Photon Flux	Energy Flux	TS
0.000–0.040	1.13 ± 0.10	1.50 ± 0.08	0.97 ± 0.12	1.39 ± 0.05	0.47 ± 0.01	3245.81
0.040–0.069	1.61 ± 0.12	1.57 ± 0.07	1.16 ± 0.13	2.22 ± 0.07	0.76 ± 0.02	4707.48
0.069–0.089	2.65 ± 0.15	1.47 ± 0.06	1.28 ± 0.12	3.49 ± 0.10	1.35 ± 0.03	7196.15
0.089–0.102	4.02 ± 0.19	1.50 ± 0.05	1.60 ± 0.14	5.75 ± 0.14	2.38 ± 0.06	9788.51
0.102–0.111	6.21 ± 0.27	1.35 ± 0.05	1.55 ± 0.12	8.07 ± 0.19	3.78 ± 0.09	14367.31
0.111–0.118	7.59 ± 0.29	1.39 ± 0.04	1.85 ± 0.15	10.60 ± 0.24	5.20 ± 0.12	16184.52
0.118–0.125	8.51 ± 0.31	1.37 ± 0.04	2.08 ± 0.17	12.15 ± 0.27	6.40 ± 0.15	17972.14
0.125–0.130	10.29 ± 0.38	1.32 ± 0.04	1.82 ± 0.13	13.85 ± 0.31	7.21 ± 0.16	18722.75
0.130–0.136	10.60 ± 0.37	1.28 ± 0.04	1.85 ± 0.13	14.10 ± 0.31	7.67 ± 0.17	18830.17
0.136–0.141	10.58 ± 0.37	1.24 ± 0.04	1.82 ± 0.13	13.75 ± 0.31	7.78 ± 0.18	19289.36
0.141–0.146	10.20 ± 0.36	1.21 ± 0.04	1.72 ± 0.12	12.88 ± 0.29	7.25 ± 0.16	19515.79
0.146–0.153	8.56 ± 0.30	1.25 ± 0.04	1.88 ± 0.13	11.28 ± 0.26	6.43 ± 0.15	17906.72
0.153–0.160	7.35 ± 0.25	1.35 ± 0.04	2.21 ± 0.17	10.54 ± 0.24	5.89 ± 0.14	17591.71
0.160–0.168	6.67 ± 0.25	1.18 ± 0.04	1.65 ± 0.11	8.23 ± 0.19	4.66 ± 0.11	16253.58
0.168–0.178	5.10 ± 0.18	1.36 ± 0.04	2.13 ± 0.17	7.30 ± 0.18	3.93 ± 0.10	12803.87
0.178–0.190	4.16 ± 0.16	1.31 ± 0.04	1.90 ± 0.15	5.65 ± 0.14	3.02 ± 0.07	11471.88
0.190–0.205	3.15 ± 0.11	1.36 ± 0.04	2.20 ± 0.18	4.54 ± 0.12	2.48 ± 0.06	10794.21
0.205–0.222	3.07 ± 0.13	1.25 ± 0.05	1.67 ± 0.13	3.91 ± 0.11	2.09 ± 0.05	9963.21
0.222–0.239	2.61 ± 0.10	1.34 ± 0.05	2.04 ± 0.18	3.67 ± 0.10	1.97 ± 0.05	9481.90
0.239–0.258	2.62 ± 0.11	1.28 ± 0.05	1.78 ± 0.14	3.44 ± 0.09	1.84 ± 0.05	9478.95
0.258–0.277	2.65 ± 0.11	1.26 ± 0.05	1.68 ± 0.13	3.39 ± 0.09	1.80 ± 0.05	9344.63
0.277–0.296	2.73 ± 0.11	1.14 ± 0.05	1.53 ± 0.11	3.22 ± 0.09	1.83 ± 0.05	9648.87
0.296–0.314	2.53 ± 0.10	1.18 ± 0.05	1.75 ± 0.13	3.18 ± 0.09	1.87 ± 0.05	9641.17
0.314–0.333	2.87 ± 0.12	1.08 ± 0.05	1.45 ± 0.10	3.25 ± 0.09	1.88 ± 0.05	10078.44
0.333–0.352	2.72 ± 0.11	1.09 ± 0.05	1.53 ± 0.11	3.17 ± 0.09	1.87 ± 0.05	10014.30
0.352–0.370	2.75 ± 0.11	1.15 ± 0.05	1.70 ± 0.13	3.39 ± 0.09	2.01 ± 0.05	10208.90
0.370–0.388	3.12 ± 0.13	1.02 ± 0.05	1.33 ± 0.09	3.36 ± 0.09	1.95 ± 0.05	10428.73
0.388–0.405	3.06 ± 0.12	1.04 ± 0.05	1.52 ± 0.11	3.50 ± 0.09	2.16 ± 0.05	10700.36
0.405–0.422	2.88 ± 0.11	1.02 ± 0.05	1.53 ± 0.11	3.29 ± 0.09	2.08 ± 0.05	10535.29
0.422–0.439	3.09 ± 0.12	1.00 ± 0.05	1.47 ± 0.10	3.44 ± 0.09	2.18 ± 0.05	10918.70
0.439–0.456	3.28 ± 0.13	1.03 ± 0.05	1.53 ± 0.10	3.74 ± 0.10	2.36 ± 0.06	11547.19
0.456–0.472	3.26 ± 0.13	0.97 ± 0.05	1.40 ± 0.09	3.54 ± 0.09	2.22 ± 0.06	11226.16
0.472–0.489	3.13 ± 0.12	0.95 ± 0.05	1.51 ± 0.10	3.49 ± 0.09	2.34 ± 0.06	11752.45
0.489–0.505	3.21 ± 0.12	1.00 ± 0.05	1.56 ± 0.11	3.68 ± 0.10	2.39 ± 0.06	11436.73
0.505–0.521	3.10 ± 0.11	0.98 ± 0.05	1.62 ± 0.11	3.58 ± 0.10	2.45 ± 0.06	11733.79
0.521–0.536	3.21 ± 0.12	1.07 ± 0.05	1.72 ± 0.12	3.89 ± 0.10	2.52 ± 0.06	11710.15
0.536–0.551	3.43 ± 0.13	0.95 ± 0.05	1.54 ± 0.10	3.86 ± 0.10	2.64 ± 0.07	12103.20
0.551–0.566	3.56 ± 0.13	1.01 ± 0.05	1.62 ± 0.11	4.14 ± 0.11	2.76 ± 0.07	12282.91
0.566–0.579	3.60 ± 0.12	1.06 ± 0.04	2.05 ± 0.14	4.63 ± 0.12	3.41 ± 0.09	13575.87
0.579–0.590	4.35 ± 0.13	1.07 ± 0.04	2.24 ± 0.15	5.78 ± 0.14	4.43 ± 0.11	15467.72
0.590–0.598	5.40 ± 0.15	1.07 ± 0.04	2.42 ± 0.15	7.36 ± 0.17	5.95 ± 0.15	18724.10
0.598–0.605	6.20 ± 0.17	0.93 ± 0.04	2.22 ± 0.13	8.10 ± 0.19	7.25 ± 0.18	20708.25
0.605–0.611	7.69 ± 0.21	1.01 ± 0.04	2.56 ± 0.15	10.63 ± 0.24	9.56 ± 0.24	22498.23
0.611–0.616	8.87 ± 0.23	1.03 ± 0.04	2.64 ± 0.16	12.41 ± 0.27	11.14 ± 0.27	23710.70
0.616–0.621	10.63 ± 0.29	0.98 ± 0.04	2.27 ± 0.13	14.04 ± 0.31	12.07 ± 0.29	23108.12
0.621–0.625	11.09 ± 0.29	1.05 ± 0.03	2.79 ± 0.17	15.83 ± 0.34	14.36 ± 0.35	25370.38
0.625–0.629	11.67 ± 0.30	1.03 ± 0.03	2.69 ± 0.16	16.44 ± 0.35	14.95 ± 0.37	25506.76
0.629–0.632	12.18 ± 0.32	0.98 ± 0.04	2.57 ± 0.15	16.85 ± 0.36	15.66 ± 0.38	24202.92
0.632–0.636	12.68 ± 0.33	0.96 ± 0.04	2.47 ± 0.14	17.30 ± 0.37	16.13 ± 0.39	26613.65
0.636–0.640	12.78 ± 0.33	0.98 ± 0.03	2.54 ± 0.15	17.63 ± 0.38	16.43 ± 0.40	26267.52
0.640–0.643	12.75 ± 0.34	0.99 ± 0.03	2.47 ± 0.14	17.42 ± 0.37	15.62 ± 0.37	24828.33
0.643–0.647	12.36 ± 0.33	1.00 ± 0.04	2.54 ± 0.15	17.04 ± 0.37	15.47 ± 0.38	25853.23
0.647–0.651	11.07 ± 0.29	1.09 ± 0.03	2.89 ± 0.18	16.02 ± 0.35	14.06 ± 0.35	23601.34
0.651–0.656	10.06 ± 0.27	1.09 ± 0.03	2.66 ± 0.17	14.19 ± 0.31	11.86 ± 0.29	22516.26
0.656–0.661	8.41 ± 0.23	1.05 ± 0.04	2.51 ± 0.16	11.59 ± 0.26	9.77 ± 0.24	22277.76
0.661–0.668	6.53 ± 0.18	1.16 ± 0.03	2.93 ± 0.20	9.56 ± 0.22	7.83 ± 0.20	20510.87
0.668–0.676	5.53 ± 0.17	1.10 ± 0.04	2.24 ± 0.15	7.39 ± 0.17	5.46 ± 0.13	17998.09

Table D.3 (cont'd)

Phase Bin	N_0	Γ	E_c	Photon Flux	Energy Flux	TS
0.676–0.688	3.65 ± 0.11	1.29 ± 0.04	2.76 ± 0.21	5.42 ± 0.13	3.65 ± 0.09	13188.91
0.688–0.705	2.73 ± 0.09	1.18 ± 0.04	2.15 ± 0.16	3.67 ± 0.10	2.42 ± 0.06	11521.43
0.705–0.731	1.68 ± 0.07	1.13 ± 0.05	1.77 ± 0.14	2.08 ± 0.06	1.29 ± 0.04	8116.35
0.731–0.765	1.13 ± 0.06	1.27 ± 0.06	1.71 ± 0.17	1.46 ± 0.05	0.77 ± 0.02	5485.69
0.765–0.803	0.92 ± 0.05	1.36 ± 0.07	1.74 ± 0.19	1.26 ± 0.05	0.61 ± 0.02	4494.97
0.803–0.845	0.88 ± 0.06	1.28 ± 0.07	1.39 ± 0.15	1.07 ± 0.04	0.50 ± 0.02	3846.55
0.845–0.893	0.64 ± 0.04	1.36 ± 0.08	1.44 ± 0.18	0.82 ± 0.04	0.36 ± 0.01	2715.60
0.893–0.948	0.70 ± 0.08	1.22 ± 0.12	0.84 ± 0.12	0.67 ± 0.04	0.26 ± 0.01	1878.69
0.948–1.000	0.66 ± 0.08	1.56 ± 0.11	0.95 ± 0.14	0.85 ± 0.04	0.27 ± 0.01	1860.06

Note. — An exponentially cutoff power law with $b = 1$ was used to fit the spectrum in each fixed-count phase bin of the Geminga light curve. The differential flux prefactor N_0 is given in units of $10^{-9}\,\mathrm{cm}^{-2}\,\mathrm{s}^{-1}\,\mathrm{MeV}^{-1}$; cutoff energy E_c in GeV; photon flux in $10^{-6}\,\mathrm{cm}^{-2}\,\mathrm{s}^{-1}$; and energy flux in $10^{-9}\,\mathrm{erg\,cm}^{-2}\,\mathrm{s}^{-1}$. Geminga has magnetospheric emission across its entire pulse phase, so the spectral parameters are constrained at all phases, and the TS is large everywhere (unlike for the Vela and Crab pulsars, which have off-peak phase bins in which $TS < 1$ and the spectral parameters could not be constrained).

Appendix E

Software and Codes Used

The following software and codes were used in this thesis:

1. PRESTO (Ransom 2001; `http://www.cv.nrao.edu:~sransom/presto`)
2. PSRCHIVE (Hotan et al. 2004; van Straten et al. 2012; `http:psrchive.sourceforge.net`)
3. *Fermi* LAT science tools, specifically `gtselect`, `gtmktime`, `gtexpcube2`, `gtbin`, `gtltcube`, `gtsrcprob`, `gtlike` (with `pyLikelihood` python wrapper), and `gtmodel` (`http://fermi.gsfc.nasa.gov/ssc/data/analysis/`)
4. *Fermi* LAT user-contributed tools, specifically `bdlikeSED.py`, written by Tyrel Johnson (`http://fermi.gsfc.nasa.gov/ssc/data/analysis/user/`)
5. NASA's HEASARC `FTOOLS`, specifically `ftpixcalc` (`http://heasarc.gsfc.nasa.gov`)
6. Light curve simulation code ("toypol.c") by J. Dyks and A. Harding, used in Dyks et al. (2004)

7. Markov chain Monte Carlo likelihood fitting code by M. C. Miller (e.g., Lo et al. 2013)

Bibliography

Abdo, A. A., Ackermann, M., Ajello, M., et al. 2010a, ApJS, 188, 405

—. 2010b, ApJ, 713, 154

—. 2009a, Science, 325, 840

—. 2009b, Science, 325, 848

—. 2010c, ApJ, 708, 1254

—. 2010d, ApJ, 720, 272

—. 2010e, ApJ, 711, 64

—. 2010f, A&A, 524, A75

Abdo, A. A., Wood, K. S., DeCesar, M. E., et al. 2012, Astrophysical Journal, 744, 146

Ables, J. G. & Manchester, R. N. 1976, Astronomy and Astrophysics, 50, 177

Ackermann, M., Ajello, M., Allafort, A., et al. 2012, ApJ, 753, 83

Adler, S. L. 1971, Annals of Physics, 67, 599

Albats, P., Frye, G. M., & Thomson, G. B. 1974, Nature, 251, 400

Albert, J., Aliu, E., Anderhub, H., et al. 2008, ApJ, 674, 1037

Antoniadis, J., Freire, P. C. C., Wex, N., et al. 2013, Science, 340, 448

Arons, J. & Scharlemann, E. T. 1979, Astrophysical Journal, 231, 854

Atwood, W. B., Abdo, A. A., Ackermann, M., et al. 2009, ApJ, 697, 1071

Atwood, W. B., Ziegler, M., Johnson, R. P., & Baughman, B. M. 2006, ApJ, 652,

L49

Backer, D. C., Kulkarni, S. R., Heiles, C., Davis, M. M., & Goss, W. M. 1982, Nature, 300, 615

Bai, X.-N. & Spitkovsky, A. 2010a, Astrophysical Journal, 715, 1282

—. 2010b, Astrophysical Journal, 715, 1270

Bangale, P., McLaughlin, M., Roberts, M., et al., in preparation

Baring, M. G. 1991, A&A, 249, 581

Baring, M. G. & Harding, A. K. 1998, ApJ, 507, L55

Barker, B. M. & O'Connell, R. F. 1975, Phys. Rev. D, 12, 329

Becker, W. & Truemper, J. 1997, A&A, 326, 682

Berenger, J. 1996, Journal of Computational Physics, 127, 363

Berenger, J.-P. 1994, Journal of Computational Physics, 114, 185

Blandford, R. & Teukolsky, S. A. 1976, Astrophysical Journal, 205, 580

Blandford, R. D. 2002, in Lighthouses of the Universe: The Most Luminous Celestial Objects and Their Use for Cosmology, ed. M. Gilfanov, R. Sunyaev, & E. Churazov, 381

Blaskiewicz, M., Cordes, J. M., & Wasserman, I. 1991, ApJ, 370, 643

Boyles, J., Lynch, R. S., Ransom, S. M., et al. 2013, Astrophysical Journal, 763, 80

Brainerd, J. J. & Lamb, D. Q. 1987, ApJ, 313, 231

Breton, R. P., Kaspi, V. M., Kramer, M., et al. 2008, Science, 321, 104

Browning, R., Ramsden, D., & Wright, P. J. 1971, Nature Physical Science, 232, 99

Buehler, R., Scargle, J. D., Blandford, R. D., et al. 2012, ApJ, 749, 26

Camilo, F. & Rasio, F. A. 2005, in Astronomical Society of the Pacific Conference Series, Vol. 328, Binary Radio Pulsars, ed. F. A. Rasio & I. H. Stairs, 147

Camilo, F., Ray, P. S., Ransom, S. M., et al. 2009, Astrophysical Journal, 705, 1

Camilo, F., Thorsett, S. E., & Kulkarni, S. R. 1994, Astrophysical Journal, Letters,

421, L15

Caraveo, P. A., Bignami, G. F., De Luca, A., et al. 2003, Science, 301, 1345

Caraveo, P. A., De Luca, A., Marelli, M., et al. 2010, Astrophysical Journal, Letters, 725, L6

Carlson, P., Francke, T., Fuglesang, C., Weber, N., & Suffert, M. 1996, Nuclear Instruments and Methods in Physics Research A, 376, 271

Chaboyer, B. 1999, in Post-Hipparcos Cosmic Candles, Astrophysics and Space Science Library Vol. 237, ed. A. Heck & F. Caputo, 111

Chaboyer, B., Sarajedini, A., & Armandroff, T. E. 2000, AJ, 120, 3102

Chakrabarty, D. 2008, in American Institute of Physics Conference Series 1068, ed. R. Wijnands, D. Altamirano, P. Soleri, N. Degenaar, N. Rea, P. Casella, A. Patruno & M. Linares, 67

Cheng, K. S. 2009, in Astrophysics and Space Science Library, Vol. 357, Astrophysics and Space Science Library, ed. W. Becker, 481

Cheng, K. S., Ho, C., & Ruderman, M. 1986a, Astrophysical Journal, 300, 500

—. 1986b, ApJ, 300, 522

Cheng, K. S., Ruderman, M., & Zhang, L. 2000, Astrophysical Journal, 537, 964

Contopoulos, I. 2005, Astronomy and Astrophysics, 442, 579

Contopoulos, I. & Kalapotharakos, C. 2010, Monthly Notices of the RAS, 404, 767

Contopoulos, I., Kazanas, D., & Fendt, C. 1999, Astrophysical Journal, 511, 351

Cordes, J. M. 2002, in Single-Dish Radio Astronomy: Techniques and Applications, ed. S. Stanimirovic, D. Altschuler, P. Goldsmith, & C. Salter, 227

Cordes, J. M. 2008, in 40 Years of Pulsars: Millisecond Pulsars, Magnetars and More, ed. C. Bassa, Z. Wang, A. Cumming, & V. M. Kaspi, 567

Cordes, J. M. & Lazio, T. J. W. 2002, arXiv:astro-ph/0207156

Craig, H. A. & Romani, R. W. 2012, ApJ, 755, 137

Damour, T. & Deruelle, N. 1986, Ann. Inst. Henri Poincaré Phys. Théor., Vol. 44, No. 3, p. 263 - 292, 44, 263

Damour, T. & Taylor, J. H. 1992, Physical Review D, 45, 1840

Daugherty, J. K. & Bussard, R. W. 1980, ApJ, 238, 296

Daugherty, J. K. & Harding, A. K. 1982, Astrophysical Journal, 252, 337

DeCesar, M. E., Harding, A. K., Kalapotharakos, C., et al. 2013a, in preparation

DeCesar, M. E., Ransom, S. M., Ray, P. S., & Demorest, P. B. 2013b, in preparation

DeCesar, M. E., Harding, A. K., & Miller, M. C. 2011a, in AIP Conf. Ser. 1357, ed. M. Burgay, N. D'Amico, P. Esposito, A. Pellizzoni, & A. Possenti, 285

DeCesar, M. E., Harding, A. K., Miller, M. C., et al. 2011b, arXiv:1111.0325

DeCesar, M. E., Ransom, S. M., & Ray, P. S. 2011c, arXiv:1111.0365

Demorest, P. B., Pennucci, T., Ransom, S. M., Roberts, M. S. E., & Hessels, J. W. T. 2010, Nature, 467, 1081

Deutsch, A. J. 1955, Annales d'Astrophysique, 18, 1

Du, Y. J., Qiao, G. J., Han, J. L., Lee, K. J., & Xu, R. X. 2010, MNRAS, 406, 2671

DuPlain, R., Ransom, S., Demorest, P., et al. 2008, in Society of Photo-Optical Instrumentation Engineers (SPIE) Conference Series, Vol. 7019, Society of Photo-Optical Instrumentation Engineers (SPIE) Conference Series

Dyks, J. & Harding, A. K. 2004, Astrophysical Journal, 614, 869

Dyks, J., Harding, A. K., & Rudak, B. 2004, Astrophysical Journal, 606, 1125

Dyks, J. & Rudak, B. 2003, Astrophysical Journal, 598, 1201

Eatough, R. P., Kramer, M., Lyne, A. G., & Keith, M. J. 2013, Monthly Notices of the RAS, 431, 292

Foster, R. S. & Backer, D. C. 1990, ApJ, 361, 300

Freire, P. C., Kramer, M., & Lyne, A. G. 2001, Monthly Notices of the RAS, 322, 885

Freire, P. C. C., Abdo, A. A., Ajello, M., et al. 2011, Science, 334, 1107

Gaensler, B. M. & Slane, P. O. 2006, ARA&A, 44, 17

Gold, T. 1968, Nature, 218, 731

Goldreich, P. & Julian, W. H. 1969, Astrophysical Journal, 157, 869

Gomez-Gonzalez, J. & Guelin, M. 1974, Astronomy and Astrophysics, 32, 441

Goodwin, S. P., Mestel, J., Mestel, L., & Wright, G. A. E. 2004, Monthly Notices of the RAS, 349, 213

Grindlay, J. E., Brown, R. H., Davis, J., & Allen, L. R. 1973a, in International Cosmic Ray Conference, Vol. 1, International Cosmic Ray Conference, 439

Grindlay, J. E., Helmken, H. F., Weekes, T. C., Fazio, G. G., & Boley, F. 1973b, in International Cosmic Ray Conference, Vol. 1, International Cosmic Ray Conference, 36

Gruzinov, A. 2005, Physical Review Letters, 94, 021101

—. 2006, ApJ, 647, L119

Halpern, J. P., Camilo, F., & Gotthelf, E. V. 2007, ApJ, 668, 1154

Halpern, J. P., Gotthelf, E. V., Camilo, F., Helfand, D. J., & Ransom, S. M. 2004, Astrophysical Journal, 612, 398

Halpern, J. P., Gotthelf, E. V., Mirabal, N., & Camilo, F. 2002, ApJ, 573, L41

Hankins, T. H. & Rickett, B. J. 1975, Methods in Computational Physics, 14, 55

Harding, A. & Muslimov, A. 2005, in Multiwavelength Approach to Unidentified Gamma-Ray Sources, ed. K. S. Cheng & G. E. Romero, 63

Harding, A. K. 2009, in Astrophysics and Space Science Library, Vol. 357, Astrophysics and Space Science Library, ed. W. Becker, 521

Harding, A. K. 2013, Frontiers of Physics, arXiv:1302.0869

Harding, A. K., Baring, M. G., & Gonthier, P. L. 1997, ApJ, 476, 246

Harding, A. K., DeCesar, M. E., Miller, M. C., Kalapotharakos, C., & Contopoulos,

I. 2011, arXiv:1111.0828

Harding, A. K., Grenier, I. A., & Gonthier, P. L. 2007, Ap&SS, 309, 221

Harding, A. K. & Lai, D. 2006, Reports on Progress in Physics, 69, 2631

Harding, A. K. & Muslimov, A. G. 1998, ApJ, 508, 328

—. 2001, ApJ, 556, 987

—. 2002, ApJ, 568, 862

—. 2011a, ApJ, 726, L10

—. 2011b, Astrophysical Journal, 743, 181

Harding, A. K., Muslimov, A. G., & Zhang, B. 2002, ApJ, 576, 366

Harding, A. K. & Preece, R. 1987, ApJ, 319, 939

Harding, A. K., Stern, J. V., Dyks, J., & Frackowiak, M. 2008, Astrophysical Journal, 680, 1378

Hartman, R. C., Bertsch, D. L., Bloom, S. D., et al. 1999, ApJS, 123, 79

Heitler, W. 1954, Quantum theory of radiation

Hellings, R. W. & Downs, G. S. 1983, ApJ, 265, L39

Hessels, J. W. T., Ransom, S. M., Stairs, I. H., et al. 2006, Science, 311, 1901

Hessels, J. W. T., Roberts, M. S. E., McLaughlin, M. A., et al. 2011, in AIP Conf. Ser. 1357, ed. M. Burgay, N. D'Amico, P. Esposito, A. Pellizzoni, & A. Possenti, 40

Hewish, A., Bell, S. J., Pilkington, J. D. H., Scott, P. F., & Collins, R. A. 1968, Nature, 217, 709

Hirotani, K. 2008, Astrophysical Journal, Letters, 688, L25

Hobbs, G. B., Edwards, R. T., & Manchester, R. N. 2006, Monthly Notices of the RAS, 369, 655

Hotan, A. W., van Straten, W., & Manchester, R. N. 2004, Publications of the Astron. Soc. of Australia, 21, 302

Hulse, R. A. & Taylor, J. H. 1975, Astrophysical Journal, Letters, 195, L51

Jackson, J. D. 1975, Classical electrodynamics (New York: Wiley)

Johnson, T. J. 2011, PhD thesis, Univ. of Maryland, arXiv:1209.4000

Johnston, S., Hobbs, G., Vigeland, S., et al. 2005, MNRAS, 364, 1397

Kalapotharakos, C. & Contopoulos, I. 2009, Astronomy and Astrophysics, 496, 495

Kalapotharakos, C., Harding, A. K., Kazanas, D., & Contopoulos, I. 2012a, Astrophysical Journal, Letters, 754, L1

Kalapotharakos, C., Kazanas, D., Harding, A., & Contopoulos, I. 2012b, Astrophysical Journal, 749, 2

Keith, M. J. 2013, in IAU Symposium, Vol. 291, IAU Symposium, 29–34

Kerr, M. 2011, ApJ, 732, 38

Kolmogorov, A. 1941, Akademiia Nauk SSSR Doklady, 30, 301

Kolmogorov, A. N. 1991, Royal Society of London Proceedings Series A, 434, 9

Komissarov, S. S. 2002, MNRAS, 336, 759

—. 2006, MNRAS, 367, 19

Kramer, M. 1998, Astrophysical Journal, 509, 856

Lange, C., Camilo, F., Wex, N., et al. 2001, MNRAS, 326, 274

Large, M. I., Vaughan, A. E., & Wielebinski, R. 1968, Nature, 220, 753

Lattimer, J. M. & Prakash, M. 2004, Science, 304, 536

Li, J., Spitkovsky, A., & Tchekhovskoy, A. 2012, Astrophysical Journal, 746, 60

Lo, K.-H., Miller, M. C., Bhattacharyya, S., & Lamb, F. K. 2013, arXiv:1304.2330

Lommen, A. N. 2012, Journal of Physics Conference Series, 363, 012029

Lorimer, D. & Kramer, M. 2005, Cambridge Observing Handbooks for Research Astronomers, Vol. 4, Handbook of Pulsar Astronomy, 1st edn. (Cambridge, U.K.; New York, U.S.A: Cambridge University Press)

Lynch, R. S., Boyles, J., Ransom, S. M., et al. 2013, Astrophysical Journal, 763, 81

Lyne, A. G. 2008, in 40 Years of Pulsars: Millisecond Pulsars, Magnetars and More, ed. C. Bassa, Z. Wang, A. Cumming, & V. M. Kaspi, 561

Lyne, A. G., Manchester, R. N., Lorimer, D. R., et al. 1998, Monthly Notices of the RAS, 295, 743

Malofeev, V. M. & Malov, O. I. 1997, Nature, 389, 697

Manchester, R. N., Hobbs, G. B., Teoh, A., & Hobbs, M. 2005, Astronomical Journal, 129, 1993

Manchester, R. N., Lyne, A. G., Taylor, J. H., et al. 1978, Monthly Notices of the RAS, 185, 409

Mandal, R. D. R., Konar, S., Dey, M., & Dey, J. 2009, MNRAS, 399, 822

Mattox, J. R., Bertsch, D. L., Chiang, J., et al. 1996, ApJ, 461, 396

McKinney, J. C. 2006, MNRAS, 368, L30

McLaughlin, M. A., Cordes, J. M., Hankins, T. H., & Moffett, D. A. 1999, Astrophysical Journal, 512, 929

Michel, F. C. 1973, ApJ, 180, L133

—. 1982, Reviews of Modern Physics, 54, 1

Mignani, R. P. 2012, in Electromagnetic Radiation from Pulsars and Magnetars, Astronomical Society of the Pacific Conference Series, Vol. 466, ed. W. Lewandowski, O. Maron, & J. Kijak, 3

Moiseev, A. A., Hartman, R. C., Ormes, J. F., et al. 2007, Astroparticle Physics, 27, 339

Moiseev, A. A., Ormes, J. F., Hartman, R. C., et al. 2004, Astroparticle Physics, 22, 275

Moretti, A., Piotto, G., Arcidiacono, C., et al. 2009, A&A, 493, 539

Morini, M. 1983, MNRAS, 202, 495

Muslimov, A. G. & Harding, A. K. 2003, Astrophysical Journal, 588, 430

—. 2004, Astrophysical Journal, 606, 1143

Muslimov, A. G. & Tsygan, A. I. 1992a, MNRAS, 255, 61

—. 1992b, MNRAS, 255, 61

Ng, C.-Y. & Romani, R. W. 2008, Astrophysical Journal, 673, 411

Nolan, P. L., Abdo, A. A., Ackermann, M., et al. 2012, ApJS, 199, 31

Ord, S. M., van Straten, W., Hotan, A. W., & Bailes, M. 2004, MNRAS, 352, 804

Pavlov, G. G., Kargaltsev, O., Wong, J. A., & Garmire, G. P. 2009, ApJ, 691, 458

Phinney, E. S. 1993, in Structure and Dynamics of Globular Clusters, Astronomical Society of the Pacific Conference Series, Vol. 50, ed. S. G. Djorgovski & G. Meylan, 141

Phinney, E. S. & Sigurdsson, S. 1991, Nature, 349, 220

Pierbattista, M., Harding, A. K., Grenier, I. A., et al., in preparation

Pletsch, H. J., Guillemot, L., Fehrmann, H., et al. 2012, Science, 338, 1314

Radhakrishnan, V. & Cooke, D. J. 1969a, Astrophys. Lett., 3, 225

—. 1969b, Astrophys. Lett., 3, 225

Rankin, J. M. 2007, Astrophysical Journal, 664, 443

Ransom, S. M. 2001, PhD thesis, Harvard University

Ransom, S. M., Eikenberry, S. S., & Middleditch, J. 2002, Astronomical Journal, 124, 1788

Ransom, S. M., Greenhill, L. J., Herrnstein, J. R., et al. 2001, Astrophysical Journal, Letters, 546, L25

Ransom, S. M., Hessels, J. W. T., Stairs, I. H., et al. 2005, Science, 307, 892

Ransom, S. M., Ray, P. S., Camilo, F., et al. 2011, ApJ, 727, L16

Ray, P. S., Abdo, A. A., Parent, D., et al. 2012, arXiv:1205.3089

Ray, P. S., Kerr, M., Parent, D., et al. 2011a, Astrophysical Journal, Supplement, 194, 17

—. 2011b, Astrophysical Journal, Supplement, 194, 17

Ray, P. S., Ransom, S. M., Cheung, C. C., et al. 2013, ApJ, 763, L13

Roberts, M. S. E. 2013, in IAU Symposium, Vol. 291, IAU Symposium, 127–132

Romani, R. W. 1996, Astrophysical Journal, 470, 469

Romani, R. W. & Watters, K. P. 2010, Astrophysical Journal, 714, 810

Ruderman, M. A. & Sutherland, P. G. 1975, Astrophysical Journal, 196, 51

Rybicki, G. B. & Lightman, A. P. 1979, Radiative processes in astrophysics

Scharlemann, E. T. & Wagoner, R. V. 1973, ApJ, 182, 951

Scheuer, P. A. G. 1968, Nature, 218, 920

Seidelmann, P. K., Guinot, B., & Doggett, L. E. 1992, Explanatory Supplement to the Astronomical Almanac (Mill Valley, California: University Science Books)

Shapiro, I. I. 1964, Physical Review Letters, 13, 789

Shapiro, S. L. & Teukolsky, S. A. 1986, Black Holes, White Dwarfs and Neutron Stars: The Physics of Compact Objects (New York: Wiley)

Shklovskii, I. S. 1970, Soviet Astronomy, 13, 562

Sigurdsson, S. 2003, in Radio Pulsars, Astronomical Society of the Pacific Conference Series, Vol. 302, ed. M. Bailes, D. J. Nice, & S. E. Thorsett, 391

Sigurdsson, S. & Phinney, E. S. 1993, ApJ, 415, 631

Sokolov, A. A., Ternov, I. M., Bagrov, V. G., Gal'Tsov, D. V., & Zhukovskii, V. C. 1968, Soviet Physics Journal, 11, 4

Spitkovsky, A. 2006, Astrophysical Journal, Letters, 648, L51

Stairs, I. H. 2002, in Single-Dish Radio Astronomy: Techniques and Applications, ed. S. Stanimirovic, D. Altschuler, P. Goldsmith, & C. Salter, 251

Stairs, I. H., Splaver, E. M., Thorsett, S. E., Nice, D. J., & Taylor, J. H. 2000, Monthly Notices of the RAS, 314, 459

Sturner, S. J., Dermer, C. D., & Michel, F. C. 1995, ApJ, 445, 736

Sturrock, P. A. 1971, Astrophysical Journal, 164, 529

Takata, J., Chang, H.-K., & Cheng, K. S. 2007, ApJ, 656, 1044

Tam, P. H. T., Kong, A. K. H., Hui, C. Y., et al. 2011, Astrophysical Journal, 729, 90

Taylor, J. H. & Weisberg, J. M. 1982, Astrophysical Journal, 253, 908

The Fermi-LAT Collaboration 2013, arXiv:1305.4385

Thompson, D. J. 2001, in American Institute of Physics Conference Series, Vol. 558, ed. F. A. Aharonian & H. J. Völk, 103

Thompson, D. J. 2008, Reports on Progress in Physics, 71, 116901

Thompson, D. J., Fichtel, C. E., Kniffen, D. A., & Ogelman, H. B. 1975, ApJ, 200, L79

Timokhin, A. N. 2006, MNRAS, 368, 1055

Usov, V. V. & Melrose, D. B. 1995, Australian Journal of Physics, 48, 571

van Straten, W., Demorest, P., & Oslowski, S. 2012, Astronomical Research and Technology, 9, 237

Vats, H. O., Singal, A. K., Deshpande, M. R., et al. 1999, MNRAS, 302, L65

Venter, C. & de Jager, O. C. 2008, Astrophysical Journal, Letters, 680, L125

Venter, C., Harding, A. K., & Guillemot, L. 2009, ApJ, 707, 800

Venter, C., Johnson, T. J., & Harding, A. K. 2012, Astrophysical Journal, 744, 34

Verde, L., Peiris, H. V., Spergel, D. N., et al. 2003, Astrophysical Journal, Supplement, 148, 195

VERITAS Collaboration, Aliu, E., Arlen, T., et al. 2011, Science, 334, 69

Watters, K. P., Romani, R. W., Weltevrede, P., & Johnston, S. 2009, Astrophysical Journal, 695, 1289

Weisberg, J. M., Nice, D. J., & Taylor, J. H. 2010, Astrophysical Journal, 722, 1030

Weisberg, J. M., Romani, R. W., & Taylor, J. H. 1989, Astrophysical Journal, 347,

1030

Weisskopf, M. C., Tennant, A. F., Yakovlev, D. G., et al. 2011, Astrophysical Journal, 743, 139

Wex, N. & Kopeikin, S. M. 1999, ApJ, 514, 388

Wilks, S. S. 1938, Annals of Mathematical Statistics, 9, 60

Wunner, G. 1979, Physical Review Letters, 42, 79

Yadigaroglu, I.-A. & Romani, R. W. 1995, ApJ, 449, 211

Yadigaroglu, I.-A. G. 1997, PhD thesis, Stanford University

Yan, W. M., Manchester, R. N., van Straten, W., et al. 2011, MNRAS, 414, 2087

Yee, K. 1966, IEEE Transactions on Antennas and Propagation, 14, 302